Springer Theses
Recognizing Outstanding Ph.D. Research

Jonathan J. Scragg

Copper Zinc Tin Sulfide Thin Films for Photovoltaics

Synthesis and Characterisation by Electrochemical Methods

Springer

Springer Theses

Recognizing Outstanding Ph.D. Research

For further volumes:
http://www.springer.com/series/8790

Aims and Scope

The series “Springer Theses” brings together a selection of the very best Ph.D. theses from around the world and across the physical sciences. Nominated and endorsed by two recognized specialists, each published volume has been selected for its scientific excellence and the high impact of its contents for the pertinent field of research. For greater accessibility to non-specialists, the published versions include an extended introduction, as well as a foreword by the student’s supervisor explaining the special relevance of the work for the field. As a whole, the series will provide a valuable resource both for newcomers to the research fields described, and for other scientists seeking detailed background information on special questions. Finally, it provides an accredited documentation of the valuable contributions made by today’s younger generation of scientists.

Theses are accepted into the series by invited nomination only and must fulfill all of the following criteria

- They must be written in good English.
- The topic should fall within the confines of Chemistry, Physics and related interdisciplinary fields such as Materials, Nanoscience, Chemical Engineering, Complex Systems and Biophysics.
- The work reported in the thesis must represent a significant scientific advance.
- If the thesis includes previously published material, permission to reproduce this must be gained from the respective copyright holder.
- They must have been examined and passed during the 12 months prior to nomination.
- Each thesis should include a foreword by the supervisor outlining the significance of its content.
- The theses should have a clearly defined structure including an introduction accessible to scientists not expert in that particular field.

Jonathan J. Scragg

Copper Zinc Tin Sulfide Thin Films for Photovoltaics

Synthesis and Characterisation by Electrochemical Methods

Doctoral Thesis accepted by
The University of Bath, UK

Springer

Author
Dr. Jonathan J. Scragg
Solid State Electronics
The Angstrom Laboratory
Uppsala
Sweden
e-mail: jonathan.scragg@angstrom.uu.se

Supervisor
Prof. Dr. Laurence Peter
Department of Chemistry
University of Bath
Bath BA2 7AY
UK
e-mail: l.m.peter@bath.ac.uk

ISSN 2190-5053
ISBN 978-3-642-22918-3
DOI 10.1007/978-3-642-22919-0
Springer Heidelberg Dordrecht London New York

e-ISSN 2190-5061
e-ISBN 978-3-642-22919-0

Cover design: eStudio Calamar, Berlin/Figueres

Printed on acid-free paper

Springer is part of Springer Science+Business Media (www.springer.com)

Parts of this thesis have been published in the following journal articles:

Scragg JJ, Berg DM, Dale PJ (2010) A 3.2% efficient Kesterite device from electrodeposited stacked elemental layers. J Electroanal Chem 646(1–2):52–59.

Zoppi G, Forbes I, Miles RW, Scragg J et al (2009) $Cu_2ZnSnSe_4$ thin film solar cells produced by selenisation of magnetron sputtered precursors. Prog Photovolt 17(5):315–319.

Scragg JJ, Dale PJ, Peter LM et al (2008) New routes to sustainable photovoltaics: evaluation of Cu_2ZnSnS_4 as an alternative absorber material. Phys Status Solidi B-Basic Solid State Phys 245(9):1772–1778.

Scragg JJ, Dale PJ, Peter LM (2008) Towards sustainable materials for solar energy conversion: preparation and photoelectrochemical characterization of Cu_2ZnSnS_4. Electrochem Commun 10(4):639–642.

Dale PJ, Hoenes K, Scragg J et al Corporate Author(s): IEEE (2009) A review of the challenges facing kesterite based thin film solar cell. 34th IEEE photovoltaic specialists conference, (1–3) Jun 2009, Philadelphia, pp. 1956–1961.

Scragg JJ, Wolverson D, Zoppi G, Peter LM (2010) Optimizing sulfurisation conditions in the fabrication of Cu_2ZnSnS_4 absorber layers from electroplated precursors. Photovoltaic materials and manufacturing issues II, 1210-Q06-03 (2010), MRS fall meeting 2009, Boston.

Scragg JJ, Dale PJ, Peter LM (2009) Synthesis and characterization of Cu_2ZnSnS_4 absorber layers by an electrodeposition-annealing route. Thin Solid Films 517(7):2481–2484. Symposium on thin film chalcogenide photovoltaic materials, EMRS 2008 spring conference, May 2008, Strasbourg, France.

Supervisor's Foreword

Energy is the most important technological problem facing the world in the twenty-first century. Current world power consumption is around 13 TW, more than 80% of which is generated from oil, gas, and coal. The search for sustainable alternatives is driven by the increasing recognition that mankind's demand for energy is already causing changes in climate that will have serious long-term consequences for the planet. Part of the solution to this problem must come from increased exploitation of solar energy. The solar resource is enormous: the solar power incident on the earth is 120,000 TW; or put another way, more energy from the sun reaches the earth in 1 h than the planet consumes in an entire year. However, the widespread deployment of solar cells has resource and sustainability consequences that need to be considered as a matter of urgency. Currently there are three main commercial photovoltaic technologies: silicon, cadmium telluride (CdTe) and copper indium (gallium) diselenide (CIGS). CdTe and CIGS are examples of thin film technologies that promise to be cheaper than silicon and require less energy for manufacture. Large scale deployment of CdTe and CIGS cells is beginning now, but at some point both technologies may run into sustainability problems. Tellurium and Indium are both relatively rare elements, and in addition cadmium is toxic. These concerns justify the search for alternative materials that are earth-abundant and non-toxic. Jonathan Scragg's thesis deals with a very promising material that satisfies these requirements: copper zinc tin sulphide (CZTS). This semiconductor is a potential replacement for CIGS, but very little work had been carried out on its preparation and characterization when Jonathan started his Ph.D. work. The thesis describes a systematic study of the fabrication of CZTS via electrodeposition of the metal elements followed by annealing in sulfur. Jonathan's work has gone a long way towards unravelling the reactions taking place during rapid thermal processing of the metallic precursor films, and his characterization of the optoelectronic properties of the CZTS films produced by the electrodeposition-annealing route has paved the way for further development of this emerging sustainable thin film material. This thesis marks a significant chapter in the story of CZTS.

Bath, August 2011 Laurence Peter

Acknowledgments

First and foremost I thank my supervisor, Laurie Peter, whose breadth of interests allowed me the freedom to pursue an initially rather off-piste project. There seems to be little that he does not know, and he has been an invaluable source of ideas and inspiration. Above all, I thank him for giving the appearance of unswerving confidence that I knew what I was doing at every stage of this project.

I would also like to thank the members of the Peter group, past and present, for being excellent company throughout the trials and tribulations of the Ph.D. process.

This project would never even have begun without Phillip Dale, who got me involved in CZTS and patiently set me going with my Ph.D. research. His enthusiasm and dedication have been inspirational. Thanks also to Dominik Berg in Phil's new group at Luxembourg University, for many interesting discussions.

Guillaume Zoppi at Northumbria University has provided assistance, advice and free accommodation on many occasions, and I am very thankful for his hard work.

Various people have been invaluable for their help with XRD measurements, including Gabriele Kociok-Köhn at Bath and Omeed Karimi and Sophie Beckett at Cranfield. My thanks also go to Daniel Wolverson for providing Raman spectroscopy measurements.

Many thanks also to Paul Frith, who built the RDE setup as well as several furnaces and other miscellaneous items that were essential to this project.

Finally, of course, I thank my parents and sister, Jill and Ray and Rebecca, among other things for dinners, proofreading, and provision of 'my office', their living room, for the past few months.

All of the work presented in this thesis was carried out by the author, with the following exceptions:

(1) The Raman spectroscopy measurements presented in Chaps. 3 and 4 were made by Dr. Daniel Wolverson from the department of Physics, University of Bath.

(2) The secondary ion mass spectrometry measurements were made by Dr. Guillaume Zoppi at the Northumbria photovoltaics applications centre, Northumbria University.

Contents

Abbreviations

AAS	Atomic absorption spectroscopy
AFM	Atomic force microscopy
CE	Counter electrode
CIGS	$Cu(In,Ga)(S,Se)_2$
CIS	$CuInS_2$
CTS	Cu_2SnS_3
CZTS	Cu_2ZnSnS_4
EDS	Energy dispersive X-ray spectroscopy
EQE	External quantum efficiency
HER	Hydrogen evolution reaction
KCN	Potassium cyanide
NHE	Normal hydrogen electrode
OVC	Ordered vacancy compound
RBS	Rutherford backscattering spectrometry
RE	Reference electrode
RTP	Rapid thermal processor/processing
SEL	Stacked elemental layer(s)
SEM	Scanning electron microscopy
SIMS	Secondary Ion mass spectrometry
SLG	Soda-lime glass
TPD	Ternary phase diagram
UPD	Underpotential deposition
WE	Working electrode
XRD	X-ray diffraction

Symbols

A	Area (cm^2)
α	Absorption coefficient/Transfer coefficient/ Cu/(Zn+Sn) compositional ratio (cm^{-1}/–/–)
b	Spectral flux density (Js^{-1} cm^{-2}eV^{-1})
β	Zn/Sn compositional ratio (F) (–)
C_{hkl}	Texture coefficient (–)
C	Capacitance (F)
D	Diffusion coefficient (cm^{2}s^{-1})
d_{hkl}	Lattice spacing of *hkl* planes (Å)
E	Electrode potential/photon energy (V/eV)
E_{fb}	Flat-band potential (V)
E_g	Band gap (eV)
E_i, E_i^0	Reduction potential of species *i*, Standard reduction potential of species *i* (V)
ε_0	Vacuum permittivity (Fm^{-1})
ε_r	Sample permittivity (–)
η	Overpotential (V)
F	Faraday constant (Cmol^{-1})
$\Delta_f G$	Free energy of formation (kJmol^{-1})
h, k, l	Miller indices (–)
hv	Photon energy (eV)
I	Light intensity (Js^{-1}cm^{-2}eV^{-1})
I_{hkl}	Intensity of *hkl* peak in XRD (–)
J	Current density (mAcm^{-2})
J_{sc}	Short circuit current density (mAcm^{-2})
k	Boltzmann constant (JK^{-1})
L_n	Diffusion length (m)
λ	Wavelength (nm)
m	Mass (kg)
[M]	Concentration (mol cm^{-3})
M_R	Relative atomic mass (g mol^{-1})

N_a	Acceptor concentration (cm^{-3})
n	Molar quantity/number of XRD peaks (mol)
υ	Kinematic viscosity ($\mathrm{cm}^2\mathrm{s}^{-1}$)
P	Pressure (mbar)
$\Delta\varphi$	Degree of band bending (V)
Φ	External quantum efficiency (–)
φ	Electrodeposition efficiency (–)
Q	Charge (C)
q	Electronic charge/charge density ($\mathrm{C/Ccm}^{-2}$)
R	Gas constant/reflection coefficient ($\mathrm{J\ mol\ K}^{-1}$/–)
r	Atomic ratio (–)
ρ	Density ($\mathrm{g\ cm}^{-3}$)
σ	Degree of preferential orientation/expansion factor (–/–)
Σ	XRD peak for CZTS, CTS or ZnS (–)
T	Temperature/transmission coefficient (°C/–)
t	Time/thickness (s/m)
θ	Diffraction angle (°)
V_{Cu}	Cu vacancy (–)
V	Volume (cm^3)
W	Space charge region width (m)
ω	Rotation rate (rads^{-1})
x	Distance (m)
z	Charge coefficient on metal ion (–)

Chapter 1
Introduction

This thesis is concerned with a relatively new compound semiconductor material that has a great deal of potential for use in photovoltaic (PV) energy systems. Cu_2ZnSnS_4, abbreviated to 'CZTS', is closely related to a family of materials that have been in development for PV applications since the 1970s [1], and have reached mass production in recent years. PV systems generate power by direct transfer of the energy in sunlight into electrical current, and they have the potential to provide vast amounts of renewable energy. This fact has been long recognised, but historically the costs of PV have been high and the manufacturing capacity too low to have a significant impact on the energy generation sector. This is now changing; there are increasing concerns about the effects and causes of climate change, and the fact that current energy sources are finite, polluting and insecure.

1.1 Thin Film Photovoltaics

The fastest growing sector of the PV market is based on 'thin film' PV technologies. The 'thin film' materials in this context are semiconductors that overcome one limitation of crystalline silicon—the benchmark PV material—in that they have direct band gaps. This means that their light absorption coefficients are very high, and much thinner films of material can be used to be used to collect the same amount of light, making them less materials-intensive. In the most part, the thin film materials are compound *p*-type semiconductors, the major systems being $Cu(In,Ga)(S,Se)_2$ (CIGS), $CuInS_2$ (CIS) and CdTe. The power conversion efficiency record for laboratory scale CIGS devices has recently exceeded 20% for the first time [2]. Another key advantage of these materials as compared to Si is their tolerance to defects and grain boundaries, which allows for less stringent quality requirements [3]. At the same time, their compound nature means that the range of processing methods available to produce them is immense. The success of CIGS, CIS and CdTe is only diminished by the fact that they contain expensive and rare materials. The cost and availability of In is a particular issue that will become pressing in the context of the anticipated deployment of PVs on terawatt scales [4, 5].

J. J. Scragg, *Copper Zinc Tin Sulfide Thin Films for Photovoltaics*,
Springer Theses, DOI: 10.1007/978-3-642-22919-0_1,

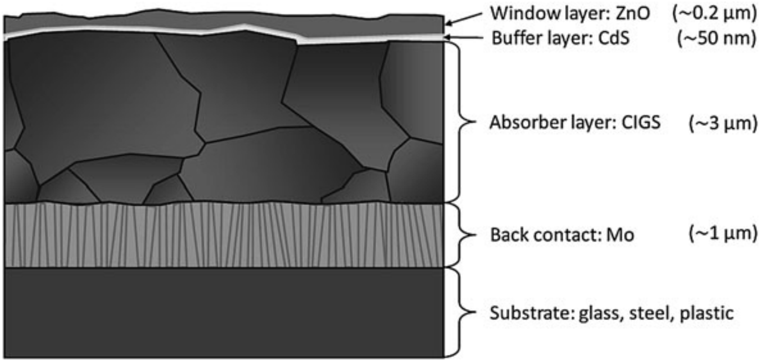

Fig. 1.1 Schematic cross-sectional diagram of a thin film PV cell, showing the layers that comprise it

For reference, a typical thin film device structure is shown in Fig. 1.1, illustrated for the case of a CIS or CIGS device. The *p*-type materials discussed above form the ‘absorber’ layer in the device, the layer where incident light is absorbed resulting in the excitation of electrons. The PV effect—the all-important generation of a potential difference that causes a current to flow—occurs at the interface between the absorber layer and a transparent *n*-type semiconductor. The *n*-type half of the device is actually composed of two layers, a ‘buffer’ layer of CdS which is very thin (~ 50 nm) and a thicker ‘window’ layer of ZnO. Electrical contact is made with the top of the device by addition of a transparent conducting oxide and metallic contact grid. The absorber layer is fabricated on a Mo-coated substrate, which provides mechanical strength and electrical contact to the back of the film.

1.2 CZTS: Properties, History and Device Efficiencies

CZTS is notionally derived from CIS by substitution of two In atoms for one Zn and one Sn atom. This isoelectronic substitution produces a material with many of the same properties of the parent compound, but one that crucially no longer contains any rare or expensive elements. The desirable properties include *p*-type conductivity, a high absorption coefficient ($\alpha > 10^4$ cm^{-1}, equivalent to 90% of the incident light being absorbed within 100 nm of the surface) and band gap of around 1.5 eV (the theoretical optimum value for solar energy conversion [6]). Another advantage of the similarity between CZTS and CIS is that CZTS may be substituted directly into the standard device structure (Fig. 1.1). The quaternary Cu–Zn–Sn–S system is also interesting from the viewpoint of fundamental science, as it further increases the complexity of the defect chemistry and electronic structure, while providing additional opportunities for materials optimisation by control of stoichiometry and compositional gradients. The compound $Cu_2ZnSnSe_4$ (CZTSe) is derived similarly, and has a band gap of around 0.9 eV [7]. The alloying of CZTS and CZTSe to form a pentanary system is another aspect that is already being explored, although this investigation is focussed only on CZTS.

The potential of CZTS was recognised around 20 years ago by Ito and Nakazawa, who prepared films by atom beam sputtering of a synthetic CZTS powder source and demonstrated a PV effect at the junction between CZTS and cadmium–tin–oxide [8]. In the following decades, Katagiri et al. [9] made steady improvements in device efficiency, which reached 6.7% in 2007 for a co-sputtered CZTS film that was annealed for three hours with H_2S. Very recently there has been huge growth in the number of publications relating to CZTS and CZTSe, with a great variety of techniques employed to synthesise and study them. The current best device efficiency is a very promising 9.6% for a $Cu_2ZnSn(S,Se)_4$-based device, which is even more interesting given that this film was synthesised using a solution-based method to deposit a precursor followed by heating with sulfur [10]. Despite these rapid improvements, the number of detailed experimental studies of the basic properties of CZTS has been relatively limited; most reports are directed at the production of devices rather than achieving an understanding of the material itself.

1.3 Fabrication Processes for Thin Film Materials

In general, the processes used to fabricate thin films fall into two categories, which we can describe as ‘single-stage’ and ‘two-stage’. As the name suggests, single-stage processes fabricate the complete, crystalline film in one step. A prime example of this is the co-evaporation of all the elements onto heated substrates, which has produced the best CIGS devices to date [2], although interestingly this is not so far the case for CZTS. Two-stage processes comprise the majority of the available preparation methods, and include most of the ‘low-cost’ approaches. The first stage is preparation of a ‘precursor’, which is generally made at room temperature, and contains either (a) only the metallic elements or (b) all the elements in an un-reacted or non-crystalline form. In the second stage, the precursor is heated, usually in an atmosphere containing a source of S (or Se). This is referred to as ‘sulfurisation’ (or ‘selenisation’). The heating stage induces formation and crystallisation of the desired phase from the precursor film. The first stage can be carried out in a great variety of different ways, examples from the CZTS literature including: electron beam evaporation [11], sputtering [9], pulsed laser deposition [12], spray pyrolysis [13], nanoparticle or suspension printing [14] and electrodeposition [15]. The second, heating stage is similar in most instances. The crystallisation of CZTS during the heating stage is therefore a matter of considerable interest and has been the subject of several publications [16–18].

1.4 Electrodeposition for CZTS Precursor Production

This project used a two-stage approach to produce CZTS films: electrodeposition of metallic precursor followed by sulfurisation. Electrodeposition is a widespread technique for fabricating films, often but not exclusively metals or metal alloys. The process consists of immersion of a substrate in a solution of the metal ions and application of a suitable voltage (potential difference) which causes the ions to be chemically reduced at the substrate surface. The advantages of electrodeposition from a commercial viewpoint are that it can be performed in ambient conditions, it uses relatively small amounts of energy and it is particularly efficient in terms of materials utilisation [19]. Electrodeposition has been used successfully to produce thin film materials for solar cells; both metallic and compound precursors have been fabricated. Notable examples are the BP Apollo process for CdTe [20] and the CISEL process for CIGS [21], both producing devices with efficiencies of around 10%.

At the start of this project, there were no reports of the use of electrodeposition to fabricate CZTS films. Early work from this project was published in 2008 [15, 22], and in the following year there were other publications based on simultaneous work in which similar approaches were used [23–25].

There are three strategies for precursor preparation by electrodeposition, which have all since been employed for CZTS: (a) direct compound deposition [26, 27], (b) co-deposition of a mixed/alloy Cu–Sn–Zn precursor [17, 24] and (c) deposition of sequential layers of Cu, Sn and Zn (the stacked elemental layer, or SEL approach) [15, 28]. The first approach is experimentally challenging and has so far not yielded working devices, although progress is promising. The latter two approaches have both given device efficiencies of around 3% for both alloy [24, 25] and SEL deposition [29]. This investigation makes use of the SEL approach.

Since the various publications concerning CZTS fabrication by electrodeposition only appeared in the latter stages of this project, they did not fundamentally inform the work carried out herein. Therefore they will only be mentioned briefly in Chap. 2.

1.5 Sulfurisation of CZTS Precursors

As mentioned above, the second stage of the two-stage process is similar regardless of the method used to produce the precursor. A typical approach is to heat the samples under a flow of H_2S in N_2 at a temperature of between 500 and 600 °C. The current best device used a multi-step deposition and sulfurisation process, and in this sense is not a classic example of sulfurisation. The previous record device was sulfurised for 3 h at 580 °C, which is more representative of the typical conditions used for CZTS [9]. The effects of sulfurisation conditions will be discussed in more detail in Chap. 4. The traditional equipment for sulfurisation is a tube furnace, which heats up and cools down relatively slowly. The formation reactions for CZTS have been described for such a process by Schurr et al. [17], and are discussed in Chap. 3. In this investigation, a rapid thermal processing (RTP) system was used to sulfurise the samples. RTP enables very short sulfurisation times and very high heating and cooling rates, and has been employed to produce CIS devices with high efficiency using sulfurisation times of only 3 min [30]. This type of approach is interesting from the point of view of mass production, since it enables high throughput. In its use of RTP, the current work is unique in the CZTS field, to the best of our knowledge, and the approach has allowed us to make some interesting time-resolved studies of CZTS formation at high heating rates, which are presented in Chap. 3.

1.6 Measuring the Opto-Electronic Properties of CZTS Films

In order to develop good processing techniques for the absorber layer of a PV device, it is essential to be able to measure its opto-electronic properties. This requires making electronic contact with the absorber layer, which in many cases is achieved by the fabrication of a complete device, as illustrated in Fig. 1.1. The properties of the device are then measured, such as its photovoltage, current under simulated solar illumination and its light-to-current conversion efficiency. Changes in the properties of the device are then attributed to changes in the absorber layer. On the one hand, this approach is expedient since it is inherently a device-optimisation strategy. On the other hand, it relies on the formation of a good junction between CZTS and the *n*-type layers, and since the fundamental properties of CZTS are not well characterised, it may be the case that the standard device configuration is not optimal for CZTS; for example, CdS may not be the perfect match to CZTS in terms of band alignment. Ideally, we would examine the properties of the absorber layer in isolation, and then design the rest of the device based on our findings. In this investigation, device fabrication was not an option since facilities did not exist at the University. However, the alternative methodology that we adopted for opto-electronic characterisation does have its own advantages, in the light of the above discussion. In this investigation, contact with the absorber layer was made by means of an electrolyte in which the layer was immersed. As will be explained in Chap. 5, this contact has similar properties to the *p*–*n* junction of a real device, but its properties are primarily determined by the absorber layer. With some exceptions, the same measurements may be carried out on this 'photoelectrochemical' system as can be carried out on complete devices.

1.7 The Objectives of This Investigation

The objectives of this investigation were as follows:

1. To develop an electrodeposition-route to fabricate CZTS precursors, using the SEL approach. The success of this objective is judged by the ability to produce a film of controlled, uniform composition which can be varied rationally as required.
2. To optimise the sulfurisation process used to convert the precursor into a CZTS film; to achieve complete conversion and demonstrate the correct phase and suitable properties for a thin film device.
3. To investigate the sulfurisation process in detail, in an attempt to attain an understanding of the reported processes used in the literature; at the same time to develop an RTP process for the absorber layers.

The first objective is the most fundamental, and in this investigation it was the ‘rate limiting’ step in terms of the progress of the latter objectives. Initial success with the electrodeposition sulfurisation method using a tube furnace achieved, in part, objectives 1 and 2. The uniformity of the electrodeposited precursors was an issue, however, and so time was then devoted to making fundamental improvements to this stage of the process. The content of the current report is based entirely on results deriving from these latter improvements in the electrodeposition step, which coincided with the arrival of the RTP system. Through improvements of the precursor uniformity, it was possible to make good progress with objective 3. The early work was published elsewhere [15, 22, 23].

1.8 The Structure of This Report

This report consists of four experimental chapters. Each chapter begins with an introduction to the relevant literature and theory that is utilised in the experimental work. After the results are presented, they are discussed in the light of the literature available, and finally conclusions are drawn. The first chapter concerns the production of precursor films by electrodeposition. The next chapter is concerned with the emergence of the CZTS phase in the initial few minutes of the rapid thermal sulfurisation process. In Chap. 4, we explore how the sulfurisation conditions and precursor composition affect the progress of the reaction, and in the closely related final chapter, the effects of these variables on the opto-electronic properties of the films in studied. At the end of the report, the conclusions from each chapter are gathered and recommendations are made for future studies.

References

1. Luque A, Hegedus S (eds) (2003) Handbook of photovoltaic science and engineering. Wiley, Chichester
2. ZSW thin-film solar cell reaches 20.1% efficiency. 4 May 2010 (cited 27 May 2010; Available from: http://www.renewableenergyfocus.com/view/9182/zsw-thinfilm-solar-cell-reaches-201-efficiency/)
3. Siebentritt S, Rau U (eds) (2006) Wide-gap chalcopyrites. Spinger, Berlin
4. Green MA (2009) Estimates of te and in prices from direct mining of known ores. Prog Photovoltaics Res Appl 17(5):347–359
5. Feltrin A, Freundlich A (2006) Material considerations for terawatt level deployment of photovoltaics. In: Symposium on materials, devices, and prospects for sustainable energy of the European-materials-research-society meeting, Pergamon-Elsevier Science Ltd, Nice, France
6. Nelson J (2003) The physics of solar cells. Imperial College Press, London
7. Zoppi G et al (2009) $Cu_2ZnSnSe_4$ thin film solar cells produced by selenisation of magnetron sputtered precursors. Prog Photovoltaics Res Appl 17(5):315–319
8. Ito K, Nakazawa T (1988) Electrical and optical-properties of stannite-type quaternary semiconductor thin-films. Jpn J Appl Phys Part 1 27(11):2094–2097 (Regular Paper Short Notes and Review Paper)
9. Katagiri H et al (2008) Enhanced conversion efficiencies of Cu_2ZnSnS_4-based thin film solar cells by using preferential etching technique. Appl Phys Express 1(4):041201
10. Todorov TK, Reuter KB, Mitzi DB (2010) High-efficiency solar cell with earth-abundant liquid-processed absorber. Adv Mater 22(20):E156–159
11. Katagiri H et al (1997) Preparation and evaluation of Cu_2ZnSnS_4 thin films by sulfurization of E–B evaporated precursors. Sol Energy Mater Sol Cells 49(1–4):407–414
12. Moriya K, Tanaka K, Uchiki H (2008) Cu_2ZnSnS_4 thin films annealed in H2S atmosphere for solar cell absorber prepared by pulsed laser deposition. Jpn J Appl Phys 47(1):602–604
13. Yoo H, Kim J (2010) Growth of Cu_2ZnSnS_4 thin films using sulfurization of stacked metallic films. Thin Solid Films 518(22):6567–6572
14. Todorov T, Mitzi DB (2010) Direct liquid coating of chalcopyrite light-absorbing layers for photovoltaic devices. Eur J Inorg Chem 2010(1):17–28
15. Scragg JJ, Dale PJ, Peter LM (2008) Towards sustainable materials for solar energy conversion: preparation and photoelectrochemical characterization of Cu_2ZnSnS_4. Electrochem Commun 10(4):639–642
16. Schorr S et al (2009) In situ investigation of the kesterite formation from binary and ternary sulphides. Thin Solid Films 517(7):2461–2464
17. Schurr R et al (2009) The crystallisation of Cu_2ZnSnS_4 thin film solar cell absorbers from co-electroplated Cu-Zn-Sn precursors. Thin Solid Films 517(7):2465–2468
18. Weber A et al (2009) In situ XRD on formation reactions of Cu_2ZnSnS_4 thin films. Phys Status Solidi C 6(5):1245–1248
19. Schlesinger M, Paunovic M (eds) (2000) Modern electroplating, 4th edn. Wiley, New York
20. Cunningham D, Rubcich M, Skinner D (2002) Cadmium telluride PV module manufacturing at BP solar. Prog Photovoltaics 10(2):159–168
21. Lincot D et al (2004) Chalcopyrite thin film solar cells by electrodeposition. Sol Energy 77(6):725–737
22. Scragg JJ et al (2008) New routes to sustainable photovoltaics: evaluation of Cu_2ZnSnS_4 as an alternative absorber material. Phys Status Solidi B Basic Solid State Phys 245(9):1772–1778
23. Scragg JJ, Dale PJ, Peter LM (2009) Synthesis and characterization of Cu_2ZnSnS_4 absorber layers by an electrodeposition-annealing route. Thin Solid Films 517(7):2481–2484
24. Hideaki A et al (2009) Preparation of Cu_2ZnSnS_4 thin films by sulfurization of co-electroplated Cu–Zn–Sn precursors. Phys Status Solidi C 6(5):1266–1268

25. Ennaoui A et al (2009) Cu_2ZnSnS_4 thin film solar cells from electroplated precursors: novel low-cost perspective. Thin Solid Films 517(7):2511–2514
26. Pawar SM et al (2010) Single step electrosynthesis of Cu_2ZnSnS_4 (CZTS) thin films for solar cell application. Electrochim Acta 55(12):4057–4061
27. Chan CP, Lam H, Surya C (2010) Preparation of Cu_2ZnSnS_4 films by electrodeposition using ionic liquids. Sol Energy Mater Sol Cells 94(2):207–211
28. Araki H et al (2009) Preparation of Cu_2ZnSnS_4 thin films by sulfurizing electroplated precursors. Sol Energy Mater Sol Cells 93(6–7):996–999
29. Scragg JJ, Berg D, Dale PJ (2010) A 3.2% efficient kesterite device from electrodeposited stacked elemental layers. J Electroanal Chem 646(1–2):52–59
30. Klaer J, Klenk R, Schock HW (2007) Progress in the development of $CuInS_2$ based mini-modules. Thin Solid Films 515(15):5929–5933

Chapter 2
Electrodeposition of Metallic Precursors

Background

Electrochemistry is an extremely broad subject area, so the following introduction will focus primarily on the concepts required for electrochemical deposition (electrodeposition). Only a brief overview will be given, and the reader is referred to Bard and Faulkner [1] for further details.

2.1 Electrochemical Deposition (Electrodeposition)

2.1.1 The Electrochemical Cell and the Deposition Reaction

In an electrochemical cell, two conductive electrodes are immersed in an electrolyte containing a certain concentration of a reducible or oxidisible component. Additionally, a large background concentration of inert ions is provided to ensure good electrical conductivity in the solution. The electrodes are connected to an external, controllable voltage (potential difference), and when a sufficient potential difference, E, is applied between them, a current may flow. Within the bulk of the electrodes the current is carried by electron drift and within the bulk of the solution an equal current is carried by drift of ions. It is at the electrode-solution interface where the field of electrochemistry becomes relevant: at this interface the current is supported by transfer of electrons between the electrode and the species in solution (Fig. 2.1).

For electron transfer to occur there must be an easily reducible ionic species in the solution. In the case of electrodeposition, a solution of metal cations is provided, and the product of electron transfer at the electrode-solution interface is an insoluble material, which should adhere to the electrode. Taking the example of Cu electrodeposition from an electrolyte containing Cu^{2+}/SO_4^{2-}, the electrochemical process at the negative electrode (the cathode), which is a reduction, can be written as:

J. J. Scragg, *Copper Zinc Tin Sulfide Thin Films for Photovoltaics*,
Springer Theses, DOI: 10.1007/978-3-642-22919-0_2,

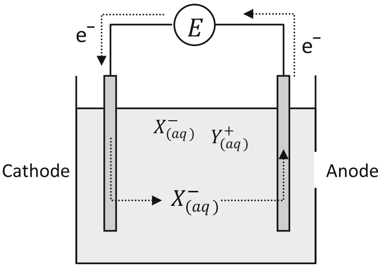

Fig. 2.1 Diagram of a two-electrode electrochemical cell under an applied potential, indicating current carrying species

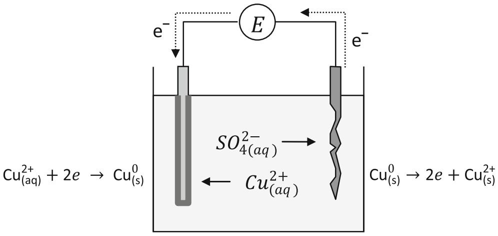

Fig. 2.2 Diagram of a two-electrode electrochemical cell undergoing electrodeposition of Cu from a solution of $CuSO_4$

$$\mathrm{Cu}^{2+}_{(\mathrm{aq})} + 2e \rightarrow \mathrm{Cu}^{0}_{(\mathrm{s})} \tag{R 2.1}$$

The $SO_4{}^{2-}$ ions do not participate in the electrochemical reaction, but their drift from the cathode to the anode supports the current flowing in the solution. Since the electrodeposited material is itself conductive, the reaction will continue while the potential difference is maintained. The concentration of Cu^{2+} ions in the solution will therefore gradually drop unless they are replenished. In the industrial case, the positive electrode (the anode) is usually made from the same metal, in this case Cu, and the reverse reaction occurs:

$$\mathrm{Cu}^{0}_{(\mathrm{S})} \rightarrow 2e + \mathrm{Cu}^{2+}_{(\mathrm{S})} \tag{R 2.2}$$

In this way the concentration of Cu^{2+} ions in the electrolyte remains constant. A film of Cu develops upon the substrate at the cathode, while the Cu anode gradually dissolves, as shown in Fig. 2.2.

The rate of growth of the Cu film is proportional to the rate of electron transfer, i.e. to the current flowing in the system, which can be easily measured. Expressed as a molar quantity, the growth rate of the film per unit area of substrate is simply:

$$\frac{\mathrm{d}n}{\mathrm{d}t} = \frac{J}{zF} \tag{2.1}$$

where J is the current density in Am^{-2}, z is the charge on the depositing ion (2 in the case of Cu^{2+}) and F is Faraday's constant, 96,500 C mol^{-1}. Since most metal ions are cations, we will always refer to electrodeposition occurring at the cathode, via reduction.

2.1.2 The Three-Electrode Cell

Upon immersion in the electrolyte, the different chemical potential of electrons in the electrode and the solution phase means that there is a certain amount of electron transfer, which occurs until the chemical potential in both phases is equalised. This creates a net charge at the surface of the metal electrode, which is compensated by an accumulation at the interface of ions from the electrolyte, forming what is known as the Helmholtz layer. The potential drop across this layer cannot be measured directly; any physical probe used to do so would also have an unknown potential drop at its own surface. Because of this fact, we can only ever measure differences in electrode potential, rather than absolute values. Potentials must therefore always be quoted with respect to some reference. Any two dissimilar materials immersed in an electrolyte will develop a potential difference between them, which may change if electrochemical processes cause alterations to their surfaces. Since in the above case of Cu deposition, both electrodes underwent changes as the reaction progressed, the potential difference between them will vary. In order to maintain a steady reference point, we introduce a third electrode, a 'reference' electrode, which is a well-defined system containing a redox couple which adopts a constant potential difference. The reference electrode is in contact with the wider electrochemical system via a 'salt bridge', a porous membrane loaded with ions that move in and out of the reference electrode chamber to communicate potential changes. The potential difference between the two other electrodes is defined and controlled with respect to the potential of the reference (Fig. 2.3). We rename these other two electrodes as the 'working electrode', which is the site of the electrochemical reaction of interest, and to which is applied the desired potential, and the 'counter electrode', which is present only to support the current flow and to which is applied whatever potential is necessary to do this. Current flows only between the working and counter electrodes to ensure that there are no chemical changes in the reference electrode. There are different kinds of reference electrodes, which are suitable for different conditions (e.g. acidic/alkaline solutions, molten salt electrolytes). Their potentials are all defined with respect to the absolute standard, the 'normal hydrogen electrode' (NHE).

In practice, we would like to apply either a constant potential difference between the working and the reference electrode, or a constant current flow between the working and the counter electrodes. The former case—constant potential difference—is more applicable to this work, and the system used to accomplish it is called a potentiostat. The potentiostat maintains a desired potential difference between the working electrode and the reference electrode, even while electrochemical changes are occurring at the working electrode surface. The current flowing between the working electrode and the counter electrode, which may vary as the electrochemistry dictates, is measured as a function of the potential. The first experiment that should be carried out when a new electrochemical system is being studied is to measure this dependence of current upon working electrode potential, since the current flowing is a direct measure of

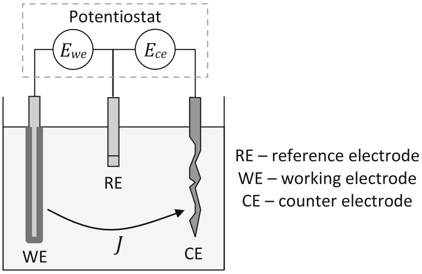

Fig. 2.3 Diagram of a three-electrode electrochemical cell undergoing electrodeposition of Cu from a solution of $CuSO_4$. The value of E_{we} is controlled as desired; the value of E_{ce} is set by the potentiostat

the rate of the electrochemical reactions occurring at the electrode surface. The procedure used for this is cyclic voltammetry.

2.1.3 Cyclic Voltammetry in Electrodeposition

Cyclic voltammetry consists of scanning the potential applied to the working electrode at a constant rate, reversing the direction of the scan when some chosen potential limits are reached. The current flow is measured throughout the procedure. As a starting point, we consider the potential at which zero current is flowing. In this situation, at the level of the electrode-solution interface, there is an equal and opposite transfer of ions across the charged Helmholtz layer—a dynamic equilibrium is established with reduction and oxidation occurring at the same rate. Since there is no net chemical change, there is also no net current. For the reaction $M^{z+} + 2e^{-} \rightarrow M^{0}$, the potential at which this equilibrium is found is denoted the 'standard reduction potential', E_{M}^{0}, and is defined under standard conditions (room temperature and pressure, 1 M concentrations) with respect to the NHE reference. When the concentrations (formally, activities, a) and temperature of the electrolyte are different from the standard values, the actual potential for zero current shifts away from E_{M}^{0} according to the Nernst equation:

$$E_M = E_{\mathrm{M}}^{0} - \frac{RT}{zF} \mathrm{In} \frac{a_M}{a_{M^{z+}}}, \tag{2.2}$$

where R is the molar gas constant (8.314 J mol^{-1} K^{-1}) and T is the temperature in K. We can now shift the potential away from E_{M} to an arbitrary value E, which takes the system away from equilibrium. We define the 'overpotential', η, as the difference between the applied potential and the equilibrium potential, i.e.:

$$\eta = E - E_M \tag{2.3}$$

Returning to the electrode–electrolyte interface, if a negative overpotential is applied then the additional build-up of negative charge in the Helmholtz layer accelerates the reduction reaction and reduces the rate of the oxidation. There is now a net chemical change resulting in a build-up of Cu at the electrode, and a corresponding net flow of current. A reduction current is negative by convention,

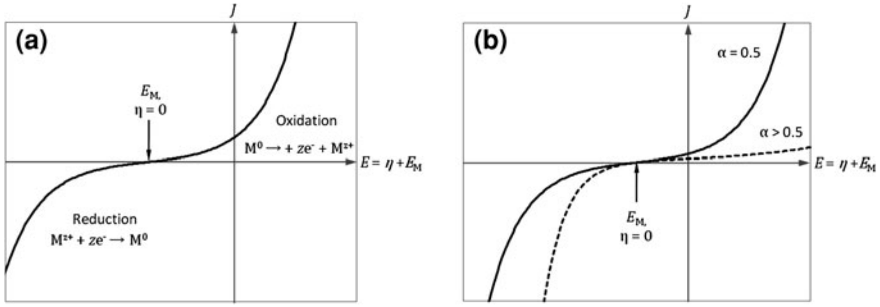

Fig. 2.4 **a** The Butler-Volmer *J*-*E* curve for a completely reversible reaction. **b** Modification of the curve for a 'less reversible' reaction, where the reduced species is favoured

and an oxidation current positive. If a positive overpotential is applied, then the oxidation reaction is accelerated, a positive current flows and the electrode begins to corrode. The Butler-Volmer equation describes the relationship between overpotential and current density, J:

$$J = J_0\left[\exp\left(\frac{-zF\alpha\eta}{RT}\right) - \exp\left(\frac{zF(1-\alpha)\eta}{RT}\right)\right], \tag{2.4}$$

where J_0 is the exchange current density, the equal and opposite current flowing across the interface at equilibrium. The parameter α represents the 'reversibility' of the electrochemical reaction, and is related to the shape of the free-energy curve going from oxidised to reduced species, i.e. the similarity of the transition state to the two end products. When α is equal to 0.5, the oxidation and reduction processes are equally responsive to the applied overpotential and the J-η curve is symmetrical; the reaction is described as 'reversible'. If the transition state between oxidised and reduced states is closer to one or the other state, then α deviates from 0.5 and the curve is non-symmetrical. The Butler-Volmer equation describes the shape of the cyclic voltammogram when there is a constant concentration of metal ions in the solution and a constant supply of metal in the electrode. The curve is the same regardless of the direction of the potential scan. Examples are shown in Fig. 2.4, where the curve has been plotted as a function of the applied potential, E.

Now consider the situation where the working electrode consists of an inert conductive substrate with only a thin layer of the metal at its surface—for example after a small amount of metal has just been electrodeposited. Then, when the overpotential is positive and oxidation occurs, there is only a finite amount of material available for oxidation. If we are scanning the potential slowly positive, then once the film has been completely oxidised the current will drop rapidly to zero. Only when the overpotential is made negative again is the film restored by reduction of the metal ions from solution. The cyclic voltammogram in this situation now exhibits hysteresis—the current depends on whether the scan is being made in the positive or negative direction, Fig. 2.5a.

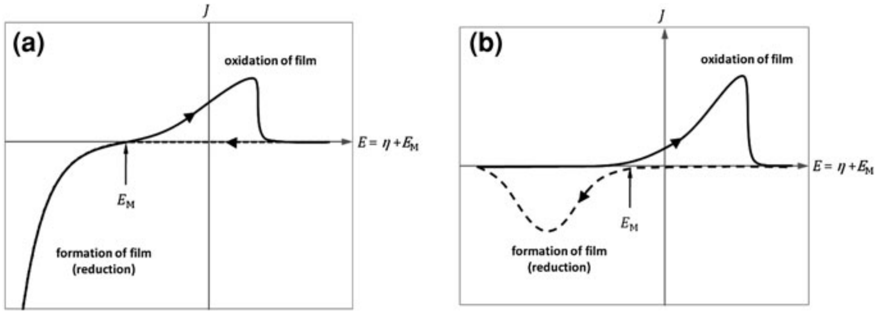

Fig. 2.5 **a** The cyclic voltammogram for a film of finite thickness. As the scan goes from positive to negative, a film is formed by reduction of metal ions, giving a negative current. As the scan goes back from negative to positive, the film is oxidised, giving a positive current, until it is completely consumed and the current drops back to zero. **b** The cyclic voltammogram for a diffusion-limited process. As the scan goes from positive to negative, a negative current arises from film growth, but the consumption of ions near the electrode causes the rate of growth to drop again. On the return scan, there is no further growth. Upon oxidation, the concentration of ions near the electrode is restored

As stated earlier, the reduction reaction consumes metal ions in the vicinity of the electrode surface; hence the concentration of metal ions drops in this region as the reduction proceeds. The reaction cannot proceed faster than the rate of replenishment of metal ions by diffusion or solution convection, and as the reduction continues, fresh ions must travel from further into the bulk of the solution. The current drops back to a small limiting value where a limiting concentration of ions near the electrode surface is maintained by diffusion and convection from the bulk. The electrodeposition is now described as being under diffusional control. When the Butler-Volmer equation is modified to account for a finite rate of ion replenishment, the cyclic voltammogram now looks like the one in Fig. 2.5b.

2.1.4 The Hydrogen Evolution Reaction

A complicating factor in electrodeposition from aqueous solutions is that water itself can be reduced at similar potentials to many metal ions. This results in evolution of hydrogen gas from the working electrode. The hydrogen evolution reactions (HER) in acidic and alkaline solutions are shown below:

$$H^{+}_{(aq)} + e^{-} \rightarrow {}^{1}\!/_{2}H_{2(g)} \tag{R 2.3}$$

$$H_2O + e^{-} \rightarrow {}^{1}\!/_{2}H_{2(g)} + 2OH^{-}_{(aq)} \tag{R 2.4}$$

Since water is present in high concentrations (approx. 55 M), the HER can proceed very quickly indeed causing very high currents to flow and large volumes of gas to be given off from the working electrode, interfering with the

Table 2.1 Hydrogen overpotentials required to achieve hydrogen evolution at a rate of 1 mA cm^{-2} for some relevant substrate materials

Substrate material	η_{H_2}(V)	Source
Pt	0.09	[2]
Mo	0.57	[3]
Cu	0.45	[2]
Sn	0.75	[2]
Zn	0.83	[4]

electrodeposition processes. Therefore the HER limits the negative potentials that can be used in aqueous systems. The standard reduction potential for the HER is defined as 0 V with respect to the NHE, but the observed potential changes with pH, according to the Nernst equation:

$$E_{H_2} = E^0_{H_2} - \frac{RT}{F}\text{In}\frac{1}{a_{H^+}} = -0.0591p\text{H}, \tag{2.5}$$

where the relation $pH = -\log a_{H^+}$ has been used, and E_{H_2} calculated at room temperature. This equation predicts the potential at which the HER is at equilibrium, with no net production of H_2.

The reversibility of the HER depends upon the electrode material. In the case of a Pt electrode, the production of H_2 is catalysed by adsorption of H atoms to the Pt surface. This makes the transfer coefficient α larger, and the reduction rate high. This is expressed by saying that the 'hydrogen overpotential', η_{H_2}, at Pt is small, i.e. that only a small overpotential is required to achieve considerable hydrogen evolution at a Pt substrate. η_{H_2} is usually defined as the overpotential required to obtain a current density of 1 mA cm^{-2} from the HER (Fig. 2.6). In other cases, the hydrogen overpotential is much larger, which allows more negative potentials to be used. Since the HER is in general an unwanted reaction, a high hydrogen overpotential is desirable, especially when metals that have a rather negative standard reduction potential are to be deposited. The hydrogen overpotentials of some relevant metals are given in Table 2.1.

As well as the HER, there may be other processes restricting the range of potentials that can be used in a given system. Examples are the oxidation of water (to O_2), which has similar behaviour to the HER but gives a positive current, and another possibility is the oxidation of the substrate material. This could potentially cause a loss of electrical contact, so is to be avoided. The cyclic voltammogram taking all these considerations into account will have a form similar to that in Fig. 2.7. The unwanted processes at the positive and negative limits of the voltammogram together define the 'electrochemical window' for the system under study. Within the electrochemical window, the major processes occurring are reduction and oxidation of the metal ion or film.

As we have seen, the cyclic voltammogram can give a lot of qualitative as well as quantitative information about the system at hand, including the electrochemical window, the (initial) rate of the metal reduction as a function of applied potential and the approximate value of the standard potential. Measurements at

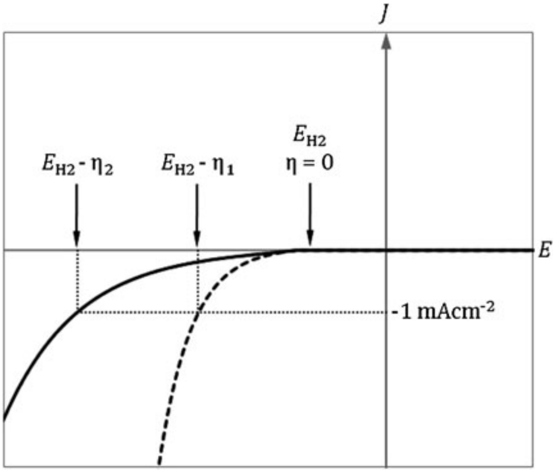

Fig. 2.6 The current flow due to hydrogen evolution resulting from surfaces with different hydrogen overpotentials ($\eta_2 > \eta_1$)

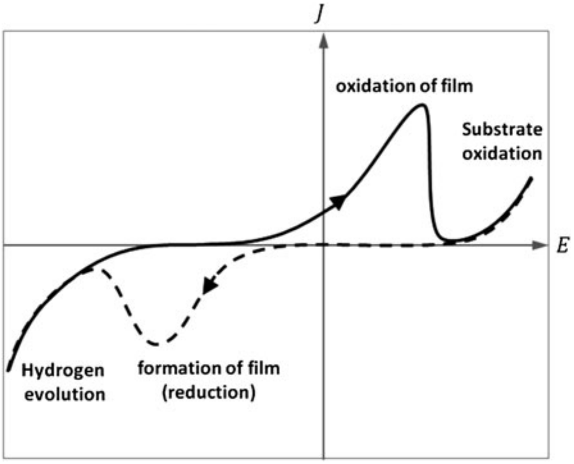

Fig. 2.7 Schematic cyclic voltammogram for an electrodeposition process showing the various reactions contributing to the overall current flow

different scan rates can also be used to determine the diffusion coefficient of the metal ion and the transfer coefficient α.

After the cyclic voltammetry has been recorded, one is able to determine a suitable potential to be used during the electrodeposition process. This potential should be in a region where the metal ions are being reduced (i.e. negative of the standard reduction potential), and ideally should avoid being near the region where hydrogen evolution is rapid. In many cases, a certain amount of concurrent hydrogen evolution is unavoidable, and the result is that not all of the current passage during electrodeposition is due to reduction of metal ions; some is as a result of the reduction of water. As shown in Eq. 2.1, the thickness of the film is related to the current flow during electrodeposition; however, due to the presence of other simultaneous electrochemical reactions, it is necessary to determine experimentally the fraction of current that is due to metal deposition, which is termed the ‘efficiency’ of the electrodeposition. This can be done by making a quantitative analysis of the electrodeposit.

2.1.5 Electrodeposition at Constant Potential

We now move back to the potentiostatic situation, where the goal is to grow a metal film of a pre-determined thickness. Having determined a suitable potential from the cyclic voltammogram, we can apply this and measure the current as a function of time, during the growth of the film. Due to the gradual consumption of the reducible species in the vicinity of the electrode, the current soon becomes diffusion limited, the resulting current density being described by the Cottrell equation:

$$J = \frac{nF[M^{z+}]\sqrt{D}}{\sqrt{\pi t}} \tag{2.6}$$

where $[M^{z+}]$ is the initial concentration of the reducible species and D is its diffusion coefficient under the conditions of the experiment. The equation implies that the current will continue to decrease indefinitely, however in practice this is not the case. During electrodeposition, an initially stagnant solution will develop convection currents due to the changes in solution density at the working electrode surface, and these currents transport fresh solution to the electrode, thus counteracting the depletion of ionic material. At longer deposition times, the current reaches a steady value under the combined influence of diffusion and convection.

In order to deposit a film of a given thickness, we must know the electrodeposition efficiency of the process. The current during electrodeposition is a summation of currents resulting from all the electrochemical reactions that are occurring, of which metal deposition should be the major contributor. The next largest fraction is likely to be hydrogen evolution from water reduction, and there may be other minor reactions occurring too. The total current density during steady state deposition, $J_{d,ss}$, can be described as the sum:

$$J_{d,ss} = J_m + J_H + \sum_i J_i \tag{2.7}$$

where the subscripts m and H represent metal deposition and hydrogen evolution respectively. Other reactions are denoted by the summation over J_i. The cumulative charge density during steady state deposition, $q_{d,ss}$, equal to the integral of current density with respect to time, t, is simply:

$$q_{d,ss} = (J_m + J_H)t = q_m + q_H \tag{2.8}$$

where we neglect the minor contributions from other reactions aside from deposition and hydrogen evolution. Note that q_m is directly related to the molar quantity of metal deposited in film, n, by the relation:

$$q_m = \frac{nzF}{A} \tag{2.9}$$

where z is the charge on the deposition species, F is Faraday's constant and A is the area of the substrate.

The efficiency of metal electrodeposition, φ_m, is the proportion of total charge flow which results in reduction of metal ions during steady state deposition:

$$\varphi_m = \frac{q_m}{q_{d,ss}} \tag{2.10}$$

In the early stages of electrodeposition, however, the system is not at a steady state. The electrochemical reactions initially occur at the substrate material, which will have a specific interaction with the depositing species, as well as its own hydrogen evolution potential. There is a transitional period as the depositing material nucleates at the substrate surface and the substrate becomes covered, after which the substrate surface properties change to become those of the deposited material. In addition, there is a period of time over which the concentration of the metal ions near the electrode decays to a steady state value as determined by the rate of replenishment of ions by diffusion and convection. Only after the surface condition and ion concentration have steadied are the equations described above valid. During the initial transitional period, the efficiency of the electrodeposition will change. When the overall deposition time is longer than the time required to reach the steady state, we can treat the amount of material deposited during the transitional period as a constant, and assume a constant efficiency of the initial deposition, such that the total charge passed during the electrodeposition is given by:

$$q_d = q_{d,ss} + q_0 = \frac{q_m}{\varphi_m} + q_0 \tag{2.11}$$

so that the part of the total charge passage which is due to metal deposition alone is finally given by:

$$q_m = q_d\varphi_m - q_0\varphi_m \tag{2.12}$$

q_d is measured directly during electrodeposition as the integrated total current flow. To determine φ_m we need to obtain values for q_m for different total amounts of deposited material, by making a quantitative analysis of the deposited film. This can be done in several ways. If the film can be dissolved in an acidic solution, then various techniques exist for determination of the concentration of the metal ion in the solution, for example atomic absorption spectroscopy (AAS), titration, UV/vis spectroscopy with the addition of a suitable coloured complexing agent, or mass spectrometry. It is also possible to measure the amount of deposited material by using a very accurate balance, and this can be done during electrodeposition using a quartz crystal microbalance as the working electrode. A convenient electrochemical approach is simply to re-oxidise (or 'strip') the film after it is deposited, by applying a potential positive of the standard reduction potential of the metal.

Assuming (a) that the film is stripped entirely, (b) that the only metal deposited was the metal of interest and (c) that no other anodic processes, such as oxidation of water or the substrate are occurring, then the current flowing during stripping is entirely due to oxidation of the film. After the film is entirely removed, the integrated current flow is equal to q_d. Experimental determination of the deposition efficiency by stripping and AAS will be presented later in this chapter.

2.2 Experimental Approaches for Cu_2ZnSnS_4 Precursor Production

Having covered the basics of electrodeposition, we can now discuss its application in the production of precursors for Cu_2ZnSnS_4 films. The aim is to produce films containing the metallic elements in a given ratio, which will later be reacted with sulfur.

2.2.1 Co-Deposition and the SEL Approach

There are two main strategies for metallic precursor production using electrodeposition. In the first case, all of the required elements (here Cu, Sn and Zn) can be deposited together in one stage to produce a mixed precursor film. Alternatively, the individual elements can be deposited in sequential layers resulting in a 'stacked' film. These two approaches are referred to as the 'co-deposition' and 'stacked elemental layer' (SEL) routes, respectively. At the start of this project, neither approach had been used for CZTS, however since that time there have been several publications concerning the co-deposition route [5, 6] and one concerning the SEL route [7], aside from the publications as a result of this work [8–11].

The Co-Deposition Route

Co-deposition should produce a homogeneously mixed precursor, which may lead to a more uniform CZTS film. However, there are some practical issues with the use of a mixed electrolyte. The main problem is that the conditions required to achieve good deposits of one metal may differ substantially from those required for another metal, due to, for example, the difference in their standard reduction potentials. When using three different metals, a potential must be chosen at which all three are concurrently reduced, and then the composition of the electrolyte must be adjusted so that all three are deposited at the desired rate. This neglects any interactions between the metals, such as preferred alloy formation or redox reactions occurring in solution. Since the stability of metal ions in aqueous solutions depends on the pH, but the range of stability depends on the particular ion, complexing agents and other additives are generally needed to keep the electrolyte stable over time, and these components have their own influence on the deposition process for each metal. All of the above means that targeting a particular composition using a co-deposition process is non-trivial, and adjusting the composition in a rational manner is very difficult.

The SEL Route

The most significant benefit of using the SEL approach is the ability to easily vary the composition of the precursor just by varying the thickness of each layer, i.e. simply leaving the sample under potential for a longer time, without changing the electrodeposition conditions. In addition, since a different electrolyte is used for each metal, the electrolyte pH and additive composition can be tailored to achieve the best quality deposit with deposition rates, high efficiency and good morphology. Electrolyte stability is critical in industrial processes, and is much easier to achieve using individual metal electrolytes. Although the elements are spatially separated in the precursor, they can be caused to mix by appropriate heat treatments, and, since the sample must anyway be heated during sulfurisation, a short pre-treatment to achieve this mixing is quite straightforward. This procedure will be described in Chap. 3.

There are some restrictions on the possible stacking orders when using the electrodeposition method to produce a layered precursor. In particular, the standard reduction potentials of Cu, Sn and Zn are very different; for example, at the potential required to electrodeposit Cu, a Zn deposit would be oxidised and stripped from the substrate. Therefore a sensible deposition sequence for the stack would be in order of increasingly negative standard reduction potential, i.e. Cu^{2+} (+0.342 V vs. NHE), followed by Sn^{2+} (−0.136 V vs. NHE) and finally Zn^{2+} (−0.76 V vs. NHE) [12]. Altering this order could result in spontaneous dissolution of the substrate upon immersion in the deposition solution, which would make control of composition and uniformity difficult. Araki et al. investigated the influence of different stacking sequences on the properties of CZTS devices produced by electron-beam evaporation followed by thermal sulfurisation [13]. They concluded, based on the device parameters, that a Mo|Zn|Sn|Cu stack was most favourable for CZTS formation and gave better adhesion to the substrate. This stacking order is not easy to achieve by electrodeposition; however, the authors also noted that placing Cu and Sn in adjacent layers was important, and at least this criterion is fulfilled by the deposition sequence dictated by the electrochemical approach.

A particular consideration for the SEL route is the uniformity of each layer. There are two levels of uniformity that we need to control:

1. Microscopic uniformity, i.e. the morphology of the electrodeposited material. As far as possible we require smooth films with complete coverage of the substrate.
2. Macroscopic uniformity, i.e. the thickness/density of coverage of the electrodeposit must be constant over as much of the sample area as possible.

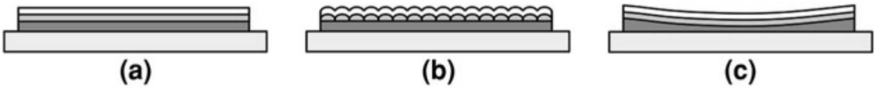

Fig. 2.8 Schematic illustration of cross-sections through **a** an ideally uniform SEL precursor, **b** a precursor with microscopic non-uniformity in the second layer, and **c** a precursor with macroscopic non-uniformity in the bottom layer. **b** and **c** result in compositional variations over the area of the sample

If each layer of the precursor stack is completely smooth and has constant thickness, then the composition is the same at all points. This is the ideal case and will give us the best chance of achieving uniformity in the final CZTS film. Microscopic non-uniformities in any of the precursor layers may lead to local composition variations in the CZTS film, while macroscopic non-uniformities in any of the precursor layers will lead to compositional gradients extending across the entire area of the CZTS film. Both effects are illustrated in Fig. 2.8. Microscopic uniformity (morphology) is primarily controlled by the electrolyte composition and deposition potential. Macroscopic uniformity will depend on the configuration of the electrodeposition cell and mass transport. We will now briefly discuss the control of these factors in electrodeposition.

2.2.2 Morphological Control in Electrodeposition

The growth mechanisms of electrodeposited films can be very complex. Briefly, we can either have ‘two-dimensional’ growth, where the film grows by successive nucleation of atomic layers, giving a rather flat surface, or we can have ‘three-dimensional’ growth, wherein material is preferentially deposited at projecting surfaces, or nucleation is faster upon the deposited material rather than the substrate. This leads to very rough, dendritic films which may show incomplete substrate coverage. The mode of growth may be influenced by the deposition potential, which is controllable, or it may be affected by the interactions between the solute and the substrate. To achieve flatter morphology, surfactants are commonly added to electrodeposition solutions to control the properties of the electrode-solution interface. The surfactant molecules selectively adsorb to surface sites with lower coordination—i.e. projecting regions—blocking the addition of further material. In this way, the growing film is smoothed out.

2.2.3 Mass Transport Control in Electrodeposition

Another important consideration in electrodeposition is the control of bulk electrolyte flow—i.e. convection. As mentioned above, natural convection currents are responsible for maintaining a constant current during potentiostatic electrodeposition;

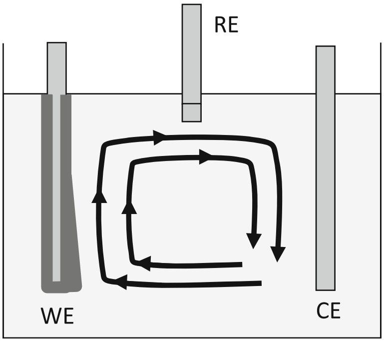

Fig. 2.9 Illustration of the natural convention currents set up during electrodeposition at a vertical working electrode

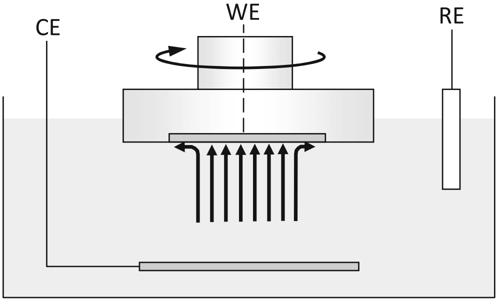

Fig. 2.10 The rotating disc electrode configuration for achieving uniform solution transport to the working electrode surface

however, the convection current set up during electrodeposition at a vertical working electrode produces non-uniform solution transport, as shown in Fig. 2.9. This results in an enhanced current density at the bottom of the electrode and a reduced current density at the top, translating to a gradient in deposit thickness across the electrode.

In order to avoid thickness variations, convection must be deliberately provided in a uniform way. There are various ways to achieve uniform ‘forced’ convection, and the simplest approach for small-scale work is the ‘rotating disc electrode’ (RDE). In this arrangement, the working electrode is positioned in one face of a cylindrical block, which is placed face-down in the solution and rotated. The electrolyte is drawn towards the rotating electrode, and the flow is constant at all points on the electrode surface, assuming that (a) the working electrode diameter is small compared to the total disc diameter and (b) that the solution extent is large compared to the diameter of the disc. The rotating disc electrode configuration is shown in Fig. 2.10.

The relationship between the limiting (i.e. mass transport controlled) current density and the rotation rate of the electrode is given by the Levich equation for the RDE:

$$J = 0.62zF[M^{z+}]v^{-1/6}D^{2/3}\omega^{1/2}, \tag{2.13}$$

where ω is the angular velocity of the disc (in rad s^{-1}) and ν the kinematic viscosity of the electrolyte, its viscosity divided by its density, which is equal to 0.01 $cm^2\ s^{-1}$ for water.

Having established the procedures to be used for electrodeposition, we now move on to the composition of the electrodeposition solutions themselves.

2.3 Electrodeposition of Cu, Sn and Zn

Industrially, electrodeposition is a very widespread process with applications in electronics, the manufacture of mechanical components, production of corrosion-resistant coatings and the finishing of decorative items [14]. There are a great many different aqueous electrolyte chemistries, and complex additive systems to control morphology, electrolyte stability and the mechanical properties of the deposit. Most of these systems are proprietary and the function of the additives is not always well-understood. In this investigation, the ultimate aim is to produce semiconducting films, and therefore we require the minimum of contamination. Relatively simple electrolyte chemistries are therefore preferred. Where possible, these were derived from industrially-relevant systems to demonstrate the applicability of the electrodeposition method for mass-production of PV systems.

A fundamental requirement of an electrodeposition electrolyte is for the metal cations to be stable in solution, in the presence of water and oxygen. Thermodynamic stability is achieved by the choice of a pH at which the cation will not undergo hydrolysis. Complexing agents are also often used to provide kinetic stability, and these also tend to influence the morphology of the deposit. In addition, a high concentration of an inert background electrolyte (which may also be the pH-determining component) is provided, so that the conductivity of the electrolyte is high. Finally, surfactants are used where necessary to improve the morphology of the deposits.

2.3.1 Electrodeposition of Cu

The electrolytes used for Cu fall into two main categories: the alkaline electrolytes, which use strong complexing agents to stabilise the Cu^{2+} ions, and acidic electrolytes, where Cu^{2+} is thermodynamically stable. For reasons that will become apparent later, only the alkaline chemistries were suitable for this investigation. The 'classic' alkaline Cu electrolyte has a pH around 14 and is based on cyanide as a complexing agent. The electrolyte is very effective in producing high-quality deposits up to around 10 μm in thickness, but toxicity of cyanide is a considerable disadvantage. Recently, alternative complexing agents have been introduced, which are commonly multi-dentate polyalcohols

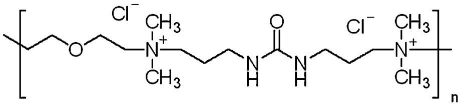

Fig. 2.11 A typical additive used in Zn electrodeposition to improve the deposit morphology: quaternized poly[bis(2-chloroethyl) ether-alt-1,3-bis[3-(dimethylamino)propyl]-urea]

such as tartrate, citrate, glycerolate and sorbitate [14]. In this work, an alkaline electrolyte containing sorbitate was used, after Carlos et al. [15]. This electrolyte was shown to give bright (i.e. very flat and uniform) Cu layers without the need for additives. Two sorbitate anions complex each Cu^{2+} ion [15].

2.3.2 Electrodeposition of Sn

Two electrolytes for Sn were used in this work. Firstly, a similar alkaline sorbitol bath as used for Cu was reported by Carlos et al. [16]. The possibility of using a similar chemistry for all the three layers was attractive since it suggests that co-deposition could also be a viable option. The stabilisation of Sn^{2+} with respect to oxidation to Sn^{4+}—which is insoluble in alkaline solutions—is of paramount importance, so a greater concentration of sorbitol is used in this electrolyte. This electrolyte was used in our earlier work, however it tended to give rather poor morphology [8, 17]. An alternative electrolyte, based on methane sulfonic acid [$CH_3SO(OH)_2$] and commonly used for the industrial electrodeposition of Sn, was adopted. Methane sulfonic acid is able to stabilise Sn^{2+} over a wide pH range, and surfactants, typically based on the quaternary ammonium cation, are commonly added to improve the surface morphology of the deposits. In the absence of additives the Sn films are usually rather rough [14].

2.3.3 Electrodeposition of Zn

The most widespread chemistry for Zn electrodeposition is the 'acid chloride' electrolyte, which is simply a pH 3–5 solution containing, for example, KCl. Zn has a very negative standard reduction potential (−0.76 V vs. NHE), and hydrogen evolution is therefore competitive. In order to avoid large changes of pH at the electrode surface (due to consumption of H^+ by the hydrogen evolution reaction), a pH buffer was used in this investigation. Additives are always used to control the morphology and help reduce hydrogen evolution [14]. A search of the patent literature indentified a typical polymeric additive, shown in Fig. 2.11.

Experimental

2.4 Description of Electrodeposition Methodology

2.4.1 Substrates

The substrates used in this investigation were usually Mo-coated soda-lime glass (Mo-SLG). The Mo layers were prepared by RF magnetron sputtering, and were approx. 1 μm thick. The glass slides themselves were 1 mm thick. After cutting to the desired size, the substrates were cleaned by sonication for 5 min in, sequentially, detergent (5 vol% decon-90), ethanol and isopropanol.

Where noted, a Pt substrate was used, which consisted of a 3 mm diameter Pt rod embedded in a plastic sheath and polished back to present a clean surface for electrochemical studies.

2.4.2 Electrolytes

The electrolytes used for electrodepositions and electrochemical studies were prepared fresh on the day of use. The solutions were prepared from distilled or milliQ water by adding first the background electrolyte and/or pH-modifying agent, followed by the complexing agent (if used), then the metal salt and finally any other additives. The chemicals used are shown in Table 2.2. In the case of the alkaline Cu electrolyte, dissolving of $CuSO_4 \cdot 5H_2O$ was assisted by heating the solution to ca. 50 °C for 10 min.

2.4.3 Electrochemical Setup

Most of the data presented herein were recorded using an Autolab 20 potentiostat. The reference electrode used depended on the pH of the solution; for alkaline solutions a Hg|HgO (1 M NaOH) reference (0.14 V vs. NHE) was used, and for acidic solutions a Ag|AgCl (saturated KCl) reference (0.197 V vs. NHE) was used. The counter electrode was a Pt sheet.

2.4.4 Cyclic Voltammetry

Cyclic voltammograms were taken by selecting a potential at which no current was flowing as a start point, and then after a few seconds of equilibration at this potential, initiating the scan in the negative direction. The scan was repeated until a steady state was reached.

Table 2.2 Electrolyte compositions used in this study

Electrolyte	Composition
Cu (Alkaline sorbitol)	3 M NaOH (Reagent grade, Aldrich), 0.2 M Sorbitol (≥99.5% (HPLC), Sigma), 0.1 M $CuSO_4 \cdot 5\ H_2O$ (≥98%, Sigma), [where stated: ≤0.025 vol% Empigen BB (N,N-dimethyl-N-dodecylglycine betaine, Sigma)]
Sn (Methanesulfonic acid)	1 M Methanesulfonic acid (≥99.5%, Sigma-Aldrich), 50 mM Sn(II) methanesulfonate (50 wt% in H_2O, Aldrich), 0.1 vol% Empigen BB (see above)
Zn (Acid chloride)	2 M KCl (≥99.0%, Sigma), 1wt% pH 3 Hydrion buffer (Sigma), 50 mM $ZnCl_2$ (98%, Aldrich), 0.2 wt% poly[bis(2-chloroethyl) ether-alt-1,3-bis[3-(dimethylamino)propyl]-urea], quaternized, 62 wt% in H_2O, Sigma)

2.4.5 Deposition Procedure at Vertical Working Electrodes

Substrates were prepared for deposition by delineating the area to be coated using PTFE tape. The substrate was mounted above the electrochemical cell (solution, counter and reference electrodes) using a crocodile clip connector. The deposition potential was applied, and then the substrate was introduced into the solution. Deposition was carried out until the integrated current (cumulative charge passage) exceeded a preset value, at which point open circuit (i.e. zero current flow) conditions were imposed. After deposition, the substrates were quickly removed from the setup and the excess electrolyte was rinsed off with milliQ water. The PTFE was removed and rinsing continued for ca. one minute. The sample was then dried under flowing nitrogen.

2.4.6 Deposition Procedure at the Rotating Disc Electrode

The rotating disc electrode (RDE) head used in this investigation was custom-built to accept the substrates in use, which were approx. 25 × 18 mm in size. A recess 27 × 19 mm and 1 mm deep was made in a cylindrical polypropylene block. A brass core was made that extended through the block to end flush with the inner surface of the recess. A hole in the other end of the brass core was made to accept the spindle coming from the RDE motor, and a small screw allowed the RDE head to be tightened onto the spindle. The RDE head is illustrated in Fig. 2.12a and the mounting of substrate and connection of the RDE head to the motor are shown in Fig. 2.12b.

Substrates were mounted into the RDE head as shown in Fig. 2.13. Two strands of copper wire (approx. 0.05 mm in diameter) were first laid over the exposed brass core inside the sample recess and held in place using kapton (polyimide) tape (a). The substrate was then placed in the recess, and the ends of the copper wires were bent around to the substrate surface to make contact with the Mo layer (b). Finally, strips of kapton tape were used to mask the borders of the substrate, whist simultaneously holding the substrate in place, affixing the copper wire connections firmly to the substrate to facilitate good electrical contact, and finally, ensuring that the only electrical connection between the working electrode and the solution was via the substrate surface (c).

The typical path resistance between the centre of the substrate surface and the working electrode connection at the potentiostat was around 1 Ω. About 0.5 Ω of this arose from the sheet resistance of the Mo, and as subsequent Cu and Sn layers were deposited, this component dropped to <0.1 Ω. The remainder of the resistance arose from the Mo-copper wire contacts.

The electrodeposition cell, the RDE and the other electrodes were mounted on a stand which was tilted at an angle of about 5° to the vertical. This was to ensure

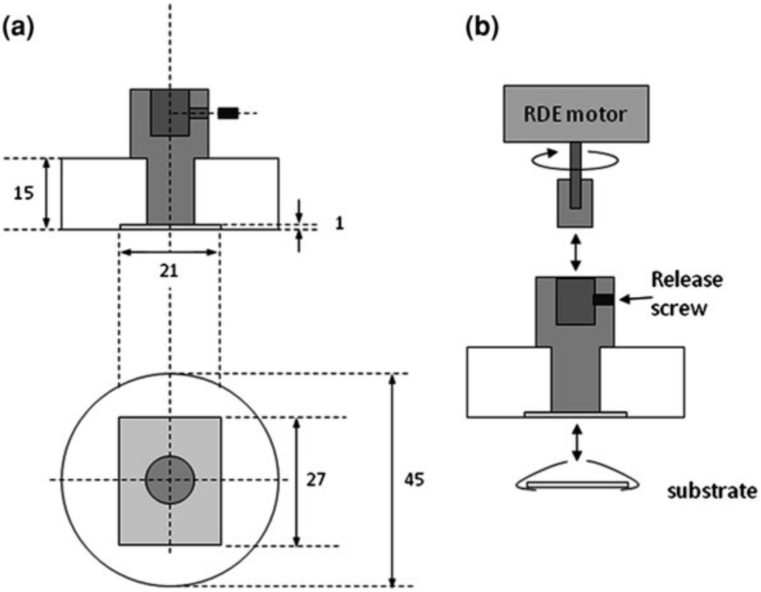

Fig. 2.12 **a** RDE head design showing cross sectional view and a view of the lower face. **b** Schematic of RDE head attachment to the RDE motor

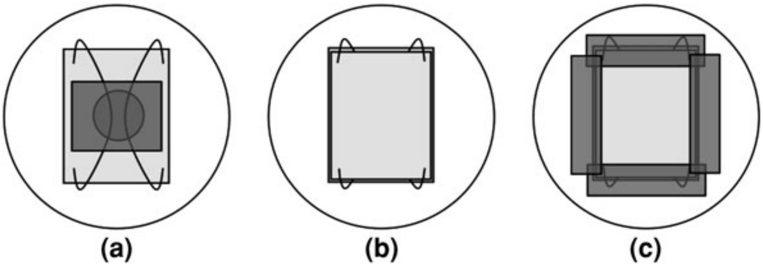

Fig. 2.13 Method of mounting substrates into the RDE head and making electrical connection to the front surface. **a** Copper wires taped onto the exposed brass core, **b** substrate placed in recess and ends of copper wire wrapped around to the front face of the substrate, **c** masking the edges of the substrate with polyimide tape

that when the RDE was lowered into the electrolyte, no air bubbles would be trapped at the working electrode surface (see Fig. 2.14).

The RDE rotation rate was controlled by a built-in tachometer. The rotation was initiated prior to immersion of the RDE head. The rest of the deposition and cleaning procedures used were the same as described in Sect. 2.4.5.

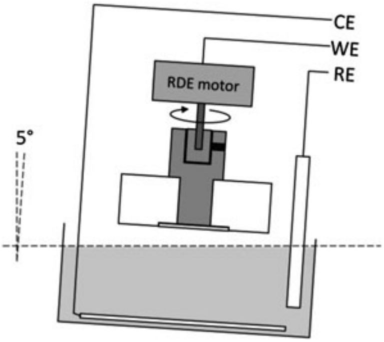

Fig. 2.14 The assembled electrochemical cell using the RDE, prior to working electrode immersion

2.5 Characterization of Electrodeposited Films

SEM images and compositions were recorded using a JEOL6480LV microscope with EDS capability (Oxford Instruments). For top-down imaging, samples were earthed by contacting the exposed area of the Mo substrate with carbon-loaded putty.

For EDS measurements, an accelerating voltage of 20 kV was used. Spectra were recorded for 100 s of live-time. The error in the EDS measurement was reduced as far as possible by calibrating the beam current using a Co standard between measurements. For a large series of measurements repeated at the same location on a sample, the absolute errors in the atomic percentages of Cu, Sn and Zn were about 0.6, 0.8 and 0.5% respectively. EDS line-scans were performed over 3 mm sections which were then concatenated. For estimation of film thickness variations over a large area, the peak heights in the EDS spectra were recorded at uniformly spaced locations on the samples. For quantitative analysis of overall sample composition, spectra were recorded at a magnification of 100 times, and averaged over several locations on the sample.

XRD spectra were recorded in Bragg–Brentano mode with a Siemens D-5000 diffractometer using a CuKα radiation source ($\lambda = 1.5406$ Å).

Results and Discussion

We will initially look at the cyclic voltammetry of the Cu, Sn and Zn electrolytes individually, and the morphology of the electrodeposits produced from them. Throughout the discussion, reduction potentials are calculated using tabulated standard reduction potentials and taking into account the pH and concentration of the electrolyte, according to the Nernst equation (Eqs. 2.2 and 2.5). The standard reduction potentials are taken from Reference [3]. The Nernst equations for some relevant electrochemical reactions are shown in Table 2.3.

Table 2.3 Reduction potentials for some relevant reactions, calculated from tabulated standard reduction potentials using the Nernst equation

Reaction	Standard reduction potential vs. NHE
$H^+ + e^- \rightarrow ½ H_2 + H_2O$	$-0.0591p\mathrm{H}$ (Eq. 2.5)
$CuO_2^{2-} + 2H_2O + 2e^- \rightarrow Cu + 4OH^-$ (alkaline)	-0.342 to $0.128 \ln([OH]^4/[Cu^{2+}])$
$Cu^{2+} + 2e^- \rightarrow Cu^0$ (acidic)	$+0.324$ to $0.128 \ln(1/[Cu^{2+}])$
$Sn^{2+} + 2e^- \rightarrow Sn^0$	-0.138 to $0.128 \ln(1/[Sn^{2+}])$
$Zn^{2+} + 2e^- \rightarrow Zn^0$	-0.762 to $0.128 \ln(1/[Zn^{2+}])$

2.6 Electrodeposition of Cu

The electrodeposition of Cu was carried out from a strongly alkaline solution, so an alkali-resistant mercury-mercury oxide (Hg|HgO) reference electrode was used, which has a potential of +0.14 V vs. NHE. In the following discussion, all potentials are given with respect to Hg|HgO.

2.6.1 Substrate Considerations

The substrate used for electrodeposition also forms the back electrical contact to the final CZTS film. Mo is usually used as it makes ohmic contact to *p*-type semiconductors such as CIGS, and CZTS is expected to behave similarly. Unfortunately, as a substrate for electrodeposition Mo has some limitations. The behaviour of Mo as a substrate depends upon the pH of the electrolyte. In acidic conditions, the electrode dissolves as Mo^{3+} ions, which in the presence of oxygen form a passivating layer of MoO_3. The cell potential will now primarily be dropped over this insulating layer as opposed to over the metal-electrolyte interface, and electrodeposition will not occur effectively. The passive layer can be removed by soaking in a solution of KOH or NH_4OH to restore the activity of the electrode [3]. This process of passivation apparently happens very rapidly; for example, even when the potential was applied prior to immersion of the working electrode, attempts to electrodeposit Cu from a typical acid chloride solution failed to give adherent films. In another example of the electrochemical SEL approach to fabricating CZTS precursors, the authors found it necessary to sensitise their electrode with palladium ions to overcome the issue of passivation [7]. In alkaline conditions however, and especially when under cathodic polarisation, Mo dissolves as MoO_4^{2-} and does not become passivated. Therefore use of an alkaline electrolyte is the natural solution for electrodepositing at Mo.

The Electrochemical Window of Mo at pH 14

The range of potentials that we can apply to a Mo electrode in a given solution is determined in the negative scan by the hydrogen evolution reaction (HER) and in the positive scan by the oxidation of Mo. The relevant electrochemical reactions

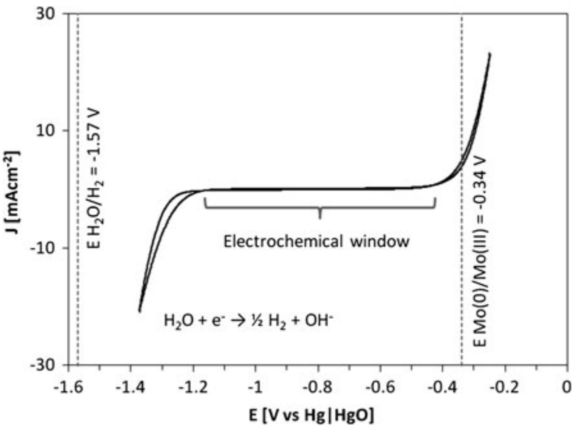

Fig. 2.15 Cyclic voltammetry of a pH 14.5 solution at a Mo electrode

and potentials at pH 14.5 (3 M NaOH) were calculated as described above in Table 2.3. The potentials are now given with respect to Hg|HgO:

$$H_2O + e^- \rightarrow \tfrac{1}{2} H_2 + OH^- \quad (E = -1.00\ V) \qquad (R\ 2.5)$$

$$Mo + 8OH^- \rightarrow MoO_4^{2-} + 4H_2O + 3e^- \quad (E = -0.34\ V) \qquad (R\ 2.6)$$

The hydrogen overpotential for Mo is about −0.57 V for a current density 1 mA cm^{-2} [3], so appreciable H_2 evolution should not be observed until about −1.57 V. To determine the electrochemical window of Mo experimentally, cyclic voltammetry was carried out in a pH 14.5 solution, as shown in Fig. 2.15. In the voltammogram for Mo, both of the above reactions can be seen close to the expected potentials. Hydrogen evolution occurs more positive than predicted, but Mo oxidation occurs where expected.

The substrate oxidation process would ideally be far positive of the oxidation of Cu, so that we are able to measure the complete cyclic voltammogram for Cu deposition at Mo substrates. However, as will be seen, the oxidation of Cu occurs at similar potentials to that of Mo, so we would see oxidation of the substrate if trying to study the complete cyclic voltammogram for Cu. For this reason, Pt electrodes were sometimes used for electrochemical studies of the alkaline Cu electrolyte, as the oxidation of platinum does not occur until much higher potentials.

2.6.2 Cyclic Voltammetry of the Alkaline Sorbitol Electrolyte for Cu

The composition of the alkaline sorbitol electrolyte for Cu is shown in Table 2.4.

A cyclic voltammogram for Cu deposition at a Pt electrode is shown in Fig. 2.16. The deposition and stripping processes (labelled) are clearly seen. At pH 14.5 and

Table 2.4 Composition of the alkaline sorbitol electrolyte for Cu [15]

Component	Concentration (M)
NaOH	3.0
Sorbitol	0.2
$CuSO_4 \cdot 5H_2O$	0.1

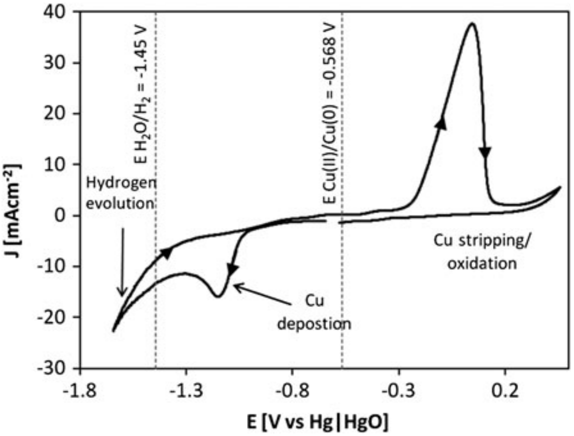

Fig. 2.16 Cyclic voltammetry of the alkaline sorbitol electrolyte for Cu at a Pt electrode. Arrows indicate the direction of the scan, which was started at −0.7 V, reversed at −1.7 V and again at 0 V. The scan rate was 50 mV s^{-1}. Dashed lines show the expected positions of Cu(II) reduction and hydrogen evolution

a Cu(II) concentration of 0.1 M, the electrochemical reaction and potential for Cu reduction and hydrogen evolution are [3]:

$$CuO_2^{2-} + 2H_2O + 2e^- \rightarrow Cu + 4OH^- \quad (E = -0.568\ V) \qquad (R\ 2.7)$$

$$H_2O + e^- \rightarrow \tfrac{1}{2}H_2 + OH^- \quad (E = -1.00\ V) \qquad (R\ 2.8)$$

Both the reduction and oxidation peaks are rather displaced from the expected potential. The negatively shifted reduction peak can be attributed to complexation of Cu^{2+} by sorbitate anions as $[Cu(O_2C_6H_8(OH)_4)_2]^{2-}$. This complexation vastly reduces the concentration of CuO_2^{2-}, and therefore by the Nernst equation (Eq. 2.2) the reduction potential of Cu should be pushed to more negative values. Taking an approximate onset of the deposition as −0.95 V, the Nernst equation gives a free CuO_2^{2-} concentration of 10^{-15} M—i.e. Cu is very strongly complexed by sorbitol. The positively shifted oxidation peak, with reference to the above voltammetry of Mo, is clearly in the same region as Mo oxidation, showing the importance of using a Pt substrate in this case. The hydrogen evolution reaction (HER) can also be seen in the figure. Based on the overpotential of Pt the HER would be expected to occur somewhere negative of −1.09 V, but it in fact occurs only at more negative potentials. This is because the Cu layer grows before the potential for the HER is reached, which increases the hydrogen overpotential of the electrode (see Table 2.1). The HER would then be expected at around −1.31 V, as is indeed observed. A suitable potential for electrodeposition of Cu based on the cyclic voltammetry is therefore around −1.1 to −1.2 V vs. Hg|HgO.

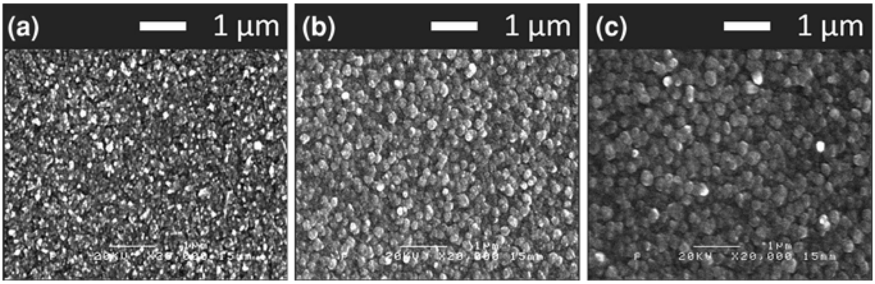

Fig. 2.17 SEM images of electrodeposited Cu films from the alkaline sorbitol electrolyte containing **a** no additive, **b** 0.015 vol% Empigen BB, and **c** 0.025vol% Empigen BB

2.6.3 Morphology of Electrodeposits

When films were deposited at a constant potential of −1.1 V, the alkaline sorbitol electrolyte gave excellent results, yielding bright, strongly adherent layers. A typical SEM image is shown in Fig. 2.17a. However, as the layer thickness was increased above around 100 nm, its morphology became worse, which indicates preferential deposition upon projections from the Cu layer, i.e. three-dimensional growth.

As mentioned in Sect. 2.2.2, this problem is typically controlled using a surfactant to reversibly block such unsaturated sites on the electrode surface. Here, a quaternary ammonium surfactant was added to the electrolyte. The structure of this molecule, which is known as Empigen BB, is shown in Fig. 2.18. The morphology of the Cu film improved upon addition of the surfactant, with larger and more uniform grains being observed—see Fig. 2.17b and c. AFM data indicated a decrease in surface roughness as more Empigen BB was added, as shown in Table 2.5. The addition of Empigen BB also reduced the rate of electrodeposition, as a consequence of blocking up surface sites, so the quantity added to the electrolyte was kept as low as possible to achieve smooth films with a reasonable deposition rate.

2.7 Electrodeposition of Sn: The Methane Sulfonic Acid Electrolyte

An acidic electrolyte was used for the deposition of Sn, and the reference electrode used in this situation was silver-silver chloride (Ag|AgCl), which has a potential of 0.197 V vs. NHE. All potentials in the following discussion are given with respect to Ag|AgCl.

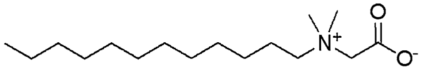

Fig. 2.18 The structure of the surfactant used in the alkaline sorbitol electrolyte, which has the trade name Empigen BB

Table 2.5 Surface roughness of Cu films from electrolytes with different amounts of empigen BB, measured by AFM

Quantity of empigen BB (vol%)	RMS surface roughness (nm)
0	28.0
0.015	20.6
0.025	17.0

Table 2.6 Composition of the methane sulfonic acid electrolyte for Sn

Component	Concentration
Sn(II) methane sulfonate $Sn(CH_3SO_2O^-)_2$	0.05 M
Methane sulfonic acid CH_3SO_2OH (50 wt% in H_2O)	1.0 M
Empigen BB (N,N-Dimethyl-N-dodecylglycine betaine)	0.1 vol%

2.7.1 Substrates

Since Sn forms the second layer in the precursor, the substrate should now be a Cu-coated Mo electrode. Due to its more negative standard reduction potential, the stripping peak for Sn is negative of that for Cu and the full cyclic voltammogram may be examined on a Cu substrate without danger of damaging the substrate.

2.7.2 Cyclic Voltammetry

The composition of the methane sulfonic acid electrolyte for Sn is shown in Table 2.6. Note that this electrolyte contains a surfactant, as recommended in the source reference [14]. The pH of the electrolyte is around 1.0.

The relevant electrochemical reactions at pH 1 are [3]:

$$Sn^{2+} + 2e^- \rightarrow Sn \quad E = -0.37V \tag{R 2.9}$$

$$H^+ + e^- \rightarrow \tfrac{1}{2}\, H_2 + H_2O \quad E = -0.26\ V \tag{R 2.10}$$

The hydrogen overpotential of Sn is −0.75 V, so the HER should not occur at a significant rate until about −1.0 V.

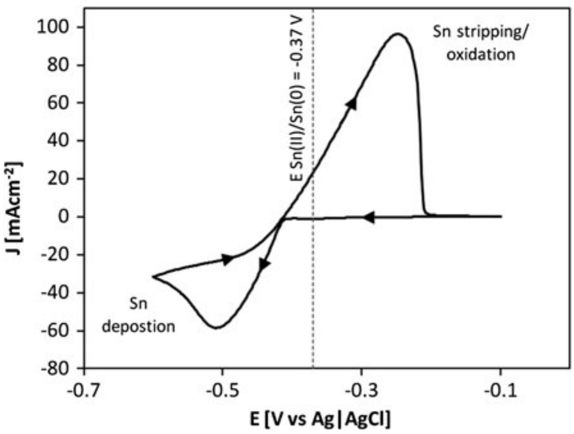

Fig. 2.19 Cyclic voltammetry of the methane sulfonic acid Sn electrolyte at a Cu electrode. *Dashed line* indicates calculated position of Sn(II) reduction

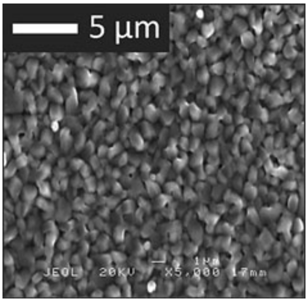

Fig. 2.20 SEM image of electrodeposit obtained from the methane sulfonic acid electrolyte for Sn at a potential of −0.55 V vs. Ag|AgCl

The cyclic voltammogram for this electrolyte at a Cu substrate is shown in Fig. 2.19. The displacement of the voltammogram towards more negative potentials than those expected from the standard reduction potential for Sn^{2+} can be explained by complexation of Sn^{2+} by MSA. There is no significant current due to hydrogen evolution in the range of potentials shown in the figure, which should mean that Sn is deposited with high efficiency.

A suitable potential for potentiostatic deposition based on the cyclic voltammetry is around −0.4 to −0.6 V vs. Ag|AgCl.

2.7.3 Morphology of Electrodeposits

The deposits obtained using this electrolyte were strongly adherent and highly reflective. Figure 2.20 shows the morphology of a typical deposit. The film is conformal with large, uniform grains.

Table 2.7 Composition of the acid chloride electrolyte for Zn

Component	Concentration
$ZnCl_2.2H_2O$	50 mM
pH 3 Hydrion® buffer	1 g per 100 ml
KCl	1 M
Polymeric surfactant (see Table 2.2)	0.2 g per 100 ml

2.8 Electrodeposition of Zn from an Acid Chloride Electrolyte

A Ag|AgCl reference electrode was used with the Zn electrolyte. In the following discussion, all potentials are given with respect to this electrode (0.197 V vs. NHE).

2.8.1 Substrates

As the final layer of the precursor, the substrates for Zn depositions should ultimately be Mo|Cu|Sn films. However, to simplify substrate preparation for studying the electrochemistry of the Zn electrolyte, Cu-coated Mo electrodes were used.

2.8.2 Cyclic Voltammetry of the Acid Chloride Electrolyte for Zn

The constituents of the electrolyte are shown in Table 2.7. Since Zn has a rather negative standard reduction potential, hydrogen evolution is expected to occur to some extent during deposition. The hydrogen evolution reaction will increase the pH in the vicinity of the working electrode because H^+ ions are consumed. The pH buffer is used to maintain a constant pH throughout the deposition so that the deposition conditions do not change.

The relevant electrochemical reactions at pH 3 are:

$$Zn^{2+} + 2e^- \rightarrow Zn^0 \quad (E = -1.00\ V) \tag{R 2.11}$$

$$H^+ + e^- \rightarrow \tfrac{1}{2} H_2 + H_2O \quad (E = -0.37\ V) \tag{R 2.12}$$

The HER should not in fact occur until around −1.20 V if the substrate becomes covered with Zn, due to its high hydrogen overpotential. The cyclic voltammetry of the acid chloride electrolyte is shown in Fig. 2.21a. The main deposition and stripping waves can be clearly seen, close to the expected potential. As well as these primary peaks, at around −0.75 V there is an underpotential deposition couple (a smaller deposition and stripping peak at more positive potentials compared to the primary peaks), which is shown more clearly in Fig. 2.21b.

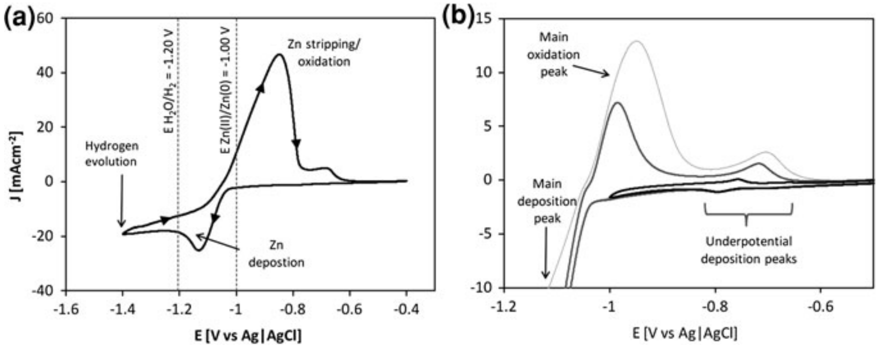

Fig. 2.21 **a** Cyclic voltammetry of the acid chloride Zn electrolyte at a Cu substrate. **b** Close-up cyclic voltammetry in the region of the underpotential peaks (several voltammograms with different reversal potentials are shown)

Underpotential deposition (UPD) occurs in the early stages of electrodeposition if a stable alloy can be formed between the substrate and the depositing species, in this case Cu and Zn respectively. Cu and Zn can alloy over a large compositional range at room temperature, as will be discussed in Chap. 3. The underpotential deposition reaction is shown below:

$$\mathrm{Zn}^{2+} + 2\mathrm{e}^- + \mathrm{Cu} \rightarrow \mathrm{Zn} - \mathrm{Cu} \qquad \mathrm{E}_{\mathrm{upd}} = -0.96 - \Delta_f G/2F \qquad (\mathrm{R}\,2.13)$$

The (negative) free energy of formation of the Cu–Zn alloy, $\Delta_f G$, shifts the reduction potential by an amount equal to $-\Delta_f G/zF$. Therefore a deposition peak is observed at more positive potentials than the primary peak. When the substrate is completely covered and the depositing species is no longer interacting directly with the original substrate material, the reduction potential returns to its usual value. Upon stripping, the alloy phase also requires a more positive potential before it can be oxidised due to the additional strength of the bonding between its elements. This entire process appears as an additional pair of peaks at more positive potentials than the main deposition and stripping peaks. $\Delta_f G$ in this case is around 54 k J mol^{-1}.

Based on the cyclic voltammetry, a reasonable potential for potentiostatic deposition of Zn films is around −1.1 to −1.3 V vs. Ag|AgCl.

2.8.3 *Morphology of Zn Electrodeposits*

Zn deposits at Cu electrodes were bright and strongly adherent, and it was found that a potential of −1.22 V gave the best results. Figure 2.22a shows the surface morphology of the Zn electrodeposit. The film completely covers the substrate and shows a uniform grain size. Some pits can be seen, which may correspond to sites of hydrogen evolution during deposition.

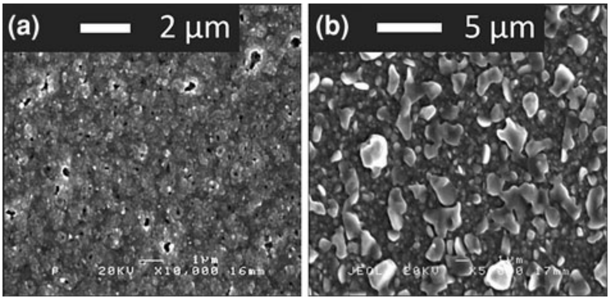

Fig. 2.22 **a** Morphology of Zn electrodeposit from the acid chloride electrolyte at a Cu electrode. **b** Morphology of Zn deposited under the same conditions at a Sn electrode

The final step in precursor preparation would be to electrodeposit Zn on top of Mo|Cu|Sn substrates; however, it soon became clear that Zn deposition at Sn electrodes was problematic. In contrast to the films produced at Cu substrates, the Zn films grown on Sn substrates were poorly adhering and had very poor coverage and morphology, as seen in Fig. 2.22b. In addition, considerable hydrogen evolution was seen when depositing at Sn, whereas it had not been seen when depositing at Cu.

The failure of Zn to nucleate at Sn could be attributed to an oxide layer on the Sn surface, but SnO_2 should be reduced to Sn at a much more positive potential than that used for the deposition of Zn (approx. −0.55 V at pH 3 cf. −1.22 V), therefore we can eliminate this as the source of the problem. Instead it seems that it is the hydrogen evolution reaction occurring at Sn that interferes with Zn deposition, blocking surface sites and therefore preventing nucleation and growth of Zn grains.

2.8.4 Understanding the Difference in Zn Deposition at Cu and Sn Substrates

The fact that the HER is the dominant reaction at Sn substrates when attempting to deposit Zn but that the same problem is not seen at Cu substrates runs contrary to the expected behaviour: the hydrogen overpotential for Sn is in fact much higher than that for Cu (0.75 V compared to 0.45 V), so if anything a Sn substrate ought to be preferable to a Cu substrate when depositing a metal with a very negative reduction potential like Zn. Table 2.8 gives values of hydrogen overpotential, η_{H_z}, for the electrode materials concerned here, as well as the potentials at which the HER is consequently expected to occur on each substrate. In the following discussion, all potentials are quoted with respect to the Ag|AgCl reference electrode.

When taking η_{H_z} into account, the HER should occur at about −1.12 V at the Sn electrode, which is positive of the potential used for Zn deposition (−1.22 V).

Table 2.8 Hydrogen overpotentials η_{HER} at different substrate materials, the potential at which evolution of hydrogen is expected to occur at a current density of 1 mA cm^{-2}

Substrate	η_{H_2} (V at 1 mA cm^{-2} current density)	$E^o_{HER} - \eta_{H_2}$ (V vs. Ag|AgCl)
Cu	0.45	−0.82
Sn	0.75	−1.12
Zn	0.83	−1.20

Thus the concurrent evolution of hydrogen when Zn is deposited at the Sn electrode is not surprising. However, since η_{H_z} at Cu is lower than that at Sn, the HER should in fact be very vigorous at Cu electrodes at −1.22 V; yet this is not observed and Zn deposits uniformly without hindrance by the HER. An explanation can be found in the cyclic voltammetry of the Zn electrolyte at different electrodes. In Fig. 2.23a, a clear underpotential deposition (UPD) wave can be seen at the Cu electrode, corresponding to the favourable formation of a Cu–Zn alloy in the initial stages of deposition. The same is not observed at a Sn electrode, Fig. 2.23b, although in other respects the voltammetry is the same. The lack of a UPD wave at the Sn electrode is due to the fact that there are no Zn–Sn alloys—the free energy of mixing is positive at all compositions in the Zn–Sn system [18]. We suggest that the possibility for underpotential deposition is the decisive factor for the electrodeposition of Zn in this instance, as will now be explained.

For Zn deposition at Cu, the UPD wave occurs positive of the HER, at about −0.75 V. Thus in the very early stages of deposition, a thin Zn layer will nucleate very quickly and η_{H_z} for the electrode will increase towards the value for pure Zn; the HER is no longer expected until about −1.20 V. At this potential, as seen in the voltammogram (Fig. 2.21), Zn deposition is already rapid compared to the HER: approx. 13 mA cm^{-2} compared to 1 mA cm^{-2}. Therefore Zn deposition out-competes the HER and we would expect an efficiency of about 93% (in fact, we find about 90%, as will be seen later in this chapter).

For Zn deposition at Sn, there is no equivalent underpotential deposition process, so the HER dominates from the outset. Since Zn cannot effectively cover the substrate, the hydrogen overpotential remains much lower than the deposition potential. The deposition efficiency is low and the resulting Zn deposit has very poor surface coverage.

2.8.5 Enabling Zn Deposition by Adding a Second Cu Layer

The solution to this problem was to deposit a second layer of Cu over the Sn layer before depositing the final Zn layer, resulting in a Cu|Sn|Cu|Zn stack. As was previously mentioned, the order of standard reduction potentials of Cu and Sn should make deposition of Cu on top of Sn difficult because the substrate ought to be oxidised at the potentials at which Cu is deposited. However, because of the

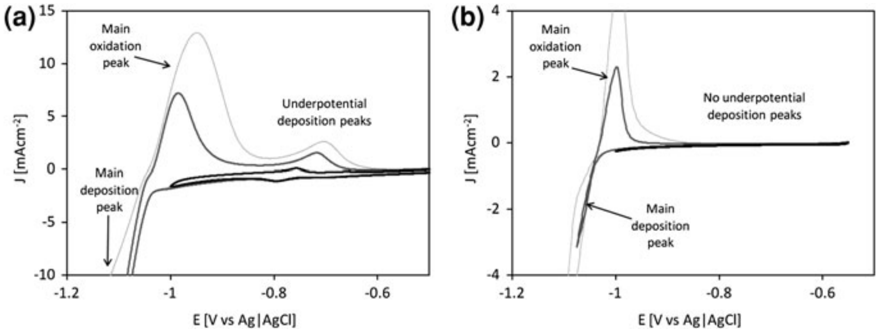

Fig. 2.23 Cyclic voltammetry of the acid chloride Zn electrolyte at **a** a Cu substrate and **b** a Sn substrate, showing **a** the presence and **b** the absence of an underpotential deposition couple at −0.75 V

Fig. 2.24 Comparison of pH 14.5 voltammetry for Cu and Sn

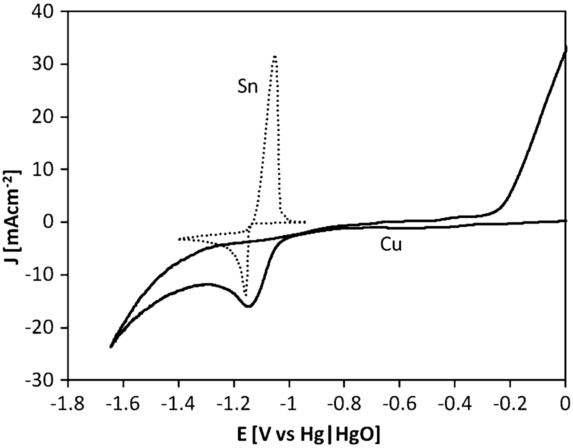

considerable negative shift of the Cu deposition wave due to sorbitol complexation, this is less of a problem. The cyclic voltammetry of the alkaline Sn electrolyte mentioned in Sect. 2.3.2 is shown in Fig. 2.24, overlaid with the cyclic voltammetry of the alkaline sorbitol Cu electrolyte. The deposition peak for Cu is actually close to that of Sn, despite the difference in their standard reduction potentials, due to the complexation of Cu(II). Sn is stripped at potentials positive of around −1.1 V, whereas Cu deposition can be carried out at more negative potentials than this, in principle allowing the deposition of Cu on a Sn substrate without substrate oxidation. In practice, a rather negative potential of −1.45 V vs. Hg|HgO was required to achieve complete coverage of the Sn substrate by Cu without substrate oxidation. This potential was therefore applied for a few seconds at the start of the deposition to obtain complete coverage, after which the potential was reduced to −1.10 V to continue Cu deposition.

2.9 Achieving Macroscopic Uniformity in the Precursor

In the previous section, conditions were established for electrodeposition of a Cu|Sn|Cu|Zn stack with good layer morphologies. As discussed, it is also important to produce layers of uniform thickness over the entire area of the substrate.

2.9.1 Issues with Electrodeposition at Vertical Working Electrodes

In earlier work, depositions were made at vertical electrodes immersed in unstirred solutions. This allowed for a simple setup and it was initially assumed that the natural convection currents created during electrodeposition would not contribute significantly to the mass transport and therefore that the films would be relatively flat. CZTS films were prepared from Cu|Sn|Zn stacks (made using the alkaline sorbitol Sn electrolyte), and the results from these were reported in references [9, 11, 17]. However, these films exhibited large variations in composition as a function of position on the sample: they were usually Zn-rich at the edges, and thicker at the bottom of the sample. A measure of the thickness of the individual layers of the precursor was made using linear EDS scans along sections of the films, which were approx. 8 × 10 mm. Figure 2.25a–f shows some examples of scans in both directions (left–right, top–bottom) across Cu, Sn and Zn films produced by electrodeposition at a vertical working electrode. Note that EDS does not give a direct measure of film thickness; the EDS signal comes from a teardrop-shaped volume of material originating at the point where the electron beam enters the sample. In all instances discussed here, Mo was visible in the EDS spectrum, which fact means that the entire depth of the precursor was being probed. Therefore variations in the strength of the EDS signal do correspond to variations in the thickness of the film (i.e. the amount of film encompassed by the teardrop volume changes), although not necessarily in a linear fashion. From the figures, it is apparent that there is a large degree of thickness variation, especially in the Cu and Sn layers, and especially from the bottom to the top of the film. The fact that the thickness variations are not the same for each element shows that the composition of the film will indeed vary considerable over the area of the sample. The pattern of thickness variations is consistent with mass transport during electrodeposition occurring by natural convection, as described in Sect. 2.2.3.

Since mass transport is strongly influencing the uniformity of the precursor, we must use forced convection to make the mass transport towards the substrate uniform at all points. A rotating disc electrode was adopted in order to achieve this.

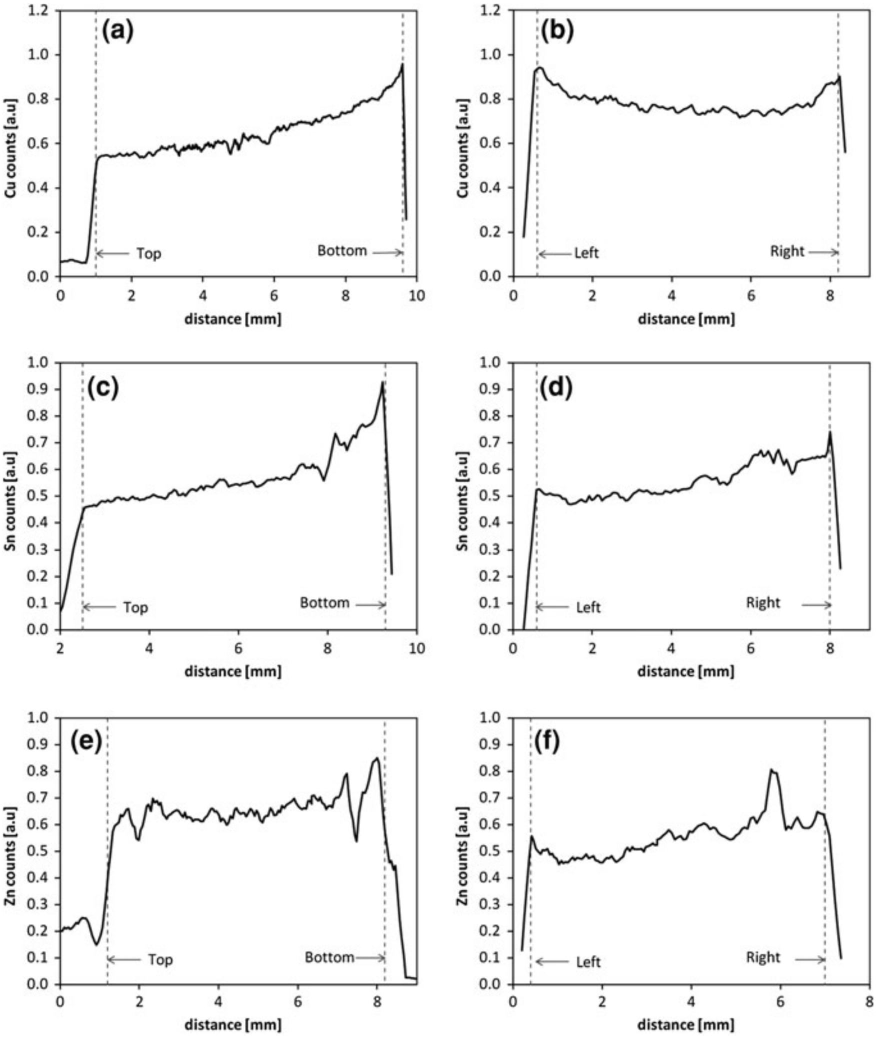

Fig. 2.25 EDS line scans showing thickness variations as a function of position in two perpendicular directions across films produced at vertical working electrodes in unstirred solutions: Cu (**a**, **b**); Sn (**c**, **d**); Zn (**e**, **f**)

2.10 Electrodeposition at the Rotating Disc Electrode

2.10.1 Influence of Forced Convection on the Cyclic Voltammetry

A rotating disc arrangement was designed as described in Sect. 2.4.6. The rotation rate controls the rate of mass transport towards the electrode surface. When the deposition is under diffusion control, this will therefore control the current density.

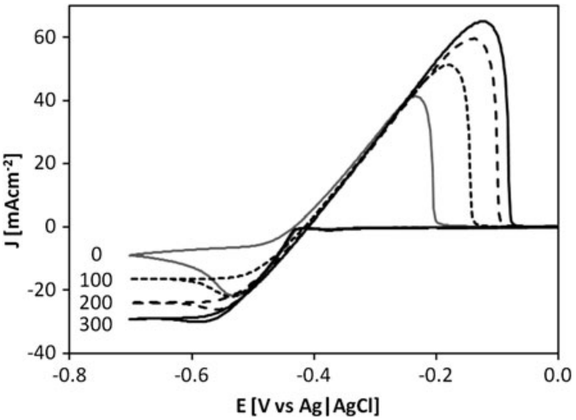

Fig. 2.26 Influence of RDE rotation rate on cyclic voltammetry of Sn deposition at a Cu electrode. Numbers indicate the rotation rate in revolutions per minute (rpm)

This is illustrated for Sn in Fig. 2.26. In the cyclic voltammetry, it can be seen that increasing the rotation rate increases the current density at potentials negative of the peak that is seen in the unstirred voltammogram—i.e. in the region where the deposition was diffusion controlled, the RDE accelerates the deposition. At higher rotation rates, there is no peak at all, because the replacement of the solution at the electrode surface by convection is more rapid than its consumption. The Levich equation (Eq. 2.13) was used to calculate diffusion coefficients based on the limiting current density as a function of rotation rate. Values of 2.2×10^{-6}, 8.5×10^{-6} and 8.3×10^{-5} cm^2 s^{-1} were derived for Cu, Sn and Zn respectively. The diffusion coefficient for Zn is considerably higher than for Cu and Sn, which explains why the uniformity of Zn was less affected by natural convection currents when depositing at a vertical working electrode (see Sect. 2.9.1).

2.10.2 Uniformity of Films Deposited Using the RDE

Plots of EDS signal magnitude as a function of position are shown in Fig. 2.27 for Cu films deposited using the RDE. For rotation rates of 200 and 300 rpm, the standard deviations in signal magnitude were 3.0 and 2.4% of the mean values respectively, over an area of 15 × 15 mm. This is a considerable improvement on the data presented in Fig. 2.25a and b. Similar plots, Fig. 2.28a and b, were made for Sn layers deposited from the methane sulfonic acid electrolyte at 100 and 300 rpm, where the standard deviations in thickness were 4 and 2% of the mean values respectively.

In the case of Zn, the behaviour is different. A rotation rate of 100 rpm gave the most uniform films, while faster rotation rates caused the films to become cloudy. The diffusion coefficient of Zn^{2+} is much higher than the values for Cu and Sn, so the deposition rate depends not upon mass transport but on the rate of reaction of Zn^{2+} at the electrode surface. Variations in the magnitude of the potential

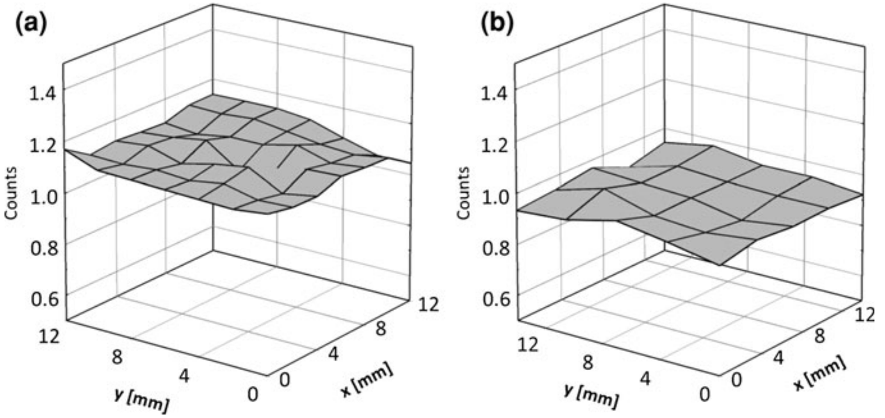

Fig. 2.27 EDS maps of Cu electrodeposits showing thickness variations at **a** 200 rpm and **b** 300 rpm

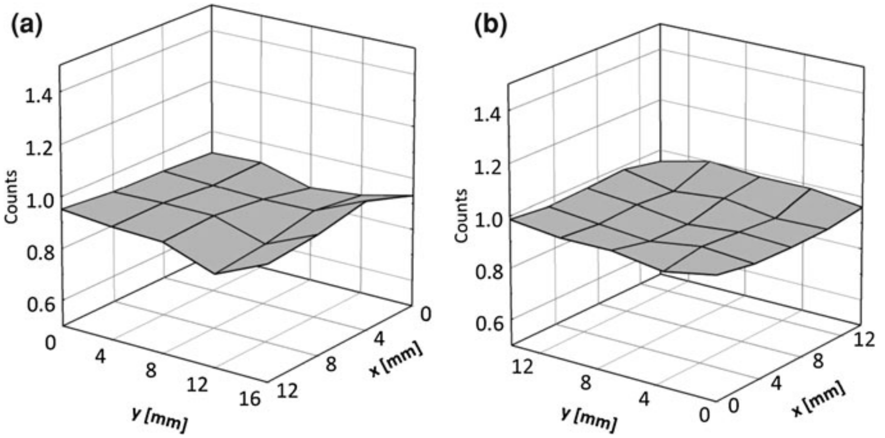

Fig. 2.28 EDS maps of Sn electrodeposits showing thickness variations at **a** 100 rpm and **b** 300 rpm

difference as a function of position can therefore affect the thickness of the deposit. It is important in this case to have a uniform distribution of the electric field between the working and counter electrodes, which can be achieved by using a symmetrical arrangement of the counter and working electrodes. There is a general tendency for electric field lines to concentrate at the edges of electrodes [12], which can be offset to some extent by using a higher concentration of background electrolyte, providing a higher ionic conductivity. Figure 2.29a and b show the effect of increasing the background electrolyte concentration in the case of Zn deposition at the RDE. In (a), 1 M KCl was used as a background electrolyte, and the edges of the film are clearly thicker than the central region. In (b), with a

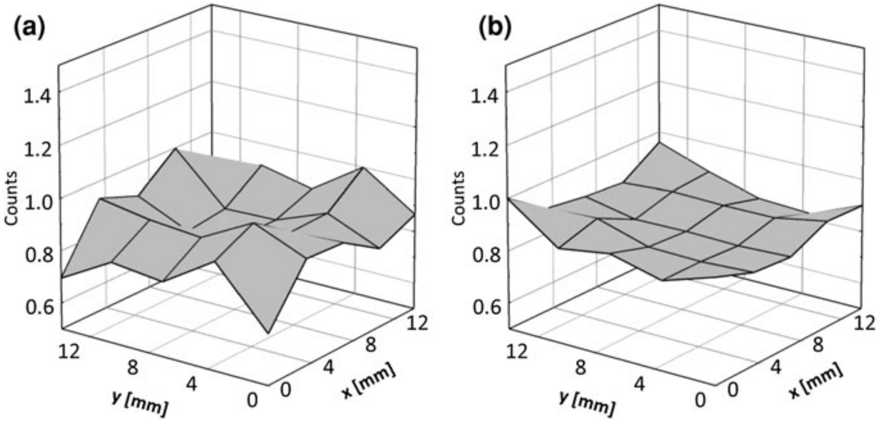

Fig. 2.29 Effect of background electrolyte concentration on relative thickness of electrodeposited Zn films as a function of position: **a** 1 M KCl, **b** 2 M KCl

concentration of 2 M, this effect is present but much reduced. The standard deviations as a percentage of the mean values were 10 and 5% respectively.

Within the available time frame, and given the limitations of the equipment, the layer uniformity could not be improved further. The uniformity of the Cu and Sn layers would benefit from a larger RDE diameter and a much larger volume of electrolyte, in order better to meet the conditions for uniform mass transport at the RDE as described in Sect. 2.2.3. The working electrode radius should be small compared to total RDE radius, and the solution depth should be large compared to RDE radius. In the present case, these conditions are not truly met, so there will be disruptions to the ideal flow scenario resulting from interactions of the flow pattern with the sides of the deposition vessel and the counter electrode, as shown in Fig. 2.30. The volumes of chemicals required to approximate the ideal case would be prohibitive for small-scale work. On a larger scale, there are many successful approaches for achieving good film uniformity by controlling mass transport (either laminar or turbulent flow can be used) [14]. However, with the small-scale process developed herein, there will be some inherent limitations placed on the compositional uniformity of the final CZTS film.

2.11 Finalised Deposition Conditions for Precursor Stacks

We can now summarise the finalised electrodeposition conditions for each layer of the precursor stack. These are shown in Table 2.9.

Current–time curves for potentiostatic depositions of each layer under the conditions described in Table 2.9 are shown in Fig. 2.31. The structure of the curves in each case is similar: there is an initial spike of current at the instant of electrode immersion which corresponds to charging of the double layers at the

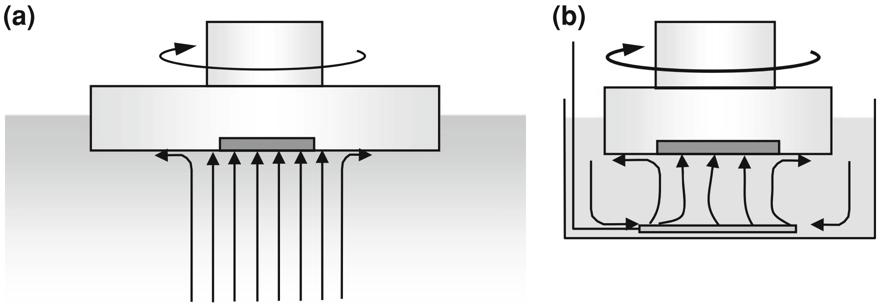

Fig. 2.30 Schematic flow diagrams in the RDE setup for **a** the ideal RDE geometry—large RDE diameter compared to working electrode diameter, large solution depth compared to RDE diameter—giving laminar flow; **b** the experimental geometry employed herein

Table 2.9 Electrodeposition solutions and conditions for each stage in the preparation of Cu|Sn|Cu|Zn precursors

Layer	Electrolyte composition	Potential [V vs. (ref)]	Rotation rate (rpm)
Cu (1)	3 M NaOH, 0.2 M Sorbitol, 0.1 M $CuSO_4{\cdot}5H_2O$, 0.025 vol% Empigen BB	−1.08 (Hg|HgO)	300
Sn	1 M methane sulfonic acid, 50 mM Sn(II) methane sulfonate, 0.1 vol% Empigen BB	−0.55 (Ag|AgCl)	300
Cu (2)	As above.	−1.45 for 2 s, then −1.10 (Hg|HgO	300
Zn	2 M KCl, 1 wt% pH 3 hydrion buffer, 0.2wt% polymeric surfactant (see Table 2.2)	−1.22 (Ag|AgCl)	100

surface of the electrodes. This occurs very quickly, and then deposition begins. The current decreases to a steady value when the rate of replenishment of the electrolyte at the electrode surface is equal to the rate of consumption of the ions by deposition. For the first layer of Cu deposition, Fig. 2.31a, this process is quite protracted and the current drops substantially over about 40 s despite the high rate of stirring. This perhaps indicates that there is some change in the deposition mechanism over time. In contrast, the curves for Sn and Zn (Fig. 2.31b and d) show equilibration within a few seconds. The second layer of Cu deposition, Fig. 2.31c, has two sections corresponding to the two potential steps employed. The current is negative at all times, which means that stripping of the Sn substrate was negligible.

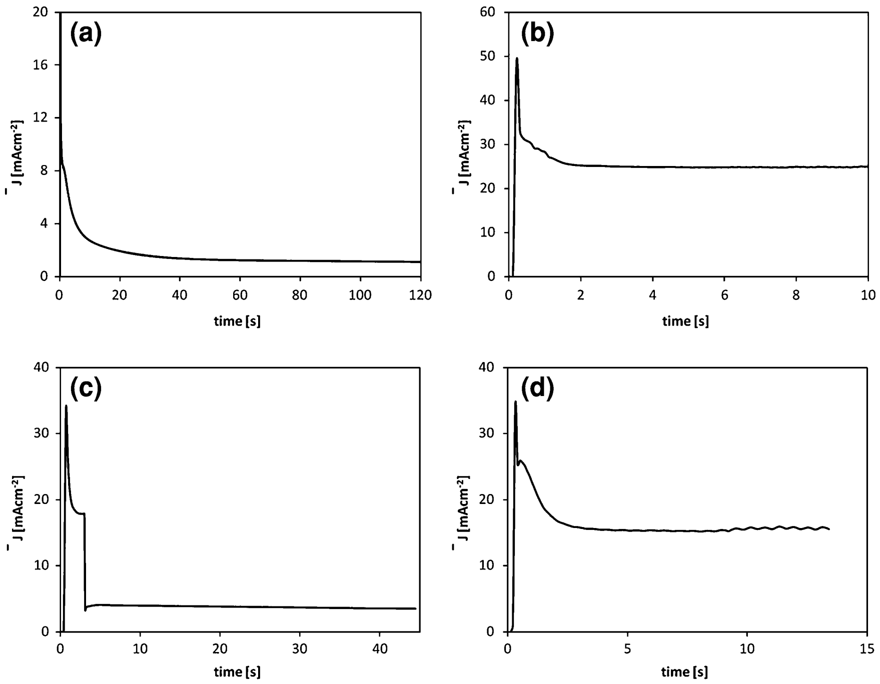

Fig. 2.31 Current-time curves for each stage of Cu|Sn|Cu|Zn precursor deposition: **a** Cu deposited at Mo, **b** Sn deposited at Cu, **c** Cu deposited at Sn, and **d** Zn deposited at Cu. Deposition conditions are given in Table 2.9

2.11.1 Efficiency of Electrodeposition Steps

Having determined conditions to deposit each layer of the precursor stack with good morphology and uniformity, it is now necessary to determine the deposition efficiency for each layer, in order that a stack with the desired composition and thickness can be produced. In Sect. 2.1.5 an expression was derived that related the total deposited charge, q_d, to the charge due to metal deposition alone, q_m, which is repeated below:

$$q_m = q_d \varphi_m - q_0 \varphi_m, \tag{2.14}$$

where φ_m is the efficiency of electrodeposition—the fraction of the charge that is due to metal electrodeposition at steady state—and q_0 is a constant amount of metal deposited during the early stage of deposition before the solution concentration and surface properties have reached a steady state. The q_d is automatically recorded during electrodeposition. Determination of q_m is easily made for Sn and Zn on Cu substrates, by switching to a potential at which the deposit is re-oxidised, i.e. stripping the film, immediately after deposition. An example of this experiment is shown in Fig. 2.32a. Zn was deposited for 60 s at a potential of −1.1 V vs.

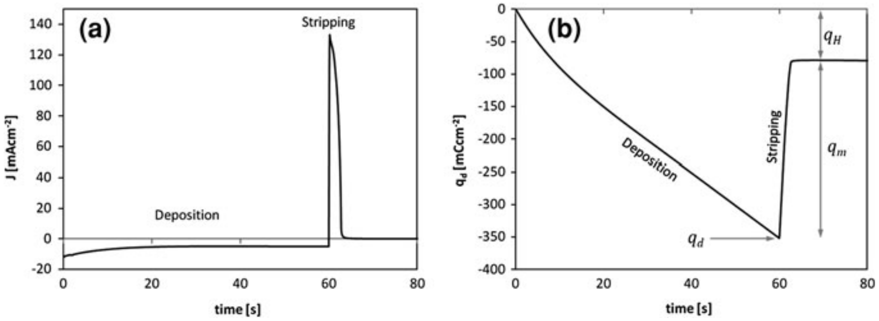

Fig. 2.32 **a** Current flow and **b** charge passage during deposition and subsequent stripping of a Zn film. Deposition potential = −1.1 V vs. Ag|AgCl, stripping potential = −0.4 V vs. Ag|AgCl

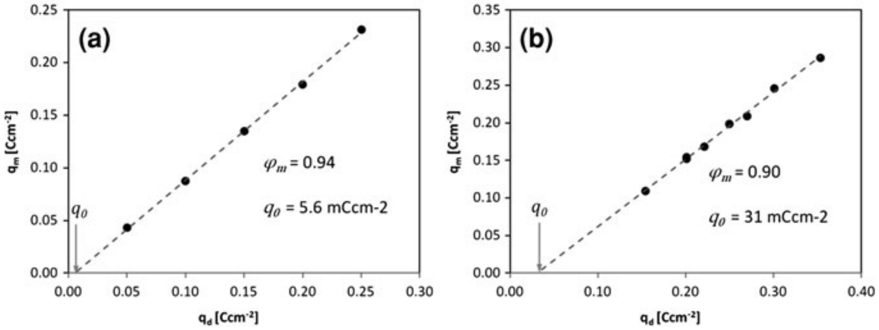

Fig. 2.33 Stripped charge as a function of the amount of charge passed during deposition for **a** Sn deposited at Cu, and **b** Zn deposited at Cu. Electrodeposition conditions were given in Table 2.9

Ag|AgCl and then immediately stripped by switching to a potential of −0.4 V. The current is negative during deposition, corresponding to reduction of Zn^{2+}, and positive during stripping, as Zn is re-oxidised. The stripping current is much higher than the deposition current since the concentration of Zn in the electrodeposit is significantly higher than the concentration of Zn^{2+} in the solution. The integrated current density (equivalent to cumulative charge density) is shown in Fig. 2.32b. It increases steadily during deposition, and, upon switching of the potential, rapidly drops as the electrodeposit is removed. The values of q_m and q_d are indicated on the plot, as well as the charge passed that was due to other reactions, most likely hydrogen evolution, q_H.

In this way, q_m was measured for a series of films with different total deposition charges q_d. A plot of q_m against q_d yields the deposition efficiency from the gradient and q_0 from the x-intercept. This is shown for Sn and Zn in Fig. 2.33.

In the case of Cu, q_m cannot be measured by stripping because of the aforementioned oxidation of the Mo substrate. Instead, the deposited films were

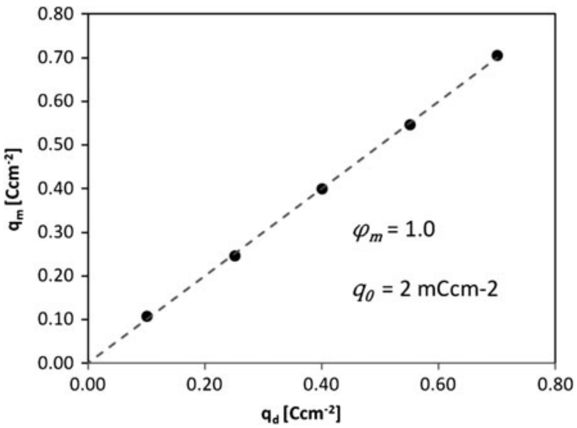

Fig. 2.34 Quantity of Cu recovered by AAS experiment (expressed as equivalent charge) as a function of charge passed during electrodeposition. Electrodeposition conditions were given in Table 2.9

Table 2.10 Steady state electrodeposition efficiencies, φ_m for each metal, and constant charge density q_0 corresponding to initial hydrogen evolution at substrate

Metal	E [V vs. (Ref)]	$E_{HER} + \eta_{HER}$ [V vs. (Ref)]	φ_m (%)	q_0 (C cm^{-2})
Cu	−1.08 (Hg|HgO)	−1.31 (Hg|HgO)	100	0.002
Sn	−0.55 (Ag|AgCl)	−1.00 (Ag|AgCl)	94	0.006
Zn	−1.22 (Ag|AgCl)	−1.20 (Ag|AgCl)	90	0.031

Also shown are the deposition potentials, E, and the potential at which hydrogen evolution is expected, E_{HER}, taking into account the hydrogen overpotential, η_{HER}, of the depositing material

dissolved in acid and the resulting solutions analysed by atomic absorption spectroscopy (AAS) to determine the concentration of Cu^{2+} ions. The absolute quantity of Cu in the film was then derived by knowledge of the precise solution volumes, and this was converted to an equivalent deposition charge, according to Eq. 2.9. The results are shown in Fig. 2.34. The derived deposition efficiencies and values of q_0 are shown in Table 2.10 for each metal.

As can be seen in Table 2.10, the depositions in each case are very efficient. Based on the potential difference between the deposition potential and the expected hydrogen evolution potential, one would predict that Zn would be the least efficient, and have the largest value of q_0, which is indeed observed. Sn would be predicted to have the highest efficiency; however, this is not the case according to these data. Knowing these parameters, we can calculate the molar quantity of metal deposited for a given charge passage, which enables us to control the composition and thickness of the precursor stack.

2.11.2 Design of Precursor Thickness and Composition

The key parameters of the precursor stack are its composition and thickness. The composition can be defined by the ratios of the atomic percentage of each metal, r_i:

$$\frac{r_{Cu}}{r_{Zn} + r_{Sn}} = \alpha \tag{2.15}$$

$$\frac{r_{Zn}}{r_{Sn}} = \beta, \tag{2.16}$$

according to the condition that:

$$\sum r_i = 1. \tag{2.17}$$

These can be rearranged to give the values of atomic percentage:

$$r_{Cu} = \frac{\alpha}{1 + \alpha} \tag{2.18}$$

$$r_{Sn} = \frac{1}{(1 + \alpha)(1 + \beta)} \tag{2.19}$$

$$r_{Zn} = \frac{\beta}{(1 + \alpha)(1 + \beta)}. \tag{2.20}$$

The thickness of the precursor, t_p, is the sum of the individual layer thicknesses, and can be expressed in terms of the molar quantity of each metal, n_i, the molar mass $M_{R,i}$ and the density, ρ_i, for a film with total area A:

$$t_p = \sum t_i = \sum \frac{M_{R,i} n_i}{\rho_i A} \tag{2.21}$$

The molar quantity of metal is proportional to the charge per unit area passed during deposition of the metal, $q_{m,i}$:

$$n_i = \frac{q_{m,i} A}{z_i F}, \tag{2.22}$$

where z_i is the charge on the metal ion and F is Faraday's constant. Combining this with Eq. 2.21 gives us an expression for film thickness as a function of the deposition charges:

$$t_p = \frac{1}{F} \sum \frac{M_{R,i} q_{m,i}}{z_i \rho_i} \tag{2.23}$$

The charge passage associated with each layer, $q_{m,i}$, is related to the atomic percentage of element i in the finished precursor by the expression:

$$\frac{q_{m,i}}{z_i} = r_i \sum \frac{q_{m,i}}{z_i} \tag{2.24}$$

This allows us to re-express Eq. 2.23:

$$t_p = \frac{1}{F} \sum \frac{q_{m,i}}{z_i} \cdot \sum \frac{M_{R,i} r_i}{\rho_i}. \tag{2.25}$$

Finally, we obtain solvable expressions for each value of $q_{m,i}$ by substituting Eq. 2.24 again:

$$t_p = \frac{1}{F} \frac{q_{m,i}}{z_i r_i} \sum \frac{M_{R,i} r_i}{\rho_i}, \tag{2.26}$$

which is rearranged to give Eq. 2.27:

$$q_{m,i} = \frac{t_p F z_i r_i}{\sum M_{R,i} r_i / \rho_i} \tag{2.27}$$

This equation allows us to calculate the deposition charge for each metal layer based on the desired composition and thickness of the finished precursor. In fact, we are more interested in the thickness of CZTS film that will form from the precursor by sulfurisation. During sulfurisation, the mass of the film increases due to S incorporation, and the density decreases as the CZTS phase forms. The thickness of the sulfurised film, t_c, is related to the precursor thickness by an expansion factor, σ.

$$\sigma = \frac{t_c}{t_p} = \frac{m_c}{A \rho_c t_p}, \tag{2.28}$$

where m_c and ρ_c are the mass and density of the sulfurised film. Deriving explicit expressions for these two variables is not straightforward, since the sulfurised film may be made of multiple phases. However, for the case of a perfect CZTS phase, ρ_c is known and we can calculate m_c simply from the fact that, based on the formula unit of CZTS, the metal atoms from the precursor account for approx. 71% of the mass of the final sulfurised film. If we make the reasonable assumption that the expansion is similar even for non-stoichiometric films, we can conclude that:

$$m_c = 1.41 m_p \tag{2.29}$$

We can calculate the precursor mass, m_p, using a similar approach as for t_p, which gives:

$$m_c = 1.41 \frac{A q_{m,i}}{F z_i r_i} \sum M_{R,i} r_i, \tag{2.30}$$

And therefore the expansion factor σ is given by:

Table 2.11 Parameters required for calculation of deposition charges in precursor fabrication

Material	M_R (g mol^{-1})	ρ (g cm^{-3})	z_i	φ (%)	q_0 (C cm^{-2})
Cu	63.55	8.94	2	100	0.002
Zn	65.39	7.14	2	90	0.031
Sn	118.71	7.35	2	90	0.006
CZTS	–	4.88	–	–	–

$$\sigma = \frac{1.41}{\rho_c} \frac{\sum M_{R,i} r_i}{\sum M_{R,i} r_i / \rho_i}. \tag{2.31}$$

For a stoichiometric film ($r_{Cu} = 0.5$, $r_{Sn} = r_{Zn} = 0.25$), σ is about 2.3, so we should expect the films roughly to double in thickness during sulfurisation.

The final expression for determining the amount of each metal to electrodeposit to obtain a CZTS film of a given thickness and composition (assuming no change in composition occurs during sulfurisation) is derived by substituting Eq. 2.31 into Eq. 2.27 and taking into account the efficiency of electrodeposition (Eq. 2.12):

$$q_{d,i} = \frac{F \rho_c}{1.41 \varphi_i} \frac{t_c r_i z_i}{\sum M_{R,i} r_i} + q_{0,i} \tag{2.32}$$

The required constants are given in Table 2.11.

In this investigation, the film thickness was usually targeted to be 1 micron after sulfurisation, since thicker samples tended to flake off the substrate during sulfurisation. For a stoichiometric film ($\alpha = \beta = 1$), Eq. 2.32 gives deposition charges of 0.433, 0.234 and 0.270 C cm^{-2} for Cu, Sn and Zn respectively. Cu was always divided equally between the two layers in the Cu|Sn|Cu|Zn stack.

2.11.3 Application of Eq. 2.32 in Precursor Design

Using the approach above, and the measured data for deposition efficiencies, two series of precursors were designed: one series with variable α ratio and constant β, and one with constant α and a variable β ratio. The samples were heat-treated at 250–300 °C for several minutes to induce alloying (see Chap. 3). The compositions of the samples were measured using EDS and the actual and predicted values are plotted in Fig. 2.35a and b. The dotted lines in the figures indicate where the predicted value is equal to the measured value. The measured β (Zn/Sn) ratio matches extremely well with the predicted ratio over a large range of composition. The measured α (Cu/(Zn+Sn)) ratio, however, deviates systematically from the prediction. There are a number of reasons this could have occurred. The first possibility is that the Cu deposition is not as efficient as was thought. The efficiency estimated from AAS was 99.7%; however, the measured and predicted data can be brought into close coincidence if the efficiency is assumed to be lower, around 80% (this is indicated in

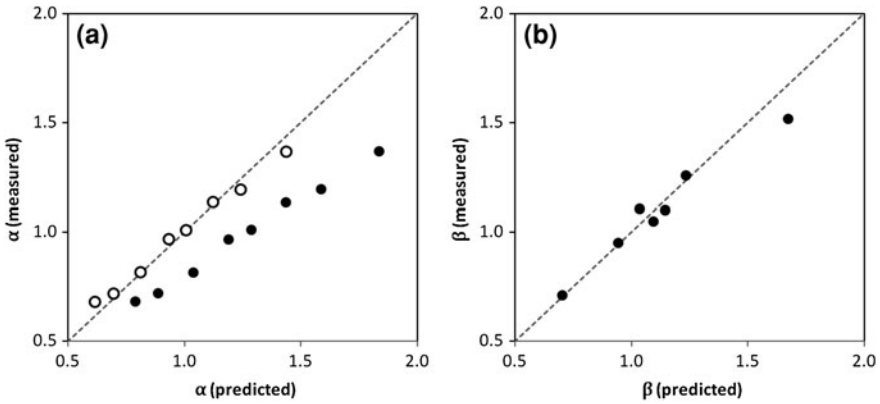

Fig. 2.35 Measured precursor compositions plotted against the predicted compositions based on charge passage during electrodeposition calculated using Eq. 2.32, for compositional ratios **a** $\alpha = \mathrm{Cu/(Zn{+}Sn)}$ and **b** $\beta = \mathrm{Zn/Sn}$. *Dotted lines* indicate where the data points should lie if the prediction is correct. The open symbols in **a** show the predicted composition if the Cu deposition is assumed to be 80% efficient (see text for explanation)

Fig. 2.35a). This modification does not affect the data for the Zn/Sn ratio, and would mean that the AAS experiment was overestimating the Cu^{2+} concentration in the dissolved samples. It is also possible that EDS was underestimating the Cu content because of a depth-dependent distribution of Cu, although the Zn/Sn estimate is apparently not affected. In both cases shown in Fig. 2.35, the measured composition varied linearly with the predicted composition, which indicates that the deposition efficiencies do not vary with the deposit thicknesses, in line with expectations.

It was decided to continue with this method of designing precursors with the assumed lower Cu deposition efficiency. Sample compositions were always measured directly by EDS rather than relying on the predicted values. As will be seen, processes occurring during and after sulfurisation can also modify the final composition of the CZTS films.

An example of the expansion of the precursor during sulfurisation is shown in Fig. 2.36, where it can be seen that the expansion factor is approx. 2.7, close to the predicted value based on the relative densities of the precursor and sulfurised films. The true value is probably larger due to the effect of voids, as seen in the figure.

2.12 Characterisation of a Complete Cu|Sn|Cu|Zn Stack

EDS maps were made of a complete precursor stack over an area of 14 × 14 mm. The compositional ratios α and β are shown in Fig. 2.37 as a function of position. The standard deviation in both cases is 3–4% of the mean

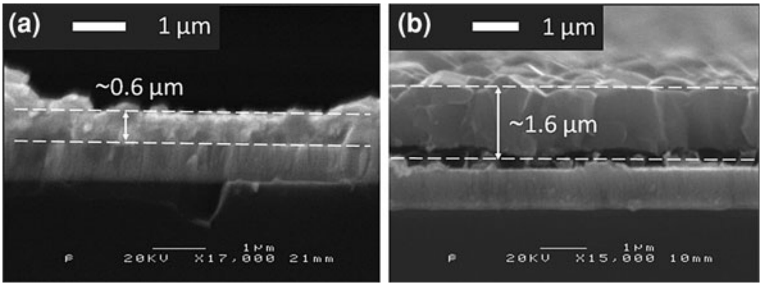

Fig. 2.36 Edge-on SEM images of **a** a precursor and **b** a section of the same sample after sulfurisation, showing the increase in film thickness due to reaction with S

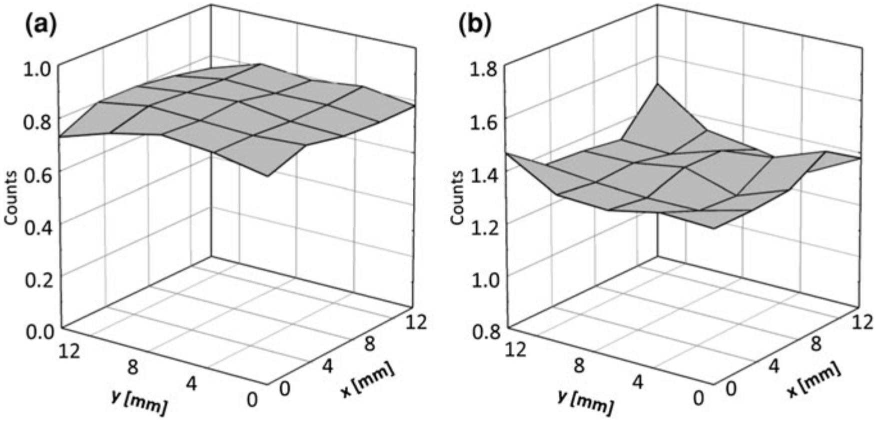

Fig. 2.37 **a** Cu/(Zn+Sn) and **b** Zn/Sn ratios as a function of position measured on a Cu|Sn|Cu|Zn precursor stack

value, similar to the random error in the measurement itself. It appears that the Zn layer is thicker at the edges, which causes α to decrease and β to rise; this limitation was discussed above. The uniformity in the central 10 × 10 mm portion of the film is, however, quite good.

The X-ray diffraction (XRD) spectrum of a precursor is shown in Fig. 2.38. Elemental Cu and Sn are visible, but Zn is not. It is possible that the Zn deposit is non-crystalline/disordered. Interestingly, there are peaks visible for the alloy phases $Cu_{0.8}Zn_{0.2}$ and Cu_6Sn_5, which may have formed during deposition and subsequently grown in the interval between deposition and the diffraction experiment. This will be discussed in greater detail Chap. 3.

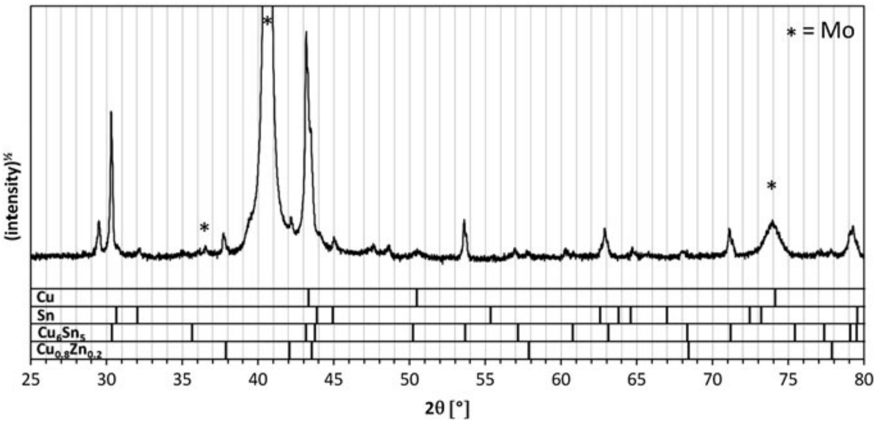

Fig. 2.38 XRD pattern for Cu|Sn|Cu|Zn bilayer on Mo-SLG

Conclusions

Electrodeposition is a widely used technique in many industries, and compared to other methods of thin film deposition it is cost-effective, uses less energy and makes efficient use of materials. The aim of this section of work was to develop an electrodeposition procedure for the preparation of Cu–Sn–Zn films upon Mo-coated substrates. These ‘precursors’ will be converted to Cu_2ZnSnS_4 films by thermal introduction of S. The requirements for the precursor films are: (1) that the Cu–Sn–Zn stoichiometry should be readily controllable, (2) that the stoichiometry should be constant over the entire area of the sample and (3) that the precursor morphology should be flat and uniform. A ‘stacked elemental layer’ (SEL) approach was favoured over co-deposition since it allows greater control of composition and optimisation of individual metal electrolytes, and is therefore a much more versatile approach for development work. The stacking order dictated by the order of reduction potentials for the three metals is Mo|Cu|Sn|Zn, which is different from the proposed ‘best’ order of Araki et al. [13] (Mo|Zn|Sn|Cu), which may have implications for the sulfurisation process.

Electrolytes for Cu, Sn and Zn were selected to be representative of real industrial versions: an alkaline non-cyanide Cu electrolyte, a methane sulfonic acid Sn electrolyte and an acid chloride Zn electrolyte. Cyclic voltammetry was used to investigate the deposition behaviour and the range of potentials for deposition and stripping were established, which in most cases simply related to the standard reduction potentials of the metal concerned. Film depositions were made and it was found that in each case surfactants were required to improve the morphology. This may lead to the incorporation of organic components into the film, which could affect the properties of the final semiconducting film.

Production of Mo|Cu|Sn|Zn stacks was not achievable due to the failure of Zn to deposit at Sn electrodes. This was attributed to vigorous hydrogen evolution occurring alongside the deposition, which is avoided at Cu electrodes because of the underpotential deposition of a Cu–Zn alloy. To circumvent this problem, suitable conditions were developed for deposition of a Mo|Cu|Sn|Cu|Zn stack, which had good morphology.

Early work using deposition at vertical electrodes in unstirred solutions gave large variations in composition over the sample area, attributed to natural convection currents arising during deposition and causing uneven mass transport. To achieve better layer uniformity, a rotating disc electrode system was adopted, which was capable of producing relatively flat films over an area of at least 16 × 16 mm. It was shown that composition variations in complete precursor stacks were vastly reduced as a consequence.

Electrodeposition efficiencies were derived on the basis of a simple two-part model for the deposition process. These efficiencies were used to calculate the required charge flow during deposition of each layer in order to produce a stack of given composition and thickness.

References

1. Bard AJ, Faulkner LR (2001) Electrochemical methods, fundamentals and applications, 2nd edn. Wiley, New York
2. Talbot J, Talbot D (1998) Corrosion science and technology. CRC Press LLC, Boca Raton
3. Pourbaix M (ed) (1974) Atlas of electrochemical equilibria in aqueous solutions, 2nd edn. NACE Celebcor, USA
4. Lee TS (1973) Hydrogen overpotential on zinc containing small amounts of impurities in concentrrated alkaline solution *LEE*. J Electrochem Soc 120(6):707–709
5. Schurr R et al (2009) The crystallisation of Cu_2ZnSnS_4 thin film solar cell absorbers from co-electroplated Cu–Zn–Sn precursors. Thin Solid Films 517(7):2465–2468
6. Hideaki A et al (2009) Preparation of Cu_2ZnSnS_4 thin films by sulfurization of co-electroplated Cu–Zn–Sn precursors. Phys Status Solidi C 6(5):1266–1268
7. Araki H et al (2009) Preparation of Cu_2ZnSnS_4 thin films by sulfurizing electroplated precursors. Sol Energy Mater Sol Cells 93(6–7):996–999
8. Scragg JJ, Berg D, Dale PJ (2010) A 3.2% efficient kesterite device from electrodeposited stacked elemental layers. J Electroanal Chem 646(1–2):52–59
9. Scragg JJ, Dale PJ, Peter LM (2009) Synthesis and characterization of Cu_2ZnSnS_4 absorber layers by an electrodeposition-annealing route. Thin Solid Films 517(7):2481–2484
10. Masato K et al (2009) Kesterite absorber layer uniformity from electrodeposited pre-cursors. Phys Status Solidi C 6(5):1241–1244
11. Scragg JJ, Dale PJ, Peter LM (2008) Towards sustainable materials for solar energy conversion: preparation and photoelectrochemical characterization of Cu_2ZnSnS_4. Electrochem Commun 10(4):639–642
12. Pandey RK, Sahu SN, Chandra S (1996) Handbook of semiconductor electrodeposition. Marcel Dekker, Inc, New York
13. Araki H et al (2008) Preparation of Cu_2ZnSnS_4 thin films by sulfurization of stacked metallic layers. Thin Solid Films 517(4):1457–1460
14. Schlesinger M, Paunovic M (eds) (2000) Modern electroplating, 4th edn. Wiley, New York
15. Barbosa LL et al (2005) Study and development of an alkaline bath for copper deposition containing sorbitol as complexing agent and morphological characterization of the copper film. Surf Coat Technol 192(2–3):145–153

16. Broggi RL et al (2006) Study of an alkaline bath for tin deposition in the presence of sorbitol and physical and morphological characterization of tin film. J Appl Electrochem 36(4):403–409
17. Scragg JJ et al (2008) New routes to sustainable photovoltaics: evaluation of Cu_2ZnSnS_4 as an alternative absorber material. Phys Status Solidi B-Basic Solid State Phys 245(9):1772–1778
18. Guaus E, Torrent-Burgues J (2003) Tin-zinc electrodeposition from sulphate-gluconate baths. J Electroanal Chem 549:25–36

Chapter 3
Conversion of Precursors into Compound Semiconductors

Conversion of the metallic precursors into Cu_2ZnSnS_4 films by thermal treatment in the presence of sulfur vapour takes place in several distinct stages, which we can summarise as follows:

1. Alloying of the precursor—interdiffusion of the precursor layers
2. Incorporation of sulfur—formation of simple sulfides
3. Crystallisation of Cu_2ZnSnS_4

As shall be seen, these three stages occur relatively quickly. In this chapter, the formation of Cu_2ZnSnS_4 from the precursor will be described, and a model will be proposed that accounts for the observed sequence of phase formation when a rapid heating rate is used. Further changes occurring in the films over longer timescales will be dealt with in the following chapter.

Background

3.1 Alloying of Precursors

Although thus far we have talked of the precursor as a stack of discrete metal layers, interdiffusion of the layers leading to alloy formation is in fact quite significant. Alloy formation between the layers begins from the very earliest moments of electrodeposition (as we saw in the under potential deposition of Zn and Sn at Cu), and continues in the finished precursor at room temperature, in some cases with appreciable rates. The heat treatment employed to introduce S into the film will accelerate this process further and lead to phase transitions depending on the relative stability of phases as a function of temperature. Characterisation of the particular phases present under different conditions is necessary, since these phases are the chemical precursors to the sulfide compounds that will form later. It is also

J. J. Scragg, *Copper Zinc Tin Sulfide Thin Films for Photovoltaics*,
Springer Theses, DOI: 10.1007/978-3-642-22919-0_3,

an option to alloy the precursor deliberately by heat treatment in the absence of sulfur. The advantages of this approach are (1) that a more homogeneous precursor with more intimate mixing of the elements would be obtained, and (2) that evaporation of the more volatile elements could be reduced by the formation of stable alloy phases. Evaporation is expected to be a particular problem in the case of Zn, which has a relatively high vapour pressure [1]. Among the possible disadvantages of alloying could be lateral segregation of elements into islands of stable phases, leading to a non-uniform composition at small length scales. Since the reaction pathway leading to CZTS will depend upon the metallic precursor phases, particular conditions may need to be present in order that desirable phases are formed and undesirable phases avoided. Initially, the possible metallic binary phases will be discussed, before moving on to ternary systems.

3.1.1 The Cu–Zn System

Figure 3.1 shows the equilibrium phase diagram for Cu–Zn. Cu–Zn alloys—referred to as brasses—form readily due to the negative free energy of mixing of the two elements, leading to a number of possible phases and solid solutions with different crystal structures.

Room Temperature Alloying of Cu and Zn

One study of particular relevance here is that by Bae [3], where the intermixing of Cu and Zn *during* electrodeposition of Zn upon an electrodeposited Cu substrate was investigated. The formation of a Cu–Zn alloy phase was observed (although the particular phase was not identified). The diffusion coefficient (at room temperature) of Zn atoms in the Cu bulk was calculated from voltammetric measurements based on the stripped charge at a potential corresponding to the Cu–Zn alloy, and was given as 4.4×10^{-19} m^2 s^{-1}. This is very high when compared to bulk diffusivities (for example 4.2×10^{-28} m^2 s^{-1} for Zn in Cu [4]), and this was attributed to a high density of lattice vacancies present in the electrodeposited Cu substrate and to the facile transport of Zn atoms along grain boundaries at room temperature. This highlights the special case of electrodeposited thin films, which are grown under non-equilibrium conditions from the point of view of the bulk phase diagram and can have quite different properties. In several examples of room temperature Cu–Zn alloy electrodeposition, phases from the entire spread of the phase diagram are seen, including β-CuZn, γ-Cu_5Zn_8 and ε-$CuZn_5$ [5–7].

Alloying of Cu and Zn at Elevated Temperatures

As can be seen in the phase diagram, the abovementioned phases have more or less vertical regions of stability up to temperatures far above those relevant in this study. Therefore any phase transitions observed as a function of temperature will only arise from continued interdiffusion modifying the composition of the alloy

Fig. 3.1 Equilibrium phase diagram for the Cu–Zn system [2]

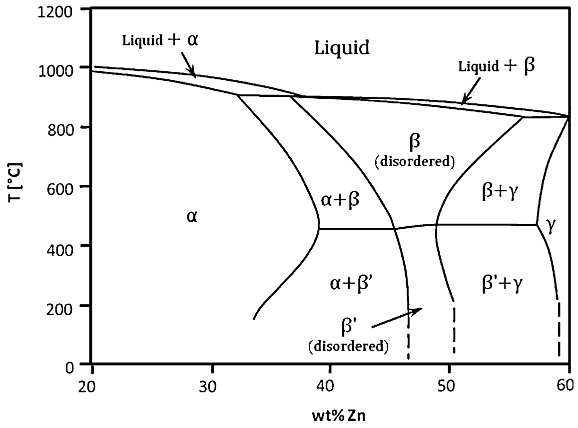

Fig. 3.2 Equilibrium phase diagram for the Cu–Sn system [8]

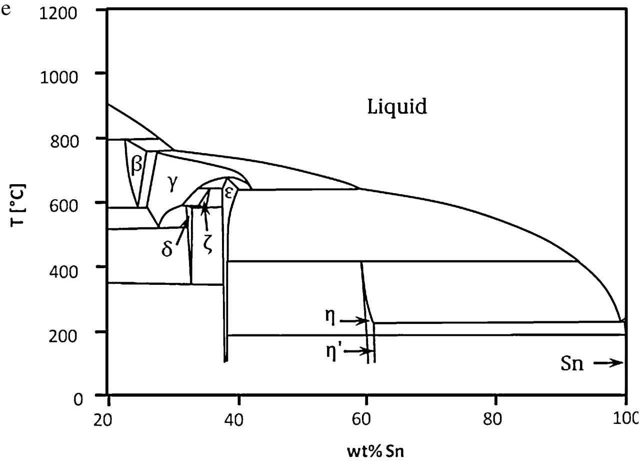

until an equilibrium stage is reached. In a sample with a 2:1 Cu–Zn ratio, a mixture of the β- and γ-phases is expected once the reaction is over.

3.1.2 Alloying of Cu and Sn

The Cu–Sn system also yields a large number of stable phases (bronzes), as seen in Fig. 3.2.

Room Temperature Alloying of Cu and Sn

According to Tu, Cu and Sn react at room temperature to form the hexagonal η-Cu_6Sn_5 phase [9]. Rutherford backscattering spectrometry (RBS) was used to observe the process, and it was shown that within 34 days at room temperature, a 200 nm layer of Sn on a thicker Cu substrate had been entirely consumed by the growth of Cu_6Sn_5. Compressive stresses appear in the Sn layer during formation of Cu_6Sn_5 as a result of its higher density, leading to lattice parameters slightly different from a bulk sample of tetragonal Sn. Cu is the dominant diffusing species, and in fact the rate of Cu diffusion in Sn is particularly fast. The diffusion of Cu into a Sn matrix has rather low activation energy, leading to diffusion coefficients of around 2.0×10^{-11} m^2 s^{-1} at room temperature, vastly higher than that for the reverse case: 1.3×10^{-27} m^2 s^{-1} was measured for Sn diffusion into a Cu matrix [4]. In general, as mentioned above, transport in thin films is also enhanced due to a great number of grain boundaries [10]. In electrodeposited Cu–Sn alloys, the Cu_6Sn_5 phase is usually seen, alongside elemental β-Sn (tetragonal) and Cu (hexagonal) [11].

Alloying of Cu and Sn at Elevated Temperatures

At higher temperatures (above 100 °C), the orthorhombic ε-Cu_3Sn phase forms from the reaction between Cu_6Sn_5 and Cu. When a Cu–Sn bilayer identical to the one described above was heated at 200 °C for 10 min, complete conversion Cu_3Sn was seen by XRD and RBS [9]. If excess Cu is not present, Cu_6Sn_5 can form Cu_3Sn with the formation of elemental Sn as a by-product. This reaction appears to occur only at higher temperatures, in the region of 450 °C [12].

3.1.3 Alloying of Sn and Zn

As can be seen from the equilibrium phase diagram, Fig. 3.3, Sn and Zn have very limited mutual solubility, less than 0.5 wt% [13]. There is no experimental evidence for any stable solid phases [14]. Alloys of Sn and Zn comprise a eutectic mixture (85.1 at% Sn) as opposed to a solid solution, and thus the only phases observed with XRD are β-Sn and hexagonal Zn. Zn atoms can, however, diffuse through a Sn matrix with low activation energy, around 50 kJ mol^{-1} compared to 189 kJ mol^{-1} for Zn diffusion through Cu [4].

An example of the indifference of these two elements is seen in the cyclic voltammetry of a mixed Sn–Zn electrolyte, which presents a simple superposition of the voltammograms for the individual elements, showing that there is no favourable interaction between them [13]. Co-electrodeposited Sn–Zn films show the expected eutectic structure, and their diffractograms present only peaks for the separate elements [15].

3.1.4 The Cu–Sn–Zn Ternary System

There is limited information about the ternary Cu–Sn–Zn phase diagram at compositions relevant to this study (2:1:1 Cu:Sn:Zn), however, it is apparent that

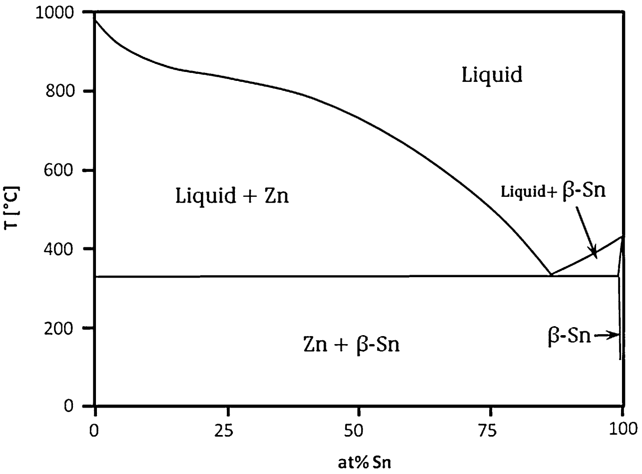

Fig. 3.3 Equilibrium phase diagram for the Sn–Zn system [14]

at temperatures up to 250 °C there are no ternary phases [4, 16]. At higher temperatures, the proportion of liquid phases increases rapidly. Chou et al. found that for a composition of 24.0% Sn, 25.0% Zn with Cu, the only solid phase at 250 °C was β'-CuZn and the remainder was a liquid [16]. Taking this composition as a point of reference, if the Zn content was reduced slightly, the γ-Cu_5Zn_8 phase formed alongside a liquid phase. When the Zn content was increased, Cu_3Sn and Cu_6Sn_5 phases also appeared. In general, due to the exceptional diffusivity of Cu through Sn, and to the high reactivity of Zn, Cu–Zn phases are formed in preference to Cu–Sn phases in the Cu–Zn–Sn system [16]. While bearing in mind that the study in Ref. [16] was performed using near-equilibrium conditions—which is not the case in this investigation—it should be noted that there was always a liquid phase present if the Cu content was greater than 25%. A CZTS precursor will have around 50% of Cu, so a liquid phase can potentially form; this has implications for the reaction processes leading to the sulfide material.

In the limited CZTS literature, little attention is given to precursor characterisation. The closest examples available are several reports of co-electrodeposited Cu–Zn–Sn precursors. Araki et al. found diffraction peaks attributable to CuZn and Cu_5Zn_8 alongside Cu and Sn in their Cu-poor, Zn-rich samples [17], in agreement with the above discussion. In the work of Schurr et al. [18] the phases observed after deposition included Cu_3Sn and CuZn when Cu was present in excess, and also Cu_6Sn_5 and Sn for Cu-poor samples. This is in contradiction to Araki et al. however, in general, the particular alloys formed by electrodeposition may be non-equilibrium phases, and will also depend upon the conditions of the electrodeposition, which were quite different in the two cases just mentioned.

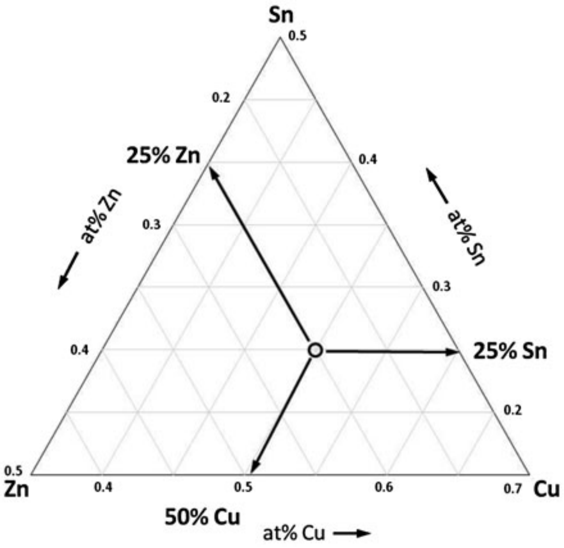

Fig. 3.4 Ternary composition diagram showing the position of stoichiometric CZTS

3.2 Incorporation of Sulfur: The Cu–Zn–Sn–S System

3.2.1 The Representation of Sample Compositions

The representation of composition in a quaternary system can be rather complex. Since each element can in principle be varied independently of the others, we have to be very careful when using terms such as ‘Cu-poor’, ‘Zn-rich’ etc., which are commonly employed to describe CZTS films. These terms are intelligible when only one component varies, but when two or more components deviate from stoichiometry, the terminology can be misleading. The problem is simplified if we assume that the S-content of the film is not an independent variable. Since S is introduced by reaction with the precursor, the amount that is incorporated depends on the amount of the metal elements and their valency: Cu(I), Sn(IV) and Zn(II). This simplifies the quaternary system to a ternary one. In the CZTS literature, the ratios of atomic percentages Cu/(Zn + Sn) and Zn/Sn are often used to represent the composition of the metallic elements in the material. Both ratios are equal to one when the material is stoichiometric. However, these ratios are not independent, and therefore do not clearly show the deviations from stoichiometry in a particular case. A ternary phase diagram is the most useful way to summarise compositions in the Cu–Zn–Sn system. An example of a ternary phase diagram is shown in Fig. 3.4.

The three sides of the plot each show the atomic percentage of one of the three metal elements. At any point in the diagram, the three values read off the axes will sum to unity. The scales used on this plot encompass the entire range of

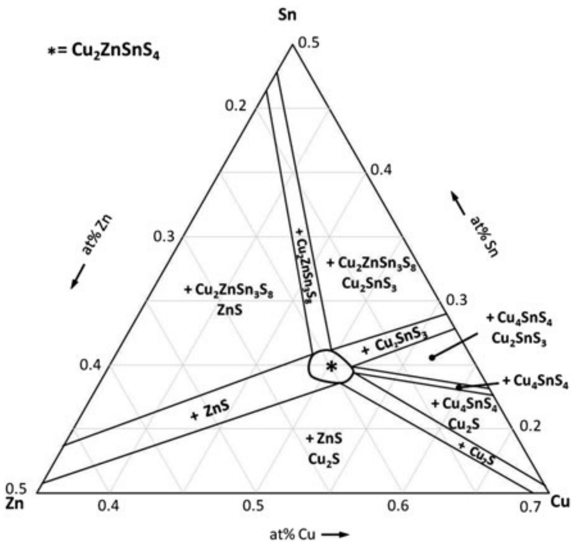

Fig. 3.5 Ternary phase diagram adapted from Ref. [19], showing the expected secondary phases at 400 °C

compositions presented in this report, and for ease of reference will be kept constant in all further figures. A point corresponding to the stoichiometric composition of CZTS is shown.

3.2.2 Phases in the Cu_2S–ZnS–SnS_2 Pseudo-Ternary System

A comprehensive analysis of the Cu_2S–ZnS–SnS_2 pseudo-ternary system was carried out by Olekseyuk et al. [19], who presented a phase diagram for the system at 400 °C. Their phase diagram was adapted for use in this work, and is shown in Fig. 3.5. Cu_2ZnSnS_4 as a single phase is present only within a rather narrow range of compositions, which is indicated with an asterisk at the centre of the plot. In all other regions of the phase diagram there are up to two additional secondary phases present, *always alongside* CZTS.

There are five two-phase fields, in which one secondary phase will be observed in addition to CZTS. In between these are five three-phase fields, where the secondary phase from both of the bordering regions will be formed alongside CZTS. Other phases not in this diagram but seen during the formation of CZTS in other reports include Cu_4SnS_6 and SnS_2 [18]. Aside from the small region of single phase material, we can usefully define six regions, shown in Fig. 3.6, as "Cu-poor", "Cu-rich", "Sn-poor" etc. These are the labels which will be applied to compositions in this report, and by this definition they tell us which secondary phases should be expected to form at that composition. The "Zn-poor" region encompasses several related secondary phases (Cu–Sn–S) Table 3.1.

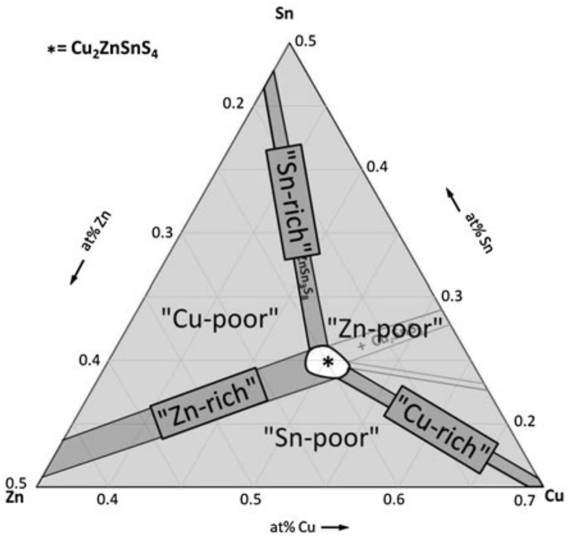

Fig. 3.6 Ternary phase diagram defining the compositional labels used throughout this text

Table 3.1 Definition of composition descriptions used in this report, in terms of the expected secondary phases

Composition description	Expected secondary phases
"Cu-poor"	$Cu_2ZnSn_3S_8 + ZnS$
"Sn-rich"	$Cu_2ZnSn_3S_8$
"Zn-poor"	Cu–Sn–S + $Cu_2ZnSn_3S_8/Cu_2S$
"Cu-rich"	Cu_2S
"Sn-poor"	Cu_2S, ZnS
"Zn-rich"	ZnS

A Note on the New Quaternary Phase $Cu_2ZnSn_3S_8$

The second quaternary phase $Cu_2ZnSn_3S_8$ was first reported by Olekseyuk et al. in their study of the Cu_2S–ZnS–SnS_2 phase diagram, forming from the reaction of SnS_2 with CZTS below 700 °C [19]. It was reported to crystallize in a tetragonal structure, with very similar lattice parameters to CZTS. Although no further literature on this phase could be found, there are abundant equivalents, collectively known as 'thiospinels'. $Cu_2FeSn_3S_8$, $Cu_2NiSn_3S_8$, $Cu_2CoSn_3S_8$, $Cu_2CdSn_3S_8$ and $Cu_2MnSn_3S_8$ are all known, so an equivalent in the Cu–Zn–Sn–S system is not unexpected. These structures are rather interesting, being characterised by the presence of a large number of empty lattice sites (the relevance of this will become clearer in Chap. 5) [20]. This has led to them being investigated for use in Li batteries [21]. $Cu_2ZnSn_3S_8$ should form in Cu-poor or Sn-rich samples, and therefore we can expect it in this investigation.

Given the detailed study made of the Cu_2S–ZnS–SnS_2 pseudo-ternary system by Olekseyuk et al. in 2004 [19], it is perhaps rather surprising that the equilibrium phase diagram presented therein—and reproduced above—has barely been cited in the CZTS thin film literature since that time. Where CZTS film preparation was the objective, we could only find two reports that cite the article (one by the present author): [22, 23]. The argument that the equilibrium phase diagram is inapplicable under the conditions of thin film formation is hardly watertight, because sulfurisation times of many hours' duration are routinely used in the fabrication of CZTS films (see Sect. 4.1.1), allowing a reasonable time for the equilibrium phases to emerge. The phase diagram has been cited on a further two occasions where formation processes of CZTS films were being investigated [24, 25]. The Cu–Sn–S phases observed matched those expected from the phase diagram.

Considering the narrow range of compositions for which CZTS is the sole phase, coupled with the extremely large variation in compositions presented in the CZTS literature, it is even more important to refer to the phase diagram because secondary phases will have a strong influence on the morphology and optical properties of the films. In this investigation, the phase diagram will be referred to wherever possible, and it will be seen that it provides useful insights on several occasions.

One reason that the presence of secondary phases has perhaps not been given due attention is the difficulty in detecting them, as will now be discussed.

3.3 Distinguishing Phases in the Cu–Zn–Sn–S System

Two techniques will be used in this investigation to examine the crystal structures of the phases present in thin film samples: and Raman spectroscopy.

3.3.1 X-Ray Diffraction

X-ray diffraction in Bragg–Brentano mode is a commonly used technique for structural characterisation of polycrystalline thin films. A monochromatic X-ray beam, wavelength λ, is directed at the sample, which is positioned at a defined plane. The X-ray source orbits around the sample, impinging at an angle θ, and constructive interference between X-rays reflected from lattice planes in the sample gives a high intensity reflection when the Bragg condition, $n\lambda = 2d \sin \theta$, is satisfied, where d is the spacing of the lattice planes and n is an integer. Reflection intensity is displayed as a function of the angle between the source and the detector, equal to 2θ. For a sample that has randomly oriented grains, the pattern of reflections and their intensity depends only on the symmetry of the crystal structure and its unit cell parameters. In practice, the crystallites in a thin film are often oriented non-randomly, so the intensity pattern can change.

X-ray diffraction can usually assign a phase with confidence, unless there happen to be several coexisting phases with similar symmetry and lattice parameters. Unfortunately, in the case of CZTS, there are several secondary

Table 3.2 Secondary phases present in the Cu_2S–ZnS–SnS_2 pseudo-ternary system at 400 °C

Phase	Structure	Lattice constants (Å)	Source	Occurrence in CZTS thin film literature
Cu_2ZnSnS_4	Tetragonal	a = 5.43, c = 10.85	[27]	
Cu_2S	Tetragonal	a = 3.996, c = 11.287	[28]	e.g. [26, 29–31]
ZnS	Cubic	a = 5.409	[32]	[18]
Cu_4SnS_4	Orthorhombic	a = 13.7, b = 7.75, c = 6.454	[33]	[24]
Cu_2SnS_3	Tetragonal	a = 5.413, c = 10.824	[34]	[18, 26]
$Cu_2ZnSn_3S_8$	Tetragonal	a = 5.435, c = 10.825	[19]	None

phases that fulfil both of these conditions. In addition, due to the small volume of material, the diffraction intensity from thin films is usually low, and the non-random orientation makes assignment based on peak height difficult. It has been pointed out on several occasions that if CZTS is present alongside ZnS and/or Cu_2SnS_3, that X-ray diffraction would be unable to distinguish the phases [26]. A list of the secondary phases in the phase diagram for the Cu–Zn–Sn–S system is shown in Table 3.2, along with their lattice parameters and crystal structures.

Table 3.3 shows a complete list of the X-ray diffraction standards used in this work.

3.3.2 Raman Spectroscopy

An alternative means to distinguish CZTS from some of the possible secondary phases, Raman spectroscopy measures the spectrum of wavelength shifts of an initially monochromatic light beam, usually a laser, after it is scattered from a sample. Interaction of the laser light with phonon modes in the sample causes the photon energy to increase or decrease. Characteristic Raman shifts for CZTS were provided by Altosaar et al. for single-crystal CZTS powder synthesised from a KI melt and annealed at 1,000 K [49]. The same shifts were seen in the case of thin films of CZTS [31, 50]. The Raman shifts for some Cu–Sn–S phases have also been measured [51]. The reported values for several phases are shown in Table 3.4.

According to these shifts, therefore, it is in principle possible to distinguish CZTS from ZnS if the resolution of the experiment is within a few cm^{-1}. The phase Cu_2SnS_3 has two forms, the higher temperature cubic form being clearly distinguishable, but the lower temperature tetragonal form lying rather close to the CZTS peaks; however, CZTS has one unique peak at 287 cm^{-1}, meaning that it is possible to use Raman spectroscopy to prove the presence of CZTS, even if the concurrent presence of Cu_2SnS_3 and ZnS cannot be definitively ruled out.

Table 3.3 A list of XRD standards used in this work

Phase	Reference
Cu_2ZnSnS_4	[27]
Cu_2SnS_3	[35]
Cu_4SnS_4	[33]
Cu_4SnS_6	[36]
CuS	[37]
$Cu_{1.8}S$	[38]
Cu_2S	[28]
SnS_2	[39]
SnS	[39]
ZnS	[32]
Cu	[40]
Sn	[41]
Zn	[42]
Cu_6Sn_5	[43]
Cu_5Sn_4	[44]
Cu_3Sn	[45]
Cu_5Zn_8	[46]
$Cu_{0.8}Zn_{0.2}$	[47]
$Cu_{0.75}Zn_{0.25}$	[48]

Table 3.4 Raman shifts for some phases in the Cu–Zn–Sn–S system

Phase	Raman shifts (in order of decreasing intensity) (cm^{-1})	Source
Cu_2ZnSnS_4	338, 287, 352, 351, 368	[49]
Cu_2SnS_3 (Tetragonal, <400 °C)	336, 351	[51]
Cu_2SnS_3 (Cubic, >400 °C)	303, 355	[51]
$Cu_{2-x}S$	476	[50]
ZnS	348	[50]

3.3.3 Other Methods of Distinguishing Phases

Given the difficulty in distinguishing certain phases, or the low resolution or intensity of the techniques used, especially for small amounts of secondary phases, additional information must be obtained. Compositional (EDS) mapping in the electron microscope was used in some cases to help identify certain phases that were clearly different from the bulk based on differences in morphology. In other cases, the use of KCN etching, which selectively removes Cu–S phases, could help to assign these phases based on pre- and post-etching morphology.

The possible effects of the various secondary phases on the opto-electronic properties of CZTS films will be covered in Chap. 5.

3.4 Crystal Structures of Cu_2ZnSnS_4

3.4.1 Kesterite and Stannite

Crystallographically speaking, CZTS is derived from the chalcopyrite structure of $CuInS_2$ by replacement of In atoms with Sn and Zn atoms. Based on symmetry arguments, this operation produces two principal structures of lower symmetry, known as the stannite-type (space group $I\bar{4}2m$) and kesterite-type (space group $I\bar{4}$) structures [52]. The two structures are similar, consisting of a cubic close-packed lattice of S anions, with half of the tetragonal interstices occupied by cations. Sn atoms occupy the same fixed positions in both structures, and it is the differing arrangement of Cu and Zn atoms that distinguishes the two cases [53]. In its natural state, CZTS is found to crystallise with the kesterite structure [54]. In agreement with this observation, calculations have shown that the kesterite structure has a lower energy than the stannite structure for CZTS, however, the difference is small: values of 3.4, 3 and 1.3 meV per atom have been reported [55–57].

It is not known how to deliberately fabricate CZTS with the non-equilibrium stannite structure, so there is as yet no experimental evidence for a solid solution between the two structures. However, we can look to the case of CZTS (kesterite) and the mineral stannite, Cu_2FeSnS_4· $Cu_2FeStnS_4$ at equilibrium crystallises in the stannite structure, and so the solid solution $Cu_2Fe_xZn_{1-x}SnS_4$ exhibits a transition between the two structures. The mechanism, determined by neutron scattering, is a three-stage process of cation rearrangement. It had previously been proposed, and was definitively shown by the neutron scattering experiments, that there exists a partially disordered form of kesterite wherein the Cu and Zn atoms can be randomly arranged on their shared lattice plane [53]. The lattice sites in the Cu/Zn planes have an equal probability of being occupied by Cu or Zn, which means that the partially disordered kesterite structure has the same space group as the stannite structure, $I\bar{4}2$ m [55]. Therefore there is no crystallographic reason why a solid solution should not form. A view of the kesterite, partially disordered kesterite and stannite structures along the [100] direction is illustrated in Fig. 3.7.

Based on the fact that Cu_2FeSnS_4 and Cu_2ZnSnS_4 can form a solid solution, and the fact that in CZTS the kesterite structure is only slightly lower in energy than the stannite structure, we can reasonably expect, under non-equilibrium conditions, that the stannite structure for Cu_2ZnSnS_4 could form a solid solution with the kesterite structure with the same composition. The stannite form would be metastable, and given the required thermal energy for atomic rearrangement and sufficient time, a pure kesterite phase should be seen.

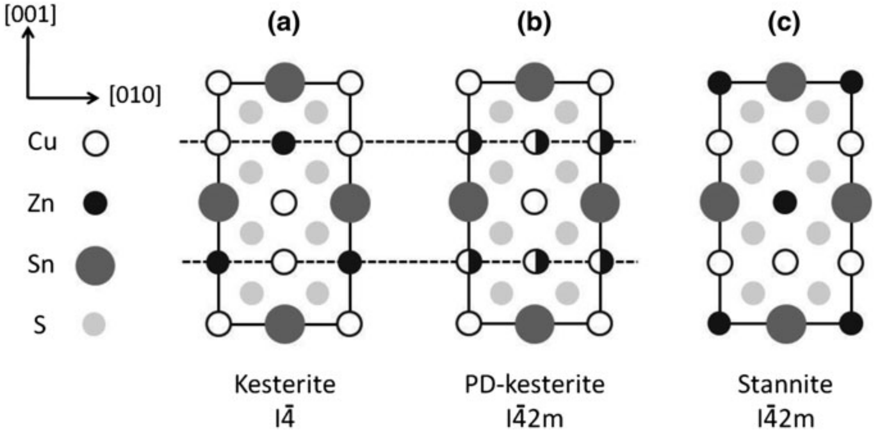

Fig. 3.7 Crystal structures of **a** kesterite, indicating planes of Cu–Zn disorder, **b** partially disordered kesterite, and **c** stannite. Note the Cu/Zn ordering in the three structures

The structural similarity of kesterite and stannite and the existence of disorder in the kesterite means that they are very difficult to distinguish experimentally [58, 59]. Neutron scattering has been used to distinguish the two structures for Cu_2ZnSnS_4 and Cu_2ZnFeS_4 [53], but with the more commonly employed X-ray diffraction technique, as used in this investigation, the intensity and resolution are insufficient to tell the structures apart, especially for thin, polycrystalline films. Therefore we need to define some terms used herein. 'Kesterite' and 'stannite' will only be used when referring directly to the structural type. 'CZTS' will be used when referring to the phase observed in the X-ray diffraction spectra, which could be accounted for by either structural type or a mixture of the two.

3.5 Formation Reactions of Cu_2ZnSnS_4

Hergert and Hock used a crystallographic model to predict two parallel pathways for CZTS formation from binary sulfides [60]. The first pathway is a direct reaction of the three phases, and the second goes via the intermediate Cu_2SnS_3 phase. The reactions are summarised below:

$$\mathrm{CuS/Cu_2S} + \mathrm{ZnS} + \mathrm{SnS/SnS_2} \rightarrow \mathrm{Cu_2ZnSnS_4} \tag{R 3.1}$$

$$\mathrm{CuS/Cu_2S} + \mathrm{SnS/SnS_2} \rightarrow \mathrm{Cu_2SnS_3} \tag{R 3.2}$$

$$\mathrm{Cu_2SnS_3} + \mathrm{ZnS} \rightarrow \mathrm{Cu_2ZnSnS_4}. \tag{R 3.3}$$

Once the binary sulfides have formed, crystallisation of the CZTS phase appears to be rapid. On the basis of in situ X-ray diffraction experiments as a function of temperature, Weber et al. calculated a second order rate constant of between 2×10^{-9} and 3×10^{-10} cm^2 s^{-1} for an assumed diffusion-limited process of CZTS formation from stacked binary sulfides (CuS, ZnS, and SnS). They concluded that, at 500 °C, the formation of CZTS should be complete within 10–70 s [26].

Schurr et al. [18] conducted in situ X-ray diffraction experiments on co-electrodeposited Cu–Zn–Sn films during the sulfurisation process. Their work is the closest equivalent to that undertaken here. They prepared precursors with a composition Cu/(Zn + Sn) = 0.9–0.96 and Zn/Sn = 1.1. The precursors were coated with a layer of sulfur by evaporation, and heated at a rate of 0.8 °C s^{-1} to around 630 °C, and diffractograms in the range $2\theta = 0$–$45°$ were recorded continuously during this heating stage and for a further 300 s thereafter. The precursor was observed to contain Cu_6Sn_5, CuZn and Cu_3Sn as mentioned previously. The following sequence of reactions was then observed:

$$Cu_6Sn_5 + S \rightarrow SnS_2 + Cu_{2-x}S + Cu_3Sn \quad (170 - 300°C) \qquad \text{(R 3.4)}$$

$$Cu_2S + SnS_2 \rightarrow Cu_4SnS_6 \quad (\text{up to } 570°C) \qquad \text{(R 3.5)}$$

$$2CuZn + 3S \rightarrow Cu_{2-x}S + ZnS \quad (510°C) \qquad \text{(R 3.6)}$$

$$Cu_4SnS_6 \rightarrow 2Cu_{2-x}S + SnS_2(\text{melt}) \quad (570°C) \qquad \text{(R 3.7)}$$

$$Cu_{2-x}S + SnS_2(\text{melt}) \rightarrow Cu_2SnS_3 \quad (>570°C) \qquad \text{(R 3.8)}$$

$$Cu_2SnS_3 + ZnS \rightarrow Cu_2ZnSnS_4 \quad (575°C) \qquad \text{(R 3.9)}$$

At the end of the heating period, the material was still multi-phase: $Cu_2ZnSnS_4 + Cu_2SnS_3 + ZnS$.

Araki et al. [61] produced stacked electrodeposited precursors and sulfurised them for 2 h under flowing nitrogen with elemental S. They showed some diffractograms of samples sulfurised at different temperatures. At 300 °C, elemental Sn and a Cu-containing phase (not assigned but matches spectra for e.g. Cu_6Sn_5, Cu_5Zn_8) were still present after the sulfurisation. The emergence of sulfide phases appeared to begin between 300 and 400 °C. The CZTS phase was assigned above 400 °C, and only peaks assignable to CZTS/CTS/ZnS remained after 2 h of sulfurisation at 600 °C.

3.6 Rapid Thermal Processing

In this investigation, a rapid thermal processing system was used to sulfurise the precursors. Such a system allows very fast heating and cooling, and very short annealing times are possible. This allows us to investigate the relatively fast formation processes of the films by quenching (quickly cooling) the sample at any given point in the reaction. It is assumed that the phases present after rapid cooling are representative of the phases that were present at the time of the quench.

3.6.1 Description of the RTP System

An RTP has three key features: (1) a very low thermal mass, (2) high-power infrared lamps which can deliver the required energy density, and (3) an active cooling system. Traditional tube furnaces have a high thermal mass to conserve heat and reduce temperature fluctuations. A side-effect of this is that they are slower to heat and cool. The low thermal mass of the RTP system means that it can be heated and cooled very rapidly (±20 °C s^{-1} or faster). A feedback loop with very short interval times is required to balance the heat transfer to/from the process zone in order to achieve the required temperature. To achieve the desired uniformity of the thermal profile within the process zone, a 'susceptor', a covered plate of a material (usually graphite) with high thermal conductivity and good chemical resistance is used to contain the samples. The samples are placed within this container, which is assumed to have an even temperature at all points. Thermocouples contacting the susceptor allow measurement of the sample temperature.

The maximum heating rate used was 10 °C s^{-1}, to avoid cracking the glass substrates. The substrates also limit the maximum temperature to about 580 °C. The maximum cooling rate was around 10 °C s^{-1} for the first 200 °C of temperature drop.

The RTP system used here (AS-micro, Annealsys) had a rotary pump to allow a vacuum of around 10^{-2} mbar and a N_2 purge line to flush the system and a provide a background pressure of inert gas during sulfurisation up to a maximum of 1 atm. The temperature was controlled via up to two thermocouples in contact with the graphite susceptor.

3.6.2 Sulfur Sources in the Two-Stage Process

In the two-stage process, the sulfur source can be either elemental S (added to the furnace as a solid) or H_2S gas. There are many examples of both in the CZTS and CIS literature. The use of H_2S has the advantages that one need not worry about evaporation and condensation processes, and that it is easy to introduce the gas to the reaction chamber and to control its quantity compared with the same operations for a solid material. The disadvantage of using H_2S is that specialist equipment is required to handle its corrosivity and toxicity. Using elemental S is comparatively safe, although it is still rather corrosive to sensitive components such as thermocouples. Elemental S can be introduced in several ways:

1. Loading solid sulfur into the reaction chamber with the precursors (sealed chamber): e.g. [61].
2. Evaporation of S onto samples after precursor deposition: e.g. [18].
3. Use of a separately heated effusion source in the reaction chamber: e.g. [24].

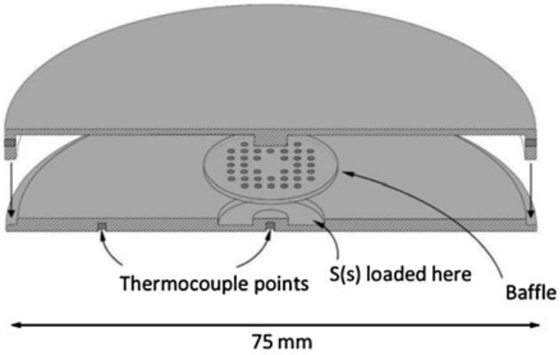

Fig. 3.8 Cross section of the graphite susceptor (sample container) used in the RTP system

In each case, S vapour will be transported from the source down temperature gradients to the cooler regions of the system, where it will condense. In cases one and two, the lost S cannot then be replenished, so its partial pressure will drop and the useful 'residence time' of S vapour near the samples will be inherently limited. Only method three allows the partial pressure of S to remain constant throughout heat treatment, but requires specialist equipment. In this investigation, method one was used, and a graphite susceptor with a lid was employed to confine the vapour around the samples for as long as possible.

The vapour pressure of S at 550 °C (a typical conversion temperature) is about 3,800 mbar [62], well in excess of the background pressure in the reaction chamber, so evaporation will be rapid and complete (Fig. 3.8).

Experimental

3.7 Precursor Preparation

The substrates were standard soda-lime glass (SLG) slides, 75 × 25 mm, coated with an approx. 1 μm thick layer of Mo produced by RF sputtering. The substrates were cut into quarters of approx. 19 × 25 mm. They were then cleaned ultrasonically in, sequentially, detergent, ethanol and propan-2-ol before being dried under flowing nitrogen.

Electrodeposition was carried out at the rotating disc electrode. Sample mounting and masking was described in Sect. 2.4.6. After masking, the exposed sample area was approx. 17 × 21 mm. Precursor preparation consisted of up to four sequential electrodeposition steps to produce binary Cu|Zn or Cu|Sn, or ternary Cu|Sn|Cu|Zn stacks (where the right-most element is at the surface). The electrodeposition solutions and conditions are described in Table 3.5. Depositions were made in potentiostatic mode with an Autolab 20 potentiostat, using a Pt counter electrode and either a Ag|AgCl or Hg|HgO reference electrode, depending

Table 3.5 Electrodeposition solutions and conditions used for precursor preparation

Layer	Electrolyte composition	Deposition potential	Rotation rate (rpm)
Cu(1)	3 M NaOH (Reagent grade, Aldrich), 0.2 M Sorbitol (≥99.5% (HPLC), Sigma), 0.1 M $CuSO_4 \cdot 5H_2O$ (≥98%, Sigma), 0.025 vol% Empigen BB (N,N-dimethyl-N-dodecylglycine betaine, Sigma)	−1.08 V vs. Hg|HgO	300
Sn	1 M Methanesulfonic acid (≥99.5%, Sigma-Aldrich), 50 mM Sn(II) methanesulfonate (50 wt% in H_2O, Aldrich), 0.1 vol% Empigen BB (see above)	−0.55 V vs. Ag|AgCl	300
Cu(2)	See above	−1.45 V, 2 s, then −1.10 V vs. Hg|HgO	300
Zn	2 M KCl (≥99.0%, Sigma), 1 wt% pH 3 Hydrion buffer (Sigma), 50 mM $ZnCl_2$ (98%, Aldrich), 0.2 wt% Poly[bis(2-chloroethyl) ether-alt-1,3-bis[3-(dimethylamino)propyl]-urea], quaternized, 62 wt% in H_2O, Sigma)	−1.22 V vs. Ag|AgCl	100

on the electrolyte (see Table 3.5). In between deposition of each layer, the mask was removed and the films were thoroughly washed in deionised water.

The compositions of the precursors in this chapter were intended to be 2:1:1 Cu:Sn:Zn, and the amount of charge to pass during deposition was calculated on the basis of a 1 μm thick CZTS film after sulfurisation, according to the method in Sect. 2.11.2.

3.8 Description of Annealing/Sulfurisation Procedures

Precursors prepared using the RDE system had external dimensions of approx. 19 × 25 mm, while the area of the electrodeposited film was approx. 17 × 21 mm. In a typical experiment, these samples were cut into quarters to yield four nominally identical samples. These samples were placed inside the susceptor along with solid S, if required, and covered with the susceptor lid. After the samples had been loaded, annealing or sulfurisation (annealing with S) proceeded in three stages. In the first stage, pumping and purging cycles were used to remove any oxygen from the system. The purging gas used was N_2. After three cycles of purging, the furnace was filled to the desired pressure with N_2. The next stage was the heating programme. In most instances this consisted of a fast ramp to a set temperature followed by a fixed dwell period. The pressure was monitored using a Pirani gauge and the temperature by a thermocouple in contact with the susceptor. The temperature variation during the dwell period was better than ±4 °C. In the final stage, the chamber was cooled at the maximum rate to 200 °C, and the system was then pumped down and purged. The samples were removed once the temperature was below 50 °C.

It was observed that the S-containing atmosphere was corrosive to the inconel-coated thermocouples, especially at higher temperatures. To avoid destruction of the thermocouples, the temperature was controlled by calibrating the power input to the system so that thermal programmes could be run without the thermocouple in place. The accuracy of the temperatures obtained this way was periodically checked by re-installing the thermocouples, and was found to be satisfactory.

The furnace was cleaned periodically by heating at 600 °C for 1 h while filled with an atmosphere of 10% H_2–N_2, and then a further 1 h period at 600 °C under vacuum.

3.9 Characterization of Converted Material

SEM images and compositions were recorded using a JEOL6480LV microscope with EDS capability (Oxford Instruments). For top–down imaging, samples were earthed by contacting the exposed area of the Mo substrate with carbon-loaded putty. For edge-on images, the samples were re-mounted and coated with gold by evaporation to enhance the resolution. For EDS measurements, an accelerating voltage of 20 kV was used. Spectra were recorded for 100 s of live-time. The error in the EDS measurement was reduced as far as possible by calibrating the beam current using a Co standard between measurements. For a large series of measurements repeated at the same location on a sample, the absolute error in the atomic percentages of Cu, Sn and Zn were about 0.6, 0.8 and 0.5% respectively. For estimation of film thickness variations over a large area, the peak heights in the EDS spectra were recorded at uniformly spaced locations on the samples. For quantitative analysis of overall sample composition, spectra were recorded at a magnification of 100 times, and averaged over several locations on the sample.

XRD spectra were recorded in Bragg–Brentano mode with a Siemens D-5000 diffractometer using a CuKα radiation source ($\lambda = 1.5406$ Å).

Raman spectra were recorded using 532 nm excitation, with a triple-grating spectrometer consisting of a subtractive double stage followed by a 1 m dispersing stage with a 300 g/mm grating (resolution $\sim 2\ \mathrm{cm}^{-1}$), and a liquid N_2 cooled CCD.

MiniSIMS depth profiles were recorded using a Millbrook Instruments bench-top instrument with a 6 keV Ga+ ion beam.

3.10 Etching

Etching of samples was carried out where stated in 5 or 10 wt% aqueous KCN solution. The samples were thoroughly rinsed afterwards, and the KCN residues oxidised using a sodium hypochlorite solution.

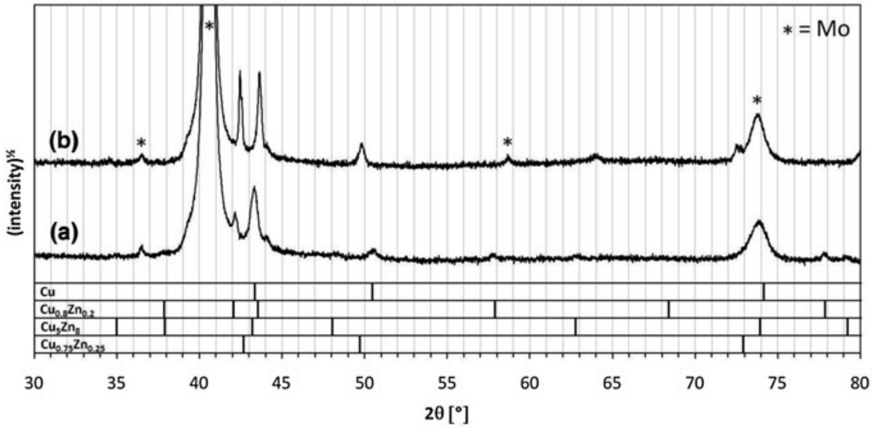

Fig. 3.9 XRD spectra of **a** as-deposited Cu|Zn bilayer, and b Cu|Zn bilayer annealed at 400 °C for 2 min. The composition of the bilayer was approx. 2:1 Cu:Zn

Results and Discussion

3.11 Annealing of Metal Stacks in the Absence of Sulfur

3.11.1 Annealing Cu–Zn Bilayers

Figure 3.9a shows the XRD spectrum of an as-deposited Cu/Zn bilayer. Aside from the substrate peaks at 36.48, 40.50, 58.65 and 73.85°, the principal peaks can be assigned with reasonable confidence to Cu and Cu_5Zn_8. The assignment is shown in Table 3.6a. The assignment to Cu is clear because there are two matching peaks. Elemental Zn cannot be assigned with confidence because its three most intense reflections would overlap either with the Cu(111) peak or with the substrate peaks at 36.38 and 40.50°, and no peak is observed at the location of the fourth most intense reflection (70.08°). The lack of clear XRD evidence for elemental Zn suggests that the electrodeposited material is disordered, or that alloying has actually gone to completion at room temperature, resulting in the disordered *β*’ phase predicted in the phase diagram. It should be noted that the visual appearance of the sample (white–grey film with specular reflectivity) had not changed, so there was at the very least a surface layer of pure Zn present.

The presence of the Cu-rich alloy phase, $Cu_{0.8}Zn_{0.2}$ is clear, and there is a suggestion of the Zn-rich phase Cu_5Zn_8. These phases may have formed initially during the first stages of electrodeposition of Zn at Cu, and continued to grow at room temperature as discussed in Sect. 3.1.1.

Table 3.6 Peak assignment for (a) as-deposited Cu/Zn bilayer and (b) Cu|Zn bilayer annealed at 400 °C for 2 min. Refer to Fig. 3.9

(a)					(b)			
2θ (°)	d_{obs} (Å)	Cu d(hkl) (Å)	$Cu_{0.8}Zn_{0.2}$ d(hkl) (Å)	Cu_5Zn_8 d(hkl) (Å)	2θ (°)	d_{obs} (Å)	$Cu_{0.8}Zn_{0.2}$ d (hkl) (Å)	$Cu_{0.75}Zn_{0.25}$ d (hkl) (Å)
29.25	3.05				42.46	2.13		2.12 (111)
42.16	2.14		2.15 (002)		43.61	2.07	2.08 (101)	
43.32	2.09	2.09 (111)	2.08 (101)	2.09 (330)	49.79	1.83		1.83 (200)
44.08	2.05				63.99	1.45		
50.46	1.81	1.81 (200)			72.52	1.30		1.30 (220)
57.79	1.59		1.59 (102)					
62.80	1.48			1.48 (600)				
77.90	1.23		1.23 (103)					
79.10	1.21			1.21 (633)				

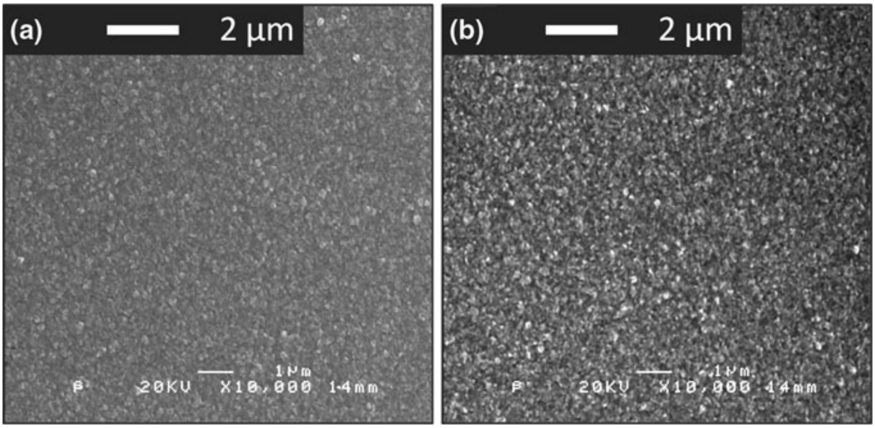

Fig. 3.10 SEM images of Cu/Zn bilayer **a** before, and **b** after heat treatment at 400 °C for 2 min. The composition of the bilayer was approx. 2:1 Cu:Zn

Upon heating, the sample becomes a golden colour, which is clear evidence of advanced alloy formation. The XRD spectrum of Fig. 3.9b shows that the peaks for elemental Cu have disappeared, and the spectrum is now entirely described by a mixture of $Cu_{0.8}Zn_{0.2}$ and $Cu_{0.75}Zn_{0.25}$, and it is possible (and in fact required by the composition of the sample) that the disordered β' phase is also present.

SEM images of the Cu/Zn film before and after the heat treatment are shown in Fig. 3.10a, b. It can be seen that there are no significant changes to the microstructure, which follows since the heat treatment was performed well below the liquidus temperature.

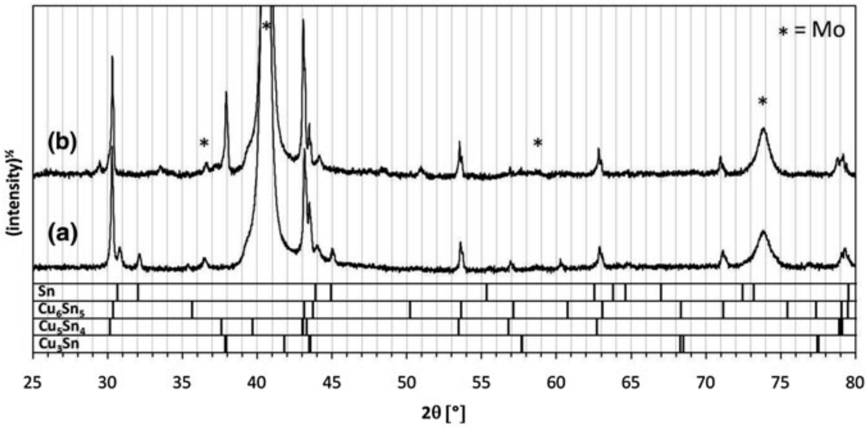

Fig. 3.11 XRD spectra of Cu/Sn bilayers **a** before and **b** after heat treatment at 400 °C for 5 min. Sample composition was approx. 2:1 Cu:Sn

3.11.2 Annealing Cu–Sn Bilayers

The XRD spectrum of an as-deposited Cu/Sn bilayer is shown in Fig. 3.11a. In this sample, elemental Cu is not seen, although the main peak for Cu does coincide with the intense reflections for Cu_6Sn_5 at around 43°, so a small amount could be present. There are several weak reflections corresponding to elemental Sn. The alloy phases Cu_6Sn_5 and Cu_5Sn_4 explain the rest of the spectrum, showing that in the case of this sample, room temperature alloying has advanced considerably in the period between sample preparation and the diffraction experiment (approx. 8 days). Upon heating, Fig. 3.11b, the Sn phase disappears completely and the higher-temperature alloy phase Cu_3Sn can be seen. The other peaks then match most closely to Cu_6Sn_5 (Table 3.7).

With reference to the Cu–Sn phase diagram (Fig. 3.2), it can be seen that the melting point of pure Sn is around 230 °C. The liquidus temperature starts to rise rapidly as Cu becomes incorporated, which corresponds to a time axis during the alloying process. If the rate of increase of the liquidus temperature due to in-diffusion of Cu is lower than the heating rate, it is possible to exceed the liquidus temperature and melt the bulk material. This is highly undesirable, as can be seen in Fig. 3.12, as the melted material can then de-wet from the substrate, forming isolated regions of alloy and leaving the substrate exposed.

At the other extreme, slow heating or prolonged annealing can also have undesirable effects due to the very high diffusivity of Cu in Sn. The transport of metal atoms in a direction perpendicular to the plane of the film is desirable and necessary to produce a film of uniform composition, but the atoms may also diffuse in the plane of the film. Given sufficient time, phase separation such as that seen in Fig. 3.13 can occur, where the darker patches in Fig. 3.13b have a higher

Table 3.7 Peak assignment for (a) as-deposited Cu/Sn bilayer and (b) Cu|Sn bilayer annealed at 400 °C for 5 min. Refers to Fig. 3.11

(a)					(b)			
2*θ* [°]	d_{obs} (Å)	Cu_6Sn_5 d (hkl) (Å)	Cu_5Sn_4 d (hkl) (Å)	Sn d (hkl) (Å)	2*θ* (°)	d_{obs} (Å)	Cu_5Sn_4 d (hkl) (Å)	Cu_3Sn d (hkl) (Å)
30.28	2.95	2.95 (100)			29.44	3.03	3.03 (21-1)	
30.81	2.90			2.92 (200)	30.31	2.95	2.96 (311)	
32.11	2.79			2.79 (101)	33.52	2.67		
35.35	2.54		2.55(20-2)		37.92	2.37		2.37 (002)
43.16	2.09	2.10 (110)			43.08	2.10	2.10 (232)	
43.49	2.08	2.07 (102)			43.48	2.08		2.08 (211)
44.03	2.05			2.06 (220)	44.17	2.05		
45.03	2.01			2.02 (121)	48.37	1.88	1.89 (215)	
53.60	1.71	1.71 (201)			50.91	1.79		
56.93	1.62		1.62 (430)		53.53	1.71	1.71 (523)	
60.28	1.53		1.54 (51-1)		56.89	1.62	1.62 (430)	
62.89	1.48	1.47 (202)			57.60	1.60		1.60 (221)
71.12	1.32	1.32 (211)			62.82	1.48	1.48 (622)	
79.21	1.21	1.21 (300)			70.96	1.33	1.33 (543)	
					77.00	1.24	1.24 (34-3)	
					78.95	1.21	1.21 (060)	

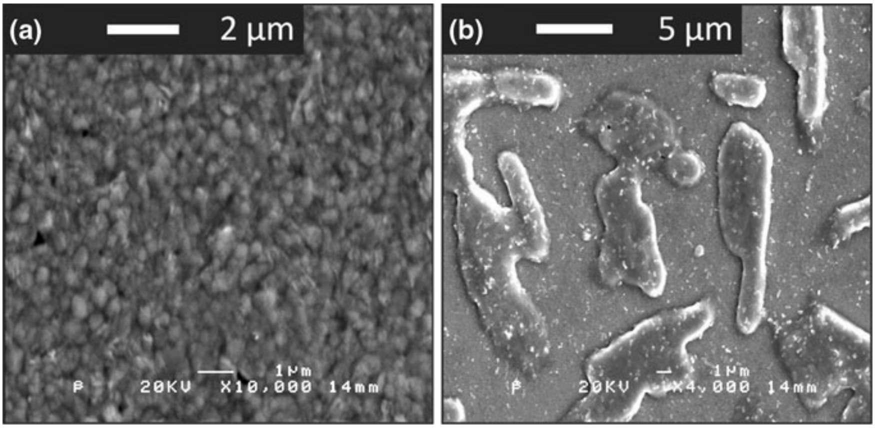

Fig. 3.12 SEM images of Cu|Sn bilayer **a** before, and **b** after rapid heating to 400 °C (heating rate ~6 °C s^{-1}). EDS shows that the areas between the large crystals in **b** are uncovered Mo

Cu content than the bulk. This sample was heated at 100 °C min^{-1} to 180 °C then at 10 °C min^{-1} to 350 °C where it was held for 5 min. The total time above 100 °C was therefore around 18 min. The two phases shown in the XRD spectrum (Cu_3Sn and Cu_5Sn_4) appear to become separated over this timescale, which would be a source of non-uniformity in the converted film.

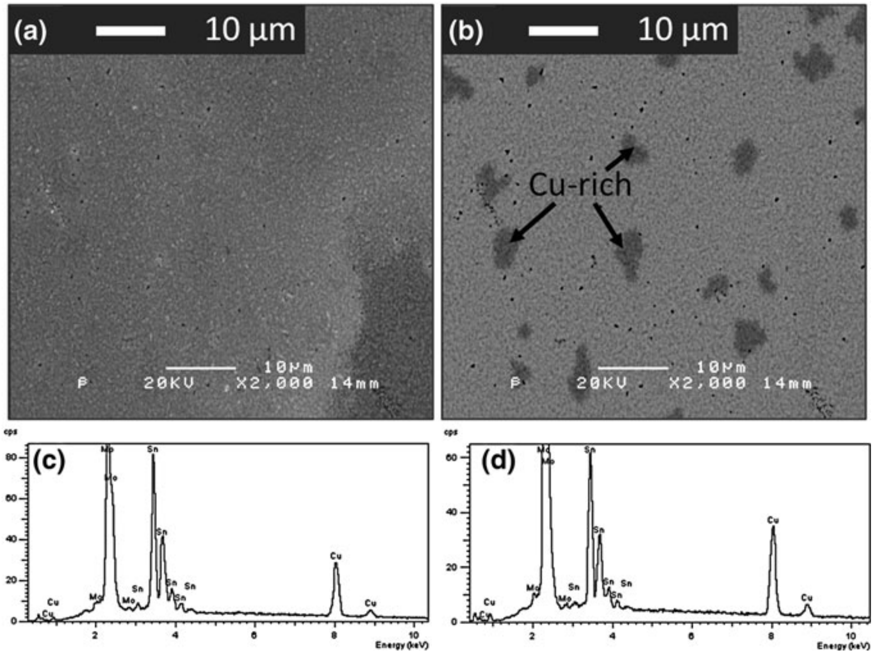

Fig. 3.13 Formation of distinct phases in an annealed Cu/Sn bilayer. **a** Secondary electron image showing morphology. **b** Backscattered electron image showing differences in density. **c** EDS spectrum of lighter areas. **d** EDS spectrum of darker areas

3.11.3 Annealing Cu–Sn–Zn Films

Interestingly, the ternary system Cu/Sn/Zn shows slower rates of Cu–Sn alloying than the binary: as shown in Fig. 3.14, the as-deposited sample contains no obvious Cu–Sn phases. The as-deposited Cu/Sn bilayer (Fig. 3.11a) showed almost complete transformation to alloy phases. This might be because in the Cu/Sn/Zn case, the additional layer of Zn limits the diffusion of vacancies from the top surface, therefore restricting the rate that Cu is able to diffuse towards the surface, although it cannot be ruled out that the samples here and in Fig. 3.11a had different thermal histories. The spectrum does show very strong reflections for Sn and Cu, and surprisingly also a small amount of the $Cu_{0.8}Zn_{0.2}$ phase, which may have arisen from poor alignment of the mask used for electrodepositing the three layers, although, as noted in Sect. 3.1.3, Zn does have a high diffusivity in Sn. As before, elemental Zn is not definitively assignable in these spectra Table 3.8.

The Sn peaks in this and other spectra are shifted slightly towards higher angles as compared to the reference, which is indicative of strain in the as-deposited film. The lattice parameters for the tetragonal β-Sn were calculated using the relationship in Eq. 3.1:

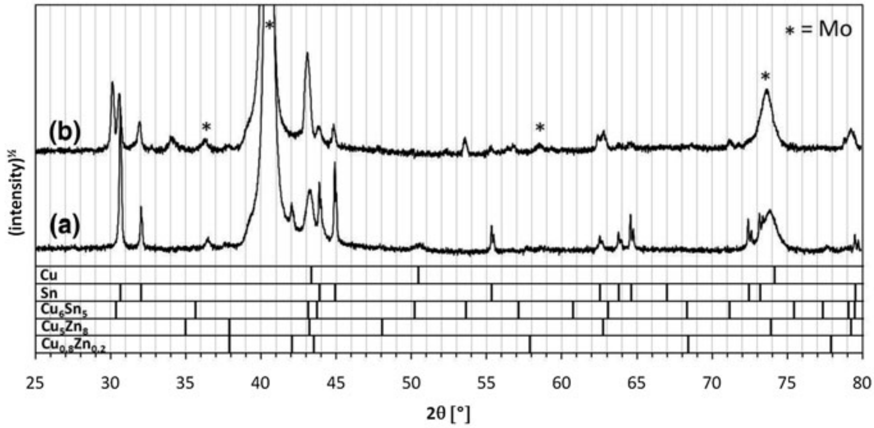

Fig. 3.14 XRD spectra of Cu/Sn/Zn trilayer **a** as-deposited, and **b** after heat treatment at 400 °C for 5 min. Sample composition was approx. 2:1:1 Cu:Sn:Zn

$$\left(\frac{1}{d_{hkl}}\right)^2 = \left(\frac{h}{a}\right)^2 + \left(\frac{k}{b}\right)^2 + \left(\frac{l}{c}\right)^2, \tag{3.1}$$

where d_{hkl} is the spacing of the atomic planes described by the Miller indices h, k and l, and $a, b,$ and c are the unit cell dimensions. In the case of tetragonal symmetry, a = b ≠ c. The calculated values for a and c were 5.826 and 3.180 Å respectively, compared to the standard values 5.832 and 3.181 Å. This means that the as-deposited layer is under a compressive volume strain of −0.1%. Built-in strain is not uncommon in electrodeposited films, occurring for such reasons as an abundance of dislocations, a large number of grain boundaries or because of hydrogen incorporation within the lattice [63] (Fig. 3.15).

Upon heating the Cu/Sn/Zn trilayer, the Cu phase disappears to be replaced by Cu_6Sn_5. Complete consumption of elemental Sn and the formation of Cu_3Sn would have been expected based on previous results (e.g. Fig. 3.11b), but Cu_3Sn has not formed in this instance and Sn remains. This is evidence of the preferential formation of Cu–Zn alloys where Zn is present, as described in the introduction to this section and in Reference [16].

3.11.4 Annealing Complete Cu|Sn|Cu|Zn Precursors

It is now evident that alloying of the precursor occurs to some degree at room temperature and is accelerated by relatively short heat treatments. It is potentially beneficial to apply such a heat treatment prior to sulfurisation. The mobility of the component elements is greater in the metallic phase than in the sulfide phases that will later appear, since the latter have a covalent character. One would initially

Table 3.8 Peak assignment for (a) as-deposited Cu/Sn/Zn trilayer and (b) Cu/Sn/Zn trilayer annealed at 400 °C for 5 min. Refers to the spectra in Fig. 3.14

(a)

2θ (°)	d_{obs} (Å)	Sn d (hkl) (Å)	$Cu_{0.8}Zn_{0.2}$ d (hkl) (Å)	Cu d (hkl) (Å)
30.74	2.91	2.92 (200)		
32.12	2.78	2.79 (101)		
42.14	2.14		2.15 (002)	
43.31	2.09		2.08 (101)	2.09 (111)
43.99	2.06	2.06 (220)		
45.00	2.01	2.02 (121)		
50.55	1.80			1.81 (200)
55.43	1.66	1.66 (031)		
62.63	1.48	1.48 (112)		
63.87	1.46	1.46 (040)		
64.68	1.44	1.44 (231)		
72.50	1.30	1.30 (240)		
73.25	1.29	1.29 (411)		

(b)

2θ (°)	d_{obs} (Å)	Sn d (hkl) (Å)	Cu_5Zn_8 d (hkl) (Å)	Cu_6Sn_5 d (hkl) (Å)
30.22	2.96			2.95 (101)
30.66	2.91	2.92 (200)		
31.99	2.80	2.79 (101)		
34.22	2.62			
34.98	2.56		2.56 (222)	
37.90	2.37		2.37 (321)	
43.16	2.09		2.09 (330)	2.10 (110)
43.96	2.06	2.06 (220)		2.07 (102)
44.93	2.02	2.02 (121)		
47.83	1.90		1.89 (332)	
53.63	1.71			1.71 (201)
55.35	1.66	1.66 (031)		
62.74	1.48	1.48 (112)		
63.86	1.46	1.46 (040)		
64.60	1.44	1.44 (231)		
71.23	1.32			1.32 (211)
79.26	1.21		1.21 (633)	1.21 (300)

expect that a well-mixed precursor should result in a more uniform CZTS film and reduce the volatility of Zn atoms. On the other hand, it has also been seen that longer heat treatments can cause phase segregation. Also, at the typical compositions in use here, according to [16], a liquid phase will form if alloying is allowed to go to completion and therefore de-wetting becomes likely. In our experience, higher temperatures and longer alloying times frequently resulted in the entire precursor film receding to the edge of the substrate, presumably via a molten state.

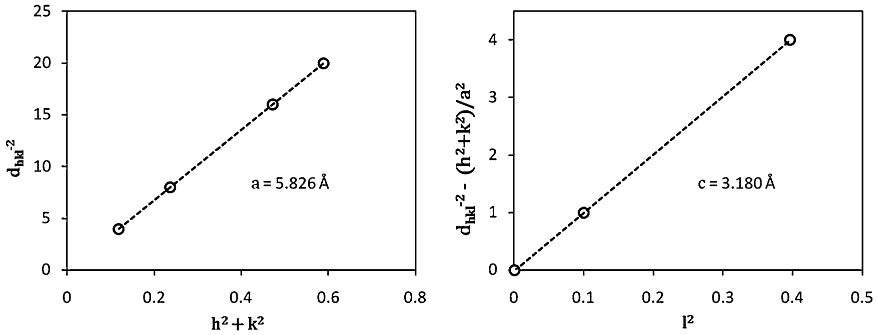

Fig. 3.15 Plots to determine lattice parameters for tetragonal β-Sn. Note that in the right-hand figure, there are between three and five coincident data points at each value of l^2

A compromise was adopted: a 3–5 min treatment at 250–270 °C was found to achieve partial alloying without de-wetting or lateral phase separation. The morphology of the alloyed precursor was similar to that of the precursor itself—i.e. fine grained, showing specular reflectivity. The colour of the film changed from the white–grey of the Zn top layer of the precursor to a grey-gold attributed to alloy formation.

The XRD spectra for an as-deposited and an alloyed sample are shown Fig. 3.16, and the accompanying peak assignments in Table 3.9. After the heat treatment, all Cu was found to be in an alloyed state and the Cu_5Zn_8 phase had formed. The colour of the precursor had changed, which was taken to indicate that all elemental Zn had been consumed (the XRD spectra being ambiguous about the presence or absence of elemental Zn). Sn was still present, as predicted by the Cu–Sn–Zn phase diagram at this temperature [16].

Depth profiles were measured using secondary-ion mass spectrometry (SIMS). The extent of room temperature alloying is clear in Fig. 3.17a, which was measured approx. one week after precursor deposition. The x-axis is a timescale which is proportional to depth if the ion beam penetrates through the sample at a constant rate. Near the film surface there are distorting effects attributed to oxide formation. The approximate positions of the 'true' surface, and the back contact, are indicated in the figures. The data here are not quantitative, but give instead the relative changes in concentration of an element as a function of depth. It was not possible to perform a measurement immediately after precursor preparation to obtain a clearer image of the layers after electrodeposition, since the instrument was installed at a collaborating institution.

After a week at room temperature, the base layer of Cu seems to have migrated through the Sn layer to become concentrated in an intermediate layer between the Sn and Zn. The Cu concentration is higher in the region of greater Zn content, suggesting that Cu–Zn alloys have formed to a greater extent than Cu–Sn alloys (both are seen in Fig. 3.16a). The precursor surface is clearly Zn-rich. In the heated sample, the Cu profile is much more level, and although the surface of the sample

Table 3.9 Peak assignments for XRD spectra in Fig. 3.16: (a) as-deposited Cu/Sn/Cu/Zn stack, (b) Cu/Sn/Cu/Zn stack annealed at 270 °C for 3 min. Stack composition was approx. 2:1:1 Cu:Sn:Zn

(a)						(b)				
2θ [°]	d_{obs} (Å)	Sn d (hkl) (Å)	$Cu_{0.8}Zn_{0.2}$ d (hkl) (Å)	Cu_5Sn_4 d (hkl) (Å)	Cu d (hkl) (Å)	2θ (°)	d_{obs} (Å)	Sn d (hkl) (Å)	Cu_5Zn_8 d (hkl) (Å)	Cu_6Sn_5 d (hkl) (Å)
29.47	3.03			3.03 (21-1)		30.23	2.95			2.95 (101)
30.29	2.95			2.96 (311)		30.70	2.91	2.92 (200)		
30.71	2.91	2.92 (200)				32.05	2.79	2.79 (101)		
32.12	2.78	2.79 (101)				34.99	2.56		2.56 (222)	
35.02	2.56			2.55 (20-2)		37.85	2.38		2.37 (321)	
37.71	2.38		2.37 (100)			43.16	2.09		2.09 (330)	2.10 (110)
42.25	2.14		2.15 (002)			45.00	2.01	2.02 (121)		
43.17	2.09			2.10 (232)	2.09 (111)	48.00	1.89		1.89 (332)	
43.45	2.08		2.08 (101)			53.57	1.71			1.71 (201)
44.12	2.05	2.06 (220)				62.79	1.48	1.48 (112)		
45.06	2.01	2.02 (121)				71.12	1.32			1.32 (211)
47.61	1.91					79.18	1.21		1.21 (633)	1.21 (300)
48.62	1.87									
50.65	1.80				1.81 (200)					
53.59	1.71			1.71 (523)						
56.92	1.62			1.62 (430)						
57.76	1.59		1.59 (102)							
60.28	1.53			1.54 (51-1)						
62.85	1.48	1.48 (112)								
64.69	1.44	1.44 (231)								
67.98	1.38		1.37 (110)							
71.10	1.32			1.33 (543)						
77.03	1.24			1.24 (34-3)						
77.83	1.23		1.23 (103)							
79.13	1.21			1.21 (060)						

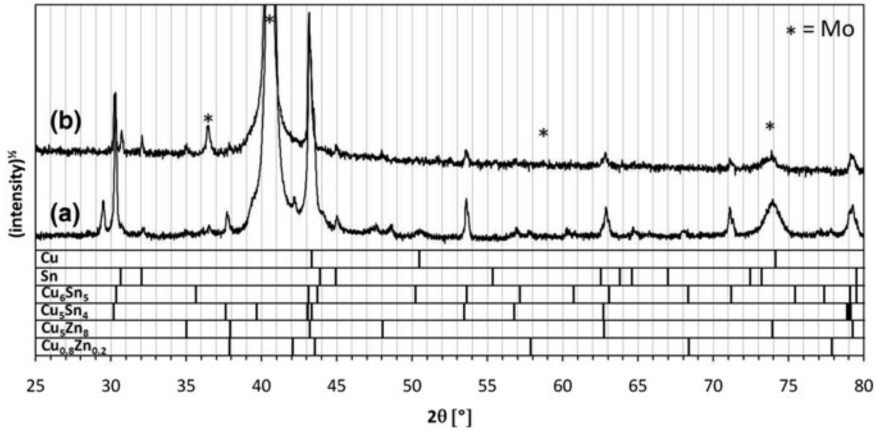

Fig. 3.16 XRD spectra of **a** as-deposited Cu/Sn/Cu/Zn stack, **b** of a Cu/Sn/Cu/Zn stack annealed at 270 °C for 3 min. Stack composition was approx. 2:1:1 Cu:Sn:Zn

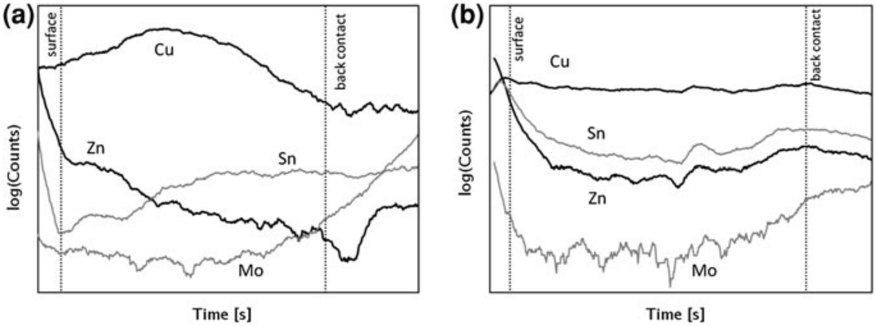

Fig. 3.17 SIMS depth profiles of Cu|Sn|Cu|Zn films: **a** as-deposited, **b** heated to 300 °C for 5 min

is still Zn-rich and now also Sn-rich, both elements extend though the depth of the film, which shows that the precursor has become almost homogeneous.

3.12 Annealing Precursor Stacks in the Presence of Sulfur

3.12.1 Incorporation of Sulfur into the Precursor

In the strategy adopted in this investigation, the emergence of the CZTS phase must be preceded by complete incorporation of sulfur into the metallic precursor. This is expected to occur via the formation of intermediate binary and ternary phases, including Cu_2S, CuS, ZnS, SnS, SnS_2 and Cu_2SnS_3 [60]. The rate of this

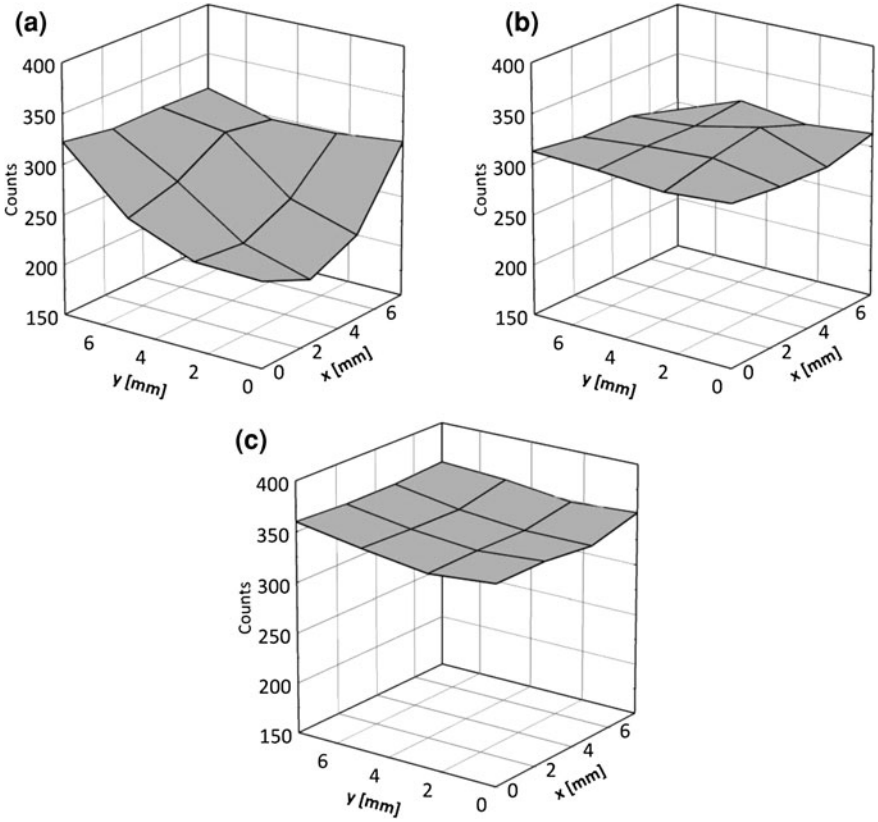

Fig. 3.18 EDS maps of S concentration as a function of position after **a** 10 s, **b** 60 s, and **c** 150 s of sulfurisation at 500 °C, at 10 mbar. The sulfur source (20 mg) was placed at the corner corresponding to x = 7, y = 7 on the plot

initial reaction with S is rapid. Figure 3.18 shows the spatially resolved penetration of S into a precursor at short sulfurisation times.

Sulfur uptake is initially non-uniform, beginning at the side nearest the solid S source, as shown by the higher count rate in the (7, 7) corner of the plot at t = 10 s. After 60 s, the uptake of S is even, and has reached the same level across the whole sample as was initially only found along the x = 7 and y = 7 edges. Between 60 and 150 s, the S content rises uniformly. The observed pattern of S uptake shows that the rate of the reaction between S and the precursor (leading to the initial formation of binary sulfides) is quicker than the rate of arrival of S vapour by convection. If the reverse were true, then the S content should rise uniformly across the entire sample. The phase composition of these samples will be discussed in Sect. 3.12.2.

Figure 3.19b shows a SIMS depth profile of a film after 10 min of sulfurisation at 420 °C. It can be seen that S has penetrated through the entire depth of the film.

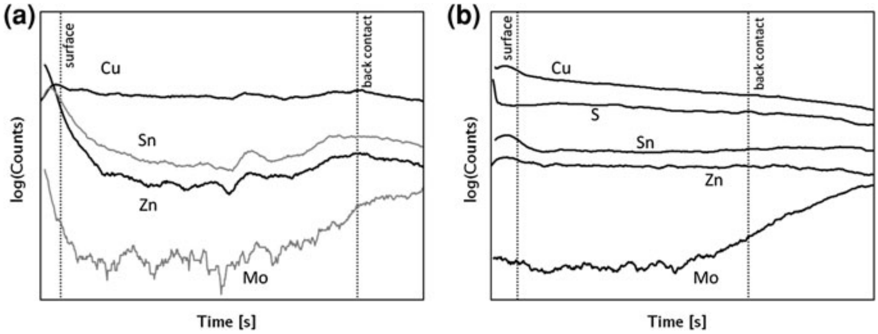

Fig. 3.19 SIMS depth profiles for **a** an alloyed precursor, and **b** a sample sulfurised for 10 min at 420 °C. Sample composition approx. 2:1:1 Cu:Zn:Sn

In comparison to Fig. 3.19a, which shows the depth profile of an alloyed precursor, the profiles of the metal elements have also levelled out, although there is a gradual increase in the Cu content towards the surface of the film.

The rapidity of sulfur uptake (sulfurisation) and the reported rate of formation of CZTS [26] suggest that the system is well suited to rapid thermal processing. The rapid thermal process used for most of this work consists of three segments: fast ramping ($\sim$10–20 °C s^{-1}), a dwell at constant temperature and finally a fast cool. As soon as the S is vaporised and in contact with the sample (i.e. the atmosphere is reactive) and the sample is at sufficient temperature to initiate a reaction with the S (the sample is reactive), then sulfurisation will commence. When heating is rapid, we can assume that the major part of the reaction occurs during the dwell period, not during heating. Reactions can continue during the dwell either until they are complete or until the reactivity of the atmosphere has dropped due to S diffusion away from the hot zone. Rapid cooling will quench any reactions that are in progress and—aside from solidification of molten phases—we can assume that further phase transformations during cooling are minimal. Importantly, this means that the phase composition of the cooled sample is more or less identical to that of the sample during the dwell, and therefore determination of the phases present in the cooled sample (e.g. by XRD) enables us to say which phases were present during the sulfurisation at high temperature.

In the following discussion, we will look at the phases formed as a function of temperature with short dwell times. After that, we will turn our attention to the changes that occur as a function of time at a fixed temperature.

3.12.2 Phase Formation as a Function of Temperature

A series of identical precursors was prepared, and each was sulfurised for 5 min at a temperature from 250 to 550 °C in increments of 50 °C. A heating rate of 10 °C s^{-1} and the maximum possible cooling rate were used. This treatment

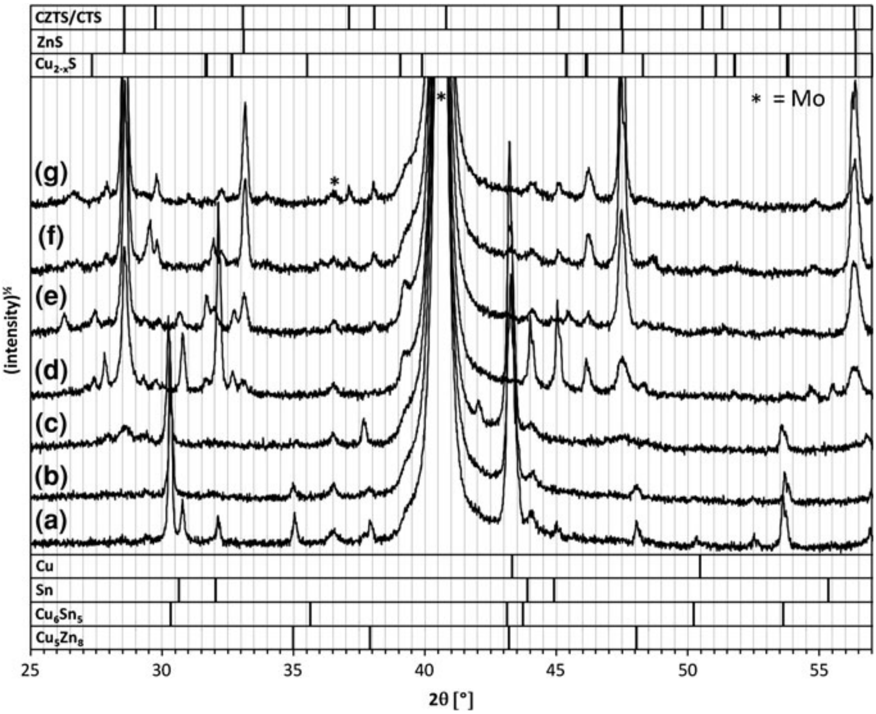

Fig. 3.20 Phase structure as a function of temperature for a series of precursors sulfurised at increasing temperatures: **a** 250, **b** 300, **c** 350, **d** 400, **e** 450, **f** 500, and **g** 550 °C. Other sulfurisation conditions: t = 5 min, p = 16 mbar, 20 mg of sulfur. Sample **a** was an alloyed precursor—no sulfur was used

allows time for the stable phases at a given temperature to form to an extent that they can be observed. It is assumed that most of the phase transformations occur during the dwell period since the ramp stage is very short.

The samples were analysed by powder X-ray diffraction, Raman spectroscopy (for the samples sulfurised from 400 to 550 °C, and also a sample sulfurised at 600 °C) and electron microscopy. All of these data will now be discussed in parallel. The XRD spectra are displayed in Fig. 3.20, with the most important peaks and their intensities shown as a function of temperature in Fig. 3.21. Figures 3.22 and 3.23 show SEM images of the samples, and the Raman data are displayed in Figs. 3.25 (spectra) and 3.26 (peak intensities).

These figures will now be discussed according to the temperature sequence.

Alloyed Precursor

Figure 3.20a shows that the alloyed precursor consists of Cu_5Zn_8, elemental Sn and Cu_6Sn_5. These phases will be the initial sources of sulfide materials.

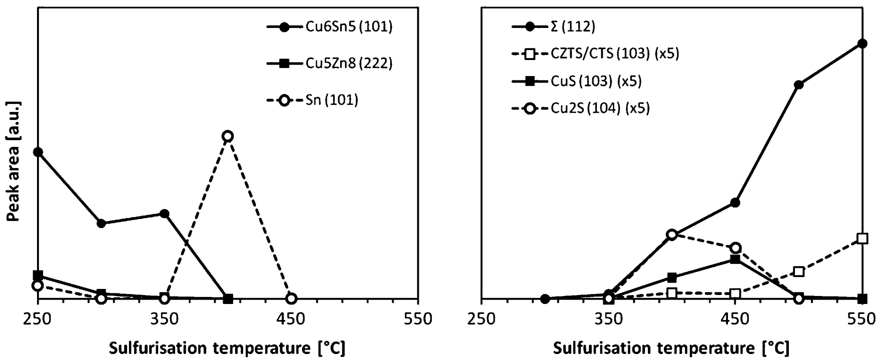

Fig. 3.21 Peak intensities as a function of sulfurisation temperature for the XRD spectra shown in Fig. 3.20. Some traces have been expanded by 5 times for clarity

300 °C

At 300 °C, the XRD data show that elemental Sn has gone, and the intensities of Cu_5Zn_8 and Cu_6Sn_5 have dropped, but there are no traces yet of any sulfide compound. The reduction in the peaks may be due to an orientation effect, or it is possible that sulfurisation has commenced with consumption of these phases but that the products are not yet crystalline or abundant enough to be visible in the diffractogram. The SEM image Fig. 3.22 a shows a similar morphology to the precursor.

350 °C

At 350 °C, the intensity of the Cu_5Zn_8 peak has dropped to zero after 5 min of sulfurisation. We now see the first sign of the important peak at 28.6°. This peak is the principal reflection present in the spectra of ZnS, Cu_2SnS_3 (CTS) and Cu_2ZnSnS_4 (CZTS)—which all have very similar lattice parameters—and corresponds to the (112) planes. It is not possible to distinguish which phase (or mixture) is giving rise to the peak. For this reason, the peak is simply referred to as the $\Sigma(112)$, following a notation used by Weber et al. [24]. Due to their lower symmetry, CTS and CZTS show additional peaks (e.g. the (103)) that are not in the spectrum of ZnS. When these are observed it is possible to confirm the presence of the ternary or quaternary compounds but the presence of ZnS cannot be ruled out since it has no unique peaks of its own. CTS and CZTS cannot be distinguished on the basis of thin film XRD. The $\Sigma(112)$ peak is weak at 350 °C, and given the expected ratio of intensities one would not expect to see the CZTS/CTS (103) even if these phases were present. However, given the disappearance of the Cu_5Zn_8 phase, it seems likely that ZnS is the first sulfide phase to form. This is in contradiction to Schurr et al. who observed Cu_2S and SnS_2 phases before the emergence of ZnS. This may be due to the type of Cu–Zn phase present in the precursor: they found CuZn instead of Cu_5Zn_8; and also to any gradients of

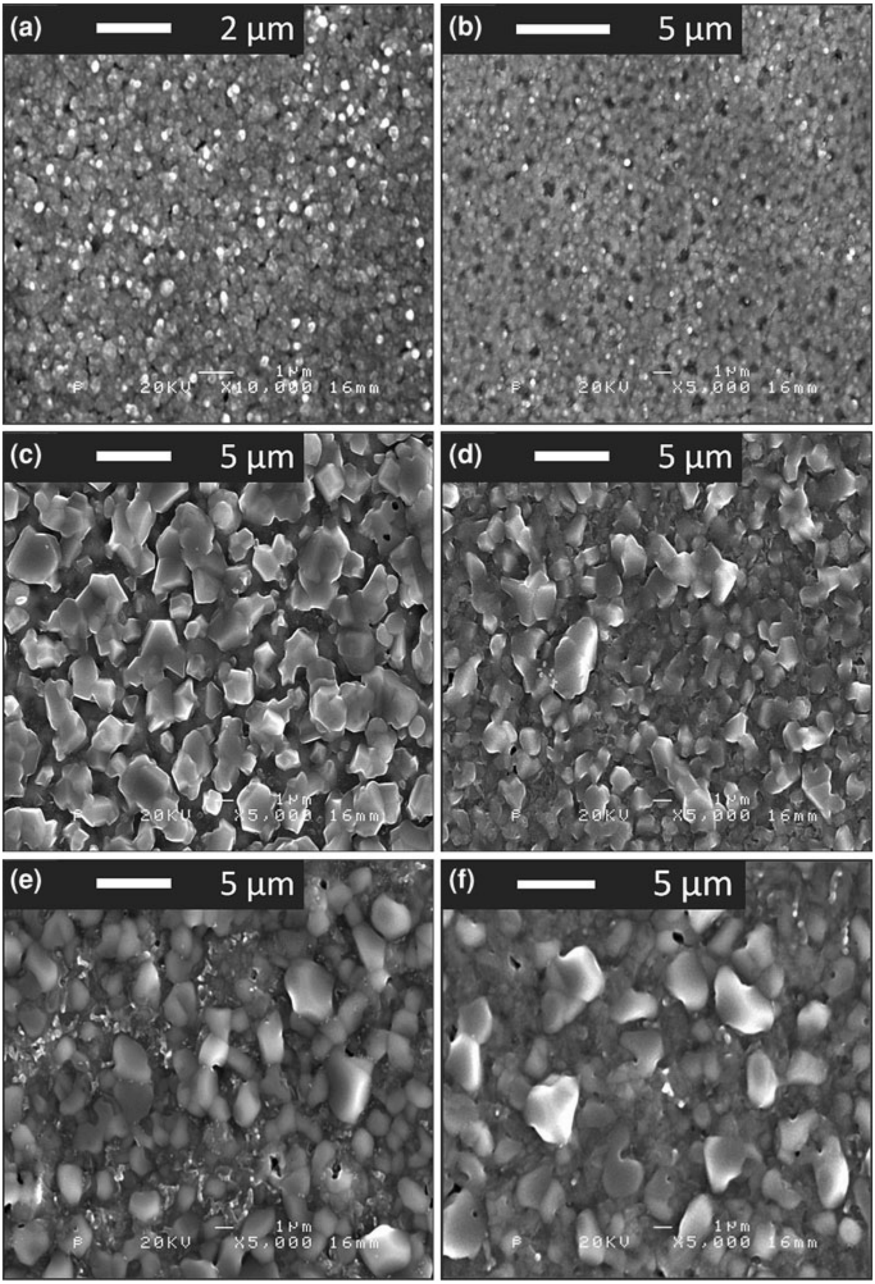

Fig. 3.22 Evolution of surface morphology as a function of sulfurisation temperature: **a** 300, **b** 350, **c** 400, **d** 450, **e** 500, and **f** 550 °C

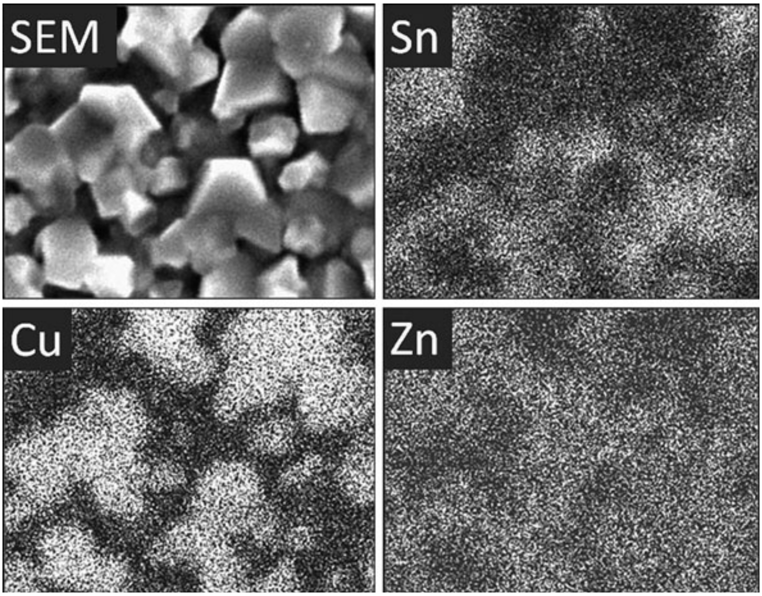

Fig. 3.23 SEM image and corresponding EDS maps of a sample sulfurised at 400 °C for 5 min

composition with depth since the reaction will begin at the surface of the film where S vapour arrives. The fate of the Cu from the Cu_5Zn_8 is unclear, as neither Cu–S nor elemental Cu can be seen in the XRD. A partial explanation may lie in the shift of the Cu_6Sn_5 peak: this now matches more closely to Cu_5Sn_4—a more Cu-rich phase—which could soak up some of the extra Cu atoms. Elemental Sn, which was seen in the precursor but disappeared at 300–350 °C, could also have absorbed some excess Cu. The SEM image, Fig. 3.22b, shows a loss of crystallinity and pitting of the surface, which confirm that some kind of reaction has initiated. A reaction scheme that explains these observations is shown below:

$$Cu_5Zn_8 + S \rightarrow (Cu, Cu_2S) + ZnS \quad \text{(R 3.10)}$$

400 °C

The phase composition and morphology after 5 min at 400 °C are interesting. Firstly, the XRD data (Fig. 3.21) show that two Cu–S phases, close to CuS (covellite) and Cu_2S (chalcocite), have emerged, while the peak for Cu_6Sn_5 has completely vanished. The formation of Cu–S phases is evident in the SEM images. Figure 3.22c shows that blocky crystallites several microns in diameter have formed on the surface of the film. These can be confirmed as Cu–S in two ways: firstly, the EDS maps in Fig. 3.23 show that the grains correlate strongly with Cu and are anti-correlated with Zn and Sn. Secondly, application of a KCN etch,

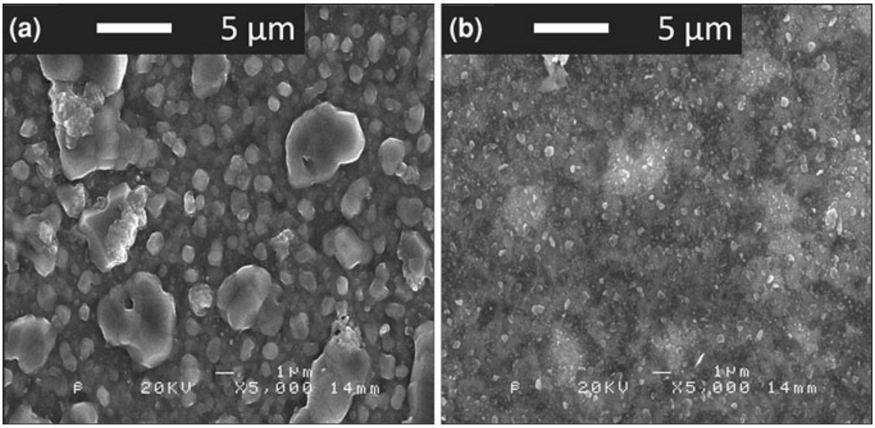

Fig. 3.24 Removal of surface phases present at 400 °C by KCN etching: **a** before, and **b** after etching for 90 s in 5 wt% KCN

Table 3.10 Compositions of sample sulfurised at 400 °C for 5 min before and after etching in 5 wt% KCN

	Cu (at%)	Zn (at%)	Sn (at%)
Before etch	22.6	15.4	16.7
After etch	1.9	23.1	24.8

which is highly preferential for Cu–S, removes these crystallites entirely, and the post-etching composition reveals that almost all the Cu in the film has been removed without any loss of Zn or Sn—see Fig. 3.24 and Table 3.10. This is interesting, because it shows that the entire Cu content of the film has migrated to the surface of the film to form Cu–S grains. This has implications for the back contact of the film, since the out-diffusion of Cu atoms can only occur if there is a corresponding in-diffusion of vacancies to replace them, which could result in voids and poor electrical contact.

Surprisingly, several peaks for elemental Sn have reappeared in the XRD pattern for the 400 °C sample, suggesting that at this temperature the sulfurisation of Sn is only occurring to a limited extent. At this temperature, Sn is certainly in the liquid phase (m.p. ~230 °C), which will be important for the diffusion and bulk mechanical properties of the film. Corroborating this, it is apparent that the Sn reflections for the 400 °C sample are highly oriented, which is probably due to recrystallisation from the melt upon cooling. Preferred orientation along the [101] axis, which corresponds to the close packed plane of tetragonal β-Sn, is commonly seen for Sn upon solidification [15]. This means that the intensity shown in Fig. 3.21 is perhaps an overstatement; however there is no evidence for $SnS/SnS_2/Sn_2S_3$ and only weak reflections for other Sn-containing phases are seen, as will now be discussed.

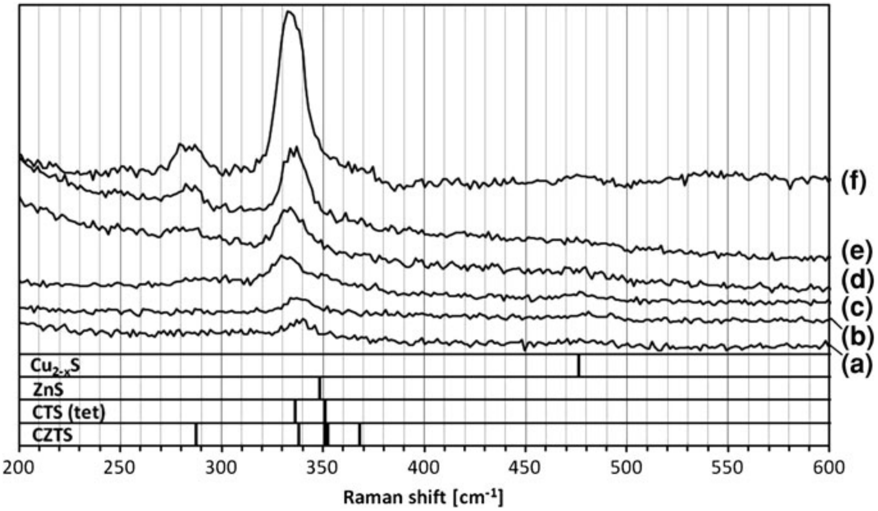

Fig. 3.25 Raman spectra for a series of precursors on Mo-quartz substrates, sulfurised at increasing temperatures: **a** 400, **b** 450, **c** 500, **d** 550, **e** 600 °C, for 5 min, and **f** at 600 °C for 30 min. Other sulfurisation conditions: p = 16 mbar, 20 mg of sulfur

Fig. 3.26 Peak intensities as a function of sulfurisation temperature for the Raman spectra in Fig. 3.25 a–e

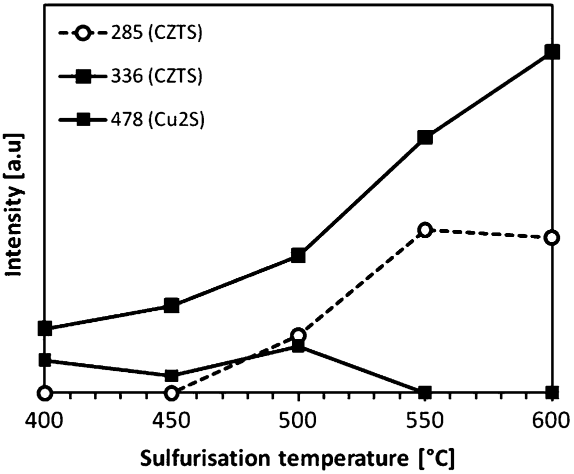

Turning now to the higher-order phases, the Σ(112) peak has grown and a CZTS/CTS (103) peak has become visible. The Raman data (Figs. 3.25 and 3.26) reveal two main peaks which match the literature values for CZTS. Unfortunately, the presence of CTS and ZnS cannot be entirely ruled out: they could overlap with the main CZTS peak. A peak at the position anticipated for Cu_2S is also seen.

According to the EDS data (Table 3.10) only 12% of the original Cu remained after etching this sample, and therefore this is the maximum amount that could be in the CZTS phase (assuming CZTS is not itself etched). The phase composition at this temperature is therefore a small amount of CZTS alongside Cu–S, ZnS, and elemental Sn. There may also be some CTS.

A reaction scheme that explains the observations at 400 °C is shown below:

$$\mathrm{Cu_6Sn_5} + 1.5\mathrm{S_2(g)} \rightarrow 3\mathrm{CuS} + 5\mathrm{Sn(1)} \tag{R 3.11}$$

$$2\mathrm{Cu_5Zn_8} + 10.5\mathrm{S_2(g)} \rightarrow 5\mathrm{Cu_2S} + 16\mathrm{ZnS} \tag{R 3.12}$$

Combined with:

$$\mathrm{Cu_2S} + \mathrm{Sn(l)} + \mathrm{ZnS} + \mathrm{S_2(g)} \rightarrow \mathrm{Cu_2ZnSnS_4},\ \mathrm{Cu_2SnS_3} \tag{R 3.13}$$

According to Hergert and Hock [60], the formation of CZTS (R 3.13) should occur via the formation of CTS or SnS_2 as intermediates. No SnS_2 is observed by XRD or Raman, but CTS cannot be ruled out based on either technique.

Equations (R 3.11) and (R 3.12) result in the almost total transport of Cu to the film surface as Cu_2S, which is clearly undesirable for film uniformity, in terms of the separation of elements and in the introduction of vacancies.

450 °C

At 450 °C, elemental Sn is no longer observed and the Σ(112) and CZTS/CTS (103) peaks are larger than at 400 °C. There are two possible explanations: either that a different reaction pathway occurs at this higher temperature, which does not go via the liquid Sn phase; or that the reaction sequence (R 3.11)–(R 3.13) has continued to completion within 5 min. It will be shown below that the latter is more likely. The Raman data also show a slight increase in the size of the CZTS peak. The SEM image, Fig. 3.22d, still shows Cu–S grains, but when compared to the 400 °C sample, the grains are smaller and appear better integrated into the bulk of the sample—i.e. they have not segregated completely to the surface as seen at 400 °C. This suggests that at 450 °C the reactions that consume Cu_2S and lead to CZTS occur more rapidly, limiting the extent of the Cu_2S segregation process. This is one reason to favour the use of a rapid temperature ramp: to avoid spending time at temperatures where the gross segregation of Cu_2S to the surface occurs.

500–600 °C

At 500 °C, Cu-sulfides do not appear in the XRD spectra, while the Σ peaks continue to increase up to 550 °C. Note that the softening point of glass limits the temperatures that can be used here. The Raman samples were prepared on quartz substrates which have a much higher softening point. Cu_2S is still visible to the surface-sensitive Raman at 500 °C, but has disappeared by 550 °C. At 600 °C, the CZTS Raman peak is still increasing. The SEM images show no significant changes to the surface morphology between 500 and 600 °C, with some large Cu–S grains still visible.

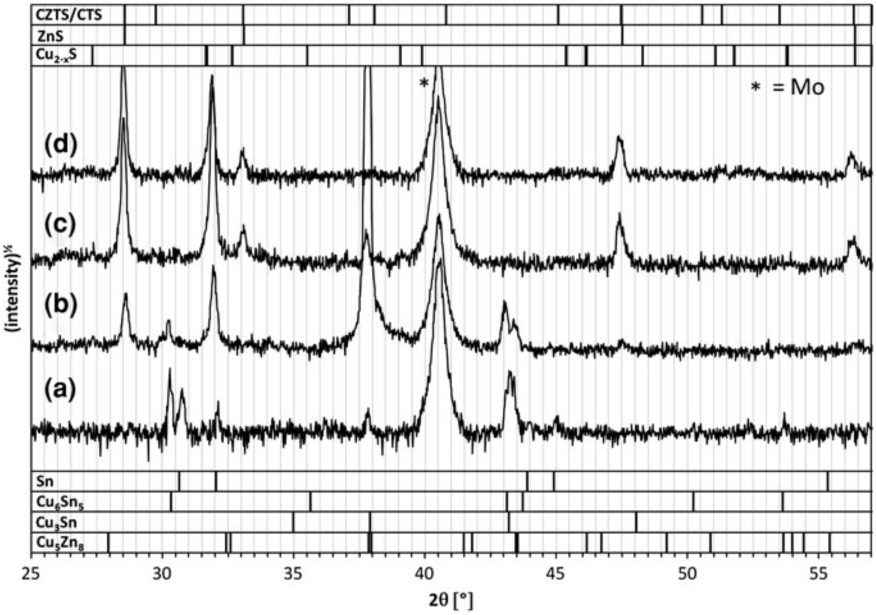

Fig. 3.27 XRD spectra as a function of sulfurisation time at 500 °C for **a** 0 (ramped only), **b** 10, **c** 60, and **d** 150 s

3.12.3 Development of Phases as a Function of Time at 500 °C

To obtain further information about phase formation at short sulfurisation times, a time-resolved study was carried out at 500 °C. Identical samples were sulfurised by ramping quickly to 500 °C and then holding for 0, 10, 60 and 150 s respectively before quenching by rapid cooling. The XRD spectra for these samples are shown in Fig. 3.27 and the intensities of the key peaks are shown in Fig. 3.28.

At the start of the dwell period, i.e. immediately after the ramp, only the precursor phases Cu_6Sn_5 Cu_5Zn_8 and Sn are observed. No sulfide phases are seen, which confirms that very little transformation occurs during the fast heating stage, either because the sulphur vapour has not yet reached the sample or because the reaction has not had time to generate sufficient quantities of material. After 10 s, the Σ(112) peak is seen, probably attributable to ZnS, alongside a weak reflection from the (102) planes of Cu_2S. The most interesting feature after 10 s is the simultaneous emergence of the Sn (101) and Cu_3Sn (201)/(002) peaks, while the Cu_6Sn_5 peak diminishes. The intensities of both new peaks (particularly Cu_3Sn) point to a preferential orientation. Noting that the melting point of Cu_6Sn_5 is around 415 °C, this can be explained by the crystallisation of Cu_3Sn from molten Cu_6Sn_5, leaving behind molten Sn, which in turn crystallises upon cooling of the

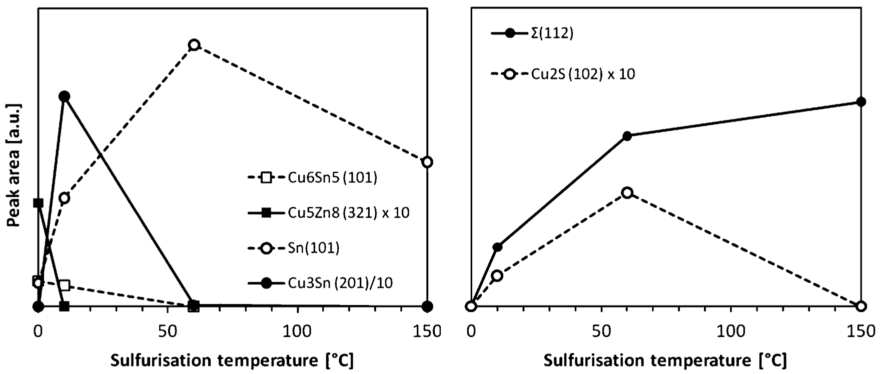

Fig. 3.28 XRD peak intensities as a function of sulfurisation time at 500 °C (refers to Fig. 3.27)

sample below 230 °C. The melting point of Cu_3Sn is much higher, around 680 °C. Therefore in the early stages of sulfurisation we have the reactions:

$$Cu_5Zn_8 + S_2(g) \rightarrow Cu_2S + ZnS \tag{R 3.14}$$

$$Cu_6Sn_5(s) \rightarrow Cu_6Sn_5(l) \text{ (starting around } 400\,^{\circ}\text{C)} \tag{R 3.15}$$

$$Cu_6Sn_5(l) \rightarrow 2Cu_3Sn(s) + 3Sn(l) \tag{R 3.16}$$

By 60 s, Cu_6Sn_5 has disappeared altogether, by the continuation of (R 3.16). The Cu_3Sn phase has also vanished, which, given the further increase in the Sn (101) and Cu_2S (102) peaks, must be due to a reaction such as:

$$2Cu_3Sn + 3S \rightarrow 3Cu_2S + 2Sn(l) \tag{R 3.17}$$

Note that in the temperature study above, the steps (R 3.15)–(R 3.16) were previously described by a single step, which explained the products present after 5 min of sulfurisation.

After 150 s, the amounts of Sn and Cu_2S are decreasing while the Σ(112) increases, which points to the formation of CTS or CZTS. As shown in Figs. 3.21 and 3.26, the only phases remaining after 5 min/300 s of sulfurisation are CZTS, Cu_2S, and possibly CTS.

Before we present a model of CZTS film growth from the stacked electrodeposited precursor, there are several aspects of the foregoing data that require further examination.

3.12.4 Surface Segregation of Cu_2S and Formation of Voids

During film growth, Cu tended to migrate towards the film surface to form Cu_2S, as shown by SEM and EDS analysis alongside etching experiments. At 400 °C this reaction had almost gone to completion, while at higher temperatures, the Cu_2S

grains were more buried, suggesting that other reactions took over before the material could rise completely. The reason for this surface segregation can be understood in terms of a vacancy diffusion mechanism discovered by Kirkendall, resulting from the interdiffusion of two species which have very different bulk diffusivities [64]. Net material transport occurs due to an unequal likelihood of the different atoms moving into adjoining vacancies [65], meaning that the process is best described as a net flux of vacancies. For example, at the interface between Cu and a Cu_3Sn alloy, the high diffusivity of Cu compared to Sn in the alloy causes the Cu-alloy interface to move into the alloy phase leaving large concentrations of Cu vacancies, which originated at a surface, at the Cu–Cu_3Sn interface [66]. Mobile lattice vacancies can coalesce into voids (Kirkendall voids), especially at higher temperatures. For example, in the case of Zeng et al. after 20 days of heating a Cu_3Sn–Sn bilayer at 150 °C, voids several microns in extent occupied more than 70% of the Cu_3Sn–Cu interface [66]. Since Kirkendall void formation is a diffusion-based process, it is thermally activated and therefore much higher rates can be expected at the temperatures used in this study.

In a striking example of this process, hollow spheres of CdS can be formed from the reaction of initially solid Cd nanoparticles with S, due to the unequal diffusivity of Cd^{2+} and S^{2-} ions. Cd^{2+} vacancies flow inwards from the surface of the growing CdS layer and Kirkendall voids form and grow in the centre of the nanoparticle until the reaction is complete and the particle is completely hollow [67]. Figure 3.29 illustrates the Kirkendall effect in the growth of Cu_2S from a Cu film.

Returning to the material at hand, "Cu_2S" is generally non-stoichiometric, having a deficiency of Cu(II) ions. This is represented by the incorporation of small amounts of CuS [68]:

$$\mathrm{xCuS} + (1 - \mathrm{x})\mathrm{Cu_2S} \rightarrow \mathrm{Cu_{2-x}S} \qquad \text{(R 3.18)}$$

This process creates Cu vacancies, the bulk diffusivities of which are very high, especially at elevated temperatures [69], while the rate of diffusion of S^{2-} anions is much slower. This presents ideal conditions for the Kirkendall effect. Liu et al. studied the growth of Cu_2S pillars out of a Cu metal surface exposed to H_2S, and presented a growth mechanism driven by the diffusion of ionic vacancies from the reacting surface into the bulk material [70]. The mechanism involved the addition of S^{2-} anions—which can be considered as having adjoining Cu^+ vacancies—to the Cu surface. Cu^+ cations diffuse out of the Cu bulk into these vacancies (equivalent to in-diffusion of the vacancy) to join the absorbed S^{2-} and form Cu_2S. Initially, a uniform layer of Cu_2S formed, but cracks due to expansion seeded the nanowires, which grow anisotropically due to faster vacancy diffusion along the [001] direction. The wires grew outwards by continued diffusion of vacancies down the wire towards the substrate. The net effect of this mechanism was transport of Cu out of the film and accumulation of vacancies inside the film.

In the particular case of CZTS film formation, the Kirkendall effect can be invoked to explain the observed morphology after 5 min of sulfurisation at 400 °C.

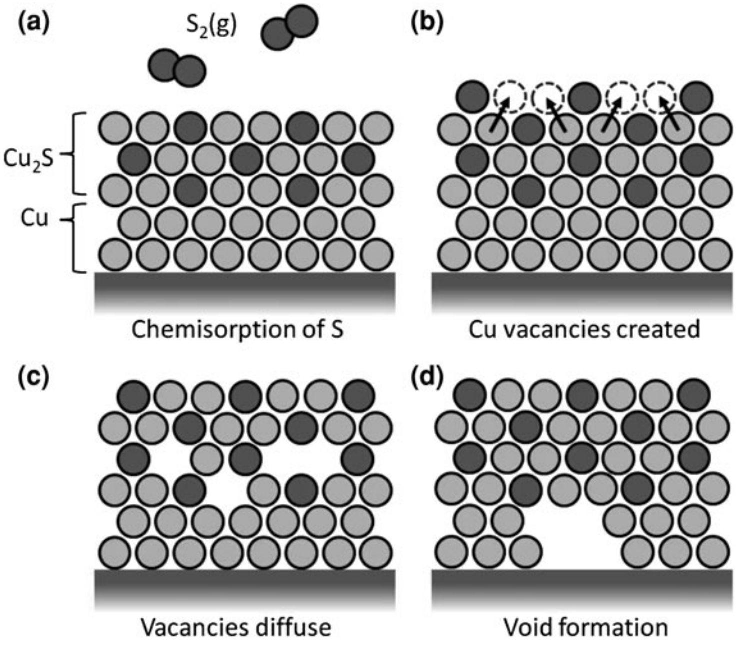

Fig. 3.29 Schematic diagram showing Kirkendall void formation in a layer of Cu reacting with S vapour. **a** A thin Cu_2S overlayer forms. **b** S atoms from the vapour become adsorbed at the surface, Cu vacancies are created alongside them. **c** Diffusion of Cu vacancies away from their site of formation, with a net flux of Cu atoms towards the surface. **d** Accumulation of vacancies to form a void at the bottom of the film. Note that the layer of Cu_2S has increased in thickness as a result

In the present case, we have Cu_6Sn_5 as a Cu source and S vapour reacting at the surface. Initially, Cu_2S can form easily and cover the Cu_6Sn_5 surface. In order for the Cu_2S grains to grow, we require transport of Cu^+ ions out of the Cu_6Sn_5 phase, through the covering Cu_2S layer to the outer surface, where they can combine with S^{2-}. This process is best described by continuous diffusion of Cu^+ vacancies from the surface into the film. Cu transport from deeper in the film is presumably enhanced as the Cu_6Sn_5 phase melts, and, as we have seen, is able to continue until nearly all the Cu has moved from the bulk of the film to the surface leaving behind only molten Sn (ZnS having already formed). At the end of the reaction, a high concentration of vacancies will remain at the Mo–Sn interface.

We have already seen an instance that shows an unfavourable interaction of Sn with Mo: the de-wetting of liquid Cu–Sn alloys from Mo as seen in Sect. 3.11.2. This makes void formation by vacancy agglomeration at the Sn–Mo interface especially likely, because the interfacial energy will be reduced. We can attribute the fact that the film does not de-wet the substrate to the presence of a solid layer of Cu_2S and ZnS at the surface. Voids at the Mo-CZTS interface are frequently reported in the CZTS literature (see for example [31]), and an example is shown in

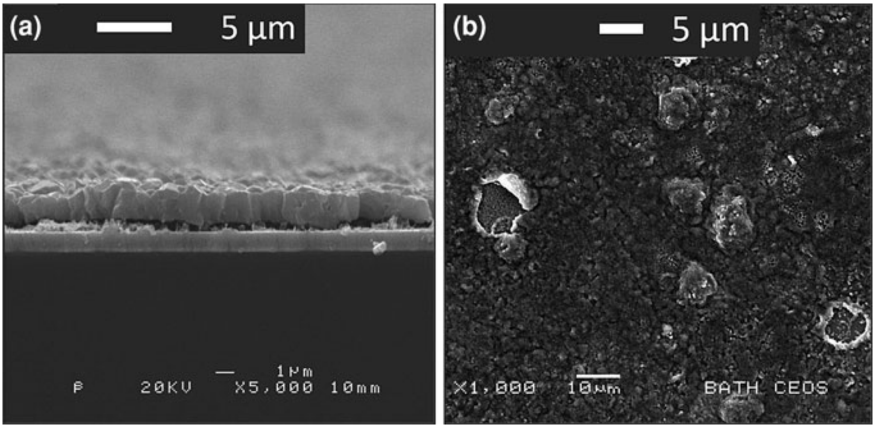

Fig. 3.30 **a** Void formation under CZTS layers. **b** Presence of intact and collapsed bubbles in the film. Composition of films approx. 2:1:1 Cu:Zn:Sn Sulfurised at 550 °C

Fig. 3.30a. Similar void formation at Cu_3Sn–Cu interfaces resulted in considerable losses of electrical conductivity and mechanical strength [66], the former being of great concern in this case.

3.12.5 *The Presence of Liquid Sn, the Absence of Sn_xS_y*

The second feature requiring explanation is the presence of liquid elemental Sn during film growth. One consequence of the liquid phase could be that void formation by vacancy agglomeration is enhanced, which may in extreme cases result in bubbles. Features such as those in Figs. 3.30b and 3.31 are consistent with the formation and collapse/bursting of bubbles underneath the film, leaving 'pin-holes' where the Mo substrate is exposed. This will have severe consequences for the electronic properties of the film due to formation of electrical shorting pathways.

Another interesting aspect is that the Sn does not form Sn–S phases; one or other of the binaries SnS, SnS_2 or Sn_2S_3 should start to form from around 150 °C if elemental Sn is in contact with S vapour [18, 71]. At the same time, we do see the emergence of other sulfide phases (Cu_2S, ZnS), so there must be S vapour present above the sample. We can only conclude that the formation of solid sulfides (particularly Cu_2S) at the surface of the film prevents direct contact between Sn and S vapour. This is in agreement with the relative densities of the phases as shown in Table 3.11. Transport of S to the Sn layer can then only occur via diffusion of S^{2-} anions through Cu_2S or ZnS, in which case it is likely that a ternary or quaternary phase would be formed rather than Sn_xS_y. This process

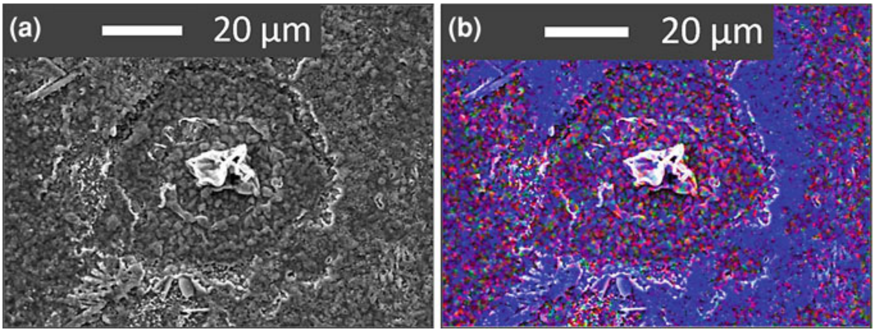

Fig. 3.31 Features commonly seen in Sn-rich films, consistent with the formation and collapse of bubbles in the presence of liquid Sn. **a** SEM image. **b** EDS map (colour) showing Cu in red, Zn in green and Sn in blue. S was present uniformly over the entire area

Table 3.11 Densities of some selected phases

Phase	Density (g cm^{-3})
ZnS	3.9–4.2
Cu_2S, CuS	5.5–5.8, 4.6–4.8
Sn (l)	6.99

should be relatively slow, which explains why elemental Sn is seen for a considerable time into the reaction sequence (e.g. see Fig. 3.27).

The EDS maps of Fig. 3.32 (reproduced from Fig. 3.18) show two stages of sulfurisation: one rapid step between 10 and 60 s that levels out the S content of the film, and a second, slower step where the S content increases uniformly. These two stages may well correspond to the reactions elucidated above, i.e. firstly the formation of ZnS and Cu_2S, and then, at a slower rate, the penetration of S through these materials to the underlying Sn leading to formation of the higher phases.

Given the similarity of the approach of Schurr et al. [18] to ours, we need to explain the stark differences in the observed Sn-containing phases. In that work, SnS_2 was seen to form and later to melt before the emergence of ternary phases. No liquid Sn was seen, although it must be pointed out that if liquid Sn was formed by the same mechanism as we propose (i.e. rejection from a molten Cu–Sn phase), it would not have been observed in the in situ XRD experiment, it would only become detectable on cooling. The principal difference between their experiment and ours is the two orders of magnitude difference in the heating rates: 0.8 °C s^{-1} in the cited work compared to 10 °C s^{-1} in this work. During a slow ramp, the most thermodynamically stable phases are likely to be formed, as diffusion processes leading to the formation of new phases have more time to occur. Therefore SnS_2 is observed alongside Cu–S and Zn–S phases. However, if the ramping rate is high, phase formation will be dominated by kinetic concerns, such as the proximity of reactive materials. In the present work, it appears that Cu_2S and ZnS quickly

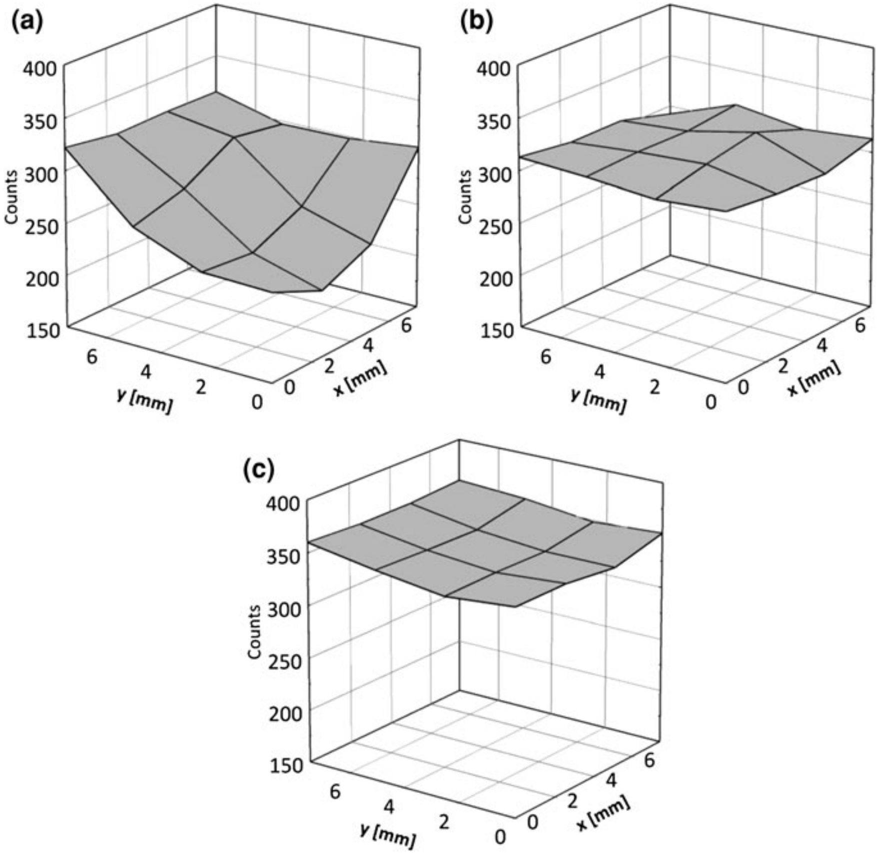

Fig. 3.32 EDS maps showing S concentration as a function of position after 10, 60 and 150 s of sulfurisation. The S source was placed at the point corresponding to x = y = 7 on the plots

cover the precursor surface, which suddenly becomes reactive in the presence of S vapour as the temperature is rapidly increased. In order to react with Sn, S atoms would be required to diffuse through these solid sulfides. If this diffusion process is relatively slow compared with the ramping rate, then the temperature at which SnS_2 reacts with Cu_2S and/or ZnS may be reached before any observable quantity of SnS_2 has built up. In this case, SnS_2 would never be seen because it is consumed as rapidly as it is formed. The case may be similar for Cu_6SnS_4, which is another intermediate phase observed by Schurr et al. but not seen here. It therefore appears that at faster ramp rates, direct reaction of the binary phases without any intermediates is more likely. Both pathways (from binaries or via CTS) were predicted by Hergert and Hock [60].

It appears that the ramping rate is very important in deciding the reaction sequence that leads to the final CZTS film by sulfurisation of a stacked metallic precursor. Schurr et al. [18] presented a model for the reaction sequence that occurs when slow ramping rates are used, and we will now present one for higher ramping rates.

3.13 Proposed Model for CZTS Formation with High Heating Rates

Based on the findings in the previous section, we now present a model of the reaction processes that appear to be occurring when a high ramp rate is employed to sulfurise a metallic Cu–Zn–Sn precursor. The XRD and Raman data showing phase formation as a function of time and temperature allow us to derive a reaction sequence with reasonable confidence, although the mechanistic details remain to be studied. It should be noted that this scheme is only a proposal that adequately describes the data herein, and should be treated as a working hypothesis to be revised in light of future investigations.

3.13.1 Reaction Sequence at 500–550 °C

The phases present prior to sulfurisation (after a short alloying stage) are Cu_5Zn_8, Cu_6Sn_5 and Sn. The first stage is the direct reaction of S vapour with the Zn-rich surface:

$$Cu_5Zn_8 + S_2(g) \rightarrow Cu_2S + ZnS \qquad \text{(R 3.19)}$$

All the Zn appears to be consumed during this stage, which is complete within 1 min.

Further growth of Cu_2S now occurs by the adsorption of $S_2(g)$ at the Cu_2S surface, causing the creation of Cu^+ vacancies, V_{Cu}. These vacancies diffuse into the film, which is equivalent to a transport of Cu towards the surface from the underlying Cu_6Sn_5 phase. As it loses Cu, Cu_6Sn_5 (which may melt) undergoes a phase transition to form Cu_3Sn and molten Sn. There are thus two spatially separate reaction processes mediated by the flux of Cu vacancies; firstly at the surface:

$$\tfrac{1}{2}S_2(g) + Cu_2S(s) \rightarrow 2Cu_2S(s) + 2V_{Cu}, \qquad \text{(R 3.20)}$$

and then, following diffusion of vacancies into the sample:

$$Cu_6Sn_5(s) + 3V_{Cu} \rightarrow Cu_3Sn(s) + 4Sn(l) \qquad \text{(R 3.21)}$$

This process continues with the formation of further molten Sn until the Cu_3Sn phase is also consumed:

$$Cu_3Sn(s) + 3V_{Cu} \rightarrow Sn(l) \qquad \text{(R 3.22)}$$

The net effect of (R 3.20)–(R 3.23) is:

$$\mathrm{Cu_6Sn_5(s) + 1.5S_2(g) \rightarrow 3Cu_2S(s) + 5Sn(l)} \qquad \text{(R 3.23)}$$

The validity of this reaction is apparent when one compares the heats of formation of Cu_6Sn_5 and Cu_2S, which are −7.04 [72] and −79.4 kJ mol^{-1} [73] respectively; there is a strong thermodynamic driving force for the formation of Cu_2S by decomposition of Cu_6Sn_5. In the above processes, the influx of vacancies may be the source of voids that form at the Mo-Sn interface. These voids could in principle coalesce easily while liquid Sn is present, which may be favourable to reduce the interfacial energy.

This first stage of sulfurisation resulting in Cu_2S, ZnS and Sn(l) is complete after 60–150 s at 500 °C. The next stage is slower, because S atoms have to penetrate the solid surface layers in order to reach the underlying Sn. It takes 3–5 min to consume the liquid Sn phase in the growth of CZTS (and maybe CTS), which appears to occur directly from the binaries:

$$\mathrm{Cu_2S + Sn + 2S + ZnS \rightarrow Cu_2ZnSnS_4,\ Cu_2SnS_3} \qquad \text{(R 3.24)}$$

This reaction would presumably begin where Cu_2S, Sn and Zn are in mutual contact.

Note that at no stage in this discussion has the phase $Cu_2ZnSn_3S_8$ been mentioned. This is because there is very limited information available about the phase at present, except that the structure and lattice parameters are close to those of CZTS. If this Sn-rich phase were to form, then a likely location would be in the lower regions of the film, where the concentration of Sn is highest during growth.

A schematic diagram showing these reactions occurring within the film is given in Fig. 3.33, the stages of which will now be described. Diagram (a) shows a cross-sectional representation of the precursor on a Mo-SLG substrate. In (b) is shown the initial reaction of S vapour with the surface, forming grains of ZnS and Cu_2S. Diagram (c) illustrates the Kirkendall mechanism of Cu_2S growth, the vacancy influx causing the Cu_6Sn_5 phase to eject liquid Sn and form Cu_3Sn. Vacancies accumulate at the back surface to form voids. This process continues until all the Cu is consumed, (d). At this point in the scenario, we have an underlying layer of liquid Sn, and, essentially floating above, a surface layer of ZnS with large Cu_2S grains embedded in it. CZTS growth now starts at the interface between the three metal-containing phases, (e) and continues to spread away from these interfaces until all the source material is consumed (f). An edge-on image of a CZTS film is shown in Fig. 3.34 for comparison.

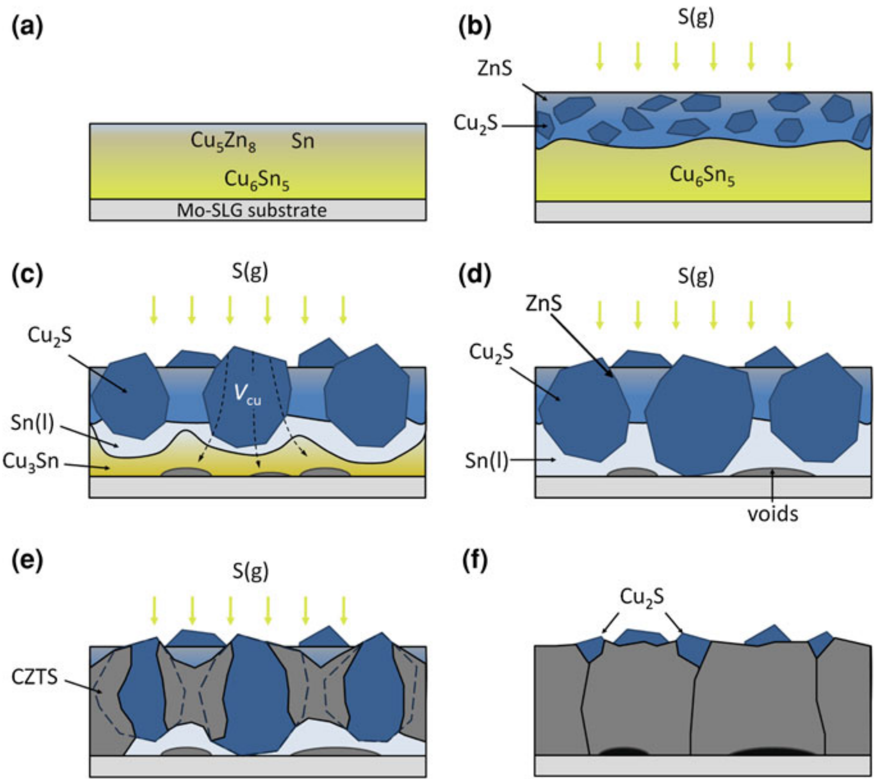

Fig. 3.33 Proposed formation sequence of CZTS films when high ramp rates are used. See text for explanation

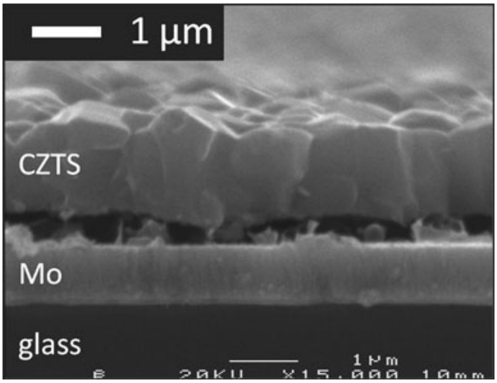

Fig. 3.34 Edge-on image of a CZTS film showing large crystals in the vertical direction and voids at the Mo-CZTS interface

Conclusions

The goal of this section of work was to demonstrate conversion of the electrodeposited Cu–Sn–Zn precursors developed in Chap. 2 into films of which the primary phase was Cu_2ZnSnS_4, by reaction with S vapour at elevated temperatures. The equipment used to achieve this was a Rapid Thermal Processor (RTP), which has very high heating and cooling rates. The foundation of much of the work in this chapter and those that follow is the ability of the RTP to cool a sample rapidly, such that the phases present at the annealing temperature are preserved. Very short annealing intervals can be employed, and in this way the progress of the reactions occurring at high temperature can be indirectly inspected. The main characterisation techniques available were scanning electron microscopy (SEM), X-ray diffraction and Raman spectroscopy.

Initially, a study of the effects of heating precursor films in the absence of S vapour was carried out. This was done in order to determine which alloy phases would comprise the chemical precursors to the sulfide phases, once S was introduced. The primary alloy phases formed in Cu–Sn bilayers after heating were Cu_5Sn_4 and Cu_3Sn, and those in Cu–Zn bilayers were $Cu_{0.8}Zn_{0.2}$ and $Cu_{0.75}Zn_{0.25}$. In the complete Cu|Sn|Cu|Zn stack, after a 3 min heat treatment at 270 °C, the phases observed were Sn, Cu_5Zn_8 and Cu_6Sn_5, showing that Cu was completely involved in alloy formation and that Cu–Zn alloys formed preferentially to Cu–Sn alloys, leaving behind un-reacted elemental Sn. This is in agreement with the literature. SIMS depth profiles showed that the interdiffusion of Cu was complete, and the surface of the alloyed precursor was Sn- and Zn-rich. Therefore this short heat treatment was sufficient to emulate the fabrication of a mixed precursor, such as might be produced from a co-electrodeposition approach.

The reaction of S vapour with samples at a series of increasing temperatures was studied. Phase formation began with the emergence of ZnS and Cu–S phases between 300 and 350 °C. The most notable effect was the almost total segregation of Cu–S phases to the film surface at 400 °C, leaving a liquid Sn phase underneath. Raman spectroscopy definitively showed the CZTS phase emerging between 400 and 450 °C, although the presence of Cu–Sn–S phases could not be ruled out. Studies of the phase emergence as a function of time at 500 °C were performed.

The primary result from this chapter was a proposed reaction sequence and model for film formation. This was rather different from that found by Schurr et al. [18], but the differences were adequately explained by the different heating rates; their experiment may be regarded as being carried out approx. under equilibrium conditions, whereas this one is dominated by kinetic concerns due to the rapid heating rate. The model accounts in large part for the observed morphology, including the formation of interfacial voids, as well as defects such as pin-holes and ‘bubble-like’ structures. A vital component of the model was the migration of Cu atoms to the surface of the film, on the basis of the Kirkendall vacancy diffusion mechanism. A side effect of this is the generation of a liquid Sn phase beneath solid sulfide covering layers, which prevented direct reaction of S with Sn.

Some key implications/predictions of the model described for high heating rates are listed below:

1. Void formation at the Mo-film interface is unavoidable when Cu is present in the lower regions of the precursor film. This explains the observation by Araki et al. that having Cu as a base layer in a stacked precursor gave poor adhesion in the final CZTS film [22]. They suggested that the best stacking order was Mo|Zn|Sn|Cu, i.e. with Cu at the top. This order would minimise the potential for void formation. In the electrodeposition approach this stacking order is difficult to achieve; a Cu base layer was actually required to obtain good deposits. An alternative approach could be to use a thin Cu base layer, followed by Sn|Cu|Zn layers. The ramping rate should then be as high as possible, to bypass the temperatures at which Cu segregation occurs.
2. The decomposition of Cu–Sn and Cu–Zn phases is an intrinsic part of the reaction sequence. Thus there is perhaps no benefit in preparing a mixed precursor or attempting to alloy a stacked precursor, as was done in this investigation. This was later corroborated by opto-electronic studies of films produced from alloyed and non-alloyed precursors—there were no significant differences between them (see Chap. 5).

An important result of this study was further evidence that the formation of CZTS is very rapid, occurring within about 3 min above 500 °C. Therefore the long sulfurisation times found in the literature require some explanation.

References

1. McKinley JD, Vance JE (1954) The vapor pressure of zinc between 150 and 350 °C. J Chem Phys 22(6):1120–1124
2. Copper Development Association (CDA) (1963) Equilibrium diagrams of copper alloys, 3rd edn. London
3. Bae IT (2008) Alloy formation at electrodeposited zinc–copper electrode interfaces at room temperature. J Electrochem Soc 155(5):D395–D399
4. Date M et al (2004) Interfacial reactions and impact reliability of Sn–Zn solder joints on Cu or electroless Au/Ni(P) bond-pads. J Mater Res 19(10):2887–2896
5. Carlos IA, de Almeida MRH (2004) Study of the influence of the polyalcohol sorbitol on the electrodeposition of copper–zinc films from a non-cyanide bath. J Electroanal Chem 562(2):153–159
6. Dominguez-Rios C et al (2008) Effect of tartrate salt concentration on the morphological characteristics and composition of Cu–Zn electroless plating on zamak 5 zinc alloy. Surf Coat Technol 202(19):4848–4854
7. Juskenas R et al (2007) Electrochemical and XRD studies of Cu–Zn coatings electrodeposited in solution with D-mannitol. J Electroanal Chem 602(2):237–244
8. Dissemination of IT for the promotion of materials science (DoITPoMS) library (2010). http://www.msm.cam.ac.uk/doitpoms/miclib/phase_diagrams.php
9. Tu KN (1996) Cu/Sn interfacial reactions: thin-film case versus bulk case. Mater Chem Phys 46(2–3):217–223

10. Clevenger LA et al (1998) Interdiffusion and phase formation in Cu(Sn) alloy films. J Appl Phys 83(1):90–99
11. Carlos IA et al (2000) Effect of tartrate on the morphological characteristics of the copper-tin electrodeposits from a noncyanide acid bath. J Appl Electrochem 30(8):987–994
12. Kang SK, Purushothaman S (1998) Study of interfacial reactions between tin and copper by differential scanning calorimetry. J Electron Mater 27(11):1199–1204
13. Guaus E, Torrent-Burgues J (2003) Tin-zinc electrodeposition from sulphate–gluconate baths. J Electroanal Chem 549:25–36
14. von Appen J, Dronskowski R, Hack K (2004) A theoretical search for intermetallic compounds and solution phases in the binary system Sn/Zn. J Alloys Compd 379(1–2):110–116
15. Ashiru OA, Shirokoff J (1996) Electrodeposition and characterization of tin–zinc alloy coatings. Appl Surf Sci 103(2):159–169
16. Chou CY, Chen SW (2006) Phase equilibria of the Sn–Zn–Cu ternary system. Acta Mater 54(9):2393–2400
17. Hideaki A et al (2009) Preparation of Cu_2ZnSnS_4 thin films by sulfurization of co-electroplated Cu–n–Sn precursors. Physica Status Solidi (c) 6(5):1266–1268
18. Schurr R et al (2009) The crystallisation of Cu_2ZnSnS_4 thin film solar cell absorbers from co-electroplated Cu–Zn–Sn precursors. Thin Solid Films 517(7):2465–2468
19. Olekseyuk ID, Dudchak IV, Piskach LV (2004) Phase equilibria in the Cu_2S–ZnS–SnS_2 system. J Alloys Compd 368(1–2):135–143
20. Garg G, Bobev S, Ganguli AK (2001) Single crystal structure and electrical properties of $Cu_8Ni_4Sn_{12}S_{32}$. J Alloy Compd 327(1–2):113–115
21. Eisenberg M (1980) The sulfospinel-lithium battery system—initial study of 3 sulfospinels. J Electrochem Soc 127(11):2382–2383
22. Araki H et al (2008) Preparation of Cu_2ZnSnS_4 thin films by sulfurization of stacked metallic layers. Thin Solid Films 517(4):1457–1460
23. Scragg JJ, Dale PJ, Peter LM (2009) Synthesis and characterization of Cu_2ZnSnS_4 absorber layers by an electrodeposition-annealing route. Thin Solid Films 517(7):2481–2484
24. Weber A, Mainz R, Schock HW (2010) On the Sn loss from thin films of the material system Cu-Zn-Sn-S in high vacuum. J Appl Phys 107(1):013516
25. Weber A et al (2007) Formation of Cu_2ZnSnS_4 and Cu_2ZnSnS_4–$CuInS_2$ thin films investigated by in situ energy dispersive X-ray diffraction. Thin-Film Compd Semicond Photovolt 2007 1012:201–208
26. Weber A et al (2009) In situ XRD on formation reactions of Cu_2ZnSnS_4 thin films. Physica Status Solidi (c) 6(5):1245–1248
27. Bonazzi P, Bindi L, Bernardini GP, Menchetti S (2003) (XRD): Cu_2ZnSnS_4. Can Mineral 41:639–647
28. Janosi A (1964) (XRD): Cu_2S. Acta Crystallogr A 17:311–312
29. Zhang J et al (2006) Cu_2ZnSnS_4 thin films prepared by sulfurization of ion beam sputtered precursor and their electrical and optical properties. Rare Metals 25:315–319
30. Tanaka T et al (2010) Influence of composition ratio on properties of Cu_2ZnSnS_4 thin films fabricated by co-evaporation. Thin Solid Films 518(21):S29–S33
31. Yoo H, Kim J (2010) Growth of Cu_2ZnSnS_4 thin films using sulfurization of stacked metallic films. Thin Solid Films 518(22):6567–6572
32. Rabadanov MK (1995) (XRD): ZnS. Kristallografiya 40:21–27
33. Jaulmes S, Rivet J, Laruelle P (1977) (XRD): Cu_4SnS_2. Acta Crystallogr Sect B–Struct Crystallogr Cryst Chem 33:540–542
34. Chen X, Wada H, Sato A, Mieno M (1998) J Solid State Chem 139:144–151
35. Chen X, Wada H, Sato A, Mieno M (1998) (XRD): Cu_2SnS_3. J Solid State Chem 139:144–151
36. Chen XA, Wada H, Sato A (1999) (XRD): Cu_4SnS_6. Mater Res Bull 34:239–247
37. Takeuchi Y, Kudoh Y, Sato G (1985) (XRD): CuS. Zeitschrift fuer Kristallographie 173:119–128

38. Donnay G, Donnay JDH, Kullerud G (1958) (XRD): $Cu_{1.8}S$. Am Mineral 43:228–242
39. Oftedal I (1926) (XRD): SnS_2. Norsk Geologisk Tidsskrift 9:225–233
40. Swanson HE, Tatge E (1953) (XRD): Cu. Nat Bur Stand (U.S.) Circ 539:1–95
41. Lee JA, Raynor GV (1954) (XRD): Sn. Proc Phys Soc Lond 67:737–747
42. Brown JR (1955) (XRD): Zn. J Inst Met 83:49–52
43. Gangulee A, Das GC, Bever MB (1973) (XRD) Cu_6Sn_5. Metall Trans 4:2063–2066
44. Lidin S, Larsson AK (1995) (XRD): Cu_5Sn_4. J Solid State Chem 118:313–322
45. Knoedler H (1966) (XRD): Cu_3Sn. Metall (Berlin) 20:823–829
46. Brandon JK et al (1974) (XRD): Cu_5Zn_8. Acta Crystallogr Sect B–Struct Crystallogr Cryst Chem 30:1412–1417
47. Massalski TB, King HW (1962) (XRD): $Cu_{0.8}Zn_{0.2}$. Acta Metallurgica 10:1171–1181
48. Ng SC, Brockhouse BN, Hallman ED (1967) (XRD): $Cu_{0.75}Zn_{0.25}$. Mater Res Bull 2:69–73
49. Altosaar M et al (2008) Cu_2Zn_1-xCdxSn(Se1-ySy)(4) solid solutions as absorber materials for solar cells. Physica Status Solidi a-Appl Mater Sci 205(1):167–170
50. Fernandes PA, Salome PMP, da Cunha AF (2009) Growth and raman scattering characterization of Cu_2ZnSnS_4 thin films. Thin Solid Films 517(7):2519–2523
51. Fernandes PA, Salomé PMPA, da Cunha F (2010) Cu_xSnS_{x+1} ($x = 2, 3$) thin films grown by sulfurization of metallic precursors deposited by dc magnetron sputtering. Physica Status Solidi (c) 7(3–4):901–904
52. Schorr S (2007) Structural aspects of adamantine like multinary chalcogenides. Thin Solid Films 515(15):5985–5991
53. Schorr S, Hoebler HJ, Tovar M (2007) A neutron diffraction study of the stannite-kesterite solid solution series. Eur J Mineral 19(1):65–73
54. Hall SR, Kissin SA, Stewart JM (1975) Stannite and kesterite–distinct minerals or components of a solid-solution. Acta Crystallogr Sect A 31:S67–S67
55. Chen SY et al (2009) Crystal and electronic band structure of Cu_2ZnSnX_4 (X = S and Se) photovoltaic absorbers: first-principles insights. Appl Phys Lett 94(4):041903
56. Persson C (2010) Electronic and optical properties of Cu_2ZnSnS_4 and $Cu_2ZnSnSe_4$. J Appl Phys 107(5):053710
57. Paier J et al (2009) Cu_2ZnSnS_4 as a potential photovoltaic material: a hybrid Hartree-Fock density functional theory study. Phys Rev B 79(11):1–8
58. Friedlmeier TM, Dittrich H, Schock HW (1998) Growth and characterization of Cu_2ZnSnS_4 and $Cu_2ZnSnSe_4$ thin films for photovoltaic applications in ternary and multinary compounds, vol 152. Taylor and Francis, London, pp 345–348
59. Bernardini GP et al (2000) EPR and SQUID magnetometry study of Cu_2FeSnS_4 (stannite) and Cu_2ZnSnS_4 (kesterite). Phys Chem Miner 27(7):453–461
60. Hergert F, Hock R (2007) Predicted formation reactions for the solid-state syntheses of the semiconductor materials Cu_2SnX_3 and Cu_2ZnSnX_4 (X = S, Se) starting from binary chalcogenides. Thin Solid Films 515(15):5953–5956
61. Araki H et al (2009) Preparation of Cu_2ZnSnS_4 thin films by sulfurizing electroplated precursors. Sol Energy Mater Sol Cells 93(6–7):996–999
62. Peng D-Y, Zhao J (2001) Representation of the vapour pressures of sulfur. J Chem Thermodyn 33(9):1121–1131
63. Pandey RK, Sahu SN, Chandra S (1996) Handbook of semiconductor electrodeposition. Marcel Dekker, Inc, New York
64. Smigelskas AD, Kirkendall EO (1947) Zinc diffusion in alpha brass. Trans AIME 171:130–142
65. Nakahara S, McCoy RJ (1980) Kirkendall void formation in thin-film diffusion couples. Appl Phys Lett 37(1):42–44
66. Zeng KJ et al (2005) Kirkendall void formation in eutectic SnPb solder joints on bare Cu and its effect on joint reliability. J Appl Phys 97(2):024508
67. Cabot A et al (2008) Sulfidation of cadmium at the nanoscale. ACS Nano 2(7):1452–1458
68. Sanchez S et al (1995) Copper diffusion in solid copper sulfide electrode. Electrochim Acta 41(7–8):1331–1339

69. Lukashev P et al (2007) Electronic and crystal structure of Cu_2–xS: full-potential electronic structure calculations. Phys Rev B 76(19):195202
70. Liu X, Mayer MT, Wang D (2010) Understanding ionic vacancy diffusion growth of cuprous sulfide nanowires. Angew Chem Int Ed 49:3165–3168
71. Sugiyama M et al (2008) Preparation of SnS films by sulfurization of Sn sheet. Jpn J Appl Phys 47(6):4494–4495
72. Gangulee A, Das GC, Bever MB (1973) X-ray-diffraction and calorimetric investigation of compound CU_6SN_5. Metall Trans 4(9):2063–2066
73. Hermann WA (ed) (1999) Synthetic methods of organometallic and inorganic chemistry, vol 5. Thieme, New York

Chapter 4
The Influences of Sulfurisation Variables and Precursor Composition on the Development of the CZTS Phase

We saw in the previous chapter how the CZTS phase forms from metallic precursors in the early stages of sulfurisation. Bearing in mind the model for phase formation developed in that chapter, we now turn our attention to the effects of changing the sulfurisation conditions and precursor composition, paying particular attention to: (1) phase formation, (2) the observed morphology and (3) the issue of element loss during sulfurisation.

Background

4.1 The Effects of Sulfurisation Conditions on Film Growth

4.1.1 Sulfurisation Conditions in the Literature

For efficient devices, the morphology of the absorber layer is of paramount importance. In general terms, the important features of a good absorber layer include large grains to achieve good carrier transport and reduce opportunities for carrier recombination, a relatively smooth surface, to avoid shorting from pinholes and good physical contact with the substrate, to achieve a good electronic contact. Secondary phases are to be avoided in most cases; however, the least desirable secondary phases are those with smaller band gaps than the absorber, as these could reduce the open circuit voltage of the device and enhance recombination, or worse, conductive phases, which could create shorting pathways through the absorber layer. The presence of secondary phases will in large part be due to the composition of the precursor. However, poorly chosen sulfurisation conditions can lead to secondary phases by (1) not allowing the formation reactions to go to completion, so that transient phases remain, and (2) promoting

J. J. Scragg, *Copper Zinc Tin Sulfide Thin Films for Photovoltaics*,
Springer Theses, DOI: 10.1007/978-3-642-22919-0_4,

Table 4.1 Development of sulfurisation parameters in the work of Katagiri

Year	Temp. (°C)	Time (h)	Heating rate (°C min^{-1})	Cooling rate (°C min^{-1})	Total duration (h)	Process gas	Best cell efficiency (%)
1997 [10]	500	1–3	20 (to 300 °C); 2–10 (to 500 °C)	Not given	4.6–7.9	N_2 + 5% H_2S at 10 sccm	0.66
2003 [6]	550	3	10 (to 200 °C); 2 (to 550 °C)	2 (to 300 °C)	10.3	N_2 + 5% H_2S at 10 sccm	5.45
2007 [1]	580	3	5	5 (to 200 °C)	7.6	N_2 + 20% H_2S at 10 sccm	5.74
2008 [7]	580	3	Not given	Not given	–	N_2 + 20% H_2S	6.77

When no cooling rate is given, cooling time is estimated as 3 h from top temperature, 2 h from 300 °C and 1.5 from 200 °C. The process gas, where mentioned, was N_2 + 5% H_2S flowing at 10 sccm

evaporation of certain components during heat treatment, resulting in changes in stoichiometry.

Until very recently, the best-performing CZTS devices—maximum cell efficiency 6.77%—had been produced by the group of Katagiri [1–10], and their work certainly represents the largest published body of literature pertaining to CZTS devices. Precursors are deposited using physical deposition methods (electron beam evaporation or RF (co-)sputtering) before being sulfurised in an atmosphere of N_2 containing H_2S. In as much as this is a two stage process (precursor formation-sulfurisation), the method is similar to that used in this work, and is therefore a useful resource in understanding the effects of sulfurisation conditions. Table 4.1 shows how the sulfurisation process used in the Katagiri group has evolved over time. These annealing conditions have been determined for a Cu-poor precursor, having a Cu/(Zn + Sn) ratio of around 0.85.

As can be seen from the table, the annealing times are rather long, and slow heating and cooling rates appear to be important to get high quality material. This would imply that there is some rather slow process involved in the generation of such material, the extent of which can be increased by allowing longer times and higher temperatures. The annealing temperature has been increased close to the limit imposed by the softening point of the glass substrates, and total annealing times of around 8 h are clearly unsuitable for an industrial process, in terms of both time and energy usage. This requirement for long annealing times is especially interesting in the light of the results from the previous chapter, and those published elsewhere [11], which suggest that the CZTS phase is very quick to emerge above around 500 °C. The performance-limiting process is therefore more likely to be a later stage of film modification, for example grain growth, impurity segregation or, potentially, cation rearrangement (the latter two will be discussed in Chap. 5). There are several cases in the CZTS literature where larger grains have been seen to result at higher sulfurisation temperatures [12, 13], but the effect is not dramatic, for example, changing the temperature from 450 to 550 °C in a 1 h heat treatment resulted in an approximate grain size increase of 30% [12]. To the best of our knowledge, no functioning devices have been produced from material sulfurised for less than one hour. It is clearly important to understand these effects in order to choose more economical sulfurisation strategies. It should be pointed out the rapid thermal processor used herein still allows long sulfurisation times, if required, but has the additional capability of providing fast heating and cooling.

In general, changing the sulfurisation conditions has not been seen to lead directly to secondary phase formation when the temperature is above around 500 °C, but there are significant issues with evaporation of certain components, the rate of which is primarily dependent on the background pressure during sulfurisation, as will now be discussed.

4.1.2 Zn-Loss During Sulfurisation

Zn-loss from CZTS films has been reported on several occasions [14, 15]. The vapour pressure of ZnS is low, but that of elemental Zn reaches 2×10^{-2} mbar by 350 °C and rises to about 12 mbar by 600 °C [16, 17]. Zn-loss has only been reported to occur during vacuum deposition methods using ZnS [15] or Zn [14] sources; it has not been seen to occur directly from CZTS films. The stacking order of the precursors in this investigation is fixed by the electrochemistry used for their production: Zn is at the surface, being the element with the most negative reduction potential. Therefore Zn-loss is anticipated to be a problem, which is one reason why pre-alloying of the precursor stacks was attempted.

4.1.3 SnS-Loss During Sulfurisation

There are many cases in the CZTS literature where Sn-loss has been reported, e.g. see [14, 15, 18–20]. The vapour pressure of liquid Sn is far too low to see direct evaporation of the element [21], but it is well known that the molecular Sn sulfides are volatile, with the decomposition series below leading to evaporation of SnS [22]:

$$2\mathrm{SnS_2(s)} \rightarrow \mathrm{Sn_2S_3(s)} + \tfrac{1}{2}\mathrm{S_2(g)} \rightarrow \underline{\mathrm{2SnS(g)}} + \tfrac{1}{2}\mathrm{S_2(g)} \qquad \text{(R 4.1)}$$

Weber et al. [18] studied the loss of SnS from CZTS films and multilayers of binary sulfides in detail using XRD and XRF with QCM measurements, and concluded that, aside from direct evaporation of SnS, there was also a decomposition pathway of CZTS[18]:

$$\mathrm{Cu_2ZnSnS_4(s)} \rightleftharpoons \mathrm{Cu_2S(s)} + \mathrm{ZnS(s)} + \underline{\mathrm{SnS(g)}} + \tfrac{1}{2}\mathrm{S_2(g)} \qquad \text{(R 4.2)}$$

and for the secondary Cu–Sn–S phases:

$$2Cu_2SnS_3(s) \rightleftharpoons Cu_4SnS_4(s) + \underline{SnS(g)} + \tfrac{1}{2}S_2(g) \qquad \text{(R 4.3)}$$

$$Cu_4SnS_4(s) \rightleftharpoons 2Cu_2S(s) + \underline{SnS(g)} + \tfrac{1}{2}S_2(g) \qquad \text{(R 4.4)}$$

The rate of loss decreased in the order $Cu_2SnS_3 > Cu_4SnS_4 > Cu_2ZnSnS_4$.

The possibility of the second quaternary phase $Cu_2ZnSn_3S_8$ was not discussed, but we can infer that, since all the phases above lost Sn in measurable quantities with the most Sn-rich compounds decomposing the fastest, there is a similar reaction for this phase:

$$Cu_2ZnSn_3S_8(s) \rightleftharpoons Cu_2ZnSnS_4(s) + \underline{2SnS(g)} + S_2(g) \qquad \text{(R 4.5)}$$

The evolution of three gas molecules would push this equilibrium to the right compared with the previous reactions.

The loss of SnS is clearly exacerbated by the use of low pressures and higher reaction temperatures (>550 °C). It was proposed that the use of a background pressure of an inert gas during heat treatment would limit the problem, and it can also be inferred from the above reaction that maintaining a constant supply of S vapour will help to keep the equilibrium position towards the left [18].

4.2 The Effects of Precursor Composition on Film Growth

4.2.1 The Effect of Cu-Content on the Growth of $CuInSe_2$ and $CuInS_2$ Films

In the case of $CuInSe_2$, the presence of even a small excess of Cu during film growth has significant effects on the properties of the absorber layer: large grains with a (112) orientation are seen, as opposed to fine grains with (220)/(204) orientation in the Cu-poor case. These differences are attributed to the presence of Cu–Se binary phases during film growth. During co-evaporation of a $CuInSe_2$ film, a liquid or quasi-liquid layer of CuSe coating the surface of growing $CuInSe_2$ grains was proposed to enhance their growth by solubilising and transporting incoming In and Se to the surface of the grain [23]. In two-stage processes, where a precursor is heat-treated to recrystallise the desired material, the presence of excess Cu enhances the recrystallisation process [24]. Upon cooling, $Cu_{2-x}Se$ is found segregated at the film surface and at grain boundaries [25]. The case is similar for sulfide systems as well [23]. The presence of $Cu_{2-x}Se$ or $Cu_{2-x}S$ phases is very detrimental to the performance of the absorber layer, since they are degenerate semiconductors, but they may be removed by chemical etching in aqueous cyanide. If the sulfurisation/selenisation conditions are well-chosen, then complete surface segregation of the phases may be achieved, in which case, after etching, highly efficient $CuInS_2$ can be produced using metallic CuIn precursors with a 60% excess of Cu, see for example [26]. An interesting point in this case is that the sulfurisation time required to produce high-quality material is very short, only around 3 min. This is in stark contrast to the sulfurisation procedures so far used for CZTS.

4.2.2 *Observed Effects of Cu-Content on the Growth of CZTS Films*

Although the chemistry of the Cu–Sn–Zn–S system should not be expected to be identical to the Cu–In–S system, the Cu-content of CZTS precursor layers also appears to have a rather dramatic influence on film characteristics. In terms of film morphology, a considerable increase in grain size has been observed in Cu-rich samples, i.e. those where Cu/(Zn + Sn) is greater than one [27–30]. In one example, the grain size observed after a 2 h sulfurisation was eight times larger for a Cu/(Zn + Sn) ratio of 1.28 compared with that for a ratio of 0.82 [27]. Clearly, such a large excess of Cu should result in secondary phases of Cu_2S, as predicted by Olekseyuk et al. [31], and indeed this was the case in all the examples just cited. Interestingly, Yoo and Kim saw Cu_2S grains at the surfaces of stoichiometric films as well as Cu-rich ones, using XRD and Raman spectroscopy [32].

Despite the attractive morphological characteristics of Cu-rich CZTS films, devices have been poor or non-functional when Cu-rich or stoichiometric absorber layers were used [13, 33], although in those cases it was not mentioned whether or not KCN etching was employed. With reference to the ternary phase diagram in Fig. 3.5, we can see that there is only a relatively narrow region where Cu_2S alone is present as a secondary phase. It may be the difficulty in avoiding Cu–Sn–S phases that has so far prevented this approach from working effectively.

Experimental

Precursor preparation, sulfurisation and characterisation were described in Sects. 3.7–3.10.

Grain size estimates were obtained from SEM images. Several images were taken in different locations on each sample, using a magnification where the grains were clearly visible. A series of lines were drawn over each image, and the number of intersections between the lines and grain boundaries were counted. The average grain diameter is equal to the average distance between intersections, if the line intersects a large number of grains.

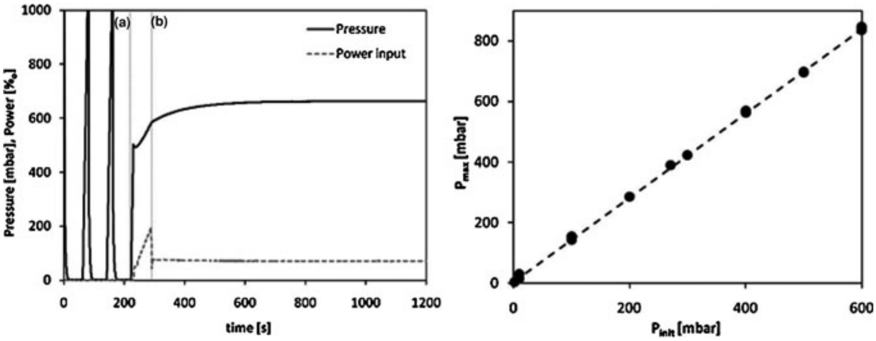

Fig. 4.1 *Left*: output power and pressure profiles during the various stages of the sulfurisation process. The *dashed vertical* lines show **a** the filling of the chamber to 500 mbar (which takes about 10 s), and **b** the end of the temperature ramp. *Right*: the maximum pressure reached during sulfurisation as a function of the initial pressure, at 560 °C

A Note on True Pressure During Sulfurisation

Since the RTP system is filled to the desired pressure prior to heating, the actual pressure during sulfurisation becomes higher than the pressure specified in the sulfurisation recipe. Changing the sulfurisation temperature also affects the actual pressure during the process. These effects must be quantified so that they can be accounted for in the following analysis. The left hand side of Fig. 4.1 shows how the pressure inside the RTP varies during the sulfurisation process. The two pressure spikes between 0 and 220 s correspond to repeated purging and refilling of the chamber in preparation for sulfurisation. At t = 220 s (point (a) in the figure) the chamber was filled to 500 mbar, and immediately afterwards the heating stage was initiated (as seen by the power spike).

During the temperature ramp, the pressure increases rapidly. After the ramp, (marked (b) in the figure), the pressure continues to rise slowly as the furnace equilibrates (as the cold walls adopt a new equilibrium temperature) which appears to take about 8 min. The evaporation of S will have negligible effect on the pressure in the reaction chamber, as it is present in relatively small quantities.

The equilibrium pressure during sulfurisation as a function of the initial pressure (or set pressure) is shown on the right of Fig. 4.1.

The ideal gas laws would predict a slope of 2.7 based on a temperature rise from 30 to 560 °C, and neglecting the change in the number of gas molecules as a consequence of the evaporation of 20 mg of S. A lower slope is observed, due to the fact that the temperature being measured is that of the susceptor in the centre of the furnace, while there is in fact a temperature gradient between the susceptor and the cold walls of the furnace. For the same reason, the change in pressure due to using different anneal temperatures in the range 520–580 °C was small, only around 5%.

In all discussions of sulfurisation pressure, the equilibrium/maximum pressure is quoted rather than the set pressure. The range of pressures available was determined by the specification of the RTP system. The base pressure was around 4×10^{-2} mbar at room temperature. The system is designed to operate at lower-than-atmospheric pressure: the pressure during sulfurisation was not allowed to rise above about 900 mbar because beyond that point the door seal tended to leak and samples became oxidised.

Results and Discussion

This discussion is separated into three main themes: the effects of pressure, time and precursor composition. Within each theme, we pay attention to the aspects described in the introduction, i.e. phase formation, morphological features and element losses. After the results for each variable have been shown, a general discussion on these three aspects will be undertaken.

4.3 Effects of Sulfurisation Pressure

Considerable differences in sample appearance and properties were observed when the background pressure during sulfurisation was varied. ‘Background pressure’ in this context is the partial pressure of nitrogen introduced to the reaction chamber (which is then sealed) prior to the start of the thermal cycle. As we will show, the background pressure has striking effects on post-sulfurisation composition, the rate of phase formation and grain size and orientation.

4.3.1 The Behaviour of Elemental S in the Sulfurisation Process

The background pressure is supplied by nitrogen, an inert gas. Since we do not expect the background atmosphere to have any direct role in the CZTS formation reactions, all the observed effects of background pressure must be due to its influence on other gas-phase processes, e.g. mass transport by diffusion or convection. The influence of background pressure on the propagation of S vapour throughout the reaction chamber will now be examined.

The reaction chamber in the RTP system is sealed prior to heating, i.e. the system has a constant volume. Solid S, typically 20 mg, is loaded into a graphite susceptor, which is covered with a lid. The lid simply rests on the base plate; it is not fixed in place by any other means. The internal volume of the susceptor is much

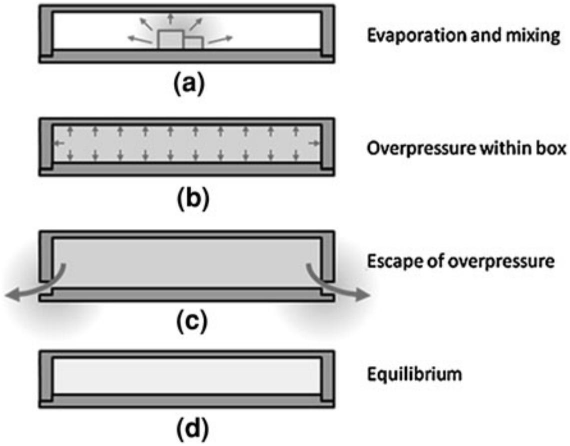

Fig. 4.2 Stages in the evaporation of the S source: **a** evaporation of solid S and mixing with the internal atmosphere of the susceptor, **b** build-up of pressure inside the susceptor, **c** release of a proportion of the internal atmosphere to equalise pressure, and **d** the equilibrium situation with a lower internal partial pressure of S2 (g)

smaller than the total chamber volume, 12 cm^3 compared to approx. 1,500 cm^3. The vapour pressure of S is very high at the temperatures used for CZTS growth, and this fact, coupled with the rapid rise in temperature, means that its evaporation will be essentially instantaneous. The partial pressure of $S_2(g)$ inside the susceptor if it were sealed would rise to around 1,800 mbar. The susceptor lid weighs 12.4 g, with a cross-sectional internal area equal to 40 cm^2, and therefore requires only an internal pressure 0.3 mbar above the background in order to lift it, at which point equilibration of the internal and external pressures would occur. In the equilibration process, a proportion of the internal atmosphere (including some $S_2(g)$ molecules) will exit the susceptor by convection, until the internal pressure has dropped to the point where the lid drops again and closes off the exit pathway. These stages are illustrated in Fig. 4.2. This entire process must occur very rapidly, so we can consider that it has finished by the time sulfurisation of the samples begins. Therefore the partial pressure of S vapour around the samples during sulfurisation is lower than might be expected based on the quantity of material loaded into the susceptor. After pressure equilibration, the driving force for $S_2(g)$ transport out of the susceptor is much lower. There are no longer any pressure gradients to drive convection; there is no temperature gradient within the susceptor (due to its high thermal conductivity), S_2 molecules can now only diffuse out of the susceptor—via four small exit holes with a combined area of 3 mm^2—down the concentration gradient that is maintained by the cold walls of the reaction chamber.

Crucially, the partial pressure of $S_2(g)$ within the susceptor after the equilibration process will depend on the density of the surrounding atmosphere: if there is already a high background pressure, the relative change in pressure upon vaporisation of 20 mg of S is small, and there is only a small flow of gas out of the susceptor. If there was a complete vacuum in the chamber, then, to achieve the same pressure everywhere, almost all the S would need to leave the susceptor and distribute itself throughout the chamber. We can construct a simple model for the partial pressure of S vapour within the susceptor after equilibration, as a function of the background pressure in the reaction chamber. The model is based on the following assumptions:

1. That vaporisation of S is rapid, and that $S_2(g)$ mixes completely with the inert gas inside the susceptor.
2. That there is then a release of gas from the interior of the susceptor to equalise the pressure inside and out.
3. That the remaining S inside the susceptor is gradually lost by diffusion alone, which occurs over a much longer timescale.

When the reaction chamber is filled with nitrogen and sealed, n_N moles of nitrogen are contained in the total volume V_T. Before evaporation of S, the number of moles of gas molecules, n_B, inside the susceptor of volume V_B is given by:

$$n_B = n_N \frac{V_B}{V_T} \tag{4.1}$$

The number of moles of gas molecules outside the susceptor, n_C, is given by:

$$n_C = n_N \frac{V_C}{V_T}, \tag{4.2}$$

where V_C is the volume of the reaction chamber. Note that we conserve the total volume and number of gas molecules:

$$V_C + V_B = V_T \tag{4.3}$$

$$n_C + n_B = n_T \tag{4.4}$$

After the S has completely vaporised, the concentration of gas molecules inside the susceptor has risen by an amount n_S:

$$n'_B = n_N \frac{V_B}{V_T} + n_S \tag{4.5}$$

The internal pressure is now greater than the external pressure. This causes a fraction F of the gas molecules inside the susceptor to move out, after which the pressures are equal. Then we have:

$$n_{B,eqm} = (1 - F)\left(n_N \frac{V_B}{V_T} + n_S\right), \tag{4.6}$$

and:

$$n_{C,eqm} = n_N \frac{V_C}{V_N} + F\left(n_N \frac{V_B}{V_T} + n_S\right) \tag{4.7}$$

Now writing the internal and external pressures after equilibration explicitly, and making them equal, we have

$$P_B = RT(1-F)\left(\frac{n_N}{V_T} + \frac{n_S}{V_B}\right) = P_C = RT\left(\frac{n_N}{V_T} + F\left(\frac{n_N V_B}{V_T V_C} + \frac{n_S}{V_C}\right)\right), \tag{4.8}$$

where R is the gas constant (8.314 JmolK^{-1}) and T the sulfurisation temperature.

Rearranging for F and making the following substitutions:

$$P_{S,B} = n_S \frac{RT}{V_B}, \tag{4.9}$$

the partial pressure of S inside the susceptor if all the S had remained inside it, and

$$P_N = n_N \frac{RT}{V_T}, \tag{4.10}$$

the background pressure of nitrogen, we obtain:

$$F = \frac{P_{S,B}}{\left(\frac{V_B}{V_C} + 1\right)\left(P_{S,B} + P_N\right)} \tag{4.11}$$

We can now calculate the partial pressure of S inside the susceptor after equilibration, $P_{S,eqm}$:

$$\frac{P_{S,eqm}}{P_{S,B}} = (1-F) = \frac{\left(\frac{V_B}{V_C} + 1\right)P_N + \frac{P_{S,B}V_B}{V_C}}{\left(\frac{V_B}{V_C} + 1\right)\left(P_N + P_{S,B}\right)} \tag{4.12}$$

This is the concentration of S molecules available for the sulfurisation reaction, and it is apparent that it depends on the background pressure. We can analyse several limiting cases of this equation. Firstly, for the case where $P_N \to 0$, the situation under high vacuum, the equation reduces to:

$$\left[\frac{P_{S,eqm}}{P_{S,B}}\right]_{\lim P_N \to 0} = \frac{V_B}{V_T}, \tag{4.13}$$

which confirms that, in the absence of any other gas species, the partial pressure of S within the susceptor after equilibration is simply determined by the relative volumes of the susceptor and the reaction chamber. This equation also shows that the partial pressure of S within the susceptor will tend to zero for a small susceptor within a very large chamber. Secondly, if we allow that we have a high background pressure compared to the pressure resulting in the susceptor after S evaporation (i.e. that $P_N > P_{S,B}$), we first obtain:

$$\left[\frac{P_{S,eqm}}{P_{S,B}}\right]_{P_N > P_{S,B}} = \frac{P_N}{P_N + P_{S,B}\left(\frac{V_C}{V_T}\right)}, \tag{4.14}$$

Fig. 4.3 The modelled variation of S partial pressure within the susceptor as a function of the background pressure of nitrogen, for a constant initial quantity of solid S added to the susceptor

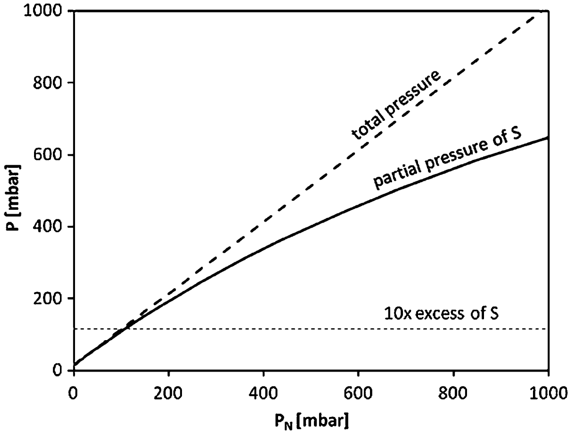

and finally when $P_N \gg P_{S,B}$:

$$\left[\frac{P_{S,eqm}}{P_{S,B}}\right]_{P_N > > P_{S,B}} = 1 \tag{4.15}$$

This shows that for a very high background pressure and a small amount of S, almost no S is transported out of the susceptor. Equation 4.1–4.12 is plotted in Fig. 4.3, using the measured properties of the RTP system, $V_T = 1{,}500\ \text{cm}^3$, $V_B = 12\ \text{cm}^3$ and for 20 mg of S. Also shown is the total pressure throughout the system after equilibration, P_T.

We can see that as the background pressure is decreased, less and less S vapour remains in the susceptor. We can also calculate the minimum quantity of S vapour required to sulfurise a typical sample. Based on the known passage of charge during electrodeposition along with the efficiency of each electrodeposition step, and assuming 2 S atoms for each Sn atom, 1 S atom for each Zn atom and 0.5 S atoms for each Cu atom, for a sample area of 1 cm^2 we require 2×10^{-6} mol of S_2(g) to just convert the sample. This is equivalent to a partial pressure inside the susceptor of about 10 mbar. The minimum partial pressure of S predicted by the model is 14.2 mbar in the limit $P_N \rightarrow 0$; however, by no means will the entire quantity of S contained in the susceptor react with the sample—there are still losses by diffusion—so we require an excess. The partial pressure of S_2(g) corresponding to a 10-fold excess is also indicated in Fig. 4.3. Where the actual partial pressure is below this, corresponding to a background pressure of around 100 mbar, incomplete conversion may be seen.

We now turn our attention to the effects of altering the background pressure, which are assumed to arise primarily from the change in partial pressure of S vapour.

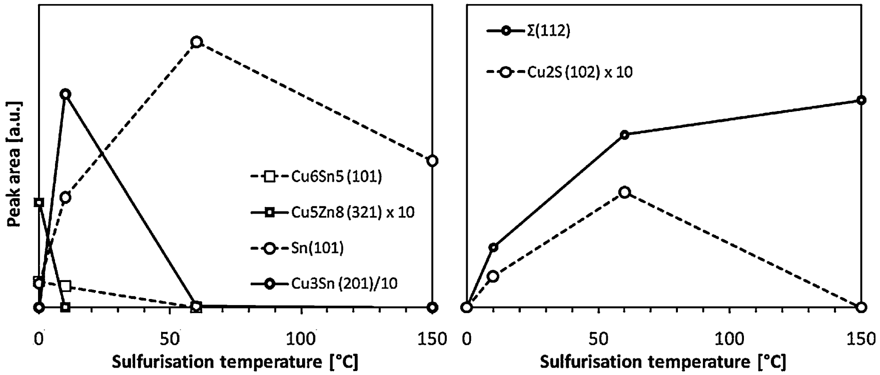

Fig. 4.4 XRD peak intensities as a function of sulfurisation time at 140 mbar. Other sulfurisation conditions: 500 °C, 20 mg S. Precursor composition approx. 2:1:1 Cu:Zn:Sn

4.3.2 *The Effect of Sulfurisation Pressure on the Rate of Sulfurisation*

An interesting effect of the background pressure is on the rate of emergence of sulfide phases. Figure 4.5 (repeated from Chap. 3) and Fig. 4.4 show the intensity of several key XRD peaks as a function of dwell time at 140 and 6 mbar respectively. The sequence of phase emergence was discussed in Sect. 3.13, and is summarised below for reference:

$$\mathrm{Cu_5Zn_8 + S \rightarrow Cu_2S + ZnS} \tag{R 4.6}$$

$$\mathrm{{}^1\!/_2S_2(g) + Cu_2S \rightarrow 2Cu_2S} + 2V_{\mathrm{Cu}} \tag{R 4.7}$$

$$\mathrm{Cu_6Sn_5} + 3V_{\mathrm{Cu}} \rightarrow \mathrm{Cu_3Sn + Sn(l);\ Cu_3Sn} + 3V_{\mathrm{Cu}} \rightarrow \mathrm{Sn(l)} \tag{R 4.8}$$

$$\mathrm{Cu_2S + Sn + 2S + ZnS \rightarrow Cu_2ZnSnS_4} \tag{R 4.9}$$

At 140 mbar, Fig. 4.4, the sulfide phases are already visible at the very start of the dwell period and the precursor phases (except Sn) are consumed within 60 s. By the end of the period covered here, the Σ(112) peak is still increasing and the Sn peak is dropping, showing that reactions (R 4.6)–(R 4.8) above have finished and reaction (R 4.9) is well under way.

When the same experiment is performed at 6 mbar, Fig. 4.5, the sulfide phases emerge more slowly—they are not seen until 10 s into the experiment—while the alloy precursor phases persist for much longer and in fact Cu_3Sn is still not fully consumed after 150 s. The Σ(112) peak also seems to stop growing after 60 s, and the Sn peak hardly decreases, which may actually indicate that the sulfurisation reaction has stopped before it is complete.

This dependence of phase emergence on pressure (and therefore on the concentration of S vapour) tells us that the rate-determining process involves S

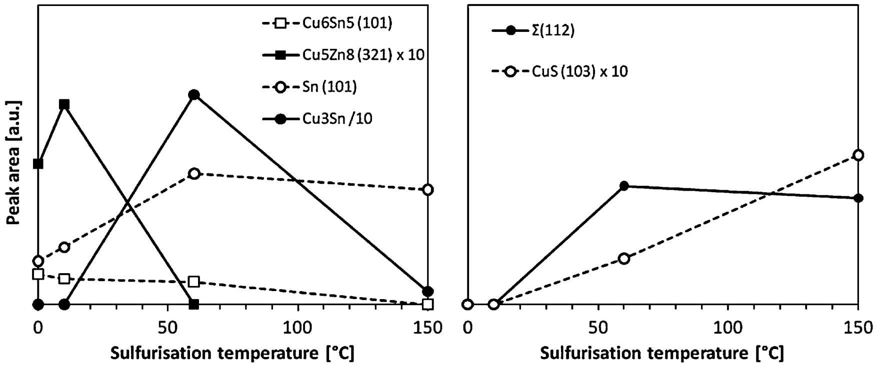

Fig. 4.5 XRD peak intensities as a function of sulfurisation time at 6 mbar. Other sulfurisation conditions: 500 °C, 20 mg S. Precursor composition approx. 2:1:1 Cu:Zn:Sn

vapour, which is consistent with the reaction sequences described above—the persistence of the Cu_5Zn_8 and Cu_3Sn phases indicates that reactions (R 4.6)—(R 4.8) have slowed. There is also evidence that the reaction has stopped early at 6 mbar, which would indicate that all the S vapour in the susceptor had either been consumed or had left the zone around the samples before the reaction could complete, consistent with the predictions of 1.3.1.

4.3.3 The Effect of Sulfurisation Pressure on Grain Size

Another feature that is dependent upon background pressure is the grain size, which is much larger at lower pressures and decreases rapidly as the pressure is increased. This can be seen in Figs. 4.6 and 4.7a, b shows the corresponding increase in XRD peak intensity at lower pressures, normalised to the Mo substrate peak. Larger grains give stronger signals since more of the film volume is occupied by ordered material, as opposed to disordered grain boundaries.

In Fig. 4.6a can also be seen the ‘scars’ left by etching of Cu–S phases. In the context of the model for grain growth proposed in the previous chapter, we suggest that the low partial pressure of $S_2(g)$ or loss of Zn prevented full conversion of the film to CZTS, leaving unconsumed Cu_2S grains which caused these holes after etching.

4.3.4 The Influence of Sulfurisation Pressure on Grain Orientation

The relative intensity of the diffraction peaks changed visibly between samples sulfurised with different background pressures. Figure 4.8 shows an expanded

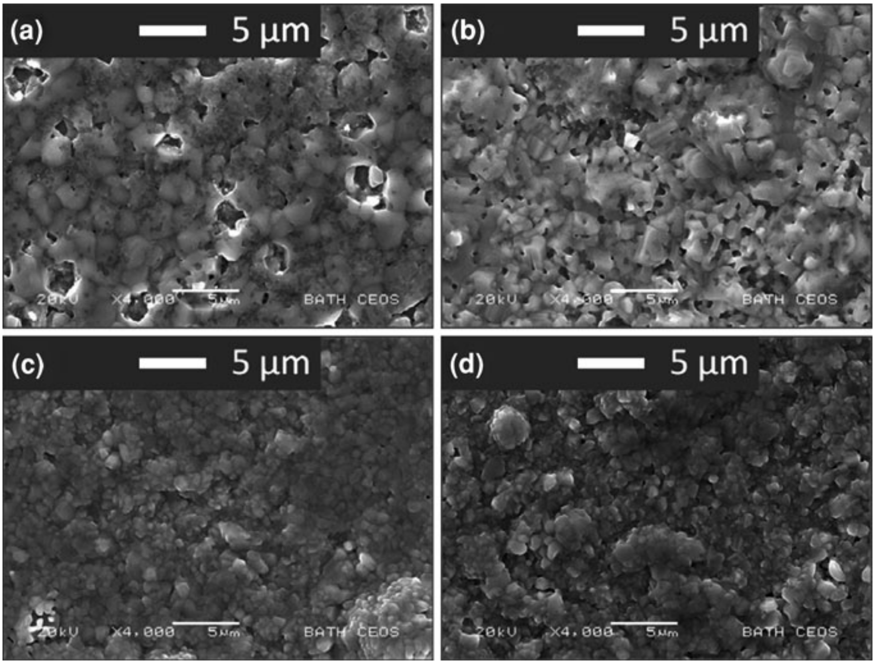

Fig. 4.6 Morphologies of CZTS films sulfurised at different background pressures of N_2: **a** 30 mbar, **b** 160 mbar, **c** 390 mbar, and **d** 570 mbar. Sample composition: Cu/(Zn + Sn) ~ 0.85, Zn/Sn ~ 1. Other sulfurisation conditions: 580 °C, 40 min, 20 mg S. Samples were etched for 2 min in 5wt% KCN

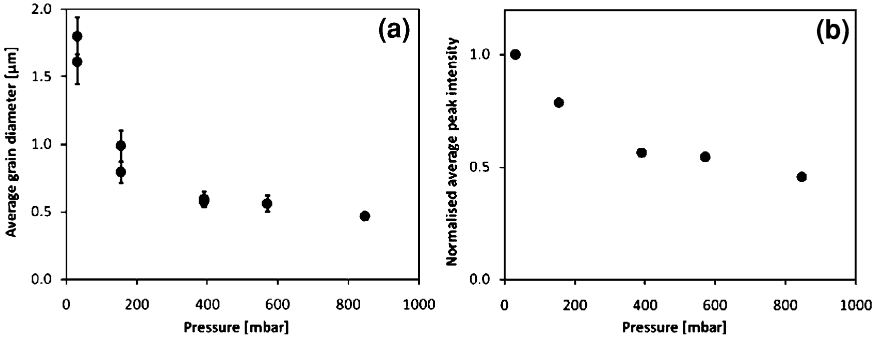

Fig. 4.7 **a** Average grain diameter for CZTS films as a function of background pressures of N2 during sulfurisation. **b** Overall intensity of diffraction peaks relative to the substrate signal (assumed constant). Sample composition: Cu/(Zn + Sn) ~ 0.85, Zn/Sn ~ 1. Other sulfurisation conditions: 580 °C, 40 min, 20 mg S

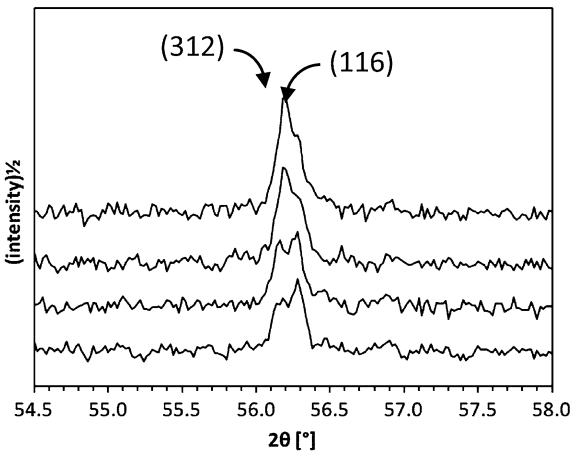

Fig. 4.8 Change in preferred orientation seen in the closely spaced (312) and (116) peaks. The (312), at 56.16°, decreases with pressure, while the (116), at 56.29°, grows

view of the closely spaced (312) and (116) peaks, where it can be seen that their intensities change in opposite senses.

Changes in relative peak intensities for a single phase polycrystalline sample indicate a degree of preferential orientation of the crystallites, which is also termed ‘texture’. Thin films often exhibit preferred orientations, due to the aspect ratio of the sample compared to the grain size. The texture coefficients, C_{hkl}, give the degree of enhancement of a particular set of *hkl* planes with respect to a reference sample (which is ideally randomly oriented) [34]:

$$C_{hkl} = \frac{\frac{I_{hkl}}{I_{r,hkl}}}{\frac{1}{n}\sum_{hkl}\left(\frac{I_{hkl}}{I_{r,hkl}}\right)}, \tag{4.16}$$

where I_{hkl} is the peak intensity of the *hkl* plane of interest, $I_{r,hkl}$ is the intensity of the same peak in the reference spectrum, and n is the number of *hkl* planes being considered. The overall degree of preferred orientation, σ, is given by:

$$\sigma = \sqrt{\frac{1}{n}\sum_{hkl}\left(C_{hkl} - 1\right)^2} \tag{4.17}$$

The possible values for σ range from zero, for a sample with the same (random) orientation of grains as the reference, up to $(n-1)^{1/2}$, for a sample which has all grains oriented in one direction. Application of this method to the series of samples sulfurised with different background pressures showed that there was a trend towards preferential orientation along the [112] direction at lower pressures. The results are shown in Fig. 4.9.

In the CZTS literature, orientation along the [112] direction is commonly reported; see for example [4, 19, 20, 35]. The change in the degree of orientation in this case was relatively small: σ would be zero for a randomly oriented sample and could reach a maximum of 2.8 for a sample with all grains oriented in the same

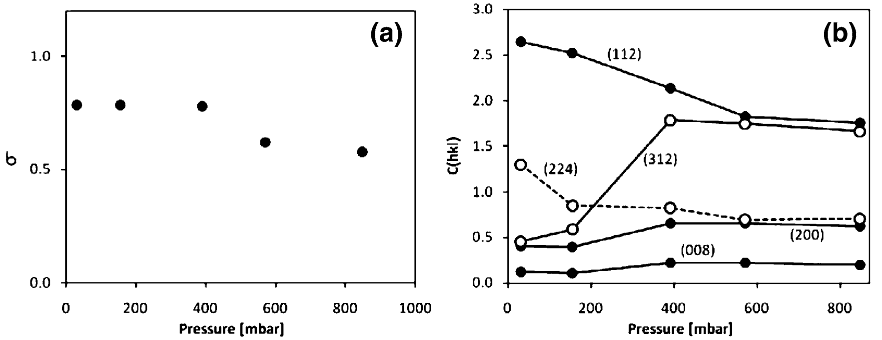

Fig. 4.9 **a** Overall degree of preferred orientation as a function of sulfurisation pressure, and **b** texture coefficients for selected diffracting planes showing the relative changes in ordering as a function of pressure

direction. The minimum and maximum values seen here were 0.5 and 0.7 respectively.

In principle the presence of ZnS could also cause the (112) peak to increase, distorting this analysis. However, if that were the case one would also expect the (200) peak to increase, but in fact it does the opposite. This shows that there is a real effect of pressure on grain orientation. The origin of this effect is not clear, but it could be related to the larger grain sizes observed at lower pressures (which also merits an explanation; this will be discussed later in the chapter). The thickness of the CZTS film was about 1 μm, and the grain size approached and then exceeded the film thickness below 400 mbar. Note that the grain size estimate was made on the basis of a 'plan view' of the film; the grains may not necessarily have the same depth. In fact, their depth is limited to the film thickness, which means that only the grains which are oriented with their growth directions in the plane of the film can continue to grow once their diameter reaches 1 μm.

4.3.5 The Effect of Sulfurisation Pressure on Composition

The Potential for Losses of Zn

As discussed in the background to this chapter, the evaporation of both elemental Zn and SnS has frequently been observed or suggested in the literature. The main factors influencing the rate of evaporation are the temperature of the sample and the pressure of the surrounding atmosphere.

Zn will evaporate in its elemental form, and Zn-loss is therefore expected to occur primarily from the precursor before it is fully converted to sulfide materials; once sulfurisation has finished, there are no volatile Zn-containing phases remaining. Figure 4.10 shows the potential for Zn-loss dramatically. It shows a

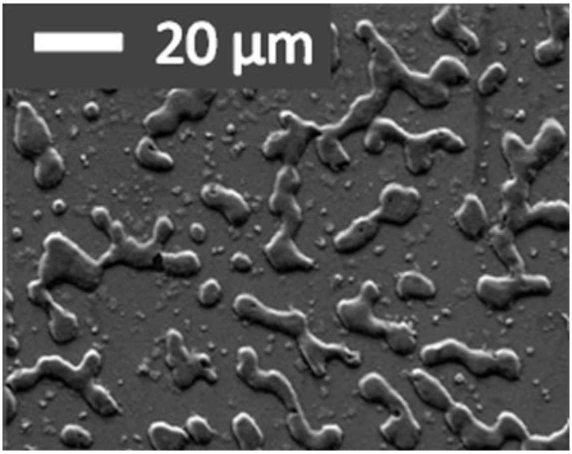

Fig. 4.10 De-wetting of Cu–Sn–Cu–Zn film from substrate after heating to 580 °C for 60 min at 710 mbar (a typical sulfurisation program), in the absence of S

Table 4.2 Composition of sample before and after heating to 580 °C for 60 min at 710 mbar (typical sulfurisation program), without S

	Cu at (%)	Sn at (%)	Zn at (%)
Before anneal (precursor)	45.1	27.8	27.1
After anneal	68.8	30.6	0.6

sample that was annealed using typical sulfurisation conditions, but without using S. The composition of the film before and after annealing is shown in Table 4.2. After the heating cycle, there has been almost total loss of Zn, accompanied by melting of the remaining material and de-wetting from the substrate. There is also some loss of Sn, but not to such an extent. XRD showed Cu_3Sn (with very high intensity, suggesting re-crystallisation from a molten phase) and Cu_6Sn_5. It should be noted that the background pressure was 710 mbar, compared to the vapour pressure of Zn at this temperature of approx. 10 mbar [16], but the anneal time was sufficient to allow complete evaporation.

The window of opportunity for Zn-loss will normally be normally very short in the rapid thermal process employed herein, but the fact that Zn forms the top layer of the precursor and that even the alloyed precursors show Zn-rich surfaces (see Sect. 3.11.4, Chap. 3) means that the potential for Zn loss is present. When using the precursor configuration Cu/Sn/Cu/Zn, rapid heating will clearly be beneficial in reducing Zn-loss.

Losses of Sn

Figure 4.11 shows the effect of background pressure upon the Zn/Sn ratio of some CZTS films as a function of sulfurisation time at 550 °C. The initial compositions of the precursors were identical, with Zn/Sn = 1.0. When working

Fig. 4.11 Effect of sulfurisation pressure on sample composition, determined by EDS

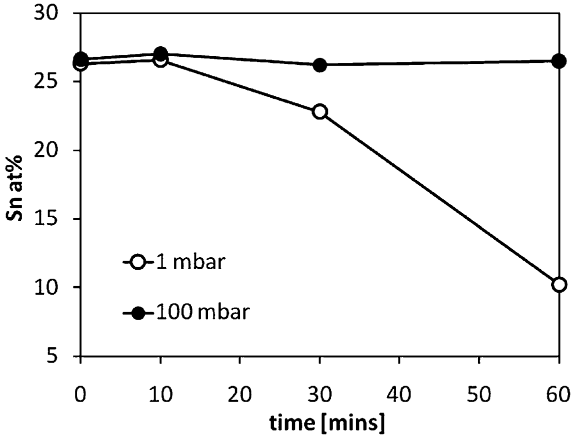

Fig. 4.12 Composition as a function of background pressure for samples sulfurised at 580 °C for 40 min. Composition before sulfurisation (indicated with *dotted line*): Zn/Sn = 0.98

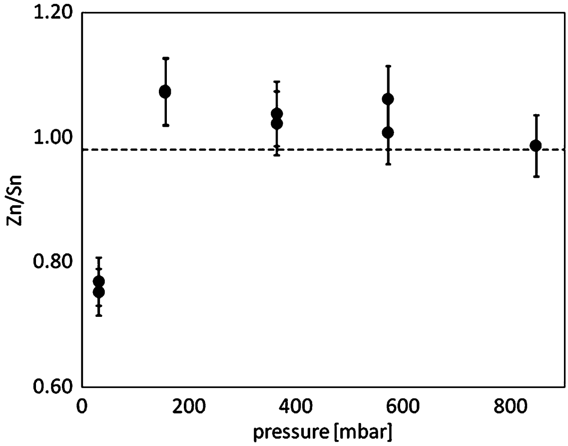

at lower pressures, there is a dramatic and accelerating loss of Sn beginning after about 10 min and after 60 min only about 30% of the initial quantity remains.

A series of identical samples were sulfurised at different pressures for a fixed time period, and their compositions are shown in Fig. 4.12. The effects of both Sn and Zn loss can be seen here. At the highest pressure, the Zn/Sn ratio is the same as that of the precursor. As the pressure is reduced, the Zn/Sn ratio initially increases due to evaporation of SnS, but at the lowest pressure, it drops sharply, which is attributed to evaporation of Zn in the initial stages of the thermal program. The Cu/(Zn + Sn) and S/M ratios did not change independently of Zn/Sn—i.e. the amount of S incorporated was constant and no Cu was lost, as would be expected.

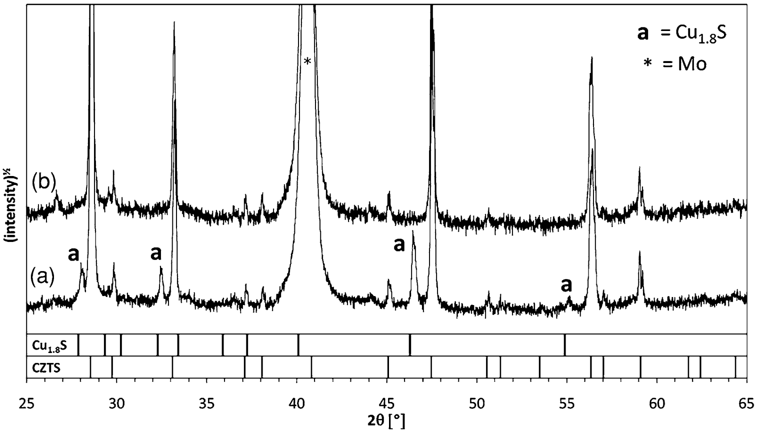

Fig. 4.13 XRD spectra of a Cu-rich film sulfurised for 60 s, before and after etching. Peaks marked 'a' closely match $Cu_{1.8}S$ (Note that the variability in composition of this phase mean the peak positions can vary)

4.4 The Effects of Sulfurisation Time

4.4.1 The Residence Time of S Vapour

It was seen in Chap. 3 that after five minutes at 500–550 °C, sulfurisation was complete and the CZTS phase had formed. However, given that in the literature much longer sulfurisation times are commonly used, we now turn our attention to changes occurring when the anneal duration is extended beyond this 5 min period. The first question is how long S vapour actually remains in the hot zone, and therefore at what stage we can consider the role of S vapour to be over. This can be investigated quite directly by looking at the prevalence of different Cu–S phases. $Cu_{2-x}S$ (chalcocite, digenite, anilite) is the higher temperature phase, and if it is cooled in the presence of S vapour, it will convert to CuS (covellite). Cu-rich films, as we have seen, retain Cu–S grains on their surfaces after sulfurisation. By looking at the particular phases present after cooling, we can tell whether S vapour was still around the samples at the time of cooling. Figure 4.13 shows the XRD spectrum of a CZTS film sulfurised for 60 s before cooling. Several peaks assignable to the low temperature phase CuS are visible, and as expected, they disappear upon KCN etching. Figure 4.14 shows an identical sample that was sulfurised for 5 min. This spectrum shows the high temperature phase $Cu_{1.8}S$ (again removed by etching).

These two figures tell us that the S vapour concentration had dropped within 5 min, to the point where the surface-dwelling $Cu_{1.8}S$ phases can no longer convert to CuS on cooling. However, we have already seen that the CZTS formation reactions are over within this time, so in principle S vapour is no longer needed anyway. In terms of longer annealing times therefore, the only roles that S vapour

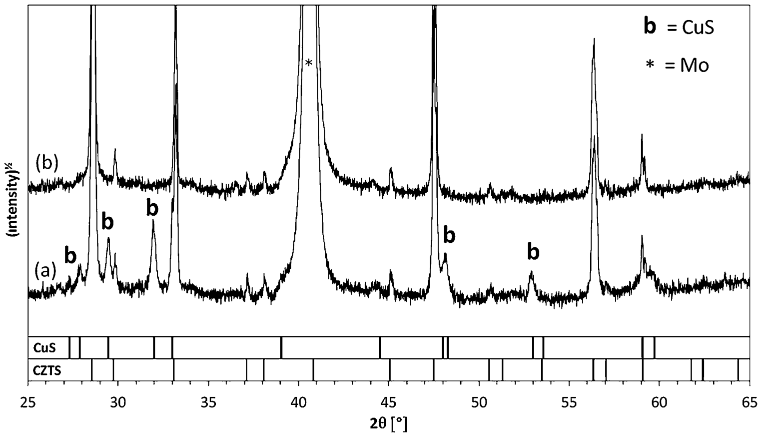

Fig. 4.14 XRD spectra of a Cu-rich film sulfurised for 5 min, before and after etching. Peaks marked ‘b’ match CuS

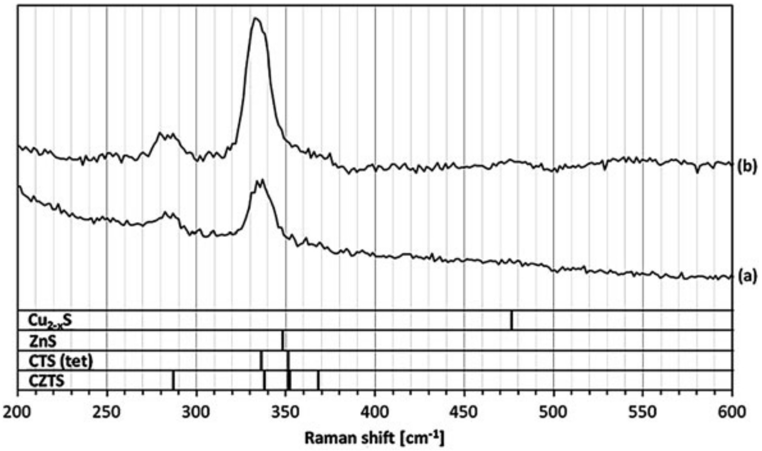

Fig. 4.15 Raman spectra for films sulfurised for **a** 5 min, and **b** 30 min. All peaks are assignable to CZTS and Cu_2S. Precursor composition approx. 2:1:1 Cu:Zn:Sn

could serve would be (a) to maintain sulfide phases in the case that some oxygen is present which attacks the film surface, or (b) to suppress any equilibria that lead to release of S vapour from the film, e.g. the loss of Sn as discussed above. We must also consider other changes that could occur in the film simply due to heating in the absence of S vapour.

The structure of the Raman spectrum does not change when the annealing time is extended from 5 to 30 min, although the peak intensity does increase, which may indicate an improvement in crystallinity (see Fig. 4.15). In agreement with the Raman data, the XRD spectra show no change in the phase composition. For

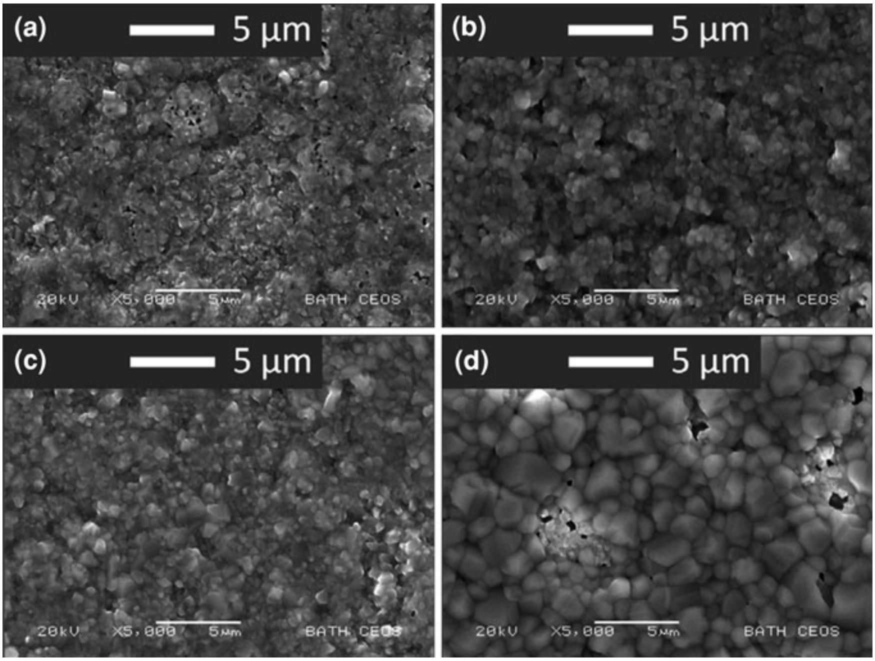

Fig. 4.16 Morphology at increasing sulfurisation times: **a** 15 min, **b** 35 min, **c** 62 min, and **d** 150 min. Sulfurisation conditions: 580 °C, 710 mbar N_2, 20 mg S. Composition: Cu/(Zn + Sn) ~ 0.85, Zn/Sn ~ 1

samples sulfurised at 600 °C at a pressure of 710 mbar for durations between 60 s and 3 h, there were no changes in peak intensity.

4.4.2 Grain Growth at Longer Anneal Times

One feature that changes visibly over a long time frame is the average grain diameter of the CZTS films. Some SEM images of films sulfurised for different times are shown in Fig. 4.16. The increase in grain diameter is a very slow process relative to the rate of sulfur incorporation and phase formation.

Figure 4.17 shows the average grain diameter as a function of sulfurisation time for a number of samples. There is a large spread to the data, making it difficult to fit a model for grain growth. The scatter may be due to compositional variations in the precursors leading to different growth rates, as well as variations in morphology over the surface of one sample. Several images were taken from each sample to help reduce this error.

From the plot, we are able to say that (a) immediately after crystallisation of the CZTS phase, the grain diameter is approx. 0.3 µm, (b) the initial rate of grain size

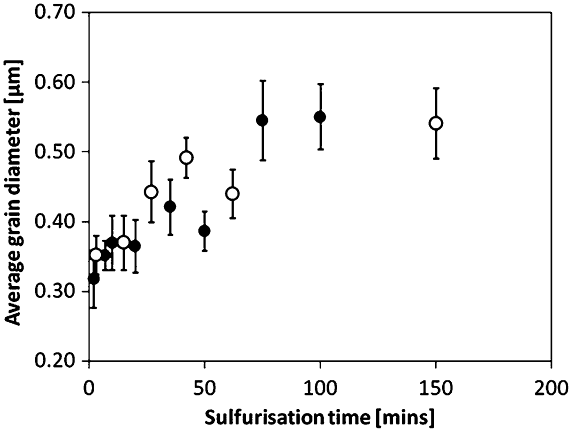

Fig. 4.17 Variation of average grain diameter as a function of sulfurisation time. Diameters were estimated by counting grain boundary intersections with a series of lines placed over the SEM images

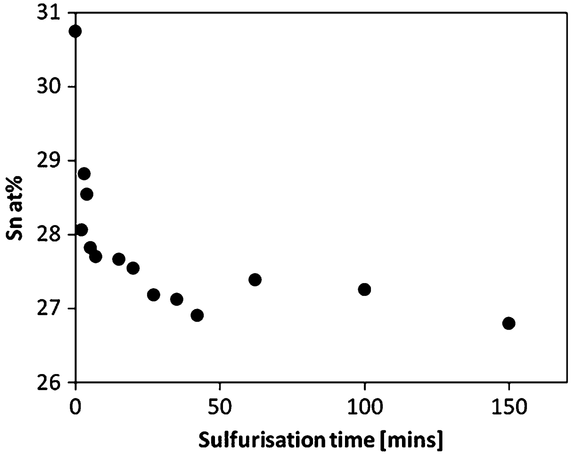

Fig. 4.18 Variation in Sn content as a function of sulfurisation time for a sample sulfurised at 560 °C at a background pressure of 750 mbar

increase is approx. 8×10^{-5} µm s^{-1} and (c) the maximum grain size observed under these conditions is about 0.55 µm.

4.4.3 Element Losses During Sulfurisation

Even when working at relatively high pressures, Sn-loss is seen to occur. The variation in Sn percentage as a function of sulfurisation time is shown in Fig. 4.18 for a sample sulfurised at 750 mbar. It initially drops rapidly but converges to a steady value rather than continuing to decrease as was seen at lower pressures (see Sect. 4.3.5). The sample in the figure was in the Cu-poor region of the ternary phase diagram. According to the diagram, the secondary phases present should be

ZnS and $Cu_2ZnSn_3S_8$. Unfortunately there is no XRD or Raman evidence for the particular Sn-containing phase that is lost.

4.5 The Effects of Changing Cu-Content

4.5.1 Experimental Approach for Compositional Measurements

To draw conclusions about sample properties based on precursor composition, we should ideally measure the composition of each sample before and after sulfurisation; however, this can be problematic because the sample could become contaminated during the measurement. To get around this issue, each electrodeposited precursor (approx. film dimensions 18 × 20 mm) was cut into quarters (about 9 × 10 mm), providing four nominally identical samples. One quarter was used to measure the precursor composition, and the other three were sulfurised. It was shown in Chap. 2 that the composition is relatively uniform over the central portion of the film, so this approach should give reliable data.

4.5.2 Precursor Compositions for the Study of Cu-Content

A series of precursors was designed having a variable Cu-content but a fixed ratio of Zn and Sn (Zn/Sn = 1.05), using the approach described in Chap. 2. The thickness of the final films was set to 1 μm in the calculation of deposition charges. The series of samples was intended to span the Cu-rich, stoichiometric and Cu-poor regions of the ternary phase diagram, while avoiding the Zn-poor or Sn-poor regions. After electrodeposition, the precursors were divided into quarters. One quarter of each sample was heated at 270 °C for three minutes to alloy the metal layers and homogenise the composition as a function of depth. The compositions of the precursors were measured using EDS, and are shown in Fig. 4.19. The Cu-content of the precursors mainly agreed with the intended values, except for the sample with the lowest Cu-content. There is a slight deviation from the line where Zn/Sn is constant, particularly at higher amounts of Cu, which may be due to changes in the deposition efficiency of Zn or Sn when the amount of charge deposited is decreased, or a failure of the precursor layers to mix completely upon heat treatment. The samples that were intended to fall into the Cu-rich region have instead entered the Sn-poor region, so we can expect ZnS as well as Cu_2S to form during sulfurisation. Despite these problems, the sample set does show a large variation in Cu-content whilst the Zn/Sn ratio stays almost constant, therefore proving suitable for studying the effects of changing Cu-content alone. Since the primary variable here is the amount of Cu, we may use the compositional ratio Cu/(Sn + Zn) as an axis against which to plot measured data.

Fig. 4.19 Compositions of precursors in the Cu-content series (*filled circles*), determined by EDS, and the values predicted from electrodeposited charges (*open circles*)

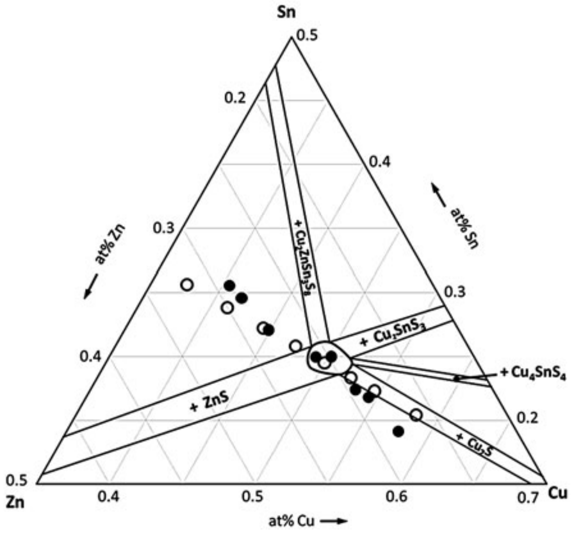

4.5.3 Compositions and Phase Structure of Sulfurised Samples

A further quarter of each sample was sulfurised for 30 min at 580 °C, with 20 mg of S and a background N_2 pressure of 700 mbar. The compositions of the sulfurised samples were measured, and the results are shown in Fig. 4.20. It is clear that there are compositional changes during sulfurisation when compared to the precursor compositions. The most Cu-rich samples have lost some Zn, moving into the Zn-poor side of the phase diagram. Based on the ternary phase diagram, we can expect the formation of Cu_2S for the most Cu-rich sample, Cu_4SnS_4 for the next most Cu-rich sample and Cu_2SnS_3 for the samples that were initially within the single-phase region. By contrast, the most Cu-poor sample appears to have lost Sn. We will return to the matter of element losses during sulfurisation shortly.

X-ray diffraction spectra for sulfurised films with different Cu/(Zn + Sn) ratios are shown in Fig. 4.21. The compositions of the samples on the ternary phase diagram are shown in Fig. 4.22.

Despite the large variation in Cu-content of these films, there is very little difference between the spectra. This would in fact be expected, since the possible secondary phases all have very similar peak positions to CZTS. All the peaks are assignable to CZTS or Mo with the exception of a small peak at about 39.2°, which is seen in the most Cu-rich sample and could correspond to Cu_2S—this is supported by the fact that upon etching this peak disappears, as shown on the left side of Fig. 4.23. Another slight difference is that the closely-spaced (312) and (116) peaks become better resolved at higher Cu-content, although the spacing remains constant (see Fig. 4.23, right hand side). There are no significant changes in peak intensity or orientation in this series.

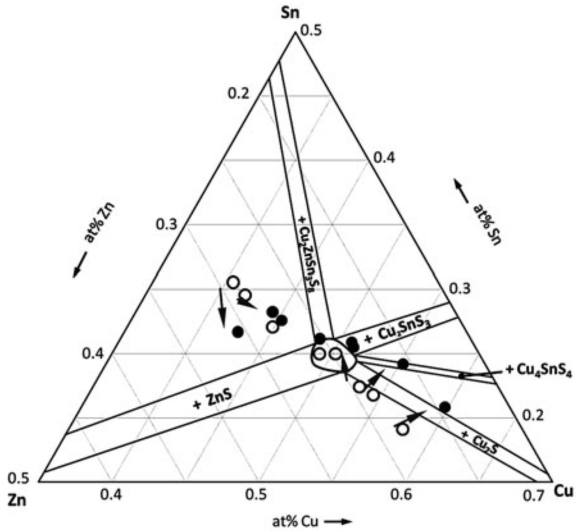

Fig. 4.20 Compositions of the samples after sulfurisation (*filled circles*), and the precursor compositions (*empty circles*), measured by EDS. Arrows indicate the related pairs of samples

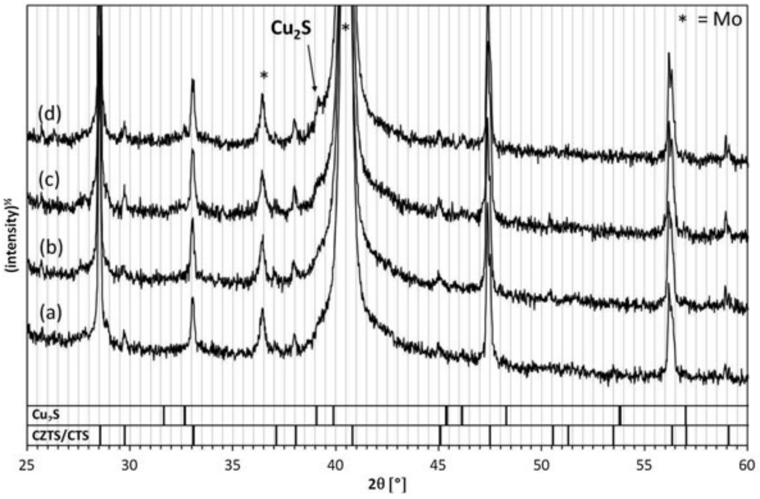

Fig. 4.21 X-ray diffractograms for selected samples in the Cu-content series. Cu/(Zn + Sn) ratios: **a** 0.75, **b** 0.83, **c** 1.04, and **d** 1.23

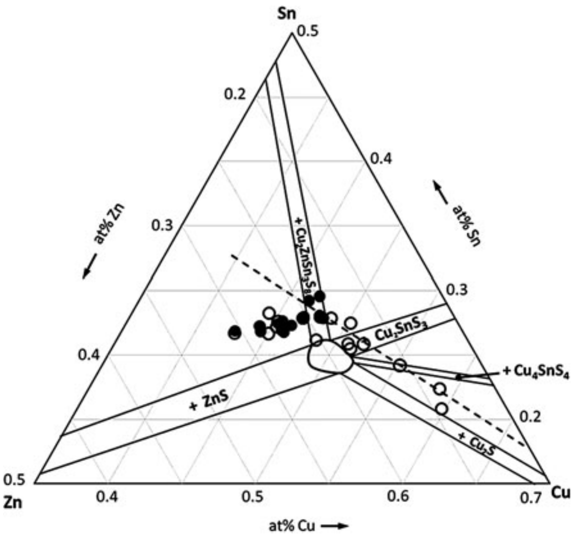

Fig. 4.22 Compositions of the samples used for X-ray diffraction in Fig. 4.21

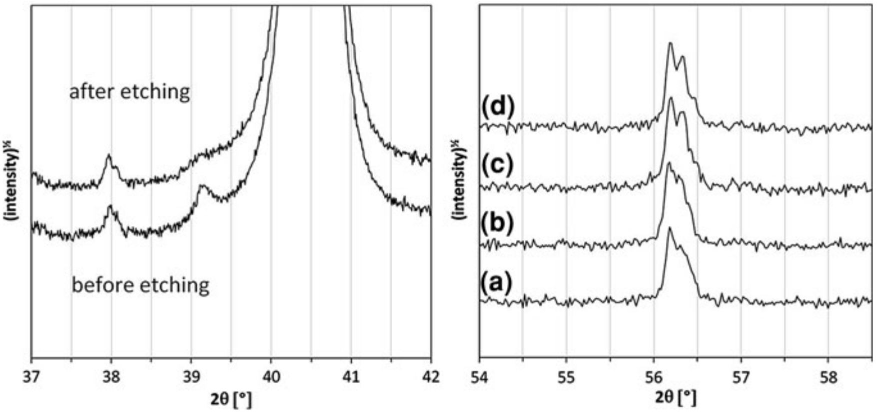

Fig. 4.23 *Left*: expansion of the peak at 39.2°, tentatively assigned to Cu_2S, showing its removal upon etching with aqueous KCN. *Right*: expansion of the peak at around 56° from Fig. 4.21, showing the increasing resolution of the (316)/(116) peaks at higher Cu-content. Cu/(Zn + Sn) ratios: **a** 0.75, **b** 0.83, **c** 1.04, and **d** 1.23

4.5.4 The Effects of KCN Etching on Samples with Variable Cu-Content

Sections of the samples sulfurised in the previous section were etched for two minutes in 5 wt% aqueous KCN. The compositions of the etched samples were then measured and are shown compared to the unetched compositions in Fig. 4.24.

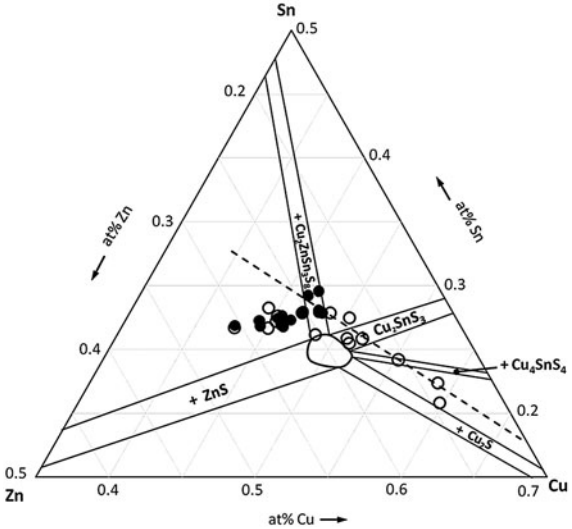

Fig. 4.24 Compositions of the samples after etching (*filled circles*) and after sulfurisation (*open circles*). The *dashed line* represents a coordinate of constant Zn/Sn ratio (0.85) upon which many of the samples lie prior to etching. The compositional changes are shown explicitly in Fig. 4.25, where this line is used as a composition axis

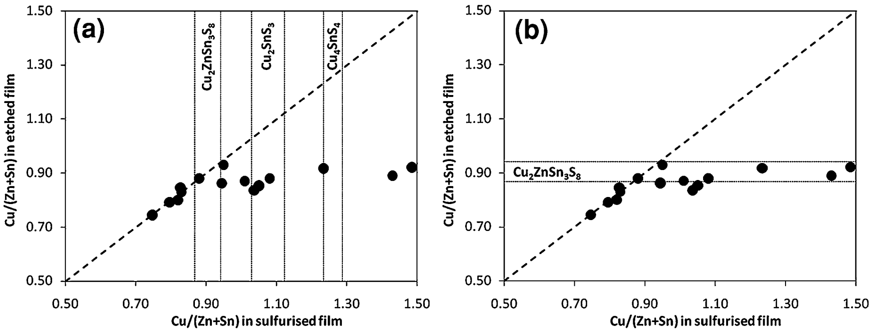

Fig. 4.25 Both figures: Cu/(Zn + Sn) ratios before and after etching. The *dashed line* indicates where there is no change in the ratio. The *dotted vertical lines* in **a** indicate the positions of the tie-lines in the ternary phase diagram, and refer to the x-axis (i.e. the composition before etching). The dotted horizontal lines in **b** indicate the positions of two tie-lines in the ternary phase diagram, and refer to the y-axis (the composition after etching)

There is a clear effect of etching, which is to reduce the Cu-content of the samples. This can be seen explicitly in Fig. 4.25a and b. It is apparent that there was no removal of Cu from the samples that were in the Cu-poor or Sn-rich zones on the ternary phase diagram—these lie on the diagonal dashed line in the figure. However, for the samples in the Cu-rich zones, the loss of Cu was significant, and

Fig. 4.26 Fraction of Sn content remaining after etching, for samples originally in the Sn-rich region lying on the *dashed line* in Fig. 4.24

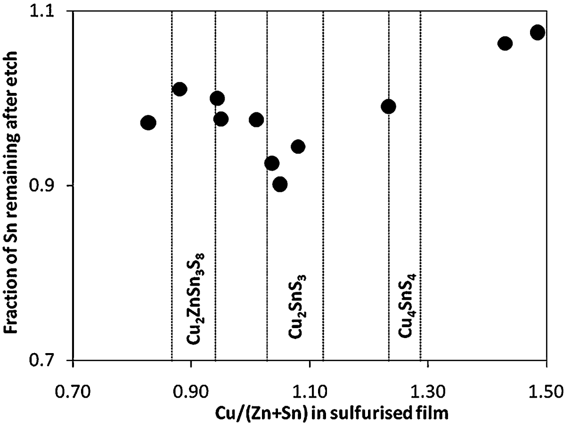

sufficient in all cases to bring the sample back into the Cu-poor or Sn-rich region of the phase diagram.

In every case, all Cu over and above that which was contained within the CZTS or $Cu_2ZnSn_3S_8$ phases was removed by etching. However, according to the phase diagram, Cu_2S itself was only present in the two most Cu-rich samples. The excess Cu in the other samples should have been incorporated in Cu_2SnS_3 and/or Cu_4SnS_4. The implication therefore is that the ternary Cu–Sn–S phases too are susceptible to etching by KCN.

The loss of Cu–Sn–S phases cannot be detected by XRD as was the case for Cu_2S (Fig. 4.23), but an analysis of the Sn-content provides some evidence. The fraction of Sn remaining after etching was calculated on the basis that the Zn-content did not change (i.e. that ZnS is not etched). The results are shown in Fig. 4.26. The figure suggests that Sn loss is greatest where the most Sn-rich secondary phase, Cu_2SnS_3, is formed. Further investigations are required to clarify this point; the Sn-excess is small since the samples are only just within the Sn-rich region at 400 °C, and changes in Sn-content are comparable to the errors in compositional analysis. The loss of Sn from CZTS films after etching was tentatively suggested in Ref. [19], although the authors assumed it was lost in the form of SnS_2.

SEM imaging shows the presence of large grains of a different material, presumably Cu–S or Cu–Sn–S phases, at the CZTS surface. The density of coverage by these grains increases as the Cu-content is increased, as seen in Fig. 4.27a, c and e. The grains are removed upon etching in KCN, leaving hollow ‘scars’, which shows that the grains were partially submersed in the film.

4.5.5 The Effect of Cu Content on Grain Size

One aspect that shows considerable variation as a function of Cu-content is the average grain diameter, which is displayed in Fig. 4.28. There is a fourfold

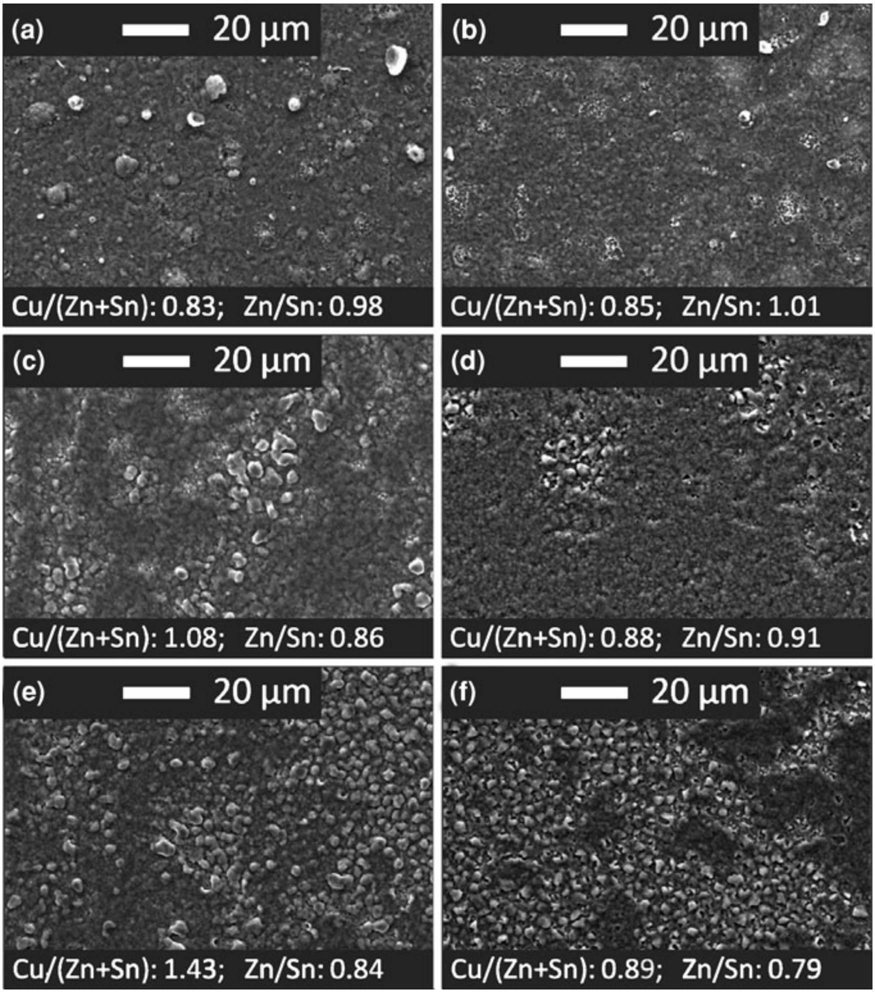

Fig. 4.27 SEM images of samples in the Cu-content series, before (**a**, **c**, **e**) and after (**b**, **d**, **f**) etching

increase in grain diameter as the Cu/(Zn + Sn) ratio is increased from 0.7 to 1.5. More specifically, the smallest grains were observed in samples which had compositions in the Cu-poor phase field, intermediate sizes were found for those that had Cu–Sn–S secondary phases, and the largest grains were found when Cu_2S itself was present (according to the phase diagram, and confirmed by XRD measurements). This increase in grain size can explain the improved resolution in the XRD spectra at higher Cu-content. These results are consistent with the effects of Cu content observed elsewhere in the CZTS literature [27–30], and suggest a possible analogy to the growth mechanism of $CuInSe_2$/$CuInS_2$ under Cu-rich conditions [23, 24].

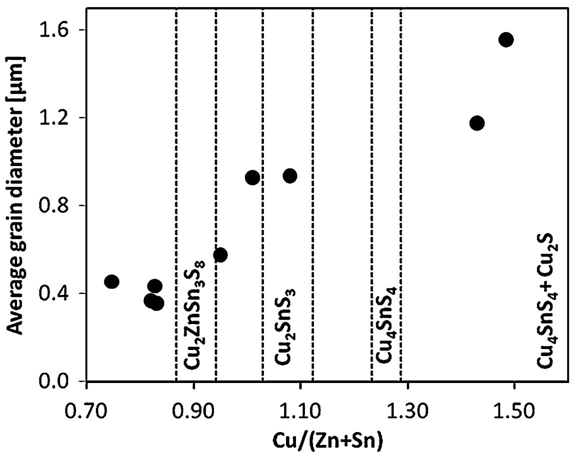

Fig. 4.28 Average grain diameter for the Cu-content series, estimated from counting the intersections of grain boundaries with a series of lines placed over the SEM images

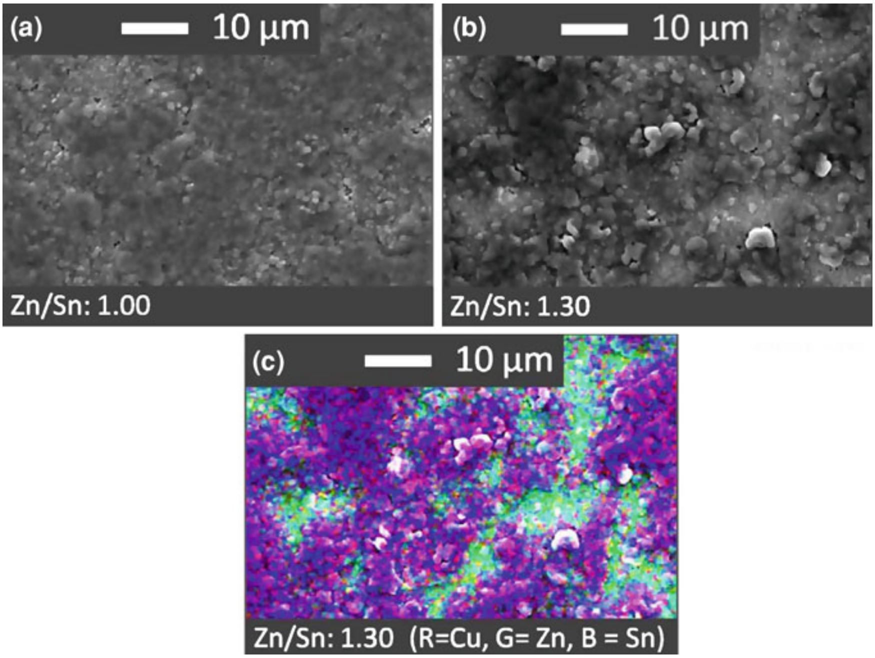

Fig. 4.29 **a**, **b** SEM images of two different areas of a single CZTS film showing different morphology and composition. The relationship between morphological and compositional uniformity is apparent. **c** EDS map (*colour*) of the region shown in b, where Cu is coloured *red*, Zn *green* and Sn *blue*

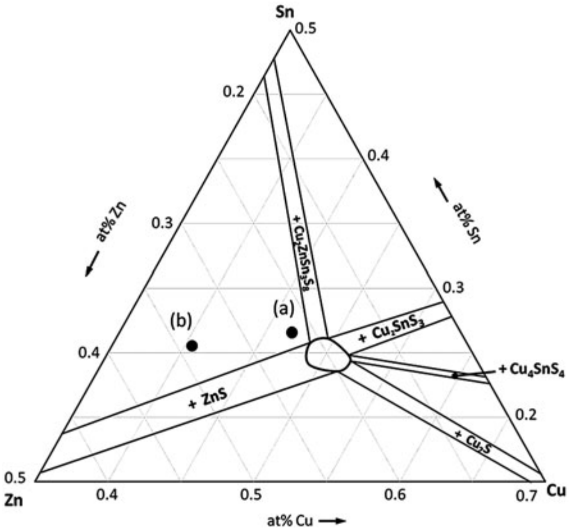

Fig. 4.30 Compositions of the sample areas shown in Fig. 4.29

4.6 Some Effects of the Zn/Sn Ratio

A dedicated study of the effect of changing the Zn or Sn content of the samples was not carried out in this work, but some morphological observations have been made which are relevant to this discussion. Despite efforts to produce highly uniform precursors, there is evidence of compositional variation on a microscopic scale in the sulfurised films. Figure 4.29a shows an image of a film sulfurised at 580 °C for 30 min. The film looks relatively uniform, and the composition of this area of the film, shown on the ternary phase diagram in Fig. 4.30, is close to the single-phase region for CZTS (at 400 °C). Figure 4.29b shows a different area of the same sample, and here there are clearly several different morphologies. This region of the sample, labelled (b) on the phase diagram, is much richer in Zn. Figure 4.29c shows an EDS map of the same region, coloured to represent the elements: Cu (red), Zn (green) and Sn (blue). The purple areas in the map contain all three elements (and S, which was uniformly distributed), and are therefore assigned to CZTS. The green areas of the image appear to contain only Zn (and S), and are assigned to ZnS. This image therefore provides a visualisation of two of the phases predicted by the ternary phase diagram, which cannot be resolved by X-ray diffraction. It is apparent that uniformity in morphology is related to uniformity in composition, and the composition can vary considerably on the microscopic scale. The observed phase separation may be due to small-scale compositional non-uniformities in the precursor, or may arise during alloying or phase formation.

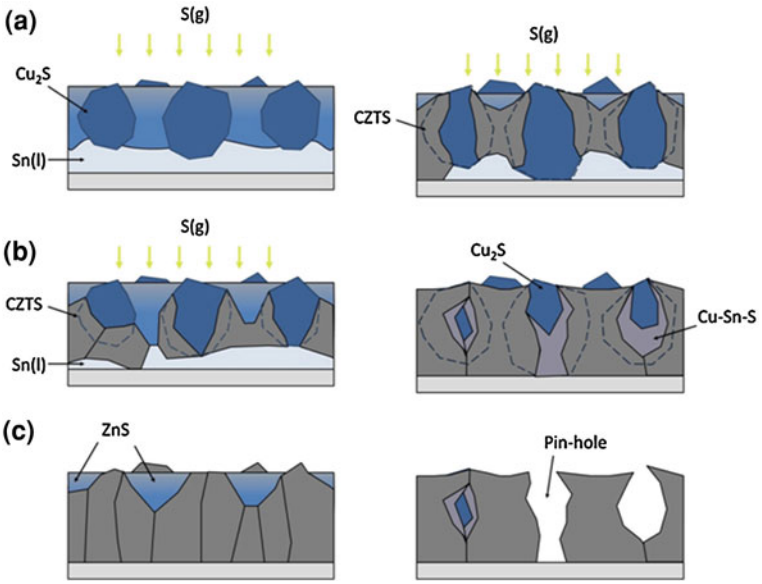

Fig. 4.31 Schematic illustrations of film formation in Zn-rich (*left-hand side*) and Zn-poor (*right-hand side*) films. See text for explanation

4.7 Modifications to the Growth Model for Deviations from Stoichiometry

Based on observations of the morphology of Zn-poor and Zn-rich films, and the expected secondary phases according to the ternary phase diagram, Fig. 4.31 shows some modifications to the film formation model described in Chap. 3 for non-stoichiometric compositions.

On the left-hand side is shown a Zn-rich sample. As previously, ZnS and Cu–S are formed at the top of the film, while Sn(l) is formed at the back of the film (a). The emergence of ternary and quaternary phases must occur where the three are in mutual contact (b). The growth of these phases continues until all Cu–S and Sn phases have been consumed, leaving the excess ZnS at the surface in ‘pools’, (c), as seen in the SEM images (e.g. Fig. 4.29). On the right-hand side of the figure is shown the Zn-poor scenario. The same growth pattern as before, (a), would now consume all the ZnS material, leaving behind partially consumed Cu–Sn–S grains buried in the film (b). If these grains are at the surface they will be removed upon etching, (c), leaving hollow ‘scars’, as seen for example in Fig. 4.27. Otherwise the Cu–Sn–S grains may remain buried within the film. Particularly large grains could extend through the depth of the film, creating pinholes after etching. Cu and Zn-rich surface layers have also been observed in CZTS films elsewhere [11, 18].

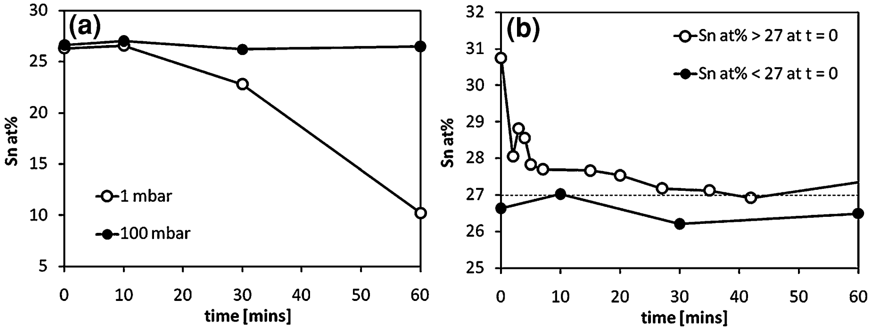

Fig. 4.32 Atomic percentage of Sn, determined by EDS, as a function of sulfurisation time, background pressure and initial Sn content. Sulfurisation temperature was 550–580 °C in each case, and Cu/(Zn + Sn) ratio approx. 0.85. **a** The time-resolved loss of Sn from a stoichiometric sample at 1 and 100 mbar. **b** The convergence of Sn-content from initially Sn-rich and Sn-poor precursors at 700 mbar—Sn loss occurs only from Sn-rich samples

4.8 Analysis of Element Losses During Sulfurisation

4.8.1 Initial Observations on Sn-Loss

A study of the vapour pressures of Sn–S phases by Piacente et al. [22] showed that the actual evaporating species responsible for the loss of Sn, $SnS(g)$, is in turn the decomposition product of the S-rich solid Sn-sulfides, which occurs via the loss of $S_2(g)$, as below :

$$2SnS_2(s) \rightarrow Sn_2S_3(s) + \tfrac{1}{2}S_2(g) \rightarrow \underline{2SnS(g)} + \tfrac{1}{2}S_2(g) \qquad \text{(R 4.10)}$$

This reaction suggests that if any of the Sn–S phases are formed, there is a pathway for the loss of Sn. The rate of loss will be accelerated at lower pressures and in the absence of $S_2(g)$ or other S sources, e.g. H_2S. In all cases investigated here, Sn-loss was seen to occur during sulfurisation, not only at particularly low pressures but also at pressures close to atmospheric. However, in each case the behaviour was different. We can distinguish two patterns of loss for different pressure regimes. At lower pressure (<100 mbar), the loss was initially slow, but its rate rapidly increased, and by the time the experiment concerned was ended, around 70% of the original Sn had been lost. When pressures above around 100 mbar were used, the loss was much more modest, and depended more upon the initial composition of the sample. In one particular example, when the atomic percentage of Sn was greater than around 27%, there was a rapid initial loss, but the rate of loss decayed until the Sn content reached a steady value. If the initial Sn percentage was less than 27%, then no loss was seen. Both trends are repeated in Fig. 4.32.

The explanation for these observations is relatively straightforward: in the first case, at lower pressures, a bulk decomposition process must be occurring in order for such large amounts of Sn to be lost. This implies the reaction scheme suggested by Weber et al.[18]:

$$Cu_2ZnSnS_4(s) \rightarrow Cu_2S(s) + ZnS(s) + \underline{SnS(g)} + \tfrac{1}{2}S_2(g) \qquad (R\ 4.11)$$

This reaction will clearly be accelerated by low pressures and the absence of $S_2(g)$. The accelerating rate of Sn loss shown in Fig. 4.32a makes sense since the film's surface area will increase as it decomposes.

In the second case, at higher pressures, we have a small, finite loss of Sn from Sn-rich samples, and no loss at all from Sn-poor samples. This can only be due to the evaporation of a secondary phase, present in small quantities, which proceeds to completion such that Sn-content reaches a steady value. Although there is no direct evidence for any Sn-containing secondary phase, the phase diagram indicates that $Cu_2ZnSn_3S_8$ should be formed in the Sn-rich region, and it may be this phase that is removed during sulfurisation at higher pressures, as for example:

$$Cu_2ZnSn_3S_8(s) \rightarrow Cu_2ZnSnS_4(s) + \underline{2SnS(g)} + S_2(g) \qquad (R\ 4.12)$$

or,

$$Cu_2ZnSn_3S_8(s) \rightarrow Cu_2ZnSnS_4(s) + 2SnS_2(s) \rightarrow\rightarrow \underline{2SnS(g)} + S_2(g) \quad (R\ 4.13)$$

It should be noted that during the growth of the CZTS phase under RTP conditions, Sn was initially buried underneath Cu_2S and ZnS layers, and did not react directly with S—there was clear evidence for this in Chap. 3. Therefore the only route available for loss of Sn is by decomposition of higher phases. It does not need to be pointed out that the decomposition of CZTS (R4.11) is highly undesirable; however, the evaporation of secondary phases (R4.12) possibly acts as a convenient composition-regulating mechanism. The extent of loss of secondary phases will be discussed in more detail below. The above data show that we can fairly easily avoid CZTS decomposition by using a background pressure of inert gas above around 100 mbar, but that the loss of certain secondary phases apparently occurs readily even close to atmospheric pressure.

4.8.2 The Effect of Element Loss on the Distribution of Sample Compositions

In this section, the compositional changes occurring in a series of 22 samples, which all experienced the same sulfurisation and etching conditions, are analysed in an attempt to uncover some underlying trends. The background pressure was kept at around 700 mbar to avoid decomposition of CZTS; however, as we have seen, Sn loss can still occur by decomposition of secondary phases. The pattern of

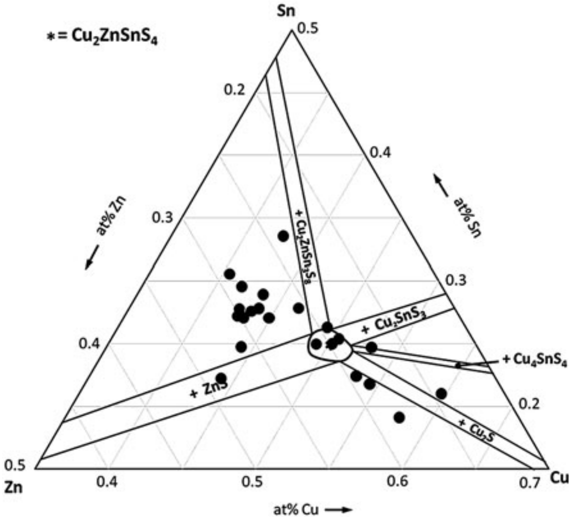

Fig. 4.33 Collected precursor compositions for 22 samples prepared over several different periods of this investigation, which were all then sulfurised using the same conditions

compositions that develops as a consequence of losses during sulfurisation is rather interesting.

The Distribution of Precursor Compositions

Figure 4.33 shows the precursor compositions for the set of samples under discussion, and it can be seen that there is a rather large spread over the phase diagram, with samples extending into most of the compositional zones defined. These samples were prepared at different stages in the investigation, for different purposes, and were later collated in this analysis because they all had the same sulfurisation conditions.

Compositions After Sulfurisation

Despite the wide spread of precursor compositions, the compositions after sulfurisation, as in Fig. 4.34, show the emergence of a clear pattern. Every sample that began in the Cu-poor region, shown by filled symbols, has moved onto the line indicated in the figure. The direction of movement—away from the Sn corner—indicates that this has occurred via a loss of Sn. The other samples, indicated by open symbols, have shifted away from the Zn corner of the diagram into the Zn-poor region. This must occur by a loss of Zn in the initial stages of heating (ZnS loss is not anticipated). In that case, the same loss of Zn must occur from all samples, since before sulfurisation they are all chemically equivalent, but for the samples in the Cu-poor region Sn-loss is more significant. Whether or not Sn-loss occurs apparently depends upon the nature of the secondary phase(s) present, as was hinted at in Fig. 4.32. Where the samples were Zn-poor, the secondary phases are Cu–Sn–S. These could decompose in a similar manner to CZTS, releasing

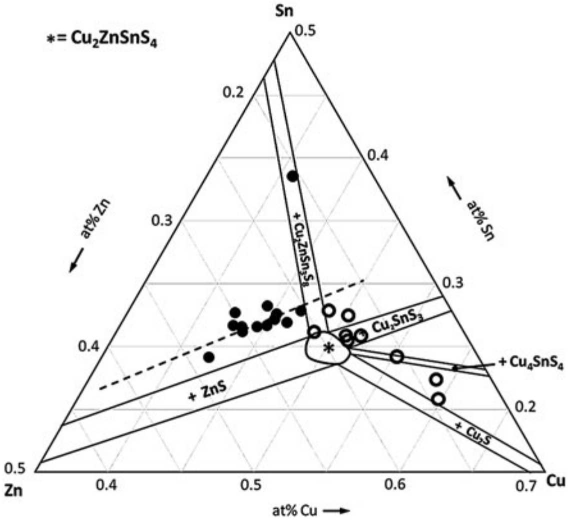

Fig. 4.34 Compositions of the samples after sulfurisation. Filled symbols: samples that had precursor compositions in the Cu-poor region. The remainder of sample are shown by the open symbols

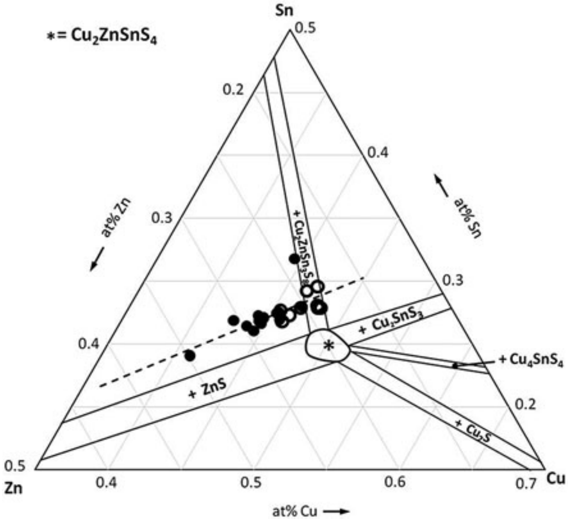

Fig. 4.35 Compositions of the samples after etching

SnS(g) [18], but, like the decomposition of CZTS, that does not seem to occur at the pressures used here. Only samples in the Cu-poor region lose Sn, and according to the phase diagram the secondary phase here is $Cu_2ZnSn_3S_8$. Therefore this phase must be rather unstable to thermal decomposition.

Compositions After Etching

After etching, the distribution is even narrower, with essentially all of the samples now lying on the same straight line (see Fig. 4.35). This tightly spaced distribution is remarkable considering the wide spread in precursor compositions—the combined processes of sulfurisation and etching with their associated losses of certain elements have left material with a rather well-defined range of compositions. We can rationalise the placement of the samples on the ternary phase diagram by noting that they are precisely aligned with the tie-line between the CZTS and ZnS phases. This phase diagram was derived for the situation at 400 °C. It is perfectly possible that at 580 °C the compositional regions have expanded, due to an increase in the entropic component of the free energy of mixing at higher temperature. This would mean that the positions of the samples are in fact defining the position of the tie-line at 580 °C.

The mechanism by which the samples transfer onto this line is explained by the proposed decomposition of $Cu_2ZnSn_3S_8$, as mentioned above (R 4.12). If this process continues until all of the $Cu_2ZnSn_3S_8$ phase has been consumed, which fits the decay pattern of Sn content as a function of time (Fig. 4.32), then the samples must by definition lie on the CZTS–ZnS tie-line, and will contain only those two phases. The data presented here provide some validation for the use of the ternary phase diagram given by Olekseyuk et al. [31] under the conditions of thin film growth.

There is one further point to make about these data which is that even the samples that were initially in the Zn-poor region—those that had Cu–Sn–S secondary phases—came onto the same line after etching, although some of these samples ended up in the Sn-rich region. In theory, if Cu–Sn–S phases were the only ones present aside from CZTS, the compositions should have hit the single-phase field based on loss of Cu and Sn during etching. This indicates that there was early separation of the film into a Cu-rich surface, which adopted the composition of the secondary phases, and an underlying Sn-rich layer. This is in agreement with the model for phase formation outlined in Sect. 3.13.

In this investigation it was not actually possible to prepare a Sn-rich CZTS sample: as was just seen, Sn loss during sulfurisation always proceeded until whichever phase bore the excess Sn had been removed. This is in contrast to films produced elsewhere in the literature—several examples of Sn-rich films can be found (which, incidentally, gave low device efficiencies [2, 33]). This fact can be attributed to the different sulfurisation method used. In both of those examples, the samples were sulfurised with a continuous supply of H_2S. Here, the residence time of S vapour was short, around 5 min, and after that time the samples were effectively being annealed in an inert atmosphere. The Sn-loss pathways described above should all be accelerated by the absence of S or H_2S. Sn-loss by decomposition of secondary phases will only be a useful tool for compositional adjustment if the S source is removed for continued sulfurisation, otherwise the secondary phases will remain. In general however, it is probably best to avoid formation of secondary Sn-containing phases in the first place by choosing an appropriate precursor composition.

Finally, we must note that there is no direct evidence for the phase $Cu_2ZnSn_3S_8$ in this investigation. However, there is also no evidence for SnS_2. This is due to the general difficulty in assigning small quantities of secondary phases in

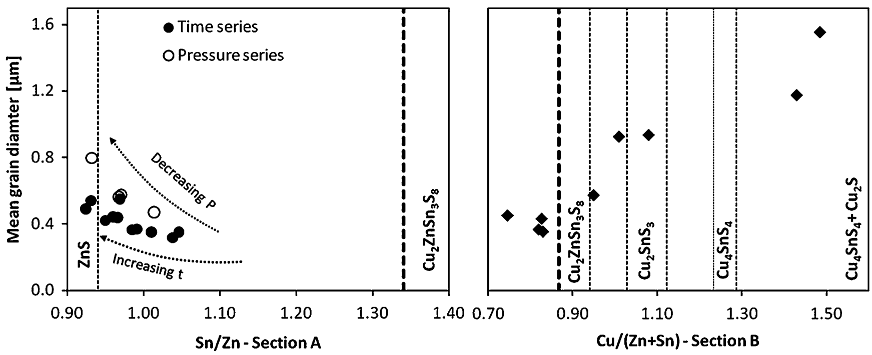

Fig. 4.36 Collected grain size data for samples in Sects. 1.4–1.6 of this Chapter, plotted along two sections of the ternary phase diagram that intersect at the CZTS-$Cu_2ZnSn_3S_8$ two-phase field. The compositions are those of the sulfurised, unetched samples—i.e. the compositions during growth

polycrystalline thin films (see Sect. 3.3). The fact remains, however, that Sn loss is clearly occurring, and in the above arguments the two phases are more or less interchangeable without affecting the outcome. If it is indeed the case that $Cu_2ZnSn_3S_8$ is present and is responsible for the loss of Sn, it is clearly a rather unstable phase with respect to decomposition into CZTS and SnS(g). The question then arises as to why it was present in the phase diagram at all. This is likely to be due to the differences in sample synthesis, with loss from the bulk samples synthesised in preparation of the phase diagram perhaps being kinetically limited as compared to loss from thin films.

4.9 Observations on Grain Size Trends

One aspect of film development that was very susceptible to the modification of sulfurisation conditions and sample composition was the average grain diameter of the CZTS phase. This was found to be larger at lower pressures, longer sulfurisation times and for higher Cu-content. While the large improvement in grain size in films with high Cu-content is consistent with the $CuInSe_2$ and CZTS literature, which suggests a fundamental change in growth mechanism, the increase in size with time was rather slow, and the increase at low pressures difficult to account for. The driving forces for grain growth are relatively weak, and include the relief of strain, the reduction of surface energy by decreasing grain boundary area, and temperature gradients (only the former two being relevant here). On this basis it is difficult to see why the background pressure should affect grain growth. However, we have just seen the role that sulfurisation pressure and time played in compositional modification, which perhaps provides additional insight. In Fig. 4.36 the average grain diameters are plotted as a function of composition along two

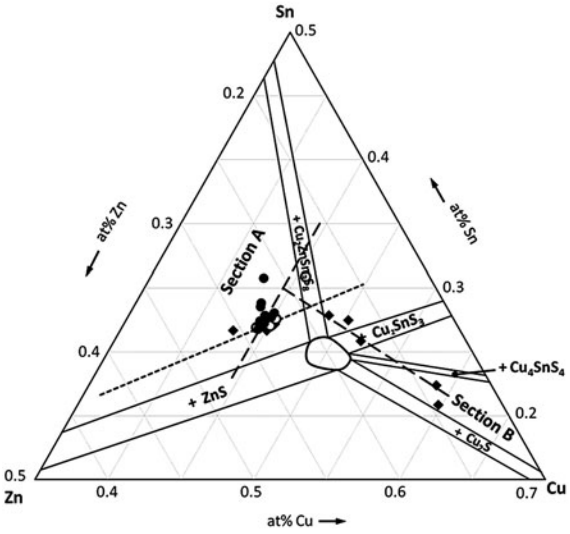

Fig. 4.37 Ternary phase diagram showing the lines of constant composition along which grain diameters are plotted in Fig. 4.36. Section A indicates a changing Sn-content in the Cu-poor region, section B indicates a changing Cu-content in the Zn-poor region. The short-dashed line indicates the location of the edge of the CZTS-ZnS two-phase field found in Sect. 4.8.2

sections of the ternary phase diagram, which are indicated in Fig. 4.37. The left-hand side of the diagram contains the samples investigated in the sulfurisation time and pressure series (Sects. 4.3 and 4.4), and the right-hand side shows those in the Cu-content series (Sect. 4.5). The vertical lines indicate the approximate positions of the tie lines in the phase diagram along these sections.

It is apparent from Fig. 4.36 that the smallest grains are seen for samples within the CZTS–ZnS–$Cu_2ZnSn_3S_8$ three-phase field. Towards the CZTS–ZnS two phase field, defined by the tie line derived in Sect. 4.8.2, the grain size increases. The pattern here is the same for both the pressure and time series of samples, which suggests that these variables are indirectly controlling grain growth through their effects on composition: at lower pressures and longer sulfurisation times, the compositions move towards the CZTS–ZnS tie line due to the decomposition of $Cu_2ZnSn_3S_8$.

There is a well-understood mechanism for the disruption of grain growth by secondary phase particles, known as Zener pinning. Growth of grains occurs by movement of grain boundaries. Small, dispersed solute particles greatly reduce the rate of grain boundary movement because the energy of a boundary can be lowered if it intersects solute particles. An additional driving force is then required to ‘un-pin’ the grain boundary such that it can continue to move and allow grain growth. Zener pinning is most significant for small, highly dispersed particles and the effect is worsened as their concentration increases. By this mechanism we can make a reasonable explanation of the observed grain size increase at lower pressures, which is otherwise hard to account for. Removal of the secondary phase by decomposition would reduce its effect on the rate of grain growth. According to the phase diagram, there is another secondary phase, ZnS, in all of the samples. The model for film growth in Sect. 4.6 of this Chapter proposed that ZnS as a secondary phase is mainly near the surface of the film, so it would have less effect on the bulk as regards grain growth. Sn was present as an underlayer, and so the $Cu_2ZnSn_3S_8$ phase would be initially concentrated at the back of the film. This means it must move completely through the film to reach the surface and decompose, which provides ample opportunity for it to disrupt grain growth in the bulk of the film.

Conclusions

The aim of this chapter was to understand how the conditions provided during sulfurisation (primarily pressure and time) affect the emergence of the CZTS phase. At the same time, the phase formation from non-stoichiometric precursors was of interest. These studies are important because the properties of the semiconducting film will be heavily dependent upon the processes occurring during sulfurisation. A key issue arising in the CZTS literature is the apparent requirement for long sulfurisation times (several hours) to achieve the best device performance. This is despite the fact that CZTS itself forms in only a few minutes, as has been shown here and elsewhere. Another question is why the best devices are usually made from Cu-poor material. The presence of excess Cu during film formation has been beneficial in fabrication of $CuInS_2$ films, and similar morphological effects have been seen for CZTS, however, no working devices have been made from Cu-rich CZTS films. Finally, losses of Sn and Zn by evaporation have frequently been reported in the literature.

The residence time of S in the hot zone of the RTP furnace was found to be of the order of several minutes, therefore any developments occurring at longer sulfurisation times are not due to the presence of S.

Losses of Zn were seen to occur, even at pressures close to atmospheric pressure, by evaporation of elemental Zn. This can only occur in the early moments of sulfurisation before reaction with S. Zn-loss was therefore finite and independent of sample composition. The loss of Zn was problematic, causing unwanted compositional changes. This is another reason to favour the proposed ‘best’ precursor stacking order of Araki et al. [36], Mo|Zn|Sn|Cu, because that configuration would presumably reduce Zn-loss. Unfortunately that stacking order is not achievable using the current electrodeposition method. In further work, Zn loss could be compensated for by providing a slight excess of Zn in the precursor.

Sn-loss occurred over longer time periods, attributed to the formation and evaporation of SnS by decomposition of higher phases. The loss of Sn from Sn-rich or Cu-poor samples was seen to occur even at pressures close to atmospheric, occurring until all of the Sn-containing secondary phase was consumed. This resulted in most samples in the investigation lying on a line in the phase diagram which was parallel to the CZTS–ZnS two-phase boundary at 400 °C, and therefore may define the same boundary at the temperatures of this study. Similar Sn-loss was not seen in literature examples when annealing with a constant supply of H_2S, and therefore the absence of S was thought to enhance the evaporation rate, in accordance with the equilibria associated with SnS evaporation.

Two roles of the background pressure of N_2 during sulfurisation were discussed:

1. The background pressure strongly influenced the partial pressure of S vapour in the sample container, as shown by a model, even though the amount of S initially introduced was constant in all cases. The observed effects of a lower partial pressure of S included a slower reaction rate, with incomplete conversion of the precursor phases. The RTP system used here should be modified so that the background pressure and S partial pressure can be varied independently.
2. The background pressure affected the rate of loss of Sn from samples during sulfurisation. Pressures lower than 10 mbar were seen to cause decomposition of the CZTS phase resulting in heavy losses of Sn, and large amounts of Zn were also lost. At the same time, smaller grains were seen in films produced at higher pressures, which was tentatively attributed to grain growth inhibition (Zener pinning) by secondary phases which would have evaporated at lower pressure.

In this study, the evaporation of Sn-containing secondary phases was seen to occur over a timescale of approx. 30 min at 560 °C and a background pressure of 700 mbar. Due to the positioning of sample compositions in the ternary phase diagram (most were Cu-poor), changes in the films as a function of sulfurisation time seemed to be primarily associated with the gradual evaporation of secondary phases, rather than any fundamental developments within the CZTS phase. The sulfurisation time had a relatively weak effect on the grain size of the CZTS films.

The Cu-content of the samples had dramatic effects on the grain size of the films. In $CuInS_2$ the same effects are seen, and are attributed to the role of Cu–S phases during growth. The preparation of pure Cu-rich films (with only Cu–S secondary phases) was attempted, but initial losses of Zn during sulfurisation caused the compositions to move into the Zn-poor region, where Cu–Sn–S phases should form alongside Cu–S. These films had a larger grain size but the morphology was affected severely because the secondary phase grains were embedded in the film, and left ‘scars’ and pinholes after etching. It appears that not only Cu–S but also Cu–Sn–S phases are removed by KCN etching: this should be investigated further.

The difficulty of assigning secondary phases in the Cu–Sn–Zn–S system has been discussed. The phase diagram was relied upon to predict the likely phase structure, and in large part the observations of other film characteristics fitted the expected presence of secondary phases. However, many further studies are required to establish the presence of certain phases in CZTS thin films, particularly $Cu_2ZnSn_3S_8$, about which little is currently known.

Based on the studies in this chapter, we can make some recommendations for future work:

1. The use of an inert atmosphere during sulfurisation is required to avoid decomposition of CZTS, especially if the partial pressure of S is low.
2. Excess Sn can be removed by annealing in the absence of S or H_2S, therefore the commonly employed method of annealing for several hours in H_2S may prevent the loss of secondary phases which could affect device performance, explaining the poor performance of Sn-rich devices.
3. To achieve larger grains, compositions in the Cu-poor or Sn-rich regions of the phase diagram should be avoided.
4. Investigation is required of the effect of Cu-excess on grain growth in samples that are in the pure Cu-rich or Sn-poor regions of the phase diagram—i.e. those that do not contain Cu–Sn–S secondary phases.
5. Investigation of element losses from samples in different regions of the phase diagram should be carried out.

References

1. Jimbo K et al (2007) Cu_2ZnSnS_4-type thin film solar cells using abundant materials. Thin Solid Films 515(15):5997–5999
2. Katagiri H (2005) Cu_2ZnSnS_4 thin film solar cells. Thin Solid Films 480–481:426–432
3. Katagiri H, Ishigaki N and Ishida (1998) Characterisation of $Cu_2ZnSnSe_4$ thin films prepared by vapor phase sulfurization in 2nd World Conference PVSEC, Vienna, 1998
4. Katagiri H et al (2001) Characterization of Cu_2ZnSnS_4 thin films prepared by vapor phase sulfurization. Jpn J of Appl Phys, Part 1-Regul Pap Short Notes Rev Pap 40(2A):500–504
5. Katagiri H et al (2009) Development of CZTS-based thin film solar cells. Thin Solid Films 517(7):2455–2460
6. Katagiri H et al (2003) Solar cell without environmental pollution by using CZTS thin film. Proceedings of 3rd World Conference on Photovoltaic energy conversion, 2003, Vols a–c, pp 2874–2879
7. Katagiri H et al (2008) Enhanced conversion efficiencies of Cu_2ZnSnS_4-based thin film solar cells by using preferential etching technique. Appl Phys Express 1(4):041201
8. Katagiri H et al (1997) Rare-metal free thin film solar cell. Proceedings of the Power Conversion Conference, Nagaoka 1997, Vols I and Ii, pp 1003–1006
9. Katagiri H et al (2001) Development of thin film solar cell based on Cu_2ZnSnS_4 thin films. Sol Energy Mater Sol Cells 65(1–4):141–148
10. Katagiri H et al (1997) Preparation and evaluation of Cu_2ZnSnS_4 thin films by sulfurization of E–B evaporated precursors. Sol Energy Mater Sol Cells 49(1–4):407–414
11. Weber A et al (2009) In situ XRD on formation reactions of Cu_2ZnSnS_4 thin films. phys status solidi (c) 6(5):1245–1248
12. Pawar SM et al (2010) Single step electrosynthesis of Cu_2ZnSnS_4 (CZTS) thin films for solar cell application. Electrochim Acta 55(12):4057–4061
13. Araki H et al (2009) Preparation of Cu_2ZnSnS_4 thin films by sulfurizing electroplated precursors. Sol Energy Mater Sol Cells 93(6–7):996–999
14. Tanaka T et al (2005) Preparation of Cu_2ZnSnS_4 thin films by hybrid sputtering. J Phys Chem Solids 66(11):1978–1981

15. Weber A et al (2009) Multi-stage evaporation of Cu_2ZnSnS_4 thin films. Thin Solid Films 517(7):2524–2526
16. McKinley JD, Vance JE (1954) The vapor pressure of zinc between 150 and 350°C. J Chem Phys 22(6):1120–1124
17. Klimova A et al (2005) Investigation of the saturated vapor pressure of zinc, selenium and zinc selenide. Glass Phys Chem 31(6):760–762
18. Weber A, Mainz R, Schock HW (2010) On the Sn loss from thin films of the material system Cu–Sn–Sn–S in high vacuum. J Appl Phys 107(1):013516
19. Fernandes PA, Salome PMP, da Cunha AF (2009) Precursors' order effect on the properties of sulfurized Cu_2ZnSnS_4 thin films. Semicond Sci Technol 24(10):105013
20. Friedlmeier TM et al (1997) Heterojunction based on Cu2ZnSnS4 and Cu2ZnSSe4 thin films. in 14th European PVSEC
21. Geiger F, Busse CA, Loehrke RI (1987) The vapor pressure of indium, silver, gallium, copper, tin and gold between 0.1 and 3.0 bar. Int J Thermophys 8(4):425–436
22. Piacente V, Foglia S, Scardala P (1991) Sublimation study of the tin sulfides SNS_2, $SN2S_3$ and SNS. J Alloys Compd 177(1):17–30
23. Klenk R et al (1993) A model for the successful growth of polycrystalline films of $cuinse_2$ by multisource physical vacuum evaporation. Adv Mater 5(2):114–119
24. Scheer R et al (1996) Scavenging of excess Cu atoms in $CuInS_2$ films by sulphur annealing. Sol Energy Mater Sol Cells 41–2:261–270
25. Scheer R, Lewerenz HJ (1994) Photoemission-study of evaporated cuins(2) thin-films.1 surface stoichiometry and phase segregation. J Vac Sci Technol, A-Vac Surf Films 12(1):51–55
26. Klaer J, Klenk R, Schock HW (2007) Progress in the development of $CuInS_2$ based mini-modules. Thin Solid Films 515(15):5929–5933
27. Tanaka T et al (2010) Influence of composition ratio on properties of Cu_2ZnSnS_4 thin films fabricated by co-evaporation. Thin Solid Films 518(21):S29–S33
28. Zhang J et al (2006) Cu_2ZnSnS_4 thin films prepared by sulfurization of ion beam sputtered precursor and their electrical and optical properties. Rare Met 25:315–319
29. Scragg JJ et al (2008) New routes to sustainable photovoltaics: evaluation of Cu2ZnSnS4 as an alternative absorber material. Phys Status Solidi B-Basic Solid State Phys 245(9):1772–1778
30. Suresh Babu G et al (2010) Effect of Cu/(Zn + Sn) ratio on the properties of co-evaporated $Cu_2ZnSnSe_4$ thin films. Sol Energy Mater Sol Cells 94(2):221–226
31. Olekseyuk ID, Dudchak IV, Piskach LV (2004) Phase equilibria in the Cu_2S-ZnS-SnS_2 system. J Alloys Compd 368(1–2):135–143
32. Yoo H, Kim J (2010) Growth of Cu_2ZnSnS_4 thin films using sulfurization of stacked metallic films. Thin Solid Films 518(22):6567–6572
33. Moriya K, Tanaka K, Uchiki H (2008) Cu_2ZnSnS_4 thin films annealed in H2S atmosphere for solar cell absorber prepared by pulsed laser deposition. Jpn J Appl Phys 47(1):602–604
34. Zoppi G et al (2006) Grain and crystal texture properties of absorber layers in MOCVD-grown CdTe/CdS solar cells. Semicond Sci Technol 21(6):763–770
35. Ito K, Nakazawa T (1988) Electrical and optical-properties of stannite-type quaternary semiconductor thin-films. Jpn J Appl Phys, Part 1-Regul Pap Short Notes Rev Pap 27(11):2094–2097
36. Araki H et al (2008) Preparation of Cu_2ZnSnS_4 thin films by sulfurization of stacked metallic layers. Thin Solid Films 517(4):1457–1460

Chapter 5
Opto-Electronic Properties of Cu_2ZnSnS_4 Films: Influences of Growth Conditions and Precursor Composition

In the final chapter of this report, we present opto-electronic characterisation of the CZTS films, using photoelectrochemical techniques. Observations of trends in these properties are discussed in the light of the results of the preceding chapters.

Background

5.1 CZTS Material Properties in the Literature

5.1.1 The Band Gap of CZTS

Reported Values from Experimental Studies

Fundamental studies of the CZTS band gap are limited. For a single CZTS crystal, it was estimated from absorption measurements as 1.39 eV [1]. Values reported for thin films vary from just below 1.4 eV to around 1.65 eV [2–14], although in fact most are within the range 1.45–1.50 eV. Variations in the band gap of $Cu(In,Ga)(S,Se)_2$ (CIGS) are usually achieved by compositional modifications [15], and this could certainly be one source of the variability in CZTS too. Larger band gaps were found for Cu-poor films in one study [16], but in another the opposite seemed to be true [8]. Although until now there have been no dedicated studies, there are indications in the literature that the band gap of CZTS depends not only on sample composition, but also on heat-treatment parameters. When sulfurisation time was extended from 1 to 3 h, an increase from 1.43 to 1.58 eV was seen [6]. In another report, the band gap increased from 1.45 to 1.55 eV when the heat-treatment temperature was raised from 300 to 500 °C [11]. Some of the highest values, 1.55–1.65 eV, have been seen when sulfurising compound precursors in vacuum [17], whereas more often sulfurisation is carried out close to atmospheric pressure, for example [6, 10, 11, 17, 18]. These are only tentative

J. J. Scragg, *Copper Zinc Tin Sulfide Thin Films for Photovoltaics*,
Springer Theses, DOI: 10.1007/978-3-642-22919-0_5,

Table 5.1 Band gap values calculated for the stannite and kesterite structures

Source	E_g(Stannite) (eV)	E_g (Kesterite) (eV)	Difference (eV)
[19]	1.38	1.50	0.12
[20]	1.42	1.56	0.14
[21]	1.295	1.487	0.192

trends; due to the extensive variability in processing methodology and film composition it is difficult to say whether these trends are always observed. The variation may also be due in part to the way that the band gap values are derived—usually from extrapolation of optical data—and in part to the presence of extensive band tails in poor quality material.

Calculations of the Band Gaps of Kesterite and Stannite

Theoretical approaches have shown that the band gap varies depending on the structural type in a given sample. Calculations of the band gap have given values of between 1.49 and 1.56 eV for the kesterite structure and 1.30–1.42 eV for the stannite structure (see Table 5.1). The band gap for the partially disordered kesterite structure was only 0.04 eV smaller than that of the ordered kesterite [19]. These values encompass the entire range of reported band gaps discussed above.

5.1.2 Defects in $CuInSe_2$ and CZTS

The main defect type giving rise to *p*-type conductivity in $CuInSe_2$ and related materials is the Cu vacancy, V_{Cu}^{-}. Also relatively low in energy is the antisite defect ln_{Cu}^{2+}, an In atom on a Cu site. The neutral defect complex $[2V_{Cu}^{-} + \text{ln}_{Cu}^{2+}]^{\circ}$ actually has a negative free energy of formation in Cu-poor material, and the accumulation of these defects in regular arrays leads naturally to the Cu-poor/In-rich phases $CuIn_3Se_5$ and $CuIn_5Se_8$, which are referred to as 'ordered vacancy compounds' (OVC) [15]. These phases are thought to enhance electron–hole pair separation, leading to higher device efficiencies [22].

There have been several first-principles studies of defect energetics in CZTS and the related quaternary compounds. In general, it was found that the role of Sn was mainly structural; that is to say that due to the greater covalent character of the Sn–S bonds the formation of point defects involving Sn is unlikely. The bonds involving Cu and Zn are almost completely ionic, therefore these elements are the most likely source of defects [23]. In several cases, the neutral defect complex $[Cu_{Zn}^{-} + Zn_{Cu}^{+}]^{\circ}$ was seen to have a low formation energy, especially when arrays of the defect were present [23, 24]. This defect can be seen to correspond to the structural disorder found in the kesterite phase, as discussed in Sect. 3.4, and it should be pointed out that only the Cu and Zn atoms on certain planes can undergo this type of disorder. Similarly to $CuInSe_2$, Cu vacancies could form easily, giving

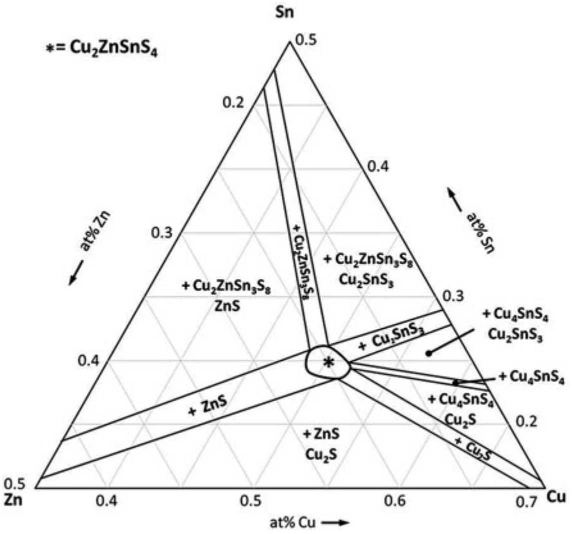

Fig. 5.1 Ternary phase diagram for the Cu–Zn–Sn–S system reproduced from Sect. 3.2

the material *p*-type character. Again analogous to $[2V_{Cu}^{-} + In_{Cu}^{2+}]^{\circ}$ in $CuInSe_2$, the defect complex $[V_{Cu}^{-} + Zn_{Cu}^{+}]^{\circ}$ was found to have a negative free energy of formation [23].

Given that the defect chemistry of CZTS is presumably even more complex than that of $CuInSe_2$, the formation of OVC seems highly likely. The study of such matters in CZTS is in its infancy; however, it is interesting to point out the following similarity between an ordered vacancy compound seen in $CuInSe_2$, and the quaternary $Cu_2ZnSn_3S_8$ phase:

$$CuInSe_2 + In_2S_3 \rightarrow CuIn_3S_5 \quad [22],$$

$$Cu_2ZnSnS_4 + 2SnS_2 \rightarrow Cu_2ZnSn_3S_8 \quad [25],$$

where the thiospinel $Cu_2ZnSn_3S_8$ does indeed belong to a class of compounds being characterised by having a large number of vacant lattice sites [26].

5.1.3 *The Effects of Secondary Phases on Opto-Electronic Properties*

The phase diagram discussed in Sect. 3.2 is reproduced below in Fig. 5.1.

In this chapter it will be useful to refer to the composition labels defined in Chap. 3; these are defined again in Fig. 5.2 and Table 5.2.

The phase diagram shows that there is a strong possibility of the formation of a number of secondary phases, and an interesting question is therefore whether any

Fig. 5.2 Ternary phase diagram defining the compositional types and their labels, as used throughout this text

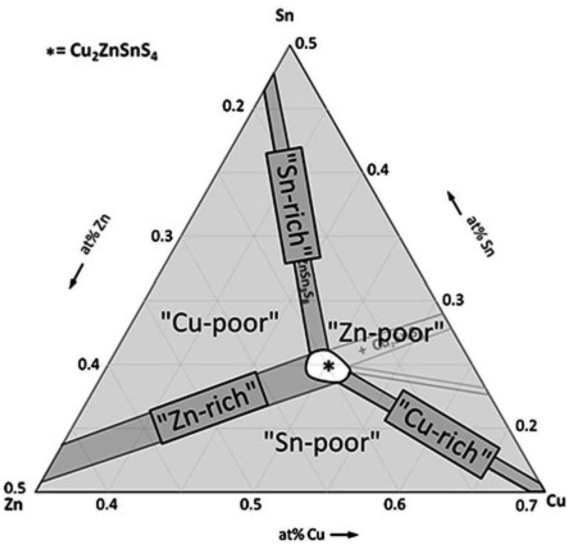

Table 5.2 Definition of composition descriptions used in this report, in terms of the expected secondary phases

Composition description	Expected secondary phases
"Cu-poor"	$Cu_2ZnSn_3S_8$ + ZnS
"Sn-rich"	$Cu_2ZnSn_3S_8$
"Zn-poor"	Cu–Sn–S + $Cu_2ZnSn_3S_8$/Cu_2S
"Cu-rich"	Cu_2S
"Sn-poor"	Cu_2S, ZnS
"Zn-rich"	ZnS

particular combination of secondary phases is preferable (or 'least harmful') in terms of their influence on film properties. We can make some initial predictions:

Cu_2 S, Cu–Sn–S

These materials are generally semiconducting, and have lower band gaps than CZTS, around 1–1.2 eV. Therefore they could act as recombination centres or reduce the open circuit voltage of a device. Degenerate $Cu_{2-x}S$ could even create shorting pathways through the absorber layer. On the other hand, as was mentioned in Sect. 4.2, the presence of excess Cu during growth can be beneficial to the morphological properties of the film, which may improve its electronic transport properties as well. Cu_2S, and—if the interpretation of data in Sect. 4.5.4 is accurate, also Cu–Sn–S—can be removed by KCN etching, but buried phases that cannot be accessed by the etchant will be detrimental to the film performance.

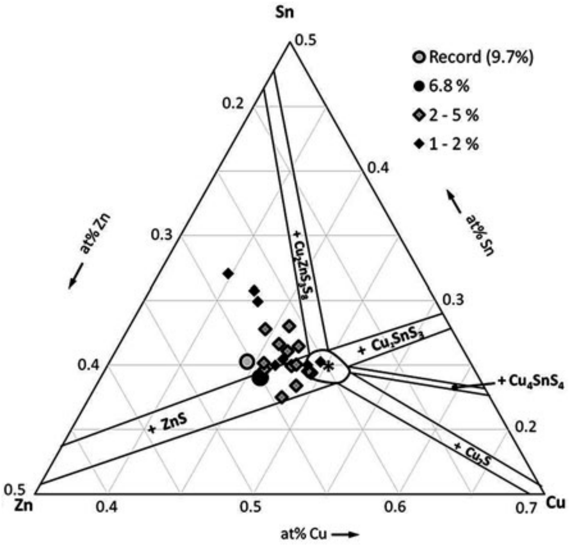

Fig. 5.3 Ternary phase diagram showing the compositions of the reported CZTS devices, sorted by device efficiency [7, 8, 10–13, 27–31]

$Cu_2ZnSn_3S_8$

This phase was first reported by Olekseyuk et al. [25], and as yet there are no reports concerning its properties.

ZnS

ZnS is a semiconductor with a band gap of around 3.6 eV. It should not therefore act as a recombination centre, but will reduce the volume of useful material. If present at the surface, as suggested in Sect. 3.1.3, then it may absorb the shorter wavelengths and reduce the current produced by the film.

5.1.4 Device Compositions for CZTS

The compositions of the reported CZTS devices to date are plotted on the ternary phase diagram in Fig. 5.3. Despite significant differences in processing conditions, there is a general consensus that the 'best' composition is not in fact within the single-phase region; instead it is in either the Zn-rich or Cu-poor regions. It should be noted that the compositions of CZTS films are rarely discussed with reference to the likely secondary phases, because of the aforementioned difficulties in assigning them. In this investigation we make full use of the Cu–Zn–Sn–S phase diagram to help understand the observed behaviour. The most commonly seen film compositions would cause the formation of ZnS and $Cu_2ZnSn_3S_8$ secondary phases.

No functioning devices have been produced from material in the Sn-rich, Sn-poor, Cu-rich or Zn-poor regions. This pattern is in accordance with the above predictions about the effects of different secondary phases.

5.2 Photoelectrochemical Characterisation Techniques

This investigation concerns the opto-electronic properties of CZTS absorber layers. In order for these to be measured, electrical contact must be made with the absorber layer surface while the surface is simultaneously illuminated. A convenient way to do this is to use an electrolyte contact: the absorber layer is immersed in a transparent, conductive solution containing a redox species capable of collecting photogenerated minority carriers from the film surface. The redox species should be an extremely efficient scavenger of minority carriers, so that these carriers do not cause photocorrosion of the film. If that condition is met, the electrolyte contact is non-damaging, reversible and much more easily made than a solid-state contact. An overview of the relevant properties of the semiconductor-electrolyte junction will be given. For further information on the semiconductor-electrolyte junction, the reader is referred to [32].

5.2.1 *Junction Formation at the Semiconductor-Electrolyte Interface*

A *p*-type semiconductor like CZTS contains a certain concentration of ‘acceptor’ impurities or defects, which are ionised at room temperature to provide ‘free’, i.e. delocalised, holes in the valence band. Holes are termed the ‘majority carrier’ in a *p*-type material. The concentration of free electrons at equilibrium, by contrast, is negligible. The energy of the majority carriers on an electrochemical scale is equivalent to the Fermi level in the semiconductor. Upon immersion in an electrolyte, charge transfer occurs between the solution and the semiconductor, until the Fermi level of the semiconductor is equal to the electrochemical potential of the redox electrolyte. We consider a situation in which the electrochemical potential of the redox couple is within the band gap of the semiconductor before contact. In this case, majority carriers—holes in a *p*-type material—can lower their energy by reacting with the electrolyte. The extraction of holes creates a concentration gradient, driving more holes to the surface. The ionised acceptor states that gave rise to the holes are localised, and so the transfer process leaves behind a region of negative charge. Net hole transfer stops when the diffusional driving force for hole extraction is balanced by the electrostatic driving force keeping the holes within the material. At this stage, the Fermi level has equalised throughout the semiconductor-electrolyte system, and there is a region within the semiconductor that is depleted of holes, known as a ‘space charge’ region, extending a

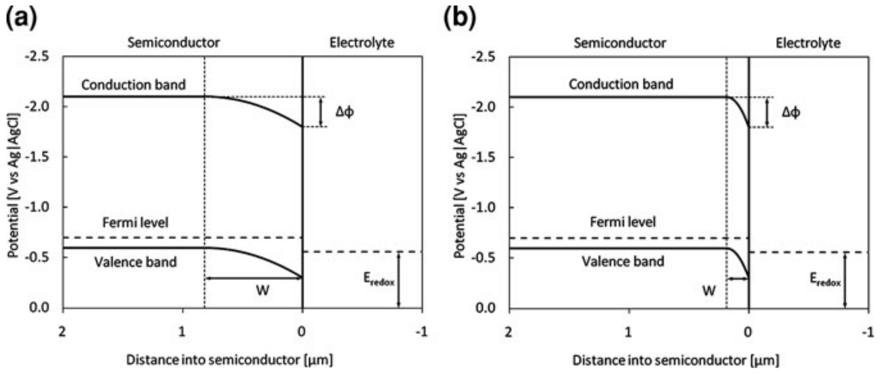

Fig. 5.4 Band structure at the interface of a *p*-type semiconductor and a redox electrolyte, indicating the space charge region width *W* for different values of acceptor concentration: **a** $5 \times 10^{14}\ \mathrm{cm}^{-3}$, **b** $1 \times 10^{16}\ \mathrm{cm}^{-3}$

depth *W* into the semiconductor. An equivalent excess positive charge is absorbed at the semiconductor surface on the electrolyte side of the interface, in a thin plane known as the Helmholtz layer. The depletion region has the properties of a rectifying contact—a Schottky barrier—and provides a mechanism for separation of photoexcited electron–hole pairs. The electric field at the surface is equivalent to a 'bending' of the conduction and valence bands over the distance *W*.

The concentration of free carriers in the semiconductor in the dark is dependent on the concentration of acceptor states. For a given initial difference in Fermi levels, a fixed amount of charge must be transferred from the semiconductor to the solution. If a large amount of charge is transferred, then the carriers must come from deeper in the bulk of the semiconductor, therefore the spatial extent of the space charge region, *W*, is governed by the acceptor concentration, N_a, as follows:

$$W = \left(\frac{2\varepsilon_0\varepsilon_r\Delta\phi}{qN_a}\right)^{\frac{1}{2}}, \tag{5.1}$$

which is derived from the Poisson equation for the electric field gradient near the semiconductor surface under depletion conditions. ε_0 and ε_r are the vacuum and material permittivities, $8.85 \times 10^{-12}\ \mathrm{Fm}^{-1}$ and approx. 10 respectively, and $\Delta\phi$ is the potential difference between the bulk and the surface of the semiconductor, and is a measure of the degree of band bending. Figure 5.4 illustrates the band structure of the semiconductor near the interface, showing the effect of different acceptor concentrations on *W*. The figures are plotted on an electrochemical scale with respect to the reference electrode used, which was Ag|AgCl. The redox electrolyte level is that of $\mathrm{Eu}^{3+}/\mathrm{Eu}^{2+}$ (−0.557 V vs. Ag|AgCl), which is commonly used with *p*-type semiconductors since it is an efficient electron-scavenger [33].

During measurements, the sample is connected to a potentiostat, and we can control its potential, *E*, with respect to a reference electrode. By doing so we are altering the position of the Fermi level within the semiconductor. Changing the

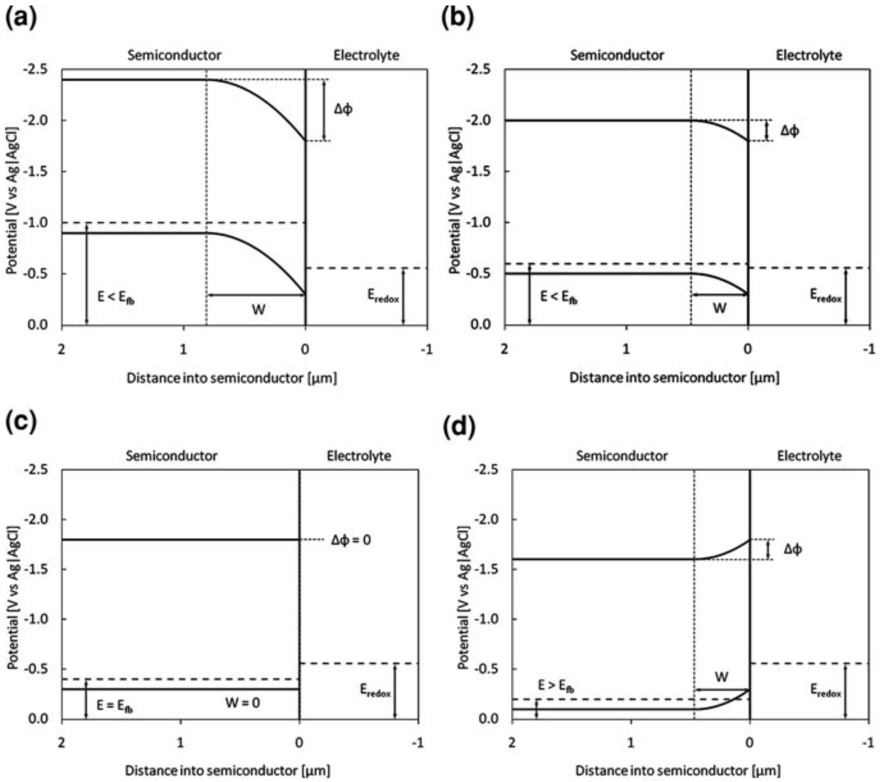

Fig. 5.5 Band structure at the semiconductor-electrolyte interface for different values of applied potential, *E*, with respect to the Ag|AgCl reference electrode: **a** −1.0 V, **b** −0.6 V, **c** −0.4 V (the flat-band potential in this example), **d** −0.2 V

Fermi level causes further charge exchange at the interface, which changes the degree of band bending, $\Delta\phi$. The electrode potential required to cause $\Delta\phi$, and therefore *W*, to drop to zero is termed the 'flat-band' potential, E_{fb}. In cases where the acceptor concentration is less than around 10^{18} cm^{-3}, most of the change in potential occurs over the space charge region, with only a small amount being dropped across the Helmholtz layer. In this case, $\Delta\phi$ is equal to $(E_{fb} - E)$, so that the dependence of *W* on applied potential is given by:

$$W = \left(\frac{2\varepsilon_0\varepsilon_r(E_{fb} - E)}{qN_a}\right)^{\frac{1}{2}} \tag{5.2}$$

Figure 5.5 shows the band structure for different values of applied potential, both negative and positive of the flat-band potential. In the former case, we have a depletion region, and in the latter case an 'accumulation region', where the semiconductor has developed negative charge near the surface.

Before moving on to the role of the space charge region in charge carrier collection, we must first discuss the generation of electron–hole pairs upon light absorption.

5.2.2 Charge Carrier Generation in Semiconductors

Generation of electron–hole pairs occurs by photo-excitation, the absorption of photons causing electronic transitions between the valence and conduction bands. CZTS is a direct gap semiconductor, so these transitions occur with high probability. Therefore light absorption is strong at energies above the band gap.

The fraction of light penetrating a depth x into the material is determined by the absorption coefficient, $\alpha(E)$, which varies with energy following the density of states of the material.

$$I(E,x) = I_0 \exp(-\alpha(E)x) \tag{5.3}$$

An approximation for the absorption coefficient for photon energies, $h\nu$, near the band gap energy, E_g, is given by the parabolic equation for a direct band gap:

$$\alpha(E) = A(h\nu - E_g)^{\frac{1}{2}} \tag{5.4}$$

The parameter A is a constant determined by the details of the electronic band structure.

The absorption coefficient can be measured directly for a known thickness of film upon a transparent substrate, according to Eq. 5.3. However, the electrodeposition method required highly conductive substrates, and there are no suitable transparent materials. Since the constant A is essentially determined by the band structure of a material, we can assume that it will not change considerably, and so we can use literature data for the absorption coefficient, such as that presented by Tanaka et al., which was measured for a film produced by hybrid sputtering [9]. The data were digitised and are reproduced in Fig. 5.6a. By fitting Eq. 5.4 to this data, as in Fig. 5.6b, we derive a value for A of approx. 2×10^4 cm^{-1} eV$^{-½}$. This is only valid within about 1 eV of the band gap; after that the parabolic band approximation is no longer applicable.

5.2.3 Charge Carrier Collection and External Quantum Efficiency

To obtain a current under illumination, the photoexcited electrons and holes must be channelled in opposite directions. The role of the semiconductor-electrolyte junction is now apparent: there is an electric field over the space charge region which provides a driving force for electrons to move towards the surface and for

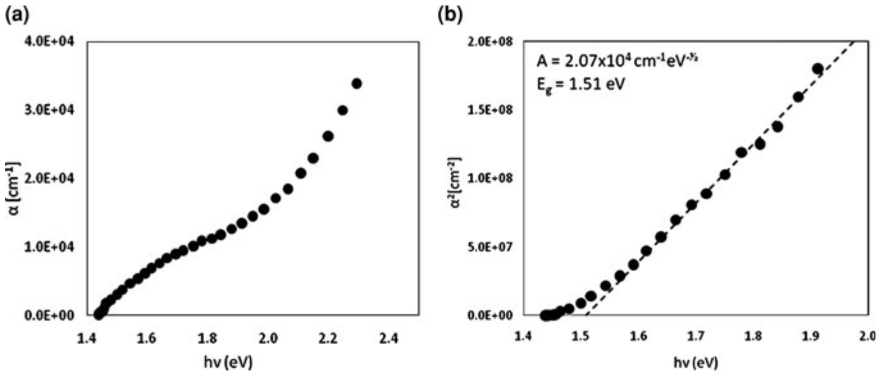

Fig. 5.6 **a** Absorption coefficient data reproduced from Ref. [9]. **b** Plot to determine the material constant A (and band gap E_g) from the absorption coefficient data

holes to move away from the surface. Coupled with this, the presence of an efficient electron-scavenger in the electrolyte means that photogenerated electrons are rapidly removed from the semiconductor, creating a concentration gradient which causes an electron flux towards the surface. The rate of hole capture by the electrolyte is negligible in contrast, so that holes diffuse away from the site of generation into the bulk of the semiconductor. In the absence of electron–hole pair recombination within the space charge region or at the surface, then all photons absorbed within the space charge region will lead to current generation. If photons penetrate further, into the charge-free region of the material, then the carriers they generate will only be collected if they diffuse far enough to reach the space charge region before recombining. The Gärtner equation summarises these collection processes in an expression for the 'external quantum efficiency' (EQE), equal to the number of electrons collected per incident photon absorbed [34]:

$$\Phi(E) = 1 - \frac{\exp(-\alpha(E)W)}{1 + \alpha(E)L_n} \tag{5.5}$$

where $\Phi(E)$ is the EQE and L_n is the minority carrier diffusion length, determined by the diffusion coefficient, D, and lifetime, τ, of the minority carriers by $L = (\pi D\tau)^{1/2}$ [35]. Figure 5.7 and 5.8 show the exponential decay of light intensity superimposed on the band structure near the semiconductor-electrolyte interface, for different incident photon energies and different applied potentials. The former alters the penetration depth of light, and the latter alters the space charge region width. The relative size of these two distances is critical in determining the EQE.

The role of the applied potential is therefore to control the width of the space charge region in order that as much light as possible is absorbed within it, so that carrier collection is maximised.

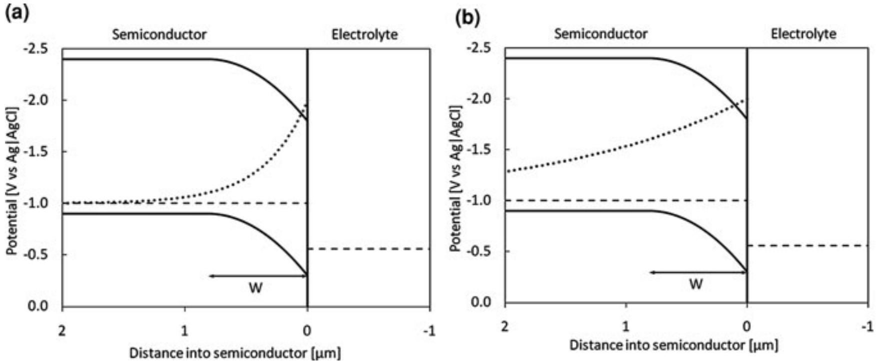

Fig. 5.7 The semiconductor-electrolyte interface showing the relative intensity of light as a function of penetration depth as a *dotted line*, for two different photon energies: **a** 3.5 eV, and **b** 1.6 eV. The percentage of light absorbed within the space charge region is 90 and 40% respectively

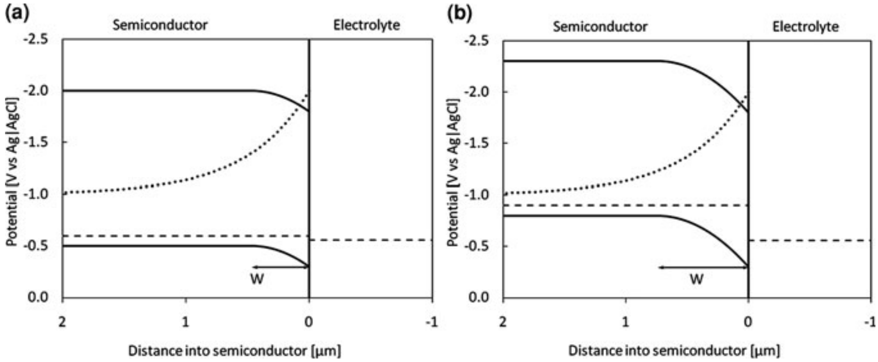

Fig. 5.8 The semiconductor-electrolyte interface showing the relative intensity of light as a function of penetration depth as a dotted line, for two different electrode potentials: **a** −0.6 V vs. Ag|AgCl, and **b** −0.9 V vs. Ag|AgCl. The percentage of light absorbed within the space charge region is 50 and 80% respectively

5.2.4 Non-Radiative Recombination

After they are excited by incident photons, charge carriers in the conduction and valence bands should ideally flow uninterrupted through the film, carrying the photocurrent. However, carriers can also become trapped in localised states within the band gap. If it is not thermally re-excited out of the trap state, a complementary charge carrier may recombine with the trapped carrier. Recombination of photogenerated charge carriers via states at the surface of the semiconductor or within the space charge region is an undesired process that reduces the collection efficiency. However, due to the chemical complexity of the compound semiconductors, and the nature of the processes used to fabricate them in thin film form, the presence of defect states is very likely, and devices and measurements must be designed such that recombination can be minimised. In this instance, the applied potential is chosen such that recombination has only a minor effect on the collection efficiency.

5.2.5 Dark Currents

So far we have talked about the photocurrent arising under illumination, but there is also the possibility that ‘dark’ currents, i.e. currents which arise from processes other than light absorption, can also flow. In an electrochemical system, these would correspond to other electrochemical processes besides collection of photogenerated charge carriers. Dark currents will be worsened when there are pin-holes in the film that allow the substrate to come into contact with the solution. Then the potential that should be dropped over the space charge region of the semiconductor—leaving only a small potential at its very surface—is instead lost entirely over the thin Helmholtz plane at the substrate surface. It is then very likely that there will be direct reduction of the redox electrolyte, i.e. $\mathrm{Eu}^{3+} + \mathrm{e}^{-}_{\mathrm{MO}} \rightarrow \mathrm{Eu}^{2+}(\mathrm{aq})$. This reaction will occur at potentials more negative than −0.58 V vs. Ag|AgCl [36]. Because of the possibility of dark currents, the photocurrent is measured using pulsed or chopped illumination. The dark current is measured during the ‘off’ period of the illumination, and subtracted from the total current measured during the ‘on’ period.

5.2.6 Measurement of EQE Spectra

Measurements of EQE are made with reference to a calibrated photodetector—which has a known EQE spectrum. The photocurrent, $\Delta J(E)$, of a sample under illumination from a spectral flux density $b(E)$ over a small range of photon energies ΔE is given by:

$$\Delta J(E) = qb(E)\Phi(E)\Delta E, \tag{5.6}$$

where q is the electronic charge. The spectral flux density is dependent on the source of illumination and its intensity. This equation holds for both the sample and the photodetector, so that when they are measured under the same illumination conditions, i.e. with a constant function $b(E)$, the sample EQE spectrum is calculated simply from the ratio of photocurrents:

$$\Phi_s = \Phi_{pd}\frac{\Delta J_s}{\Delta J_{pd}}, \tag{5.7}$$

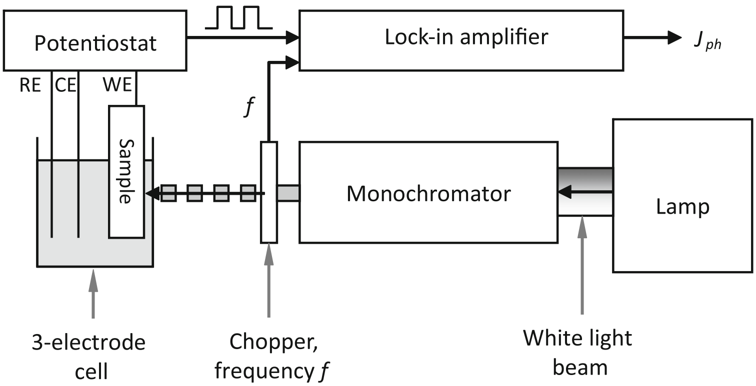

Fig. 5.9 Diagram of the photocurrent measurement setup. See text for explanation

where all parameters are functions of photon energy and the subscripts '*s*' and '*pd*' refer to the sample and the photodetector respectively.

To measure the photocurrent from the sample, a monochromatic light beam is shone onto the sample within its electrochemical cell, while a potentiostat is used to hold the sample at a potential suitable to create the desired band bending situation (see Fig. 5.8). A reasonable degree of band bending is required to minimise surface recombination, which would reduce the photocurrent at all wavelengths. The potential is measured with respect to a reference electrode in the electrochemical cell, and the photocurrent, recorded by the potentiostat, flows between the sample and a third electrode. To distinguish the photocurrent from any dark current that may be flowing (as a result of processes other than light absorption), the light beam is chopped at a constant frequency and a lock-in amplifier used to detect the modulated photocurrent at that frequency. The light beam size should be smaller than the sample and photodetector so that all of the light falls onto their surfaces in each case. The setup is shown in Fig. 5.9.

5.2.7 Correcting for Reflection and Absorption by the Electrochemical Cell

When the photodetector photocurrent is measured, the light beam is directly incident on its surface. When photoelectrochemical measurements are made, the beam must pass through the glass window of the electrochemical cell and through a certain distance of electrolyte before reaching the samples surface. Reflection at the glass-air and glass-electrolyte interfaces and absorption by the electrolyte will reduce the intensity of the light at certain wavelengths. If the original spectrum of illumination is given by *b*, then the photon flux reaching the sample at a given wavelength will be given by:

$$b' = b(1 - R_{ag})(1 - R_{ge})\exp(-\alpha_e x_e) = bT_{cell}(x), \tag{5.8}$$

where R_{ag} and R_{ge} are the reflection coefficients of the air–glass and glass-electrolyte interfaces respectively and α_e is the absorption coefficient of the electrolyte (it is assumed the glass is completely transparent at the wavelengths used). All three parameters are functions of wavelength. x_e is the path length travelled by the light beam through the electrolyte. Taken together these effects give the transmission spectrum of the front part of the cell, $T_{cell}(x)$. As a consequence of reflection and absorption, the sample photocurrent must be corrected by dividing through by $T_{cell}(x)$ when calculating the sample EQE:

$$\Phi_s = \Phi_{pd}\frac{\Delta J_s}{\Delta J_{pd}T_{cell}(x)}, \tag{5.9}$$

where it is understood that all parameters are functions of the photon energy of the illumination.

To determine $T_{cell}(x)$ for the cell used in this investigation, the photocurrent from the photodetector was measured in three different situations: (1) with the empty cell (which is enclosed by two flat, parallel glass windows 1 cm apart) between the photodetector and the light source, (2) as before but with the cell filled with electrolyte, and (3) the filled cell with a 1 mm thick piece of glass immersed in the electrolyte, parallel to the cell windows. The spectral photon flux reaching the photodetector in each case is given by:

1.
$$b_1 = b(1 - R_{ag})^4 \tag{5.10}$$

2.
$$b_2 = b(1 - R_{ag})^2(1 - R_{ge})^2\exp(-\alpha_e t) \tag{5.11}$$

3.
$$b_3 = b(1 - R_{ag})^2(1 - R_{ge})^4\exp(-\alpha_e(t - 1)), \tag{5.12}$$

where t is the spacing between the two sides of the cell. Solving these equations simultaneously yields the individual contributions to $T_{cell}(x)$ and allows us to calculate the amount of light reaching the sample when it is immersed in the electrolyte. R_{ag}, R_{ge} and α_e are shown in Fig. 5.10a–d as a function of photon energy, along with $T_{cell}(x)$ calculated for different distances into the electrolyte.

The combined reflection from the air–glass and glass-electrolyte interfaces results in about 7% of the incident light being lost at most wavelengths, which increases to around 20% in the blue region. The absorption peak of Eu(III) solution at around 1.3 eV is quite significant, since this is the region of the CZTS band gap. Therefore the importance of this correction is emphasised. It is also best to minimise the distance between the front of the cell and the sample surface. A distance of around 1.5 mm was the minimum that could be achieved in practice.

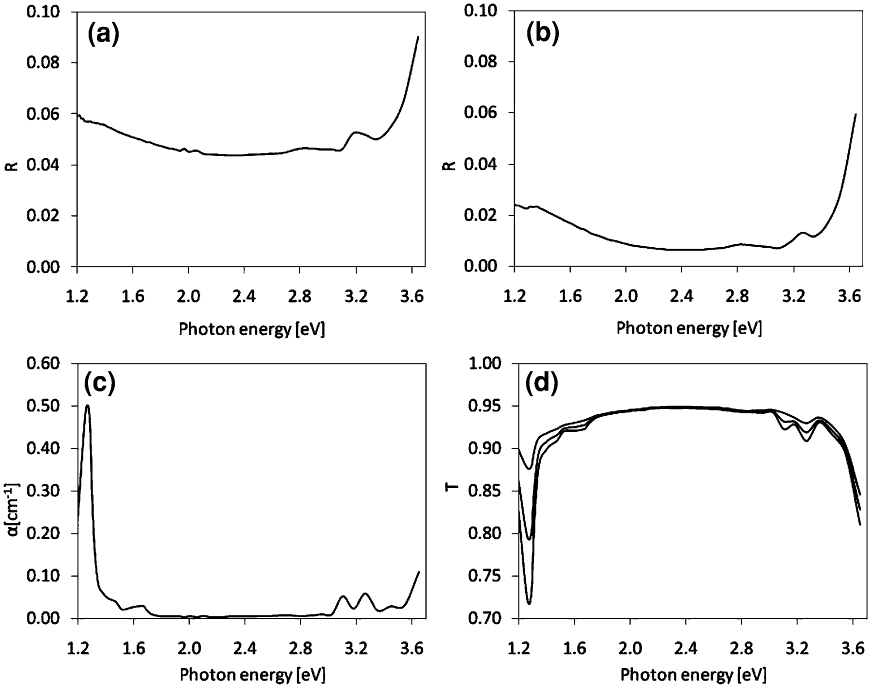

Fig. 5.10 Reflectivity spectra for **a** the glass–air, and **b** the glass-electrolyte interfaces. **c** Absorption spectrum for the Eu(III) electrolyte. **d** Calculated transmission spectra showing relative light intensity at the sample surface, for different path lengths through the electrolyte (1, 3, and 5 mm)

5.2.8 Analysis of EQE Spectra and EQE-Bias Curves

Measurement of the Band Gap

The EQE spectrum can be used to derive the band gap of a sample. If we re-write the Gärtner equation in the limit of a small minority carrier diffusion length (which is likely to be the case in a small-grained, polycrystalline material with a high concentration of defects) we obtain:

$$-\ln(1-\Phi) = \alpha W \tag{5.13}$$

Then substituting the expression for the absorption coefficient, we have:

$$-\ln(1-\Phi) = WA(h\nu - E_g)^{\frac{1}{2}} \tag{5.14}$$

Therefore a plot of $[\ln(1-\Phi)]^2$ against $h\nu$ yields a straight line which intersects the x-axis where $h\nu = E_g$. Knowing the value of A, we can also make an estimate of W from the gradient of the line.

Prediction of Short Circuit Current Density

Since EQE is a measure of the number of electrons generated per incident photon, we can also predict the maximum (short circuit) current density, J_{sc}, that could be expected under any given illumination source [37]. This is simply done by integrating the EQE over the spectrum of choice:

$$J_{sc} = q \int_{0}^{\infty} \Phi(E) b(E) dE, \tag{5.15}$$

where $b(E)$ is the spectral photon flux density ($\mathrm{m}^{-2}\ \mathrm{s}^{-1}\ \mathrm{eV}^{-1}$) and q the electronic charge. For $b(E)$ we use the AM1.5G spectrum—the standardised solar photon flux arriving at the Earth's surface.

It is important to note that, since the band gap of the material defines the lowest photon energy that can be absorbed, materials with higher band gaps absorb fewer photons. This means that the short circuit current density available from a wide band gap material is lower. However, the energy of each charge carrier is also defined by the band gap: after transition into the conduction band upon light absorption, each electron rapidly loses any excess energy and relaxes to the conduction band edge. Narrow gap materials therefore generate less energy per electron—their photovoltage is lower. There is an optimum band gap of around 1.5 eV where the product of the theoretical maximum current density and the maximum photovoltage is greatest [37]. This is one reason that CZTS is a promising candidate for thin film solar cells. As a consequence of the above, we must be careful when comparing predicted short circuit current densities from different samples—a good measure of film quality is only obtained if the band gaps of the samples are the same.

Measurement of Flat-Band Potential and Space Charge Region Width

When making measurements as a function of electrode potential, E, we are controlling the width of the space charge region, W. Therefore we re-write the Gärtner equation again by substituting the expressing for W (Eq. 5.2):

$$-\ln(1 - \Phi) = \alpha \left(\frac{2\varepsilon_0 \varepsilon_r (E_{fb} - E)}{q N_a} \right)^{\frac{1}{2}} \tag{5.16}$$

This equation is valid where $E < E_{fb}$; in all other cases $\Phi = 0$. An illumination wavelength within about 1 eV of the band gap should be used to stay within the parabolic section of the absorption spectrum. When the applied potential is equal to the flat-band potential ($E_{fb} = E$), there is no space charge region, and the only driving force for carrier collection is diffusion. If the diffusion length is small, we should expect to see little or no current under illumination. If we make E more positive than E_{fb}, then a surface barrier develops for minority carriers (see Fig. 5.5d); they cannot react with the redox electrolyte, and again we will not see a

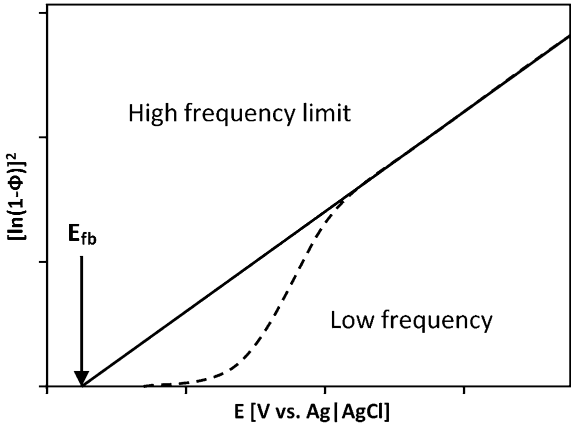

Fig. 5.11 EQE-potential plots showing the effect of surface recombination, and how this is removed by using high chopping frequencies during measurement

current flow. Only when E is negative of E_{fb} will we see a photocurrent, which will increase as the space charge region is widened. In principle, according to Eq. 5.16, a plot of $[\ln(1-\Phi)]^2$ against E should yield a straight line with intercept E_{fb} on the x-axis. In practice, this is not often observed. Surface recombination becomes increasingly rapid as $\Delta\phi$ approaches zero, because majority carriers can more easily reach minority carriers that are temporarily trapped in surface states. Therefore for low amounts of band bending ($\Delta\phi$), Φ decreases more rapidly than Eq. 5.16 predicts, as illustrated in Fig. 5.11, and can lead to E_{fb} being underestimated. There are two solutions to this problem. If there is a linear region at the higher values of band bending, then this should be extrapolated to obtain an estimate of E_{fb}. Alternatively, measurements of Φ can be performed with very high frequencies of chopped illumination, such that the measurement is made on a timescale shorter than that required for the recombination reaction [38]. The higher the frequency, the further the extent of the linear region of the plot, as also shown in Fig. 5.11.

If acceptable measurements of the EQE-potential curve can be made, then the acceptor density and flat-band potential can be derived according to Eq. 5.16.

The acceptor density and flat-band potential can also be measured using capacitance measurements as a function of potential. The space charge region has a finite capacitance, and this can be measured by applying a modulated potential and recording the component of the current 90° out of phase with the driving frequency. Applying at the same time a constant potential causes the space charge region width to change, which in turn affects its capacitance. This measurement must be made at potentials where the dark current is small. The relationship between capacitance, C, and potential is given by the Mott-Schottky equation:

$$C^{-2} = \frac{2}{qN_a\varepsilon_0\varepsilon_r A^2}\left\{(E_{fb} - E) - \frac{KT}{q}\right\} \tag{5.17}$$

A plot of C^{-2} as a function of potential should have a linear region with a gradient proportional to N_a and which can be extrapolated to give E_{fb}. Measurements of capacitance are susceptible to errors if there are pinholes present, because the pinholes have a much lower, parallel capacitance which will dominate the measurement. In this investigation, all of the above techniques were used to estimate N_a, and good agreement was usually found between them.

Experimental

5.3 Photoelectrochemical Measurements

5.3.1 Sample Preparation

Precursor preparation, sulfurisation and etching were described in Sects. 3.7–3.10.

The Mo areas at the borders of the samples became coated with MoS_2 during sulfurisation, and this was removed by abrasion with 1 μm alumina paste to expose the back contact. The edges of the samples were isolated by scribing through the film with a diamond tipped stylus, and the area to be measured was delineated with polyimide tape.

5.3.2 The Photoelectrochemical Cell

The measurement cell was a glass-sided vessel with approximate volume of 2 cm^3. All photoelectrochemical measurements on CZTS films were carried out using an aqueous solution of 0.2 M $Eu(NO_3)_3.6H_2O$ (99.9%, Alfa Aesar) as an electron-scavenging redox electrolyte. The photocurrent responses of the films were measured under potentiostatic control using Pt wire counter and Ag|AgCl reference electrodes.

5.3.3 Photocurrent under LED Illumination

Transient photocurrents were generated using pulsed illumination from a high intensity white light emitting diode (LED) and measured using an Autolab 20 potentiostat at a potential of −0.4 V vs. Ag|AgCl.

5.3.4 Photocurrent Spectroscopy (Measurement of EQE)

Photocurrent spectra were obtained using monochromatic light of variable wavelength provided by a tungsten lamp and grating monochromator. The incident light was chopped at 27 Hz, and a lock-in amplifier (Stanford Research Systems) was used to detect the photocurrent. A yellow filter was used to remove second-order harmonics from the monochromated light at wavelengths above 550 nm. The sample cell and battery-powered potentiostat were placed within a Faraday cage to eliminate external electromagnetic interference and illumination. Measurements as a function of wavelength were made at a potential of −1.0 V vs. Ag|AgCl. The spectrum was recorded twice in opposite directions to confirm that the sample was stable before performing a slower scan to record the final spectrum. Measurements in the range 1100–350 nm were performed with 20 nm intervals; those in the range 1100–700 (the absorption onset region) were made at 5 nm intervals. Measurements as a function of potential were made with an illumination wavelength of 750 nm.

The photocurrents were corrected for reflection and electrolyte-absorption as described in Sect. 5.2.7. In order to obtain the EQE of the CZTS films, the incident photon flux was calibrated using standardized Si and Ge photodiodes traceable to NBS standards.

5.3.5 High-Frequency Measurements of Photocurrent

These measurements were performed using the same setup as described above, but the illumination source was a red LED (650 nm) driven with a variable frequency between 1 and 5 kHz.

5.3.6 Capacitance-Bias Measurements

For capacitance measurements of CZTS films, the same three-electrode cell was used as described above, but the electrolyte was replaced with KCL buffered at pH3. A sinusoidal potential with amplitude of 10 mV and a frequency of 1 kHz was applied to the sample while the potential was scanned between 0.1 and −0.5 V vs. Ag|AgCl. The current at a phase angle of 90° was recorded using a lock-in amplifier, and the system was calibrated using a variable capacitor.

Results and Discussion

In this section, the effects of changing the sulfurisation parameters and precursor compositions on material properties are studied. Where the sulfurisation conditions were varied, the precursors in every case had compositions described by

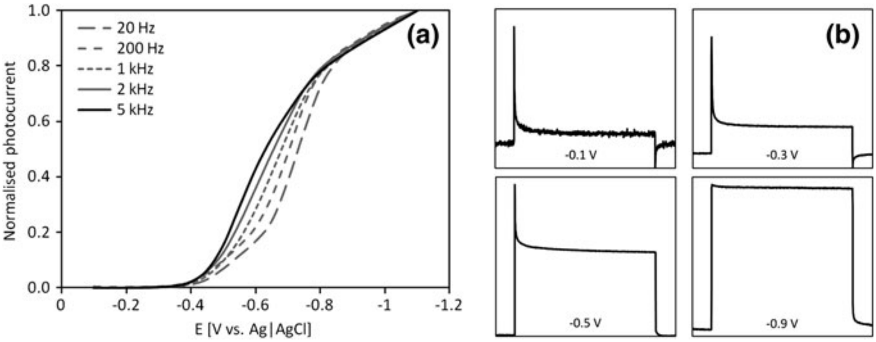

Fig. 5.12 **a** Photocurrent-potential plots made at different frequencies of pulsed illumination showing the effect of surface recombination at lower frequencies and potentials. **b** Photocurrent-time transients at different potentials showing the effect of recombination on the steady-state photocurrent

Cu/(Zn + Sn) = 0.8, Zn/Sn = 1, placing them in the Cu-poor section of the ternary phase diagram. The sulfurisation pressure (except where it was the variable under study) was kept high (700–850 mbar), in an attempt to minimise undesired compositional changes during sulfurisation. Where the effects of composition were under investigation, all samples were sulfurised at 580 °C for 30 min at a pressure of 700 mbar.

5.4 Determining Conditions for Photoelectrochemical Measurements

5.4.1 Photocurrent-Potential Measurements

In order to make meaningful measurements of sample properties, the applied potential during photoelectrochemical measurements must be chosen to avoid recombination where possible. Figure 5.12a shows photocurrent-potential curves for a sample measured under rapidly pulsed illumination.

In the potential range −0.4 to −0.8 V vs. Ag|AgCl, there is a strong dependence of photocurrent upon the frequency of the illumination pulse. This is characteristic of surface recombination. The recombination current can be visualised clearly in the shapes of the photocurrent transients at different potentials, as in Fig. 5.12b. The initial spike in photocurrent is due to the displacement current from the full quantity of photogenerated carriers. Immediately after they are generated, the carriers begin to recombine, bringing the steady-state current to a much lower level. At higher potentials, this effect is minimised. At higher frequencies, increasingly narrow sections of the initial current spike are sampled, so the effect of recombination is screened out. The data show that we can avoid

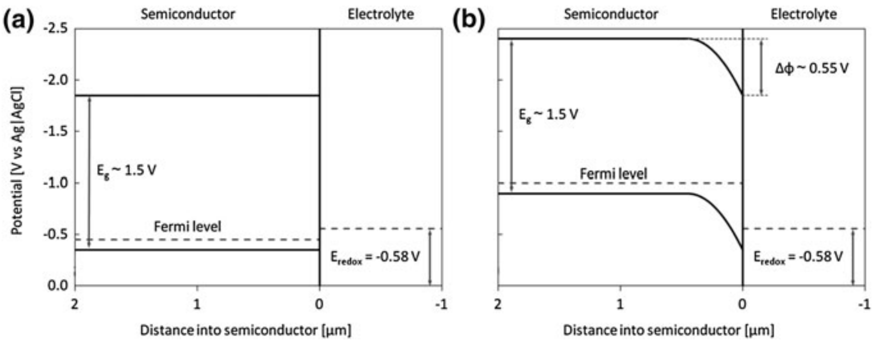

Fig. 5.13 Schematic band diagrams for CZTS in contact with an Eu(III) solution **a** under flat-band conditions ($E_{fb} = -0.45$ V), and **b** at a potential of −1.0 V vs. Ag|AgCl, as used for EQE measurements

recombination either by using very high chopping frequencies or by using potentials more negative than −0.8 V. In practice, the highest chopping frequency available in the standard EQE setup was around 800 Hz, therefore it was more convenient to make low-frequency measurements at higher potentials. Typically −1.0 V vs. Ag|AgCl was applied. A similar potential was used to make photoelectrochemical measurements on $CuInSe_2$ [33]. A simple scheme showing the band structure of CZTS in contact with a Eu(III) solution under the measurement conditions is shown in Fig. 5.13.

5.4.2 The Effect of KCN Etching

As was discussed Chap. 4, etching in KCN removes Cu–S and possibly also Cu–Sn–S particles from the sample surface. These particles can act as recombination centres, as well as causing anomalous light absorption and current generating behaviour. Therefore etching was important before photoelectrochemical measurements were made; in fact, no photocurrent at all was observed for Cu-rich/Zn-poor samples until they were etched. Figure 5.14 shows how etching a sample in 5wt% aqueous KCN for increasing times affects the EQE measured as a function of potential curve. There is a general improvement as the etch duration increases, corresponding to more efficient removal of secondary phases from the sample surface. The rate of improvement slows down after about 60 s.

In practice, aside from being vital for Cu-rich/Zn-poor samples, etching would always either improve or have no negative effect upon Cu-poor/Sn-rich samples as well. Therefore a two-minute etch in 5wt% KCN was routinely used for all samples prior to photoelectrochemical measurements.

Having covered these preliminaries, we can now move on to the main body of results derived using the photoelectrochemical measurements techniques.

Fig. 5.14 EQE-potential curves measured under white light illumination showing the effect of KCN etching duration on a Cu-rich sample

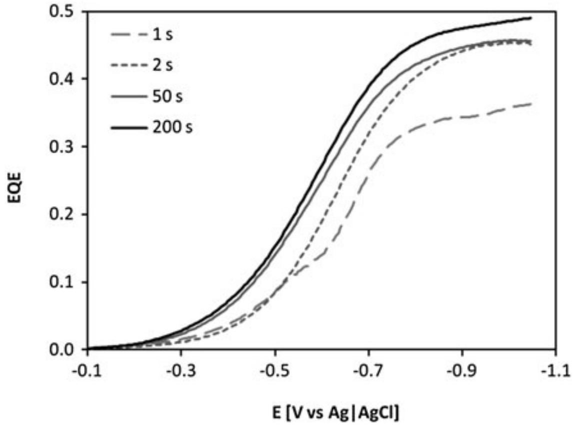

5.5 The Effect of Sulfurisation Time

As described in Chap. 4, sulfurisation times in the CZTS literature vary greatly, and extend up to 3 h. If the two-stage process is to be industrially viable, the sulfurisation time must be minimised, however, no detailed study of the effect of sulfurisation time on sample performance has yet been published. The use of a rapid thermal processing system with heating/cooling rates up to 20 °C s^{-1} allows us to perform such an experiment with excellent time resolution.

5.5.1 Evolution of Photocurrent Density with Sulfurisation Time

The photocurrent density measured using chopped illumination from a white LED is shown in Fig. 5.15 for two series of samples sulfurised for different times. Photocurrent is apparent even after just one minute of sulfurisation. There is then a steep rise, with 50% of the maximum being reached within 5 min, but the peak photocurrent is only reached after 50 min, and thereafter there is a gradual decline.

There are clearly two processes operating here: one that causes the increase in photocurrent between 0 and 50 min of sulfurisation time, and a second process that causes it to drop after 50 min.

Three stages of film formation were described in Chap. 3: (1) the incorporation of sulfur, leading initially to formation of binary sulfides, (2) crystallisation of the CZTS phase, and (3) grain growth. The first two stages were shown here and in other work [39] to be rapid, occurring within a few minutes above 500 °C. The timescale for evolution of photocurrent, however, is apparently much longer. Clearly, until CZTS has crystallised, there will be no photocurrent; however, if we suppose that the crystallisation is complete within a few minutes, then there must

Fig. 5.15 Photocurrent density as a function of sulfurisation time, measured from current transients under white light illumination. Recorded in 0.2 M Eu(III) solution at a potential of −0.4 V vs. Ag|AgCl. Other sulfurisation conditions: 600°C, 700 mbar, 20 mg s

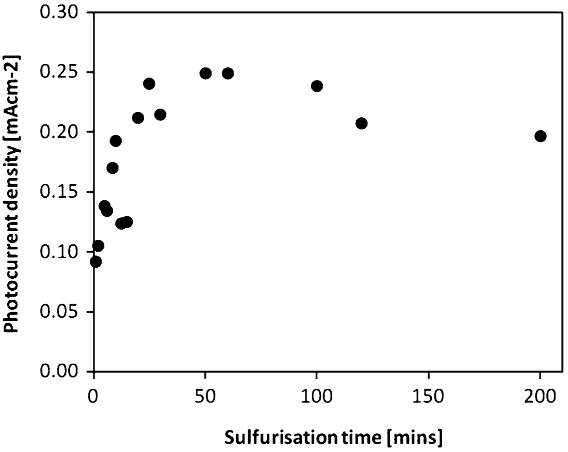

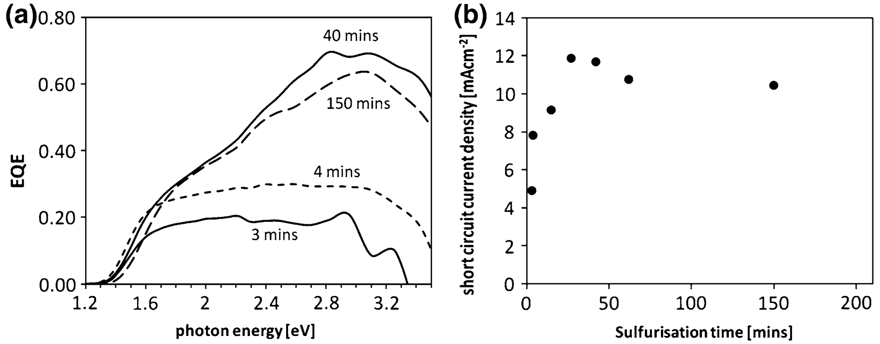

Fig. 5.16 **a** EQE spectra of samples sulfurised for different times, recorded in 0.2 M Eu(III) solution at a potential of −1.0 V vs. Ag|AgCl; and **b** the predicted short circuit current density calculated from the spectra. Other sulfurisation conditions: 580 °C, 700 mbar, 20 mg s

be a subsequent process that is responsible for the further increase in photocurrent up to around 50 min.

To learn more about the development of photoactivity with sulfurisation time, a further series of samples was prepared with a range of sulfurisation times, and EQE measurements were made. At sulfurisation times less than 2 min, the EQE response was too weak to be recorded, but after that period the response was sufficient to yield a clear spectrum. The spectra of four representative samples, corrected for reflection and absorption of the measurement cell and electrolyte, are shown in Fig. 5.16a. The band edge is clearly seen at around 1.4 eV, and the EQE rises towards a maximum at around 3 eV. The size of the band gap immediately indicates the presence of CZTS, in accordance with XRD and Raman data, since none of the possible secondary phases have similar band gaps. The magnitude of the EQE in the best case is very promising, reaching about 65% at the peak. The

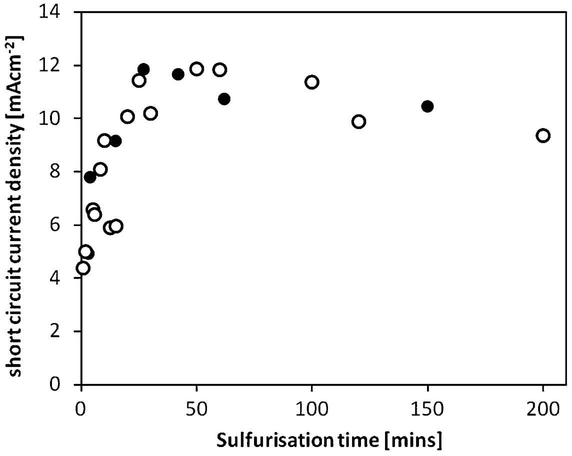

Fig. 5.17 Photocurrent densities from white light measurements of one set of samples (Fig. 5.15) superimposed on and those predicted from EQE measurements on a different set (Fig. 5.16b), showing the same trend in both cases

reduction in EQE above 3 eV is indicative of light absorption by a higher-gap covering layer, which could indicate the presence of ZnO (formed from ZnS phases under the conditions of the electrochemical measurement). The predicted short current densities under AM1.5G illumination for the entire series are shown in Fig. 5.16b.

The pattern of short circuit current densities predicted from the EQE spectra is the same as that of the photocurrents measured under white light illumination shown above in Fig. 5.15. The two are superimposed in Fig. 5.17, where the uncalibrated measurements in the latter case have been adjusted by a constant factor. The EQE data suggest that the peak in photocurrent might be reached a little earlier, after around 30 min as opposed to 50 min.

In order to test whether the rise of photocurrent up to 30–50 min is in fact due to a continued reaction with S vapour, the following experiment was carried out: one sample was sulfurised as normal for a period of 30 min. Two more identical samples were sulfurised together for five minutes only and then removed from the furnace. One of these samples was then further heated under the same conditions but without S, for a further 25 min.

EQE spectra for these three samples, corrected for reflection and absorption of the measurement cell and electrolyte, are shown in Fig. 5.18. The figure shows that, as expected from Fig. 5.15, the sample sulfurised for 5 min was worse than the sample sulfurised for 30 min. However, the sample sulfurised for five minutes and then heated without sulfur for a further 25 min was essentially the same as the sample that had been sulfurised continuously for 30 min. This shows that the photocurrent continues to develop simply as a result of the elevated temperature, and that after around five minutes (or less), the presence of S is no longer necessary. If the long sulfurisation times usually seen in the literature are to be reduced, we must understand the nature of the processes that limit the rate of formation of active material, even though CZTS itself has formed very early on.

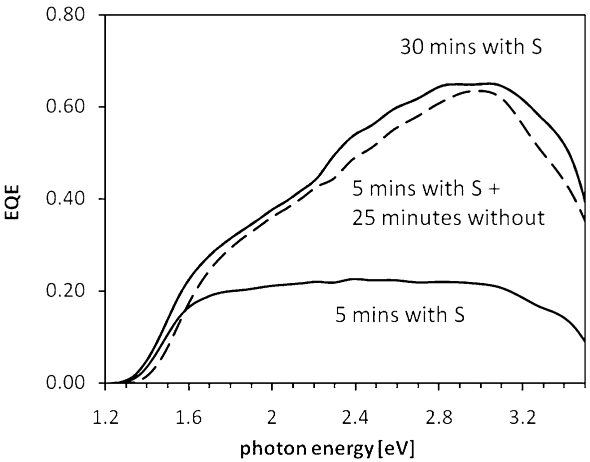

Fig. 5.18 EQE spectra showing that the role of S during sulfurisation is over after around 5 min—see text for explanation. Recorded in 0.2 M Eu(III) solution at a potential of −1.0 V vs. AglAgCl

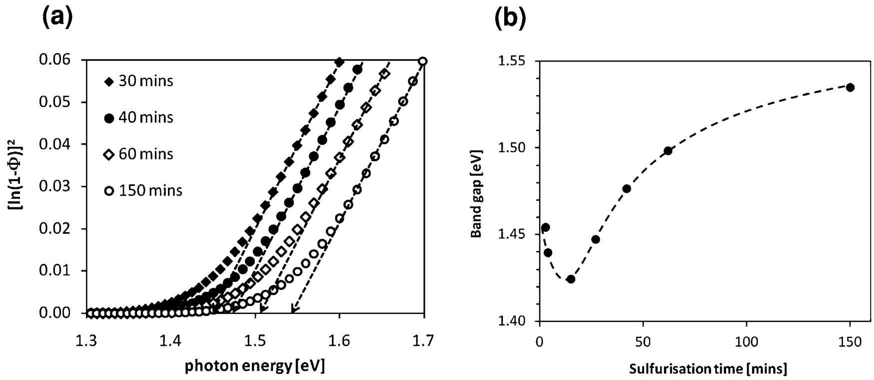

Fig. 5.19 **a** Plots constructed to derive band gaps from the onset of EQE spectra. **b** Band gaps plotted as a function of sulfurisation time. The *dashed line* in **b** is added as a guide to the eye

5.5.2 The Evolution of Band Gap with Sulfurisation Time

The band gaps of the series of samples sulfurised for different times were derived from the EQE spectra, as shown in Fig. 5.19, and are plotted as a function of sulfurisation time in Fig. 5.19b.

The evolution of the band gap is interesting; starting from a value of 1.45 eV, it drops quickly and passes through a minimum of around 1.42 eV after 15 min of sulfurisation, before rising to a limiting value of around 1.55 eV, the latter change occurring over a much longer timescale. In order to check that this trend was real and not due to scatter in the data, another series of samples was prepared, sulfurised under the same conditions (with a different set of sulfurisation times) and the measurement was repeated. The band gap values for this series are shown in

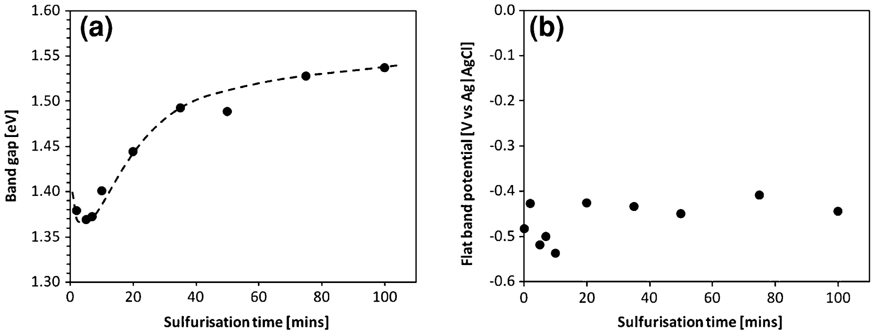

Fig. 5.20 **a** Band gaps plotted as a function of sulfurisation time for a separate set of samples, showing the same trend as those in Fig. 5.19b. The *dashed line* is added as a guide to the eye. Other sulfurisation conditions: 580 °C, 700 mbar, 20 mg s. **b** Flat-band potentials for the same sample series

Fig. 5.20a, and they do indeed show the same trend. In this case, the initial band gap and minimum value are lower, about 1.38 and 1.37 eV respectively, and the minimum occurs sooner, but the band gap at longer times still converges to 1.55 eV. The spread of band gaps covers almost the entire range that has been reported in the literature for CZTS.

The flat-band potentials, E_{fb}, were measured for this set of samples from EQE-potential plots, and are shown in Fig. 5.20b. Initially E_{fb} drops and rises within the space of 20 min, but remains constant after that time, at around −0.44 V vs. Ag|AgCl, meanwhile the band gap continues to increase. This suggests that the initial changes in band gap are accommodated by a shift in the valence band, and thereafter it is the conduction band that rises.

5.5.3 Changes in the Space Charge Region Width and Acceptor Density

Several approaches for determining W and N_a were described in Sect. 5.2 of this chapter: estimation from the slope of the EQE spectrum onset, from the slope of the EQE-bias plot at high chopping frequencies, and from measurements of capacitance. All three methods gave similar results in most cases. The acceptor concentration as a function of sulfurisation time is shown in Fig. 5.21a, as measured by capacitance and EQE as a function of electrode potential. The initial value is very high, around 2–3 $\times$ 10^{17} cm^{-3} after 3 min of sulfurisation, but it drops rapidly. N_a appears to reach a minimum after around 50 min of sulfurisation.

The size of the space charge region, W, is plotted in Fig. 5.21b. W is initially very small, less than 100 nm for a sulfurisation time of 3 min. Most of the incident

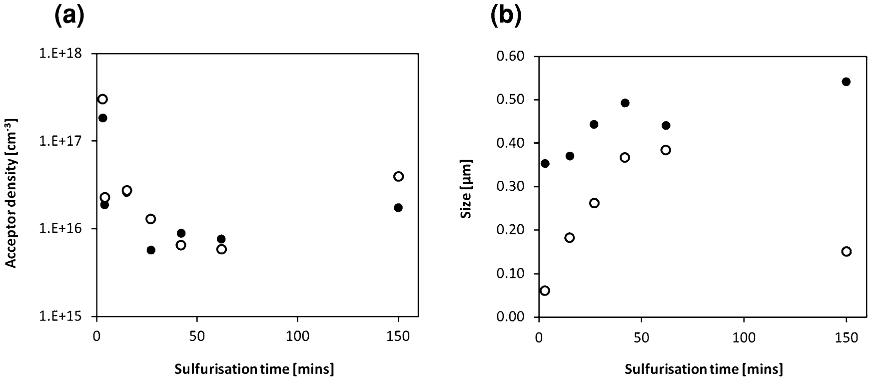

Fig. 5.21 **a** Acceptor concentration measured using both capacitance-bias (*open symbols*) and high-frequency EQE-bias measurements (*filled symbols*), as a function of sulfurisation time. **b** Values of the space charge region width (*open symbols*) as a function of sulfurisation time, compared to the average grain diameter (*filled symbols*) for the same samples

light will penetrate beyond this distance, which explains the initially low value of short circuit current density. In Fig. 5.21b, the average grain diameter estimated from SEM images is also shown. Note that the grain diameter was measured using a 'plan view', whereas W extends into the depth of the film, but we can assume that, for grain sizes less than the thickness of the film (approx. 1 µm), the grains are roughly cubic. At first, W is much smaller than the grain diameter. Between 3 and 50 min of sulfurisation time, W rises quickly, due to the drop in acceptor concentration, N_a. The rate of increase in grain diameter is much slower, and, interestingly, it seems that W may become limited by the grain size by around 50 min of sulfurisation since the initially high rate of its increase is cut short when W gets close to the grain size. At long sulfurisation times, N_a has risen and W dropped again. This is perhaps due to oxidation or element loss creating new defects.

5.5.4 Explaining the Change in Short Circuit Current as a Function of Sulfurisation Time

We are now in a position to explain the observed changes in short circuit current density, J_{sc}, as a function of sulfurisation time in this investigation. J_{sc} was seen to increase rapidly to reach a maximum value at around 30–50 min of sulfurisation. After that, it gradually decreased (see Fig. 5.17).

Of course, the first process that must occur for photocurrent to be seen is crystallisation of CZTS. Findings here and elsewhere [39] show that the CZTS phase forms very rapidly indeed, and, consistent with this, a well-defined EQE spectrum with a band gap matching that of CZTS could be recorded after just a

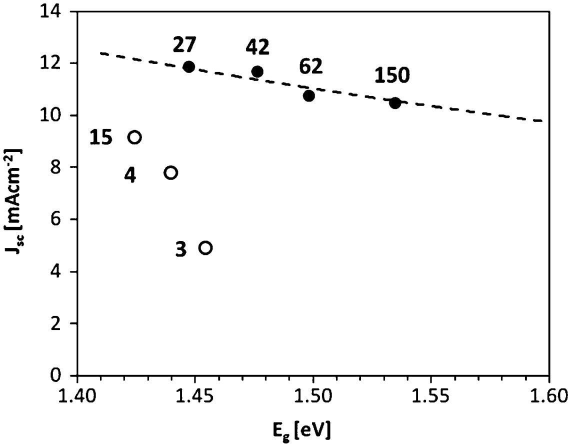

Fig. 5.22 Predicted short circuit current density for the series of samples sulfurised for different time periods plotted against their band gap. The dashed line indicates the expected effect of band gap variations on J_{sc}, and the labels indicate the sulfurisation time used

few minutes of sulfurisation. Interestingly, the photocurrent continued to improve in samples that were further heated in the *absence* of sulfur. This important result means that the processes that give rise to good photocurrent in CZTS, at least in this investigation, are not related to the presence of S beyond its role in the initial formation of CZTS. After formation of CZTS, the increase in J_{sc} occurred as a consequence of a drop in the acceptor concentration, leading to a wider space charge region and therefore more effective carrier collection. By around 30–50 min of sulfurisation, the acceptor concentration had reached a minimum and there were no further improvements in J_{sc}. The decreasing part of the J_{sc} curve at longer sulfurisation times seems to arise simply as a result of the observed band gap changes: an increasing band gap leads directly to lower current density because fewer photons are collected. This is not necessarily detrimental to the efficiency of a photovoltaic device, because in principle there is a simultaneous increase in the open circuit voltage (see Sect. 5.2.8). One limitation of the photoelectrochemical approach is that no measure of the open circuit voltage is made, so this cannot be verified here. Figure 5.22b shows that the decrease in J_{sc} at sulfurisation times above around 30 min is exactly in line with that which would be expected based purely on an increasing band gap.

Through its effect on the space charge region width, the acceptor concentration seems to be critical in determining the performance of the absorber layer. Therefore the sulfurisation time required to reach the maximum photocurrent was simply defined by the rate of decrease of the acceptor concentration. This is a key observation, because it implies that if the acceptor concentration is the only factor limiting the rate of photocurrent improvement, then shorter sulfurisation times will be possible if we can control the acceptor density that initially arises in the films. In order to do that, we need to establish (a) the nature of the acceptor states, (b) why the concentration of acceptor states decreases over time, and (c) if the high density of acceptor states is inherent to CZTS, or whether it is dependent on, for example, composition or fabrication method. The nature of the acceptor states is a

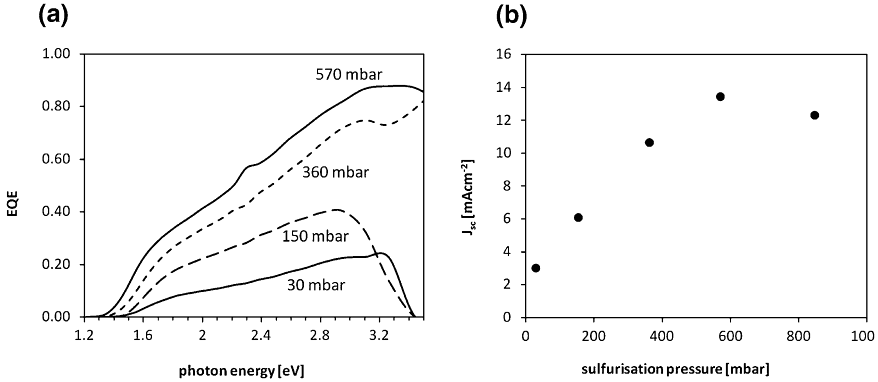

Fig. 5.23 **a** EQE spectra for a series of sample sulfurised at different pressures. Other sulfurisation conditions: 580°C, 40 min, 20 mg s. Recorded in 0.2 M Eu(III) solution at a potential of −1.0 V vs. Ag|AgCl. **b** Predicted short circuit current density under AM1.5G illumination as a function of sulfurisation background pressure

matter beyond the scope of this investigation and much further work is required to elucidate this in CZTS.

5.6 The Effect of Background Pressure During Sulfurisation

In Chap. 3 it was shown that the sulfurisation background pressure had a strong influence on grain size and orientation, which both increased at lower pressures. The rate of emergence of sulfide phases was seen to be lessened at lower pressures, due to an effective reduction in the partial pressure of S vapour within the graphite container. Bearing these effects in mind, samples were sulfurised at a range of background pressures while keeping the other conditions constant (580 °C for 40 min) and their EQE spectra were measured. These spectra and the derived values of short circuit current density under AM1.5G illumination are shown in Fig. 5.23a and b.

There is a clear relationship between sulfurisation pressure and short circuit current density. Very poor currents are obtained at low pressures, but higher pressures lead to much better values. There is also a drop in J_{sc} at the highest pressure used here.

The space charge region width was estimated from the slope of the EQE onset, and used to calculate values of N_a. The results for both parameters are shown in Fig. 5.24a and b. Figure 5.24a also shows the average grain size estimated from SEM images.

We see a similar relationship between W and grain size as in Sect. 5.3: the space charge region approaches, but never exceeds the grain size. In the pressure range 30–600 mbar W increases; meanwhile the grain size is rapidly dropping. The two

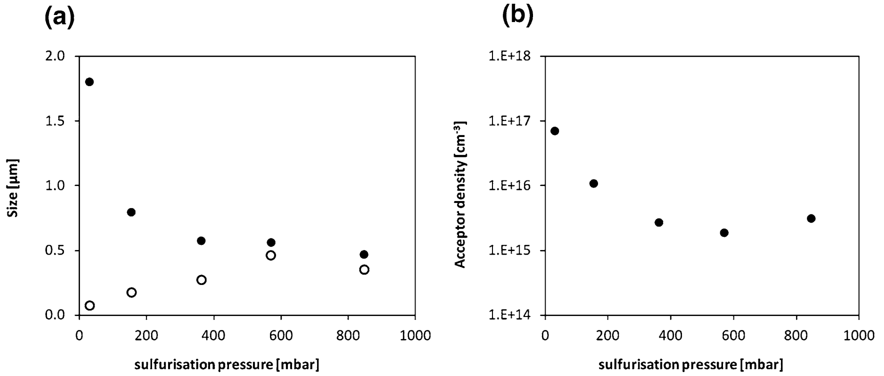

Fig. 5.24 **a** Space charge region width and average grain diameter as a function of sulfurisation pressure. **b** Acceptor concentrations derived from the values of the space charge region width

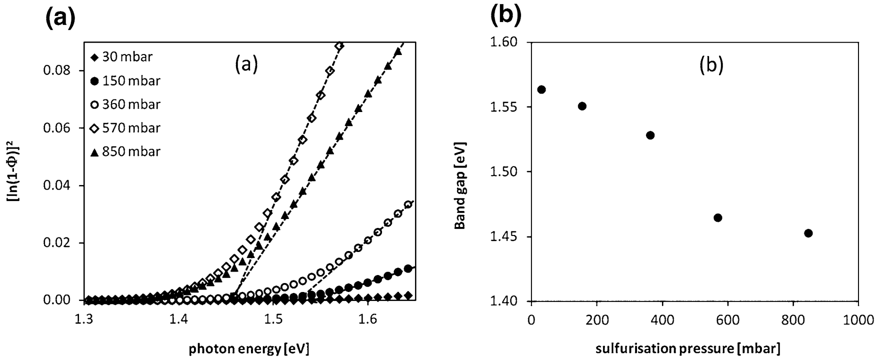

Fig. 5.25 **a** Derivation of band gaps from the EQE spectra of samples sulfurised at different pressures. **b** Band gap as a function of sulfurisation pressure

meet at around 600 mbar, and when the grain size continues to drop at higher pressures, *W* now drops with it. Note that when *W* is being limited by the grain size, N_a will be overestimated by every technique employed herein, since they all rely on measurement of the space charge region.

The variation in J_{sc}, Fig. 5.23b, is simply related to the changes in acceptor concentration. The reason for the high acceptor concentration at lower pressures, leading to a poor J_{sc}, could be related to incomplete sulfurisation or element losses by evaporation—Zn from the precursor or SnS from the sulfurised film—creating defects in the film. Both loss processes were seen in Chap. 4.

The band gaps of the sample series were derived from the EQE spectra, as shown in Fig. 5.25a, and are presented in Fig. 5.25b. There is a smooth trend in band gap between two limiting values, 1.56 and 1.45 eV. Interestingly, these values are similar to the extreme values seen for the series of samples sulfurised for different times in Sect. 5.5.2.

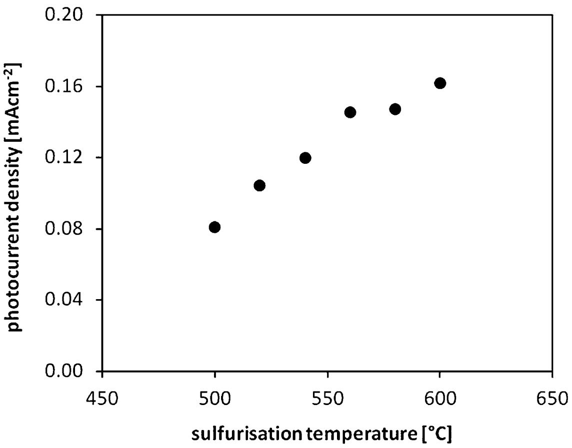

Fig. 5.26 Photocurrent density measured under white light illumination for a series of samples sulfurised with different temperatures. Other conditions: 700 mbar, 45 min, 20 mg s

5.7 The Effect of Sulfurisation Temperature

A series of samples were prepared with different sulfurisation temperatures in the range 500–600°C. The sulfurisation time and background pressure were 45 min and 600 mbar respectively. The sample photocurrent density was measured under chopped illumination from a white LED, and is shown in Fig. 5.26. There is a reasonably strong dependence upon sulfurisation temperature, probably linked to an increase in the rate of a thermally activated process. Since the sulfurisation time used here is much greater than the time required to form the CZTS phase, the effect should not be related to the actual formation reactions of CZTS, but could be due to, for example, an increased rate of grain growth leading to a larger space charge region as discussed above. This possibility was not investigated at this stage of the experimental work. It appears that the photocurrent has almost reached a maximum at 600°C, but the temperature could not be increased further due to softening of the SLG substrates.

5.8 The Effects of Cu-Content

This section concerns the opto-electronic properties of the series of samples discussed in Chap. 4 which had variable Cu-content, as well as an additional series of samples that was prepared in order to provide more data.

The compositions of the samples before and after etching are shown in Fig. 5.27a and b. The sulfurised samples are spread through the Cu-poor, Sn-rich and Zn-poor sections of the diagram. After etching, they are all within the Cu-poor or Sn-rich regions. It was seen in Chap. 4 that, while the compositions of the films were very similar after etching, some properties, for example grain size, were very different, because they depended on the amount of Cu that was present *before*

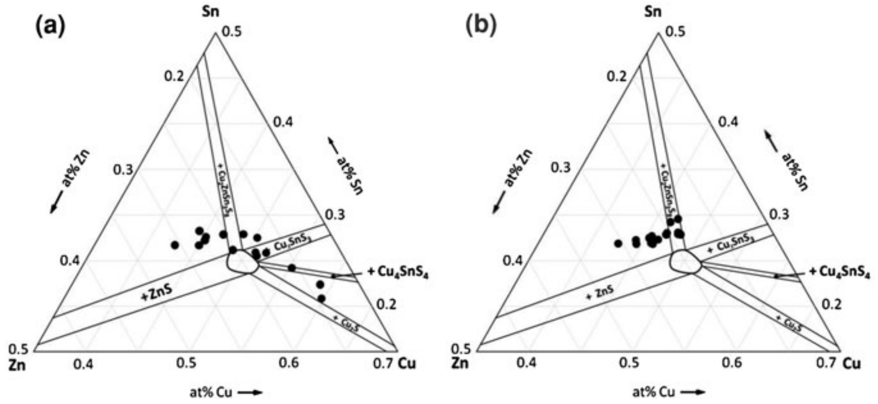

Fig. 5.27 Compositions of the samples **a** after sulfurisation, and **b** after etching

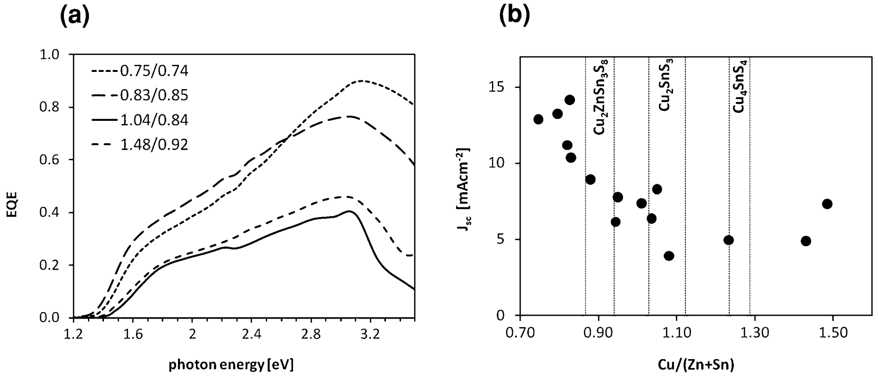

Fig. 5.28 **a** EQE spectra for a series of samples with different Cu/(Zn + Sn) ratios. The labels indicate this ratio before/after etching. Recorded in 0.2 M Eu(III) solution at a potential of −1.0 V vs. Ag|AgCl. **b** Predicted short circuit current densities as a function of Cu-content in the sulfurised film, showing the approximate positions of some *tie-lines* in the ternary phase diagram

etching (i.e. the amount that was present during film growth). The only role of etching was to remove surface phases, which can act as recombination centres. Therefore, while it is quite necessary to etch the samples in order to reveal the true opto-electronic properties of the underlying film, the properties themselves depend primarily upon the sample composition during sulfurisation, not the composition after etching. In the following discussion and data presentation, the Cu/(Zn + Sn) ratio during sulfurisation will be used as a metric.

EQE spectra for selected samples, corrected for reflection and absorption of the measurement cell and electrolyte, are shown in Fig. 5.28a. The EQE spectra are highest for the samples that had compositions in the Cu-poor or Sn-rich regions of the phase diagram prior to etching, and lower for those that were in the Zn-poor region.

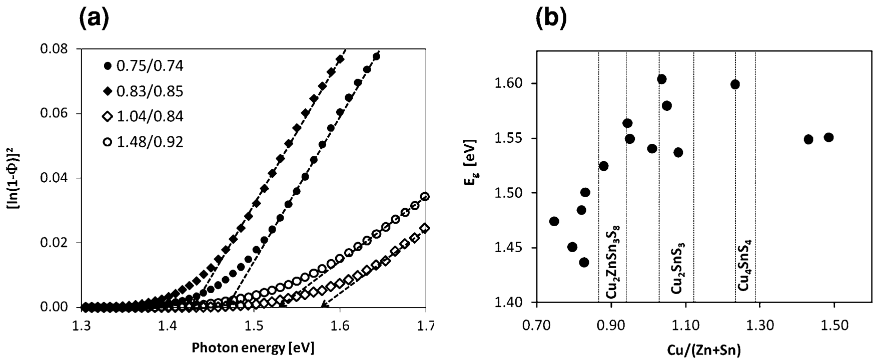

Fig. 5.29 **a** Derivation of the band gaps for selected samples with different Cu/(Zn + Sn) ratios. The values of Cu/(Zn + Sn) before and after etching are indicated. **b** Band gap as a function of Cu/(Zn + Sn) ratio in the sulfurised film, showing the approximate positions of some *tie-lines* in the ternary phase diagram

The EQE spectra in Fig. 5.28a were used to compute the expected short circuit current density, J_{sc}, that would be produced from the samples under standard AM1.5G illumination. The resulting values of J_{sc} are plotted in Fig. 5.28b. Although there is scatter in the data, there is a clear trend towards lower J_{sc} values for the films in the Zn-poor region of the phase diagram, i.e. those that had Cu–Sn–S secondary phases present before etching. It should be noted that none of the samples fell into the Cu-rich region, where Cu_2S is the only secondary phase expected, so unfortunately it is not known whether there would be different behaviour in that case.

The reason for the lower performance of the Zn-poor films is very likely related to the presence of the Cu–Sn–S phases that occur in these samples. These phases are removed by KCN etching, but there are two possible mechanisms by which the EQE of the etched film can be affected: firstly, with reference to the SEM images in Sect. 4.5.4, it is apparent that etching leaves 'scars' that cover the Zn-poor films and cause a severe reduction in the area of active material, whereas the EQE analysis so far assumes that the entire illuminated area is uniform. This would cause a general reduction in EQE at all wavelengths. Secondly, any particles of Cu–Sn–S phases that remained after etching, either because etching was incomplete or because they were inaccessible to the etchant, will act as recombination centres and reduce carrier collection for all wavelengths. This means that the short circuit current density, while a good indicator of overall film quality, is not a good indicator of the properties of the bulk photoactive material. The band gap estimated from the EQE spectrum is not affected by these issues, and therefore does tell us something fundamental about the material. The band gaps were estimated from the EQE spectra, as indicated in Fig. 5.29a, and are shown in Fig. 5.29b. For samples in the Zn-poor region, the band gap is around 1.55–1.60 eV, while for samples in the Cu-poor region, it is about 0.1 eV lower.

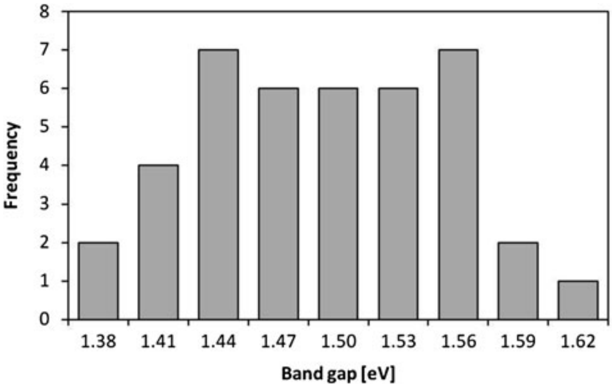

Fig. 5.30 Histogram showing the distribution of band gap values measured in this investigation

5.9 Observations on Trends in the Band Gap of Cu_2ZnSnS_4 Films

A consistent feature observed when changing the sulfurisation conditions and composition was a shift in the band gap of the CZTS films. A histogram of all the band gaps mentioned in this report (41 samples in total) is shown in Fig. 5.30. The tails of the distribution extend from 1.38 to 1.62 eV, but most samples are within the range 1.44–1.56 eV. The variation in band gap values within this investigation encompasses the entire range of values reported in the CZTS literature.

Apart from the large spread of band gap values, there are clear trends when changing, for example, sulfurisation pressure or time while keeping other variables constant. Smooth transitions between limiting values of about 1.4 and 1.55 eV are observed. This shift is considerable, and requires some explanation. Suggestions of trends can be found in the literature, with larger band gaps being seen for those films sulfurised with higher temperatures [11], lower pressures [17] and for longer times [6], but to the best of our knowledge at the time of writing, this investigation provides the clearest evidence so far for rational changes in the band gap as a function of composition and sulfurisation conditions. The key figures from Sects. 5.1–5.8 are reproduced below.

Note the similarity between the extremes of band gap in each figure. Two hypotheses are now presented, each of which can, to a greater or lesser extent, explain these trends. Further work is required to test each hypothesis, and suggestions are made as to how this could be carried out.

5.9.1 Hypothesis A: A Kesterite-Stannite Solid Solution

The two different crystal structures for CZTS, kesterite and stannite, have similar energies. Although kesterite is the thermodynamically stable phase, stannite is

Table 5.3 Band gaps, E_g, for the end members of some solid solutions, and the minimum value, $E_{g,min}$ found within the range of the solution at a given value of x

Solid solution	E_g (x = 0) (eV)	E_g (x = 1) (eV)	$E_{g,\ min}$ (x) (eV)	Source
$Cd_{1-x}Zn_xTe$	1.5	2.25	–	[43]
$CdTe_{1-x}S_x$	1.5	2.4	1.34 (0.3)	[44]
$Cu(In_{1-x}Ga_x)Se_2$	1.0	1.64	–	[45]
$CuIn(Te_{1-x}Se_x)_2$	0.95	0.95	0.85 (0.5)	[45]

Table 5.4 Band gap values calculated for kesterite and stannite

Source	E_g(Stannite) (eV)	E_g (Kesterite) (eV)	Difference (eV)
[19]	1.38	1.50	0.12
[20]	1.42	1.56	0.14
[21]	1.295	1.487	0.192

calculated to be only slightly higher in energy. Both experimental observations of the $Cu_2Fe_xZn_{1-x}SnS_4$ series [40–42] and calculations of CZTS lattice energies [19–21] point to the existence of a 'solid solution' between the two phases, with stannite existing as a metastable phase. Although the perfect structures of kesterite and stannite have different space groups (1$\bar{4}$2m and 1$\bar{4}$ respectively), the disordered kesterite structure, which has a random arrangement of Cu and Zn atoms on their shared planes, also has the 1$\bar{4}$ space group. Therefore a solid solution between metastable stannite and disordered kesterite is possible in principle. Note that this is a special case of a solid solution, since there is only structural as opposed to compositional variation.

The change in band gap throughout a solid solution is well-documented in many cases. Examples from the literature are shown in Table 5.3. The band gap in each case varies smoothly between the values of the two end members. The form of the variation is in general parabolic, and in certain cases there is a minimum in the band gap that is lower than either of the end members of the solid solution. This so-called 'bowing' behaviour is seen when both the valence and conduction bands shift in different compositional ranges of the solid solution.

Returning to CZTS, band gap values have been calculated for the kesterite and stannite forms of CZTS, and are shown in Table 5.4. The agreement between the calculated values for kesterite and stannite and the maximum and minimum values measured in this work (Fig. 5.31) is striking. Were a kesterite-stannite solid solution to exist, we can expect a smooth change in band gap as a function of the extent of cation ordering. We now attempt to apply this theory to each of the trends in Fig. 5.31a–d in turn.

First, the change in band gap as a function of sulfurisation time will be examined. In the early stages of sulfurisation, we see a lower band gap, 1.37–1.42 eV, which slowly rises towards a limiting value of around 1.55 eV at long sulfurisation times. The limiting values are in very good agreement with the predicted values for the stannite and kesterite phases. Therefore we propose that under the conditions of this study, the first phase to form is in fact stannite.

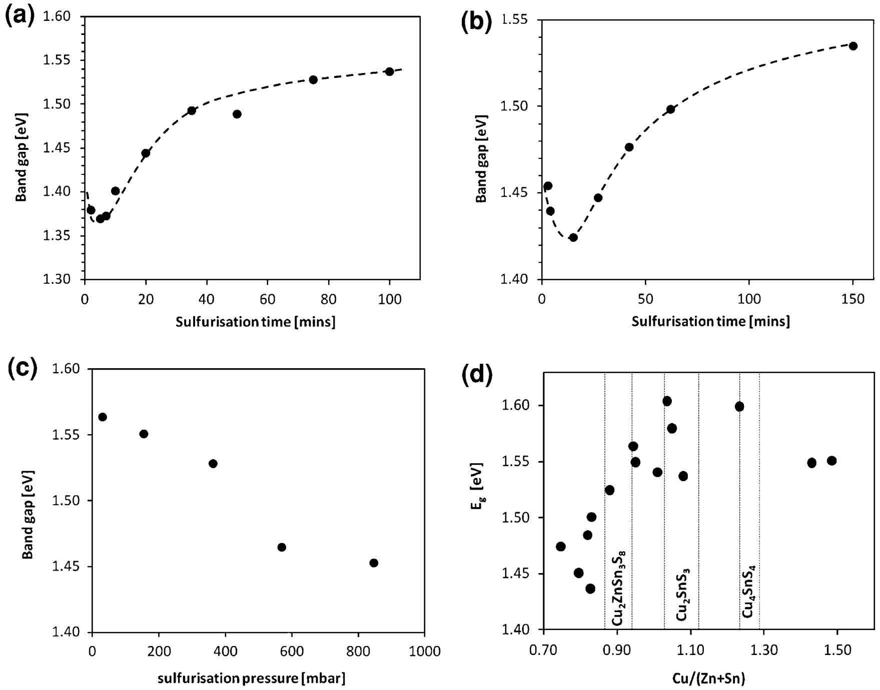

Fig. 5.31 Variations in band gap as a function of **a**, **b** the sulfurisation time, **c** the sulfurisation pressure, and **d** the composition of the sulfurised films

Although it is not the thermodynamically most stable phase, it may nevertheless be the kinetic product of the rapid formation of CZTS. Once it has formed, however, due to the lower energy of the kesterite phase, there is a driving force for conversion from stannite to kesterite. The energy difference, and therefore the thermodynamic driving force, is small, and there may also be an energy barrier to overcome to achieve the transition; however, at an elevated temperature and given a long enough period of time, a process of cation rearrangement will lead to the thermodynamic product, the kesterite phase. During the structural transition, the band gap smoothly changes in relation to the extent of cation reordering. This then, is what happens over the approx. 2 h period at 560 °C covered in Fig. 5.31a and b. That the band gap actually passes though a minimum in the early stages of the process would be an example of the commonly observed bowing behaviour in solid solutions, as seen in Table 5.3. The band gap calculated for an intermediate (albeit still ordered) kesterite-stannite structure was 1.07 eV, which lends support to this possibility [21].

When a sample in the above-mentioned series was sulfurised for 40 min, the band gap was around 1.47 eV. The sulfurisation was done at a background pressure of 700 mbar and the samples were Cu-poor. In the cases of lower pressures and high Cu-content, higher band gaps, around 1.56 eV, are seen for the same sulfurisation time. There are two possibilities: (1) that under these conditions the structural transition from stannite to kesterite is more rapid, or (2) that due to a different reaction mechanism under these conditions, the kesterite phase is the direct product of the sulfurisation reaction. In support of (2), the formation reactions in the cases of lower pressure and high Cu-content are clearly very different from those in the Cu-poor, higher pressure scenarios, since significantly larger grains were observed (see Sect. 4.5). It could therefore simply be the case that under these conditions kesterite is formed directly, resulting in the larger band gap. The reason proposed for the smaller grain size at higher pressures was the presence of secondary phases pinning grain boundaries. It is possible that these could also affect the rate of transformation between stannite and kesterite.

The strengths of this hypothesis are that it can completely explain the band gap variation as a function of sulfurisation time, as well as account for the large range of band gaps observed in the literature. The extremes of band gap match well with those predicted by computational models, and the presence of a solid solution of kesterite and stannite is very likely based on the available evidence. However, to date there is no experimental verification of the stannite structure in CZTS thin films to lend support to the theory, which is its main weakness. Explanation of the band gap shifts when composition and pressure are altered is also more difficult with this hypothesis.

In terms of experimental verification, differentiation of the stannite phase from the kesterite phase in CZTS films should be possible by the use of neutron scattering. Since the transformation is proposed to occur due only to elevated temperatures, an in situ neutron scattering experiment using a heated chamber would be an elegant way of testing the hypothesis. In addition, computer simulations of a solid solution of kesterite and stannite structures may help to explain the behaviour. More evidence obtainable using the techniques from this investigation would be the effect of sulfurisation time on band gap at low pressure or for samples with higher Cu-content.

In terms of implications for the production of thin film devices, there is no reason at this stage to favour either kesterite or stannite. However, the possibility of adjusting the band gap only by a suitable thermal treatment rather than a compositional change is very interesting, and could provide a useful tool in device optimisation.

5.9.2 Hypothesis B: A Cu_2ZnSnS_4–$Cu_2ZnSn_3S_8$ Interaction

A further possibility that fits the available data is that a Sn-containing secondary phase may influence the opto-electronic properties of the film. This possibility is suggested because in all of the experiments here there is a correlation between the presence of excess Sn and the appearance of lower band gaps. The relationship is shown in Fig. 5.32 for two adjacent sections of the ternary phase diagram, connected by the CZTS–$Cu_2ZnSn_3S_8$ tie line. The data shown in Fig. 5.32a are for the

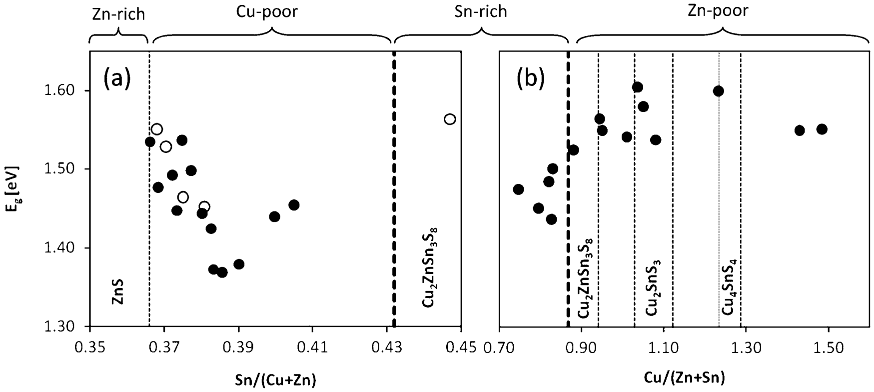

Fig. 5.32 Correlation between band gap and position in the ternary phase diagram, plotted along two sections of the diagram and intersecting at the *bold dashed line*. *Labels* and *narrow dashed lines* indicate the two-phase fields where CZTS is formed alongside a single secondary phase. The spaces between are three phase fields. **a** Samples from the sulfurisation pressure (*open circles*) and sulfurisation time (*filled circles*) series, **b** samples from the Cu-content series

samples sulfurised at different pressures and those sulfurised for different time periods. The data in Fig. 5.32b are for the samples that had different Cu-content. Following the trend from left to right, the band gap is initially about 1.55 eV at the edge of the CZTS–ZnS two-phase field (this boundary is the one defined in Sect. 4.8.2). As the samples move into the three phase field, where $Cu_2ZnSn_3S_8$ should be formed, the band gap decreases to a minimum value of 1.38 eV, before rising again as the CZTS–$Cu_2ZnSn_3S_8$ two-phase field is approached. This rising trend can be seen to continue on the left-hand side of Fig. 5.32b. After the samples move out of the CZTS–$Cu_2ZnSn_3S_8$ two-phase field, the band gap remains more or less constant, again at about 1.56 eV.

Although the phase diagram does not indicate a solid solution between CZTS and $Cu_2ZnSn_3S_8$, there may be a non-equilibrium mixture that nevertheless influences the material properties. At longer times or at lower pressures, the amount of the Sn-containing secondary phase is reduced due to evaporation, so the band gap of the pure kesterite phase is expressed. When the Cu-content is higher, there ought to be no Sn-excess, which is why the films that were in the Zn-poor region of the phase diagram during sulfurisation also had higher band gaps.

This hypothesis is much weaker because of the lack of experimental data about $Cu_2ZnSn_3S_8$. It would at least be possible to rule out the mechanism by producing films in the Zn-rich or Sn-poor regions of the phase diagram and repeating the measurement of band gap as a function of sulfurisation time: if the same shifts in band gap were observed for samples which should not in principle contain any Sn-excess, then the hypothesis can be rejected. In this instance the correlation between Sn-content and band gap may be attributable to a third variable upon which both factors depend.

Conclusions

Whereas Chap. 4 was concerned with the effects of sulfurisation conditions and precursor composition upon structural properties of the films, this chapter was concerned with the effects of those same variables upon the opto-electronic properties of the films. A straightforward photoelectrochemical approach was utilised to make measurements of the photocurrent arising from CZTS films. Measurements as a function of illumination wavelength were used to generate EQE spectra, from which values of the band gap of the films were derived. In general, good EQE spectra were recorded, with peak values up to 80% and well-defined band edges. The impurity concentration and predicted short circuit current density under standard AM1.5 illumination were also derived.

Etching in KCN was found to be particularly important to get good photocurrent responses from the films, especially if they were Zn-poor/Cu-rich.

The effects of sulfurisation time and pressure upon opto-electronic properties were studied for Cu-poor films. The photocurrent in most instances was dependent on the acceptor concentration of the films. Apart from the initial formation of CZTS, the photocurrent did not depend upon the presence of S vapour; it depended only upon the time for which the sample was heated. The increase in photocurrent occurred over a period of around 30–50 min of heat-treatment, and was simply correlated to a decrease in acceptor concentration, as measured by two different techniques. When pressure was the variable, the acceptor concentration was higher at low pressures, which may have been related to element losses or incomplete conversion of the sample.

The behaviour of films with higher Cu-content was dominated by the presence of Cu(–Sn)–S secondary phases. These were removed by etching but the post-etching morphology was very poor, which may have affected the optical properties of the films.

The main result of this study was the demonstration of smooth band gap variations as a function of sample composition and sulfurisation conditions. In the case of sulfurisation time, the data showed a clear trend: the band gap started from about 1.4 eV, passed through a minimum after about 10–15 min of sulfurisation and then rose gradually to 1.55 eV. The band gap also varied between similar extremes when the pressure and Cu-content were varied: higher band gaps were seen at low pressures and for films with higher Cu-content. Two hypotheses were presented that could explain the observations, and suggestions were made to test them. The first hypothesis was a fundamental structural rearrangement of the CZTS phase between stannite and kesterite, which have been shown theoretically to have different band gaps. The second hypothesis concerned the possibility that a Sn-containing secondary phase was responsible for affecting the optical properties of the film.

References

1. Matsushita H, Ichikawa T, Katsui A (2005) Structural, thermodynamical and optical properties of Cu_2-II-IV-VI4 quaternary compounds. J Mater Sci 40(8):2003–2005
2. Pawar SM et al (2010) Single step electrosynthesis of Cu_2ZnSnS_4 (CZTS) thin films for solar cell application. Electrochim Acta 55(12):4057–4061
3. Ito K, Nakazawa T (1988) Electrical and optical-properties of stannite-type quaternary semiconductor thin-films. Jpn J Appl Phys, Part 1-Regul Pap Short Notes Rev Pap 27(11): 2094–2097
4. Nakayama N, Ito K (1996) Sprayed films of stannite Cu_2ZnSnS_4. Appl Surf Sci Proc Seventh Int Conf Solid Films Surf 92:171–175
5. Friedlmeier TM et al. (1997) HEterojunction based on Cu_2ZnSnS_4 and Cu_2ZnSSe_4 thin films. In: 14th European PVSEC, 1997
6. Katagiri H et al (1997) Preparation and evaluation of Cu_2ZnSnS_4 thin films by sulfurization of EB evaporated precursors. Sol Energy Mater Sol Cells 49(1–4):407–414
7. Katagiri H et al. (2003) Solar cell without environmental pollution by using CZTS thin film. Proceedings of 3rd world conference on photovoltaic energy conversion, vol a–C. pp 2874–2879
8. Katagiri H (2005) Cu_2ZnSnS_4 thin film solar cells. Thin Solid Films 480–481:426–432
9. Tanaka T et al (2005) Preparation of Cu_2ZnSnS_4 thin films by hybrid sputtering. J Phys Chem Solids 66(11):1978–1981
10. Zhang J et al (2006) Cu_2ZnSnS_4 thin films prepared by sulfurization of ion beam sputtered precursor and their electrical and optical properties. Rare Met 25:315–319
11. Moriya K, Tanaka K, Uchiki H (2007) Fabrication of Cu_2ZnSnS_4 thin-film solar cell prepared by pulsed laser deposition. Jpn J Appl Phys, Part 1-Regul Pap Brief Commun Rev Pap 46:5780–5781
12. Katagiri H et al (2008) Enhanced conversion efficiencies of Cu_2ZnSnS_4-based thin film solar cells by using preferential etching technique. Appl Phys Express 1(4):041201
13. Moriya K, Tanaka K, Uchiki H (2008) Cu_2ZnSnS_4 thin films annealed in H_2S atmosphere for solar cell absorber prepared by pulsed laser deposition. Jpn J Appl Phys 47(1):602–604
14. Scragg JJ, Dale PJ, Peter LM (2008) Towards sustainable materials for solar energy conversion: preparation and photoelectrochemical characterization of Cu_2ZnSnS_4. Electrochem Commun 10(4):639–642
15. Siebentritt S, Rau U (eds) (2006) Wide-gap chalcopyrites. Spinger, Berlin
16. Suresh Babu G et al (2010) Effect of Cu/(Zn + Sn) ratio on the properties of co-evaporated $Cu_2ZnSnSe_4$ thin films. Sol Energy Mater Sol Cells 94(2):221–226
17. Pawar SM et al (2010) Effect of laser incident energy on the structural, morphological and optical properties of Cu_2ZnSnS_4 (CZTS) thin films. Curr Appl Phys 10(2):565–569
18. Scragg JJ et al (2008) New routes to sustainable photovoltaics: evaluation of Cu_2ZnSnS_4 as an alternative absorber material. Phys Status Solidi B-Basic Solid State Phys 245(9): 1772–1778
19. Chen SY et al (2009) Crystal and electronic band structure of Cu_2ZnSnX_4 ($X = S$ and Se) photovoltaic absorbers: first-principles insights. Appl Phys Lett 94(4):041903
20. Persson C (2010) Electronic and optical properties of Cu_2ZnSnS_4 and $Cu_2ZnSnSe_4$. J Appl Phys 107(5):053710
21. Paier J et al (2009) Cu_2ZnSnS_4 as a potential photovoltaic material: a hybrid Hartree-Fock density functional theory study. Phys Rev B 79(11):115126
22. Negami T et al (1995) Preparation and characterization of $CU(IN_{1-X}GA_X)(3)SE\text{-}5$ thin-films. Appl Phys Lett 67(6):825–827
23. Raulot JM, Domain C, Guillemoles JF (2005) Ab initio investigation of potential indium and gallium free chalcopyrite compounds for photovoltaic application. J Phys Chem Solids 66(11):2019–2023

24. Chen SY et al (2010) Defect physics of the kesterite thin-film solar cell absorber Cu_2ZnSnS_4. Applied Physics Letters 96(2):021902
25. Olekseyuk ID, Dudchak IV, Piskach LV (2004) Phase equilibria in the Cu_2S–ZnS–SnS_2 system. J Alloys Compd 368(1–2):135–143
26. Garg G, Bobev S, Ganguli AK (2001) Single crystal structure and electrical properties of $Cu_8Ni_4Sn_{12}S_{32}$. J Alloys Compd 327(1–2):113–115
27. Todorov TK, Reuter KB, Mitzi DB (2010) High-efficiency solar cell with earth-abundant liquid-processed absorber. Adv Mater 22(20):E156–E159
28. Katagiri H et al. (1997) Rare-metal free thin film solar cell. Proceedings of the power conversion conference, vol I and Ii. Nagaoka, pp 1003–1006
29. Araki H et al (2009) Preparation of Cu_2ZnSnS_4 thin films by sulfurizing electroplated precursors. Sol Energy Mater Sol Cells 93(6–7):996–999
30. Ennaoui A et al (2009) Cu_2ZnSnS_4 thin film solar cells from electroplated precursors: novel low-cost perspective. Thin Solid Films 517(7):2511–2514
31. Scragg JJ, Berg D, Dale PJ (2010) A 3.2% efficient kesterite device from electrodeposited stacked elemental layers. J Electroanal Chem 646(1–2):52–59
32. Morrison SR (1980) Electrochemistry of semiconductor and oxidised metal electrodes. Plenum Press, New York
33. Lincot D et al (1990) Photoelectrochemical study of para-type copper indium diselenide thin-films for photovoltaic applications. Sol Energy Mater 20(1–2):67–79
34. Gartner WW (1959) Depletion-layer photoeffects in semiconductors. Phys Rev 116(1):84–87
35. Compton RG (ed) (1989) New techniques for the study of electrodes and their reactions. Comprehensive chemical kinetics, vol 29. Elsevier, New York
36. Pourbaix M (ed) (1974) Atlas of electrochemical equilibria in aqueous solutions, 2nd edn. NACE Celebcor, USA
37. Nelson J (2003) The physics of solar cells. Imperial College Press, London
38. Peat R, Peter LM (1987) Determination of the electron-diffusion length in para-gap by intensity modulated photocurrent measurements with an electrolyte contact. Appl Phys Lett 51(5):328–330
39. Weber A et al (2009) In situ XRD on formation reactions of Cu_2ZnSnS_4 thin films. phys status solidi C 6(5):1245–1248
40. Schorr S, Hoebler HJ, Tovar M (2007) A neutron diffraction study of the stannite-kesterite solid solution series. Eur J Mineral 19(1):65–73
41. Bernardini GP et al (1990) New data on the Cu_2FeSnS_4-Cu_2ZnSnS_4 pseudobinary system at 750 and 550 °C. Eur J Mineral 2(2):219–225
42. Bonazzi P et al (2003) A model for the mechanism of incorporation of Cu, Fe and Zn in the stannite - kesterite series, Cu_2FeSnS_4-Cu_2ZnSnS_4. Can Mineral 41:639–647
43. Zelaya-Angel O et al (2004) On the bowing parameter in $Cd_{1-x}Zn_xTe$. J Appl Phys 95(11):6284–6288
44. Lane DW (2006) A review of the optical band gap of thin film CdS_xTe_{1-x}. Sol Energy Mater Sol Cells 90(9):1169–1175
45. Tinoco T, Quintero M, Rincon C (1991) Variation of the energy-gap with composition in AIBIIIC$_2$VI chalcopyrite-structure alloys. Phys Rev B 44(4):1613–1615

Chapter 6
Conclusions and Recommendations for Further Studies

The main aim of this project was to demonstrate the formation of viable Cu_2SnSnS_4 (CZTS) films from the sulfurisation of electrodeposited stacked films of Cu, Sn and Zn. The development of an electrodeposition route for 'stacked elemental layer' (SEL) precursor was described in Chap. 2. The route allows relatively good control of precursor composition, and compositional uniformity was achieved by the use of a rotating disc electrode system. Mo|Cu|Sn|Cu|Zn stacked films were produced as CZTS precursors, and were converted to CZTS films by sulfurisation in a rapid thermal processing system (RTP), which was described in Chap. 3. The use of rapid thermal processing has enabled some time-resolved studies of film formation to be carried out, and in Chap. 3 a model was proposed for film formation when fast heating rates are employed.

The rest of this investigation concerned the effects of sulfurisation conditions and precursor composition upon the observable properties of the film. Chapter 4 was concerned with the structural properties of the films: morphology (particularly grain size), the likely secondary phases present, and the changes in composition induced by element losses during sulfurisation and KCN etching. Chapter 5 was concerned with the opto-electronic properties of the same films.

The vast majority of reports concerning production of CZTS films have used two-stage processes: a precursor, which contains the metallic elements (and in some cases also the chalcogen), is heated in an atmosphere of S vapour or H_2S to induce crystallisation of CZTS. In this respect, the method used herein is relevant to much of the work carried out on CZTS. Part of the motivation for the current study comes from two as-yet unexplained observations common to the CZTS literature. These are (a) the apparent need for long sulfurisation times and (b) the preference for Cu-poor/Zn-rich compositions. As has been emphasised, long sulfurisation times (up to 8 h) are routinely used, but until now there has been no dedicated study of the effect of changing the sulfurisation time on the properties of the CZTS film. In terms of composition, the best devices in the literature are usually described as 'Cu-poor' and 'Zn-rich', although under the definition of composition labels used in this project, they are more often simply Zn-rich. There have been a few attempts to study the

J. J. Scragg, *Copper Zinc Tin Sulfide Thin Films for Photovoltaics*,
Springer Theses, DOI: 10.1007/978-3-642-22919-0_6,

influences of composition on film properties, but much more must be done to understand the relationship between composition and device efficiency.

Part of the difficulty in understanding the effect of sulfurisation conditions and sample composition is that the two are causally linked: the choice of sulfurisation conditions affects the composition by element loss processes, and therefore the composition changes as a function of sulfurisation time or pressure. In addition, the composition of the precursor also affects the formation processes leading to CZTS, for example the rate of grain growth is enhanced with a higher Cu-content, and so the required sulfurisation conditions may change.

To conclude this report, we will discuss the conditions that gave rise to the better material in the present case, compare these to the CZTS device literature, and finally make some recommendations for further studies.

6.1 The Role of Sulfurisation Conditions

In this study, the effects of changing sulfurisation conditions were investigated using Cu-poor samples ($Cu/Zn + Sn \sim 0.8$, $Zn/Sn \sim 1$). This was because Cu-poor samples have been repeatedly found to give better devices.

The first point to make is that this study found no evidence that long sulfurisation times are inherently important for CZTS. Chapter 3 showed that CZTS emergence was fast, in agreement with previous kinetic studies. Chapter 4 showed that there were no changes in the phase structure, as measured by XRD and Raman spectroscopy, after the first few minutes of sulfurisation. The only visible effects of longer sulfurisation times were a continual increase in grain size over a period of several hours, and the evaporation of a Sn-containing secondary phase aver a period of about 30 min (at 560 °C, 700 mbar). It was also found in that chapter that S vapour was resident in the hot zone of the furnace for at most 5 min. In terms of the opto-electronic properties, the external quantum efficiency (EQE) spectra continued to improve up to until 30–50 min of sulfurisation, as seen in Chap. 5. It was shown there that this rise was independent of the presence of S vapour: samples heated in the absence of S (after an initial short sulfurisation) also showed the same improvement in EQE. The changes in EQE were mainly due to changes in acceptor concentration, and occurred over the same timescale as the changes in composition. This is a key result, because it suggests that if the acceptor density can be controlled, possibly by compositional control, then the sulfurisation time can be reduced such that true rapid thermal processing is a possibility.

The effect of sulfurisation background pressure was also examined, but was closely tied to the geometry of the sulfurisation system used herein. Lower pressures resulted in lower partial pressures of S vapour, which reduced the rate and extent of sulfurisation. The defect density of films sulfurised with low background pressures was high, giving them poor opto-electronic properties.

The key themes that emerged from the study of sulfurisation conditions were variations in (a) composition, (b) grain size and (c) band gap. The composition changed as a result of evaporation of elemental Zn from the precursor and, it is thought, SnS from decomposition of other sulfide phases. The former happens in the initial stages of heating before reaction with S. The latter manifests itself in two ways: (1) bulk decomposition of CZTS at pressures lower than 10 mbar, causing an accelerating loss, and (2) decomposition of Sn-containing secondary phases, which could be SnS_2 or $Cu_2ZnSn_3S_8$, even near atmospheric pressure. In the latter case loss of Sn is finite.

The grain size was correlated to the above-mentioned changes in Sn content, i.e. grains were larger at lower pressure and at longer times, when the Sn excess was the least.

The variations in band gap were considerable, but the trends were clear: higher band gaps were found after long sulfurisation times and at lower pressures. The reasons for this are not obvious, but two hypotheses were presented that can to a greater or lesser extent account for observations. The first hypothesis was a fundamental structural rearrangement of the CZTS phase between stannite and kesterite, which have been shown theoretically to have different band gaps. The second hypothesis concerned the possibility that a Sn-containing secondary phase was responsible for affecting the optical properties of the film. The recently reported $Cu_2ZnSn_3S_8$ phase is one candidate for this, and is analogous to some ‘ordered vacancy compounds’ seen in $CuInS_2$ and $CuInSe_2$.

The results in this report do not explain the apparent requirement for long sulfurisation times in two-stage processes for CZTS films. Possible reasons for the differences include:

1. The differences in sulfurisation conditions used here compared to those elsewhere: commonly slow heating and cooling rates are employed, and a continuous source of S is supplied from a H_2S atmosphere. Here, we used rapid heating, and the S source left the hot zone after around 5 min. It would be interesting to compare the effects of the different sulfurisation processes upon identical precursors.
2. The differences in methodology for measuring sample properties. In the vast majority of cases, CZTS films are made into complete devices, by addition of CdS and ZnO *n*-type layers, before their opto-electronic properties are measured. The device performance depends strongly on the interface between CZTS and CdS. This investigation found considerable variations in the CZTS band gap, which may affect this junction. The photoelectrochemical measurement does not rely on a convenient band alignment, so would not be affected in the same way. Measurements of the band gap and photoelectrochemical performance of films should be compared to the performance of the same films in devices.

6.2 The Role of Precursor Composition

The ternary phase diagram of Olekseyuk et al. was used throughout this report, and provides a good reference point from which to understand the effects of sample composition in terms of the likely secondary phases present. The secondary phase

$Cu_2ZnSn_3S_8$ was first suggested in the same study, and although it has not been experimentally confirmed in CZTS films, there are equivalent phases in other systems. The phase diagram is reproduced a final time below, along with the definitions of the composition labels in use here. It was found in this investigation that all samples adopted compositions on the dotted line in the diagram after sulfurisation and etching were complete, and this was taken to indicate that the CZTS-ZnS two-phase region was in fact larger at the temperatures used here (550–580 °C) than at those used to derive the phase diagram (400 °C). The compositions of the best devices in the literature are also shown. It is apparent that the best device compositions from the literature are within the Zn-rich region of the diagram, and not in the Cu-poor region, as commonly stated. That the Cu-content appears low is a consequence of the formation of a non-stoichiometric CZTS phase. The positions of the data points on the diagram indicate the formation of ZnS in the best devices.

In this investigation, the effects of Cu-content were studied. It was the intention to prepare samples which spanned the Cu-poor and Cu-rich regions of the phase diagram; however, Zn losses during sulfurisation pushed samples into the Zn-poor region, where Cu–Sn–S (Cu_2SnS_3 and Cu_4SnS_4) and Cu_2S phases are expected. The secondary phases could be visualised with SEM imaging, and in the most Cu-rich samples Cu_2S could be seen by XRD. The effects of increased Cu content during sulfurisation were clear—significantly larger grains were observed. In the $CuInS_2$ literature, larger grains are also associated with excess Cu due to a role of Cu_2S during film growth. The difference in the case of CZTS is that we can have not only Cu_2S but also Cu–Sn–S phases. It is not yet clear whether Cu–Sn–S phases have a similar effect on grain size as Cu_2S, but the largest grains in this investigation were seen where the concentration of Cu_2S itself would have been highest. In the case of $CuInS_2$, Cu_2S phases segregate to the very surface of the film, and are removed by KCN etching. In this investigation, the secondary phases did not segregate neatly but remained partially buried in the film. KCN etching removed them, but the post-etching morphology was particularly poor as a result, and this dominated the film properties despite the favourable grain size: the EQE data were consistent with a high acceptor concentration or the presence of recombination centres (e.g. embedded Cu–Sn–S grains). Since surface segregation of Cu_2S is complete in $CuInS_2$, and since there appear to be many other analogies with this material, it is possible that the Cu–Sn–S phases were responsible for the failure of surface segregation in this instance. A supporting example was found in the literature, where complete surface segregation of Cu-rich secondary phases in CZTS was seen, in addition to large (~ 2 μm) grains [1], although the study was not concerned with device fabrication. The reported composition of the sample places it within the Sn-poor region of the phase diagram, where Cu–S should be formed alongside ZnS. Therefore we suggest that the surface segregation of secondary phases is only efficient for Cu–S/ZnS, not for Cu–Sn–S phases. Cu–Sn–S phases may be too similar to the bulk CZTS phase to segregate from it. The Zn-poor region of the phase diagram should therefore be avoided.

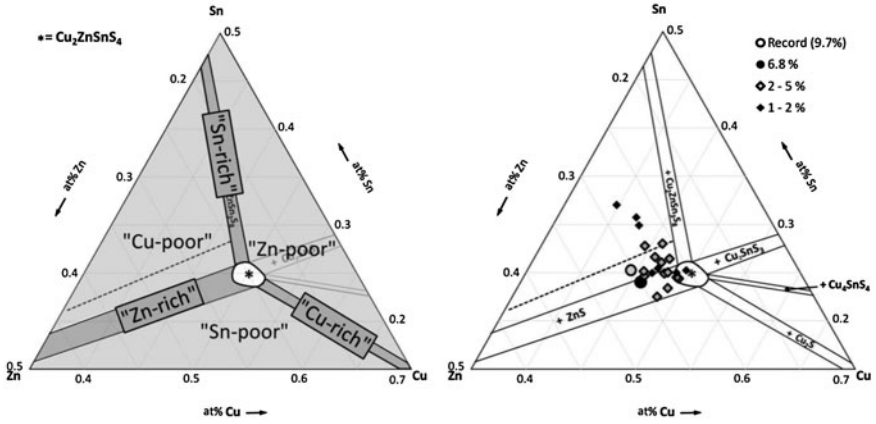

Fig. 6.1 The CZTS ternary phase diagram showing definitions of compositional labels used in this report (*left*) and the compositions of reported devices (*right*). Reproduced from Fig. 5.3

We can now, at least in part, rationalise the positions of the best devices on the phase diagram by looking at each of the compositional regions in turn:

1. *Stoichiometric*. The best devices are not in the single phase region of the phase diagram. This is interesting in itself, and could be either due to the preferential crystallisation of a non-stoichiometric phase, or to a stringent requirement to avoid certain secondary phases—presumably the Sn-bearing phases.
2. *Zn-rich*. Samples in this region should form ZnS alongside CZTS. This phase would be relatively benign in terms of the electronic properties of the film since it is effectively insulating, having a band gap of around 3.6 eV. The model of Chap. 3 placed excess ZnS at the top of the film, and so it should not have too much influence on film growth.
3. *Cu-poor, Sn-rich*. Precursors with compositions in these regions should form $Cu_2ZnSn_3S_8$, which seems to decompose during sulfurisation to yield a final composition that is in the Zn-rich region. This could certainly happen over the timescale of all the sulfurisation procedures mentioned in the literature. The loss of SnS from $Cu_2ZnSn_3S_8$ leaves only CZTS, and therefore this region would be 'second best', after the 'best' Zn-rich region, because samples can migrate into the Zn-rich region by loss of Sn. However, the growth model of Chap. 3 predicts that Sn-rich phases should form at the back of the film, and therefore before evaporating must pass through the film. As suggested by the correlation of grain size and excess Sn-content in Chap. 4, this secondary phase may inhibit grain growth. Functioning devices are found in the Cu-poor region, as seen in Fig. 6.1, but their efficiencies were low.
4. *Zn-poor, Cu-rich*. Zn-poor samples should form Cu–S and Cu–Sn–S secondary phases. In this investigation these phases appeared to be harmful to the film properties despite the increased grain size, because of their failure to surface-segregate. The pure Cu-rich region may yield good morphology without the

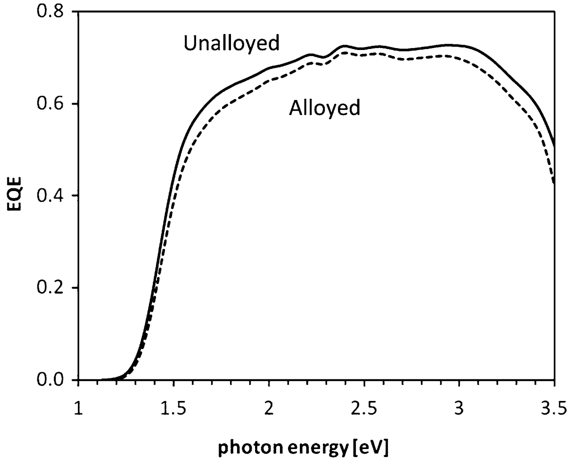

Fig. 6.2 EQE spectra recorded for a sample that had a composition in the Sn-poor region of the ternary phase diagram: Cu/(Zn + Sn) = 1, Zn/Sn = 1.4. Recorded in 0.2 M Eu(III) solution at a potential of −1.0 V vs. Ag|AgCl. Two sections of the same precursor were sulfurised. One section was alloyed beforehand, the other was sulfurised directly

harmful effects of Cu–Sn–S secondary phases, but this region is rather narrow, and no samples fell into it in this investigation due to evaporative losses of Zn. In general therefore, compositions in or near the Zn-poor region are undesirable. There are no reported functional devices with compositions in these regions, to the best of our knowledge. If good compositional control was available, then this region of the phase diagram provides the best opportunity to obtain single-phase CZTS, by etching away Cu–S after sulfurisation.

5. *Sn-poor*. No functioning devices have been produced in this region, to the best of our knowledge. However, there are some good reasons for attempting to do so. Firstly, compositions in this region should have only Cu–S and ZnS secondary phases, and avoid Sn-containing secondary phases. The growth-enhancing qualities of Cu–S (demonstrated here and elsewhere, and analogous to $CuInS_2$) should still operate, without the potentially harmful effects of Cu–Sn–S phases. The literature example cited above suggests that surface segregation of Cu–S should be achieved. After etching, which would be essential in these samples, the composition would be similar to that of the best devices, but the grain size may be enhanced.

In the current study, the importance of the phase diagram for predicting sample properties was not realised until after the final samples had been prepared—we point out that so far there is almost no discussion of phases other than CZTS in the literature, despite the highly non-stoichiometric compositions used. For this reason, a complete study of the different regions of the phase diagram was not carried out. The loss of Zn from the precursors also meant that in this investigation, most samples that were originally in the Sn-poor region moved into the Zn-poor region instead. Only one precursor fell into the Sn-poor region, due in fact to an error in the electrodeposition of the Zn layer. Limited characterisation of this sample was made at the time, but it was found later that the EQE spectrum, shown in Fig. 6.2, was far better than any seen elsewhere in the investigation: the band edge was sharper and the spectrum was flat over a large range. This provides some evidence that compositions in the Sn-poor region are indeed favourable. As a final result, this diagram also bears out a prediction of the growth model in Chap. 3: that alloying a stacked precursor will not make a significant difference to film formation. Therefore there is no need to intentionally alloy the precursor, and perhaps no benefit to manufacturing a mixed precursor.

Early work showing the apparent favourability of Cu-poor compositions may be part of the reason that there are no examples of devices in the Sn-poor region in the CZTS literature. Another possible reason for this is that the use of etching in the CZTS literature seems to be limited to only a few cases. The presence of the Cu–S phases which will inevitably occur in the Sn-poor region would be disastrous for device performance unless they were etched away before device completion.

6.3 Recommendations for Further Investigation

Based on the above conclusions, we can make some practical suggestions for future CZTS research:

1. Growth studies should be performed for samples within each region of the ternary phase diagram, with attention to the presence and distribution of secondary phases in the film.
2. The effect of sulfurisation time must be reinvestigated, both for films and complete devices, particularly with respect to the changes in acceptor concentration.
3. The acceptor concentration should be further investigated for different processing methods, and there is a clear need for more fundamental studies on the nature of defects in CZTS.
4. The observed band gap variations are interesting; and should be studied further, especially with regard to the band alignment with potential buffer layer materials.
5. The structural and optical properties of the secondary thiospinel phase $Cu_2ZnSn_3S_8$ should be studied, particularly with respect to its similarity to the ordered vacancy compounds found in the Cu–In–Se and Cu–In–S systems.
6. A hugely important contribution would be the elucidation of the ternary phase diagram in the Cu_2S–ZnS–SnS_2 system at temperatures closer to the typical CZTS synthesis conditions, i.e. around 550 °C.

In general, developments in the CZTS field are promising; device efficiencies are steadily improving and we can expect this to continue as the research effort expands. There are some useful analogies to made with the related CIS and CIGS materials, in terms of their chemistry as well as opto-electronic properties, which should be fully utilised in order to accelerate the development of CZTS. However, it is equally important to pay attention to the unique properties of CZTS, which include for example the additional secondary phases it can form, and the unique defects that it must possess. There is much further work to be done to optimise film performance, which requires both fundamental studies of the material as well as exploration of the behaviour of CZTS within device structures. The main role of this investigation has perhaps been to elaborate some fruitful areas for further study.

Reference

1. Weber A et al (2009) In situ XRD on formation reactions of Cu_2ZnSnS_4 thin films. physica status solidi (c) 6(5):1245–1248